Stability of Concentrated Dispersions

Doctoral thesis

for

the award of the doctoral degree

of the Faculty of Mathematics and Natural Sciences

of the University of Cologne

submitted by

Matthias Frangenberg

accepted in the year 2026

„If your experiment needs a statistician, you need a better experiment.“

Ernest Rutherford

Kurzzusammenfassung

Das Verhalten konzentrierter Polymerdispersionen wird durch komplexe Wechselwirkungen zwischen den Partikeln bestimmt, die sowohl die experimentelle Charakterisierung als auch die theoretische Interpretation erschweren. Die vorliegende Dissertation leistet einen Beitrag zum Verständnis der Stabilitätsmechanismen solcher Systeme, einem Forschungsfeld mit hoher Relevanz für Anwendungen in der Pharmaindustrie, bei Beschichtungen, in der Lebensmitteltechnologie und in der Entwicklung neuer fortschrittlicher Materialien wie Nanokompositen, Funktionsbeschichtungen und Hybridwerkstoffen. Herkömmliche optische Methoden stoßen bei der Untersuchung von Partikelgrößen, Zetapotenzialen und daraus abgeleiteten Stabilitätseigenschaften konzentrierter, opaker Dispersionen häufig an ihre Grenzen, da sie nicht in der Lage sind, da starke Lichtstreuung und -absorption in solchen Systemen die Anwendung optischer Verfahren erheblich einschränken. Um diese Herausforderungen zu überwinden, kombiniert die vorliegende Arbeit akustische Dämpfungs-spektroskopie (AAS) und elektroakustische Verfahren auf Basis des kolloidalen Vibrationsstroms (CVI), um wässrige Polymerlatices unterschiedlicher Partikelgröße und chemischer Zusammensetzung (PVC, SBR, PTFE, PU, PBAMM) direkt in ihrem ursprünglichen Zustand zu analysieren.

Zu den wichtigsten Beiträgen dieser Dissertation gehört die Optimierung der Bestimmung des Zetapotenzials durch die systematische Einbeziehung von Oberflächenleitfähigkeitseffekten in elektrokinetische Standardmodelle, wodurch teils erhebliche Messfehler in hochkonzentrierten Systemen vermieden werden. Darüber hinaus verbessern fortschrittliche theoretische Modelle, die explizit zwischen Oberflächenleitfähigkeit aus der stagnierenden und der diffusen Schicht unterscheiden, die Präzision von Zetapotenzialmessungen erheblich und validieren akustische Methoden gegenüber etablierten optischen Techniken.

Ein weiterer Schwerpunkt der Dissertation liegt auf der Entwicklung eines Ansatzes zur Bestimmung von Partikelgrößenverteilungen in Polymerdispersionen mit Hilfe der AAS, wobei die intrinsische Absorption der Partikel als entscheidender Faktor berücksichtigt wird. Durch die Einbeziehung dieses Faktors wird die Genauigkeit der Bestimmung mittlerer Partikelgrößen erheblich verbessert, auch wenn weiterhin Herausforderungen bei der Bestimmung der Verteilungsbreite bestehen.

Zur Bewertung der kolloidalen Stabilität erweist sich die akustische Dämpfung als ein leistungsfähiges Instrument zur Bestimmung der kritischen Koagulationskonzentration (CCC), insbesondere bei opaken und stark konzentrierten Dispersionen. Untersuchungen zur Tensidadsorption zeigen klare Zusammenhänge zwischen zunehmender Oberflächenbedeckung und verbesserter Dispersionsstabilität auf, was wertvolle Erkenntnisse für die Optimierung von Formulierungen liefert.

Insgesamt verbindet diese Dissertation modellbasierte Ansätze mit akustischen und elektroakustischen Charakterisierungsmethoden. Sie liefert methodische und konzeptionelle Fortschritte bei der Charakterisierung und Stabilisierung konzentrierter Polymerdispersionen und anderer kolloidaler Modellsysteme und eröffnet neue Perspektiven für deren Einsatz in wissenschaftlichen und industriellen Anwendungen.

Abstract

The behaviour of concentrated polymer dispersions is governed by complex interparticle interactions that challenge both experimental characterisation and theoretical interpretation. This dissertation contributes to the understanding of stability mechanisms in concentrated polymer dispersions, a field of research with high relevance for applications in the pharmaceutical industry, coatings, food technology and the development of new materials such as nanocomposites, functional coatings and hybrid materials. Traditional optical methods often fall short when probing particle size, zeta potential, and the stability properties derived from them in concentrated, opaque dispersions, because strong light scattering and absorption in such systems significantly restrict the application of optical methods. To overcome these limitations, this work combines acoustic attenuation spectroscopy (AAS) and electroacoustic approaches based on the colloidal vibration current (CVI) to analyse aqueous polymer latexes of different particle sizes and chemistries (PVC, SBR, PTFE, PU, PBAMM) in their native, undiluted state.

One of the most important contributions of this dissertation is the optimisation of zeta potential determination by systematically incorporating surface conductivity effects into standard electrokinetic models, addressing significant measurement errors in highly concentrated systems. Furthermore, advanced theoretical models that explicitly distinguishing contributions of the stagnant and diffuse layer to the surface conductivity significantly enhance the precision of zeta-potential measurements validating acoustic methods against established optical techniques.

The thesis also introduces an approach to determine particle size distributions in polymer dispersions using AAS, emphasizing the critical role of intrinsic particle absorption. By integrating this factor, the work significantly improves the accuracy of median particle-size estimates, although challenges remain for determining distribution width.

For assessing colloidal stability, acoustic attenuation proves to be a powerful tool for determining the critical coagulation concentration (CCC), especially beneficial in opaque and highly concentrated dispersions. Investigations into surfactant adsorption reveal clear correlations between increasing surface coverage and enhanced dispersion stability, yielding valuable guidance for formulation optimization.

Overall, this dissertation combines model-based approaches with acoustic and electroacoustic characterisation methods. It delivers methodological and conceptual advances in the characterisation and stabilisation of concentrated polymer dispersions and other colloidal model systems, opening new possibilities for their use in scientific and industrial applications.

Contents

1 Introduction

The stability of colloidal dispersions is a cornerstone for their successful application across diverse scientific and industrial domains, including pharmaceuticals,[1] coatings,[2] food science,[3] and new materials such as nanocomposites, functional coatings and hybrid materials.[4] These systems rely on finely dispersed particles to achieve unique properties, such as improved rheological properties,[5] enhanced stability during storage [6]or tailored optical [7] and mechanical characteristics.[8] Understanding and controlling stability are critical for ensuring functionality and performance, particularly in highly concentrated dispersions where interparticle forces and interactions play a decisive role.[9]

The characterization of colloidal particles, from synthesis to the final product, is essential to maintaining their stability. During synthesis, it is crucial to monitor compliance with process conditions to promote proper particle formation and stability. The quality of the final material must also be verified to ensure that its intended performance and functionality are preserved. This is particularly challenging in concentrated dispersions, where the interplay of factors such as particle density, size, charge and medium properties intensifies interactions, leading to greater structural and dynamic complexity. Consequently, developing effective methods for analysing such systems has become a pressing need in both research and industry.[10]

Proved characterization techniques, such as dynamic light scattering (DLS) and electrophoretic light scattering (ELS), are widely used to assess particle size and zeta potential. However, these methods rely on the detection of light, which cannot effectively penetrate concentrated dispersions. As a result, they require careful sample preparation and dilution, limiting their utility for direct measurements in concentrated systems. Addressing these limitations calls for advanced techniques that can probe the properties of dispersions in their native, undiluted state.[11]

In this context, acoustic measurement methods, including acoustic attenuation spectroscopy (AAS), also known as ultrasonic attenuation spectroscopy (UAS) and electroacoustics (EA), have emerged as powerful tools for characterizing concentrated dispersions. These techniques utilize sound waves, which can penetrate optically opaque materials, eliminating the need for complex sampling and preparation steps. By combining rapid, non-destructive analysis with applicability in concentrated systems, these methods offer a significant advantage over conventional optical techniques.[12]

This dissertation explores the stability of concentrated dispersions using polymer latices as model systems, chosen due to their underrepresentation in the literature [12,13] and employs advanced acoustic and electroacoustic characterization techniques to investigate key aspects of dispersion behaviour. Dispersion stability serves as the central link connecting all examined topics in this work. AAS provides valuable insights into particle size distribution and interparticle interactions, while EA methods, based on colloidal vibration current (CVI) measurements, are used to assess the zeta potential and offer insights into surface conductivity phenomena. The role of surfactant adsorption is further examined through its impact on the critical coagulation concentration (CCC), particularly in concentrated dispersions. This analysis provides important insights into how surfactants influence interparticle forces and enhance stability in concentrated dispersions. These measurements are complemented by optical reference methods, which are applicable only in highly diluted dispersions, enabling a comprehensive evaluation of the systems studied.

The overarching goal of this dissertation is to advance the understanding of stability in concentrated dispersions by addressing key challenges in quantifying colloidal behaviour. By integrating innovative experimental techniques with theoretical models, this research bridges the gap between theory and practice, offering strategies for the formulation of stable and functional dispersions.

2 Theoretical Background

This chapter introduces the fundamental concepts relevant to this work. The individual publications and publication drafts each contain a detailed theory section that provides a sufficiently precise basis for understanding the respective studies. Consequently, the theoretical background presented in this chapter is kept rather general and is based on well-established theoretical foundations related to the publications and drafts included in this dissertation. Its purpose is to give readers an introductory overview and orientation before the more specialized chapters that follow.

Chapter 2.1 discusses the stability of colloidal dispersions, Chapter 2.2 covers the electrokinetic phenomena and Chapter 2.3 addresses the particle size measurement methods used in this work.

2.1 Colloid Stability in Dispersions

The stability of colloidal systems is a fundamental aspect of colloid science, with significant implications in academic research and industrial applications. Colloidal dispersions are commonly classified by the physical states of the dispersed and continuous phases, with key types including suspensions, emulsions, foams, aerosols and gels. Their stability is governed by the interplay between multiple interaction forces, including van der Waals attraction, electrostatic double-layer repulsion and steric, depletion or hydration interactions.

The classical framework for describing colloidal stability is the DLVO theory, developed by Derjaguin and Landau,[14] and independently by Verwey and Overbeek.[15] This theory quantitatively accounts for the combined effects of attractive van der Waals interactions and repulsive electrostatic interactions, providing a fundamental explanation of the conditions under which colloidal dispersions remain stable or undergo aggregation. Energy–distance curves derived from DLVO theory allow for the prediction of colloidal behaviour under different conditions and have been extensively validated using model systems.

Beyond the DLVO framework, additional interaction forces can influence colloidal stability. In particular, steric stabilization arises when polymer chains are adsorbed or grafted onto particle surfaces, creating an entropic barrier that prevents aggregation. Other non-DLVO forces, such as depletion interactions and hydration forces, also contribute to the stability of colloidal dispersions and need to be considered in specific systems.

2.1.1 DLVO Theory

The DLVO theory provides a fundamental framework for understanding the stability of colloidal dispersions by considering the interplay between attractive and repulsive interactions. It was developed independently by Derjaguin and Landau [14] as well as Verwey and Overbeek [15,16] and it remains one of the most widely applied concepts in colloid science. The theory accounts for two key contributions: van der Waals attraction and double-layer repulsion, both of which determine whether particles in a suspension remain dispersed or aggregate.

To quantify these contributions, the interaction energy between two approaching colloidal particles is expressed as total potential energy V_T, that depends on the separation distance h between their surfaces. Assuming that individual interaction mechanisms act independently, the total interaction energy can be expressed as:

$$V_\mathrm{T} = V_\mathrm{EDL} + V_\mathrm{vdW}(+V_\mathrm{B}) \tag{2.1}$$

where V_EDL represents the electrostatic double-layer (repulsive) contribution and V_vdW the van der Waals (attractive) contribution. The term V_B, shown in brackets, refers to Born repulsion, while V_B is not included in the classical DLVO framework, it is often included in modern DLVO representations. [17]

The sign of V_T determines the nature of the interaction. If V_T is positive, repulsive forces dominate, preventing particle aggregation. Conversely, if V_T is negative, attractive forces predominate, which promotes particle aggregation. The van der Waals attraction originates from induced dipole interactions between molecules and acts over long ranges, leading to particle attraction. In contrast, the electrostatic double-layer repulsion arises from the overlap of electrical double layers surrounding charged particles, generating a repulsive force that counteracts attraction. The Born repulsion introduces an additional force resulting from the overlap of electronic orbitals, generating a strong short-range repulsion.

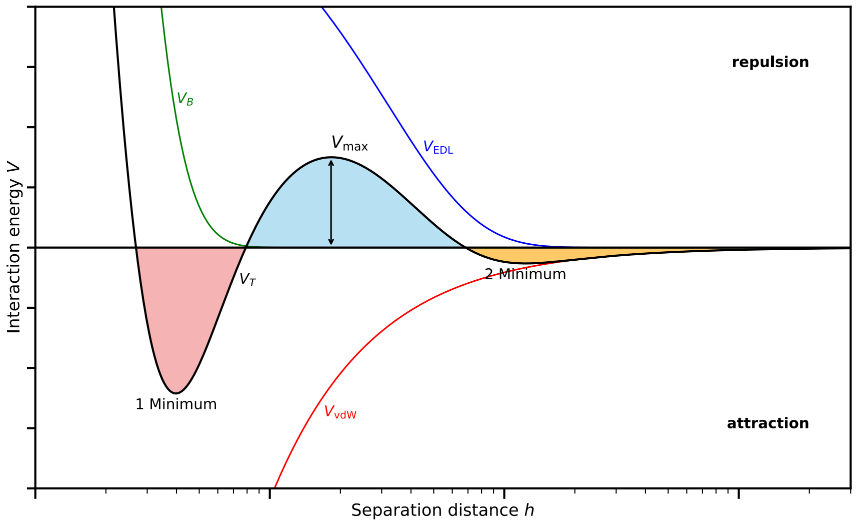

Fig. 2.1: Schematic representation of the DLVO interaction energy V_T as a function of the surface-to-surface separation distance h (log scale) between two colloidal particles. The total potential results from the superposition of van der Waals attraction V_vdW, electrostatic double-layer repulsion V_EDL and the short-range Born repulsion V_B.

Fig. 2.1 schematically illustrates how the total interaction energy V_T changes with the separation distance h, showing the combined effects of van der Waals attraction V_vdW, electrostatic double-layer repulsion V_EDL and the short-range Born repulsion V_B. The shape of the total interaction potential reveals distinct regions that determine colloidal stability. The primary minimum corresponds to a strong attractive potential, leading to irreversible aggregation of particles, also known as coagulation. In contrast, the secondary minimum appears at larger separation distances and represents a weaker attraction, allowing the formation of loosely bound structures referred to as flocculates. These aggregates remain reversible and can be redispersed by external influences, such as shear forces. The presence of an energy barrier, denoted as V_max, prevents particles from directly accessing the primary minimum. If this barrier is sufficiently high, thermal energy alone is insufficient to overcome it, thereby ensuring long-term stability. However, if the energy barrier is too low or absent, collisions between particles lead to coagulation.

Electrolyte concentration and ionic strength strongly influence the stability of colloidal systems. Increasing the ionic strength compresses the diffuse layer and reduces the effectiveness of electrostatic repulsion, leading to a lower energy barrier. At a characteristic minimum electrolyte concentration, the energy barrier V_max becomes zero, allowing rapid coagulation to occur, what is known as the critical coagulation concentration (CCC). This highlights the crucial role of surface charge and electrolyte composition in controlling colloidal stability.

2.1.1.1 Van der Waals Attraction

At an atomic or molecular level, van der Waals forces originate from three distinct contributions: Keesom interactions (dipole–dipole), Debye interactions (dipole–induced dipole) and London dispersion forces (induced dipole–induced dipole). In colloidal systems, only the latter is generally relevant, as colloidal particles, being large assemblies of atoms or molecules, tend to have no net dipole moment. London dispersion interactions arise due to temporary charge fluctuations within an atom or molecule, leading to a short-range attractive potential that decay with the inverse sixth power of the distance between atoms or molecules.

When considering macroscopic bodies such as colloidal particles, the cumulative effect of numerous atomic interactions makes the total van der Waals attraction significantly stronger than that between individual atoms or molecules. Under the classical Hamaker approach,[18] the van der Waals potential is calculated by summing pairwise interactions. For two identical spherical particles of radius a separated by distance h, the resulting potential is often written as:

$$V_\mathrm{vdW} = -\frac{A}{6}\left[\frac{2a^2}{h(4a+h)} + \frac{2a^2}{(2a+h)^2} + \ln\left(\frac{h(4a+h)}{(2a+h)^2}\right)\right] \tag{2.2}$$

where A is the Hamaker constant, which characterizes the material-dependent strength of the interaction, which depends on the materials of the particles as well as on the medium. For very small surface separations ($h \ll a$), the following approximation can be used:

$$V_\mathrm{vdW} = -\frac{Aa}{12h} \tag{2.3}$$

At larger separations, classical pairwise additivity overestimates the attractive force by neglecting the finite speed of electromagnetic fluctuations, a phenomenon known as the retardation effect. Essentially, there is a “delay” in how fluctuations in one particle influence those in the other. The Lifshitz theory [19] provides a rigorous framework for describing this behaviour by relating the van der Waals interaction to the frequency-dependent dielectric properties of the interacting media and the surrounding medium. [20,21] For the present discussion it is sufficient to note that retardation reduces the effective Hamaker constant with distance, thereby weakening the attraction at long range.[10]

2.1.1.2 Double Layer Repulsion

The electric double layer surrounding charged colloidal particles defines their individual electrostatic environment and governs their interactions in suspension. As two colloidal particles approach each other, their diffuse layers overlap, altering the local ion distribution. This overlap prevents the electrostatic potential from fully decaying between particles, resulting in an accumulation of counter-ions and a corresponding increase in osmotic pressure. Consequently, a repulsive force arises, counteracting attractive interactions.

The strength and range of this interaction depend on the thickness of the double layer, characterized by the Debye length κ^{-1}, which serves as an indicator of the extent of the electrochemical double layer:

$$\kappa^{-1} = \sqrt{\frac{\varepsilon_0 \varepsilon_\mathrm{m} k_\mathrm{B} T}{N_\mathrm{A} e^2 \sum_{i=1}^{N} z_i^2 c_i}} \tag{2.4}$$

where ε_0 is the vacuum permittivity, ε_m is the relative permittivity of the medium, k_B is the Boltzmann constant, T is the thermodynamic temperature, N_A is the Avogadro constant, e the elementary charge, z_i is the charge number of the i-th ion and c_i is its concentration.

Increasing electrolyte concentration or ion valency decreases the Debye length, enhancing electrostatic screening and reducing the range of repulsive interactions. This promotes particle aggregation. Conversely, at low electrolyte concentrations, the extended diffuse layers generate long-range repulsive forces, stabilizing the dispersion.

The electrostatic interaction between two charged particles depends on their separation distance h. When $h \gtrsim 2/\kappa$, the two double layers remain distinct, and the electrostatic potential decays to zero at the midpoint between the particles. However, when $h \lesssim 2/\kappa$, the double layers overlap, and the limited space prevents complete potential decay. As a result, the potential at the midpoint, $\psi_{h/2}$, remains finite, leading to a repulsive force. [22]

The electrostatic interaction energy V_EDL between two identical particles can be approximated by [15]:

$$V_\mathrm{EDL} = 2\pi\varepsilon_0\varepsilon_\mathrm{m} a \psi_0^2 \ln[1 + \exp(-\kappa h)] \tag{2.5}$$

where a represents the particle radius and ψ_0 is the surface potential. This approximation is valid for conditions involving relatively thin double layers (say $\kappa a > 10$) and low surface potentials [23].

For more accurate evaluations of interaction energy, methods based on osmotic pressure and the Maxwell stress tensor [24,25] or the free energy approach [26–28] are employed. These methods provide a description of how overlapping double layers modify ion distributions, surface charges, and diffuse layer structures, though their complexity typically necessitates numerical techniques to obtain precise solutions.[10]

2.1.2 Non-DLVO Forces

The classical DLVO theory, which centres on electrostatic and van der Waals forces, has proven insightful for analysing colloidal stability. However, many colloidal systems exhibit interaction forces that fall outside the scope of this classical theory. These additional interactions, collectively termed as “non-DLVO forces”, often arise at short separation distances and can significantly alter particle behaviour. They include steric repulsion from adsorbed macromolecules, depletion forces originating from excluded volume effects, hydration forces linked to structured solvent layers and hydrophobic interactions between nonpolar surfaces and neighbouring water molecules. By introducing additional repulsion or attraction, these forces can either change or completely dominate the predictions of classical DLVO theory, especially at small distances between the particles.

Steric stabilization occurs when non-ionic macromolecules such as polymers or other species adsorb onto colloidal particle surfaces and form repulsive layers that oppose van der Waals attraction. The efficiency of this effect depends on sufficient adsorption and is therefore strongly influenced by the particle surface, the properties of the adsorbed macromolecules and the solvent used. For this mechanism to be effective, sufficient and uniform adsorption is essential, as incomplete coverage can lead to bridging flocculation, where a single polymer chain connects several particles and promotes aggregation. In good solvents, the polymer chains are well solvated, extend into the medium and maximize the repulsive barrier. Under these conditions, the steric repulsion is mainly attributed to the loss of conformational entropy of the macromolecules, resulting from the spatial restriction of polymer chains as the particles approach one another. In contrast, under poor solvent conditions, the chains collapse, which diminishes the stabilizing effect. The molecular properties of the adsorbed species also play a decisive role. High molar mass increases layer thickness and range of repulsion, while charged groups add further electrostatic contributions. Steric stabilization remains effective even at high ionic strength, provided that the coverage is sufficient.[29–31]

Another mechanism is depletion, which occurs when non-adsorbing polymers, micelles, or small colloids are present in the dispersion. If the separation distance between particles falls below the characteristic size of these species, they are excluded from the gap, producing an osmotic pressure imbalance that pushes the particles together. The resulting attraction can induce flocculation, while at high concentrations structured arrangements of the solutes may lead to alternating zones of attraction and repulsion. [10,32]

When hydrophilic surfaces approach within a few nanometres in an aqueous medium, hydration forces can become significant. Although their exact origin remains under debate, most studies attribute them to strongly bound water layers or hydrated ions in the interfacial region. These give rise to a steep, exponentially decaying repulsion that persists even at high ionic strength or near the isoelectric point. The magnitude and decay length of this force are highly sensitive to surface chemistry and the organisation of adhered water molecules. [33–38]

In contrast, hydrophobic particles exhibit an additional attraction at short separations. It arises from the tendency of water to minimize contact with nonpolar surfaces, so that approaching particles reduce the interfacial area and the free energy of the system. At the molecular scale, several mechanisms have been proposed to account for this effect, including depletion or restructuring of interfacial water and density fluctuations within the restricted region. Such hydrophobic interactions can significantly enhance attraction and promote aggregation even under conditions where DLVO theory alone would predict stability. [30,39]

Non-DLVO forces can thus provide either additional repulsion or attraction beyond the classical DLVO framework. While the present work focuses on V_{EDL} and V_{vdW}, their recognition is essential for understanding colloidal behaviour in complex systems.

2.2 Electrokinetic Phenomena in Dispersions

The electrokinetic phenomena arise from the interaction between electric fields and fluid motion at charged interfaces. When a liquid flows past a charged surface (or vice versa), an electric potential is generated, governing particle movement, ion transport and electrochemical sensing. This chapter explores the principles of electrokinetics, focusing on the electrical double layer, the zeta potential and key measurement techniques for its determination.

2.2.1 Electrical Double Layer

When a charged surface comes into contact with an electrolyte solution, electrostatic interactions drive the redistribution of surrounding ions, forming an electrical double layer (EDL). This double layer consists of a region where counterions accumulate to balance the surface charge, while co-ions are repelled, creating a spatial separation of charge at the interface. As a result, the double layer behaves as an electrical capacitor, generating an electrostatic potential that influences colloidal stability.

Several theoretical models describe the structure and behaviour of the double layer, evolving over time to address increasing complexities. One of the first approaches, proposed by Gouy[40] and Chapman,[41] assumes that ions behave as point charges moving freely in solution, governed by thermal motion and electrostatic forces. This results in a diffuse cloud of counterions near the surface, with their concentration decreasing as a function of distance. The model predicts an exponential decay of the electrostatic potential with increasing distance and shows that increasing the electrolyte concentration enhances charge screening, thereby reducing the thickness of the double layer. However, the model does not consider finite ion size or specific ion-surface interactions, which limits its applicability.

The Stern-Grahame model[42,43] refines the concept of the double layer by introducing distinct structural regions as illustrated in Fig. 2.2. The double layer consists of the Stern layer near the surface and the diffuse layer extending into the bulk solution. The Stern layer, contains counterions that either adsorb specifically or remain electrostatically attracted. Within this layer, the inner Helmholtz plane (IHP) contains specifically adsorbed ions that have partially lost their hydration shell due to strong surface interactions, while the outer Helmholtz plane (OHP) marks the closest approach of fully hydrated counterions. The OHP separates the Stern layer from the diffuse layer, where ion concentration follows a Boltzmann distribution, gradually transitioning to bulk concentrations.

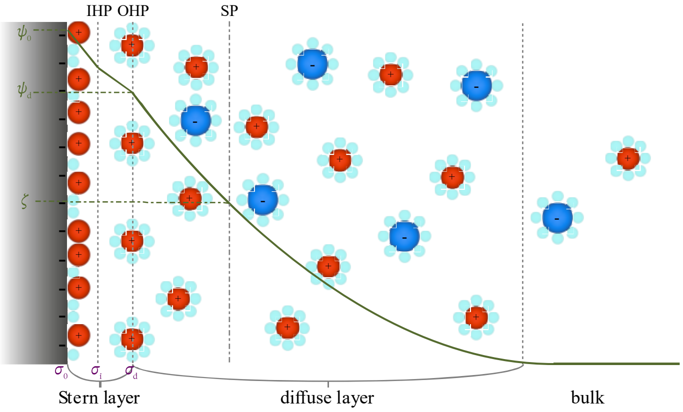

Fig. 2.2: Schematic representation of the electric double layer at a negatively charged interface. The double layer consists of the Stern layer, comprising the inner and outer Helmholtz planes (IHP, OHP) and the diffuse layer extending into the bulk solution. Key parameters such as surface potential surface potential ψ_0, Stern potential ψ_d and zeta potential ζ are indicated.

The electric potential varies as a function of distance from the charged surface due to charge separation between the surface and the ions in the Stern and diffuse layers. This separation generates an electric field, described by an electric potential ψ. At the surface, the potential ψ_0 is finite and has the same sign as the surface charge. Within the Stern layer, counterions accumulate to partially neutralize this charge, leading to a linear potential decrease. The surface charge density σ_0 represents the intrinsic charge at the surface. This charge is screened by counterions at the IHP, the remaining charge is denoted as σ_i, accounting for specifically adsorbed ions that have lost part of their hydration shell. At the OHP, where fully hydrated counterions accumulate, the charge density is further reduced and the electric potential at the interface of OHP and diffuse layer is denoted as ψ_d. Beyond the OHP, the diffuse layer extends into the bulk solution, the remaining net charge in this region is described by the charge density σ_d, which gradually vanishes as bulk equilibrium is reached. The potential $\psi(x)$ is described by the Poisson-Boltzmann equation, whose solution yields an exponential-like decay approaching zero in the bulk.

The slip or shear plane (SP) defines the boundary where the motion of the solvent transitions from a stagnant layer to bulk flow. Since ions in the Stern layer are largely immobilized, electrokinetic methods only detect the potential at the shear plane and not at the surface itself. The electrokinetic potential measured at this plane is called zeta potential ζ, providing an experimentally accessible indicator of colloidal stability and interfacial charge.

Other models have been proposed to account for additional complexities of the double layer. More advanced approaches such as the Bockris-Devanathan-Müller model[44] incorporate solvent structure and molecular interactions. Other recent studies incorporate specific ion adsorption and partial charge transfer[45] or electron transfer[46], further refining the understanding of the electrochemical double layers.

2.2.2 Zeta Potential

As stated before, the zeta potential is an important electrokinetic parameter that characterizes the electrostatic potential at the slip plane, where fluid motion separates from the charged interface. It is the experimentally accessible quantity in electrokinetic measurements and provides insight into colloidal stability, particle interactions, and interfacial charge effects.

To determine the zeta potential, various electrokinetic measurement techniques can be employed. This section focuses on the two principal methods used in this work: electrophoresis and electroacoustic techniques. Electrophoresis quantifies the migration velocity of charged particles in response to an applied electric field, providing a direct correlation with the zeta potential. Electroacoustic methods, depending on the approach, either analyse the electrical signal generated by acoustic waves interacting with charged particles or measure the acoustic response induced by an applied electric field. In this work, colloid vibration current (CVI) is the primary technique, as it allows for the determination of zeta potential in concentrated dispersions where electrophoresis is not applicable. The following sub-sections provide a detailed examination of these methods.

2.2.2.1 Electrophoresis of Particle Dispersions

Electrophoresis is a fundamental and widely utilized technique for determining the electrophoretic mobility μ of particles dispersed in an electrolyte solution. The electrophoretic mobility is defined as:

$$\mu = \frac{v_\mathrm{p}}{E} \tag{2.6}$$

where v_p is the particle velocity under an applied field and E is the electric field strength. This parameter is particularly significant as it provides valuable insights into the particle surface charge characteristics through the calculation of their zeta potential ζ. The motion of charged particles under the influence of an applied electric field E provides insight into their surface charge properties and interfacial interactions.[47]

As illustrated in Fig. 2.3, charged particles migrate toward the oppositely charged electrode when an electric field E is applied. The primary driving force arises from the particle's net surface charge interacting with the external field E_ext, while frictional shear within the fluid (referred to as viscous drag) opposes that motion by resisting the relative movement between the particle and the surrounding medium. Counterions in the EDL surrounding each particle also move in the opposite direction, dragging solvent with them and partially retarding the particle motion. This phenomenon is known as electrophoretic retardation. All these forces together contribute to the particle velocity υ_p.[48,49]

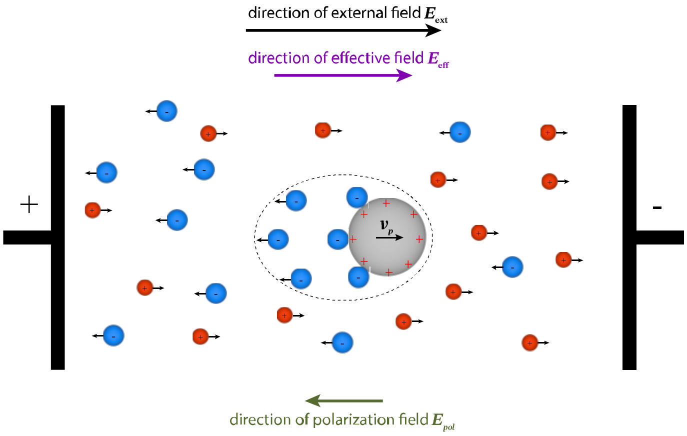

Fig. 2.3: Schematic representation of electrophoresis for a positively charged colloidal particle in an electrolyte under an applied electric field E_ext. The electrostatic force drives the particle motion with velocity υ_p, opposed by viscous drag and electrophoretic retardation. Relevant parameters such as the diffuse layer, polarization field E_pol, effective field E_eff and slip plane are indicated.

When the surface potential ψ_0 or zeta potential ζ is large, two additional phenomena can significantly alter the observed electrophoretic mobility μ. The first is the relaxation effect, or double-layer polarization, which reflects the distortion of the ionic atmosphere around the particle. As the particle moves, ions in the diffuse layer cannot instantaneously adjust, so an asymmetric ion distribution develops: excess counterions accumulate behind the particle, while a relative depletion appears in front. This asymmetry creates a polarization field E_pol that is directed opposite the externally applied field E_ext and lowers the net electrostatic force on the particle.[48] The second phenomenon is surface conductivity K^σ. The elevated concentration of counterions in the electric double layer facilitates additional current flow along the particle surface, causing part of the applied voltage to dissipate within the double layer itself. This reduces the effective field strength E_eff acting on the particle compared to the externally applied field E_ext. Consequently, the measured electrophoretic mobility μ is lower than it would be in the absence of this effect. If surface conductivity is not taken into account, the resulting zeta potential ζ is underestimated. This underestimation becomes more pronounced, when the ionic strength or dispersion medium conductivity K_m is low, or when the particle radius a is small. Under such conditions, the electric double layer becomes more extended, and a larger portion of the applied potential difference is dissipated within the double layer, further reducing the effective field on the particle. This effect is captured by the so called Dukhin number ($Du = K^\sigma / K_\mathrm{m} a$), which quantifies the relative importance of surface conductivity.[49–52]

One of the most common methods for the determination of the electrophoretic mobility μ is electrophoretic light scattering (ELS), which determines particle velocity υ_p by analysing the frequency shift of scattered laser light. The technique utilizes the Doppler effect, where the frequency of light scattered by moving particles is altered relative to a reference beam, and this shift is directly proportional to particle velocity. By precisely measuring these velocity-dependent shifts, ELS enables accurate determination of electrophoretic mobility, thereby providing insights into the zeta potential characteristics of the particles.[53,54]

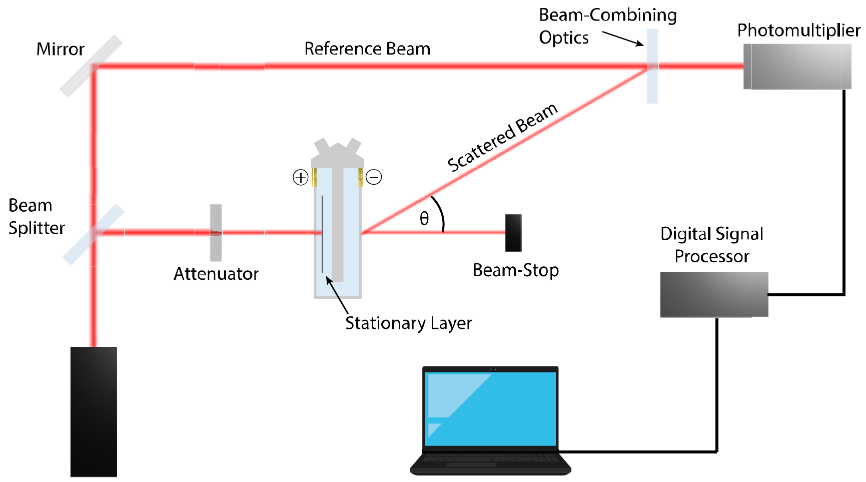

Fig. 2.4.: Schematic illustration of an electrophoretic light scattering (ELS) setup. A laser beam is divided into a reference and a probe path; the probe passes through a cuvette containing charged particles between two electrodes. The interference of the scattered and reference beams enables determination of the electrophoretic mobility from Doppler frequency shifts.

In this approach (see Fig. 2.4), a coherent laser beam is split into two paths to form an interference pattern in the sample cuvette. Traditionally, measurements were carried out in the stationary layer, defined as the region where electroosmotic flow (solvent motion induced along the charged cell walls by the applied electric field) is exactly balanced by counterflow so that the net solvent velocity is zero, thereby ensuring that particle motion was measured without artefacts from bulk fluid movement. In modern ELS instruments, however, software-based correction methods allow reliable measurements without the strict requirement to focus on this stationary layer. The dispersion, containing charged particles, is placed between two electrodes so that an external electric field can be applied. When the field is switched on, the charged particles migrate toward the oppositely charged electrode, scattering the incident laser light in the process. The scattered light is then combined with a reference beam, producing an interference signal detected at a specific angle by a photodetector. A digital signal processor analyse the fluctuations in scattered intensity to extract the Doppler shift, from which the particle velocity is obtained.[55,56]

Unlike other techniques that yield only a single mobility value, this setup provides a mobility distribution. The processed data are computationally analysed to determine the complete electrophoretic mobility distribution, resolving the magnitude and sign of the electrophoretic mobility. To derive the zeta potential from measured electrophoretic mobility, various theoretical models are employed, each applicable under specific conditions. The selection of an appropriate model is crucial, as the accuracy of zeta potential calculations can be significantly affected by ionic strength, surface conductivity, material and solvent properties (such as permittivity and viscosity), as well as particle size and shape.[49] Several theoretical models for converting electrophoretic mobility into zeta potential, including the Smoluchowski, Huckel, O'Brien and White, and Dukhin and Semenikhin approaches, are discussed in detail in the subsequent chapters.

Several methodological refinements improve the precision and accuracy of ELS measurements. In earlier implementations, measurements were often performed in the stationary layer, where bulk electroosmotic flow is absent, to minimise background scattering. Modern instruments, however, achieve the same effect through optical and software-based corrections. Incorporating an additional optical reference beam stabilizes signal processing, allowing for the analysis of weakly scattering samples. The electrode design also influences measurement accuracy by minimizing fluid flow artifacts that could otherwise affect the determination of electrophoretic mobility. These optimizations make ELS a highly reliable method for studying colloidal dispersions.[54]

2.2.2.2 Electroacoustic Methods

Electroacoustic phenomena describe how sound waves interact with charged particles in a suspension, providing insights into charge transport and electrokinetic behaviour even in opaque or highly concentrated dispersions. Conventional techniques such as electrophoresis often fail under these conditions because of multiple light scattering and sedimentation. By driving an acoustic wave through a colloidal dispersion, particles and the fluid move at different rates due to density contrasts, causing the electrical double layer around the particles to distort. This distortion redistributes ions and generates an alternating electric field that underpins electroacoustic methods.[12]

Two important measurement modes are related to this phenomenon: the colloid vibration current (CVI) and the colloid vibration potential (CVP). Both originate from the same charge displacement mechanism of the EDL but differ according to the impedance of the measuring circuit. When an ultrasonic transducer sends an acoustic pulse into the suspension, oscillating particles induce dipole moments that create an electric field. A low-impedance measurement captures the current (CVI), while a high-impedance setup measures the potential (CVP). Both signals display notable frequency dependence, with electrostatic interactions being dominant at lower frequencies and inertial or hydrodynamic effects becoming significant at higher frequencies. Fig. 2.5 A illustrates the generation of CVI and CVP. In practice, a CVI probe consists of a piezoelectric transducer to produce an acoustic pulse and two electrodes to detect the resulting electric field.

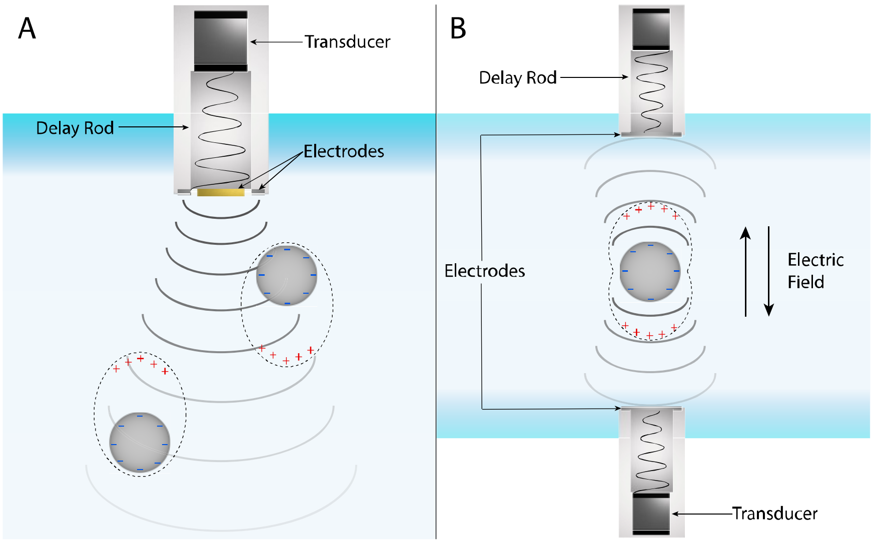

Fig. 2.5: Schematic representation of electroacoustic measurement principles. **A:** Generation of the colloid vibration current (CVI) and colloid vibration potential (CVP) by an acoustic pulse acting on charged particles. Depending on the measurement impedance, either the current (CVI) or potential (CVP) is recorded. **B:** Generation of the electrokinetic sonic amplitude (ESA) signal by applying an alternating electric field to the dispersion.

Another type of electroacoustic measurement is the electrokinetic sonic amplitude (ESA), which applies an oscillating electric field to the dispersion and monitors the resulting acoustic wave. Rather than measuring the electrical response to an acoustic wave, ESA inverts the process by creating oscillations of charged particles that generate pressure waves. The electric field is delivered by electrodes, while a transducer, often including a delay rod to reduce noise, measures the induced sound waves. The amplitude of this acoustic signal depends on factors such as the applied field strength, particle size, zeta potential, and density contrast between particles and fluid. By analysing the resulting ESA signal, the zeta potential and particle size can be determined. Fig. 2.5 B shows the generation of ESA signal.

Early theoretical descriptions of electroacoustic phenomena go back to Enderby and Booth [57,58], who developed a model incorporating surface conductivity and low-frequency effects. However, their approach did not account for interactions between particles, restricting its validity to dilute dispersions. Later refinements by Marlow, Fairhurst, and Pendse [59] sought to adapt this framework for more concentrated systems by employing the Levine cell model [60], but the complexity of the resulting equations hindered its practical use. A major shift occurred when O'Brien [61] introduced the concept of dynamic electrophoretic mobility, which unifies key parameters such as zeta potential, particle size and frequency into a coherent electroacoustic framework. He demonstrated that ESA is directly proportional to this mobility, with the proportionality factor being independent of frequency, particle size and zeta potential. Initially developed for ESA, this concept has been extended to other electroacoustic techniques. O'Brien's initial formulation, which applied only to dilute systems, was later expanded by Rider and O'Brien [62], Ohshima [63] and Ennis et al. [64] to include particle–particle interactions, thereby making it applicable to concentrated dispersions as well.[12]

Beyond O'Brien's contributions, additional theoretical developments have emerged to improve descriptions of electroacoustic behaviour in complex suspensions. Notably, Shilov, Ohshima, Dukhin and Goetz [65–67] advanced a more comprehensive theory that integrates elements of both the Enderby–Booth and O'Brien approaches. This theoretical framework plays a central role in the analyses presented in Chapters 4 and 5 of this work. Their work expanded CVI theory to encompass effects such as particle inertia, surface conductivity, double-layer relaxation, thermodiffusion and barodiffusion. Furthermore, it provided a direct link to the Smoluchowski equation, ensuring theoretical consistency across a broad range of concentrations and particle configurations.[12]

2.3 Particle Sizing Methodology

Particle size and shape are fundamental properties of colloidal dispersions. While idealized monodisperse systems are useful for theoretical studies, real-world dispersions are typically polydisperse, requiring various simplifications and approximation methods for their description.

A central concept in the characterization of polydisperse systems is the particle size distribution (PSD), which describes the relative occurrence of particle sizes within a sample. PSDs are typically visualized as histograms, density functions or cumulative distribution curves. While histograms (Hist.) and probability density functions (PDF) represent the frequency of particles across defined size intervals either as discrete bars or continuous curves, cumulative distribution functions (CDF) indicate the fraction of particles smaller than a given size. An example of such a representation is shown in Fig. 2.6, where a log-normal fit has been applied to the data to derive both PDF and CDF.[68,69]

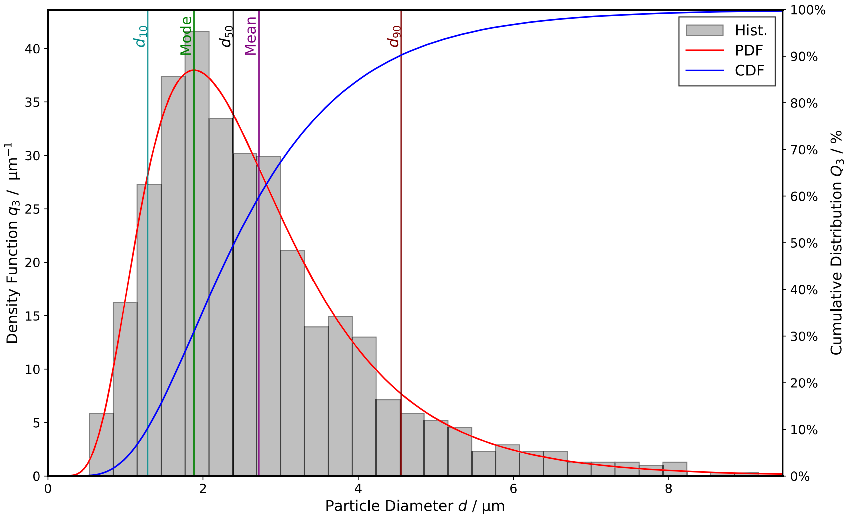

Fig. 2.6: Representation of a particle size distribution (PSD) showing histogram (Hist.), probability density function (PDF), and cumulative distribution function (CDF). A log-normal fit was applied to the histogram data, and characteristic percentiles d_{10}, d_{50} and d_{90}, as well as the mean, median, and mode are indicated.

PSD is often described using statistical parameters such as d_{10}, d_{50} and d_{90}, denoting the particle diameters below which 10 %, 50 % and 90 % of the sample lies, respectively. The median size d_{50} represents the central tendency and is less sensitive to outliers than the arithmetic mean. The width of the distribution can be characterized by the span, defined as $(d_{90} - d_{10}) / d_{50}$, or by the standard deviation, which quantifies the absolute spread of particle sizes around the mean, and is obtained as the square root of the variance of the (number-, surface-, volume-or mass-weighted) size distribution. A low span or standard deviation indicates a more uniform system, while higher values reflect broader, more heterogeneous distribution. Additional descriptors include the mean, mode and median. The mean is the arithmetic average of all particle sizes and may be calculated with different weighting schemes: number-, area-, or volume/mass weighted. The mode reflects the most frequently occurring size, indicating the dominant size class. As previously noted, the median corresponding to d_{50} divides the distribution into two equal halves and provides a robust indicator of central tendency. Different mean diameters provide insight into various aspects of the PSD. A number-weighted mean treats all particles equally, emphasizing smaller particles that tend to be more numerous. The area-weighted mean accounts for the total surface area, making it relevant for surface-dominated processes like adsorption or catalysis. The volume-weighted mean, which emphasizes larger particles due to the cubic relationship between size and volume, reflects the contribution of particle size to the overall material volume or mass and is therefore crucial when the physical impact of larger particles dominates the system's behaviour. In systems with uniform particle density, mass-weighted distributions convey the same information as volume-weighted ones, making the two effectively interchangeable for many practical applications.[68,69]

A critical consideration is that different measurement techniques probe different properties of the particle population, potentially yielding divergent results. Number-based methods are more sensitive to small particles, whereas volume-based techniques highlight larger ones. As a result, PSDs obtained using different methods are often not directly comparable.[70]

Various mathematical models are used to describe PSDs. A normal (Gaussian) distribution is appropriate when size variations result from numerous small, independent effects, producing a symmetric curve. However, log-normal distributions are more common in practice, as they better capture the multiplicative nature of particle growth and fragmentation processes. In some cases, bimodal or multimodal distributions appear, reflecting distinct particle formation or aggregation mechanisms within a system.[70]

Accurate characterization of particle size is essential in both research and industrial contexts. Since no single technique can fully describe all aspects of a polydisperse system, a combination of complementary measurement methods and appropriate statistical models is necessary to achieve a comprehensive understanding.

This chapter introduces the experimental determination of particle size distributions, beginning with Acoustic Attenuation Spectroscopy (AAS) as a method suited to concentrated and optically dense dispersions. It then turns to Dynamic Light Scattering (DLS) and Laser Diffraction Spectroscopy (LDS), which serve as optical reference methods in the dilute regime. Together, these approaches provide the basis for comparing particle size data across varying concentration ranges and measurement conditions.

2.3.1 Acoustic Attenuation Spectroscopy

Acoustic Attenuation Spectroscopy (AAS) is a powerful technique for characterizing particle size in suspensions that are too concentrated or otherwise optically opaque thus unmeasurable for conventional light-based methods. Its core principle relies on determining the overall reduction in sound intensity as it travels through a sample. This reduction is quantified through the total attenuation coefficient α, which is calculated by comparing the measured sound intensity after a known distance x to the initial intensity I_0. The calculation follows:

$$\alpha = -\frac{1}{x} ln\left(\frac{I_0}{I_x}\right) \tag{2.7}$$

where I_x is the intensity after propagation through the sample.[71] In this framework, α and the sound velocity c are connected to the complex wave number k (Eq. 2.8), with f denoting the ultrasonic frequency and i representing the imaginary unit.[72]

$$k = \frac{2\pi f}{c} + \alpha i \tag{2.8}$$

Dissipation is a natural part of sound propagation because sound waves are, at their core, moving disturbances in an otherwise balanced system. The total attenuation coefficient α can be considered as the sum of four primary mechanisms:

$$\alpha = \alpha_{\text{vis}} + \alpha_{\text{th}} + \alpha_{\text{sc}} + \alpha_{\text{int}} \tag{2.9}$$

Viscoinertial losses α_{vis} arise from the relative motion between particles and the fluid in the oscillating pressure field; the greater the density contrast between the particles and the fluid, the more pronounced the relative motion and the resulting viscous friction. Thermal losses α_{th} result from heat exchange between particles and the surrounding fluid, driven by temperature gradients that arise mainly due to viscoinertial dissipation. Scattering losses α_{sc} cause partial redirection of the sound energy via reflection, refraction, or diffraction; though these losses do not cause dissipation, they nevertheless reduce the intensity measured along the original propagation path. Intrinsic absorption α_{int} refers to the material-dependent sound absorption of both the particles and the surrounding medium and remains independent of particle size.[12]

A common assumption in many AAS models is that dispersed particles remain much smaller than the wavelength of sound. In mathematical form, this long wave regime (LWR) is expressed by:

$$ka = \frac{2\pi a}{\lambda} \ll 1 \tag{2.10}$$

where a is the particle radius and λ is the sound wavelength. When the system adheres to the LWR condition, the usual scattering effects are negligible, only pulsation and oscillation occur and the attenuation is mainly a result of dissipation (α_{vis}, α_{th} and α_{int}). With this limitation, both the theoretical analysis and the measurement technique can be significantly simplified.

These principles are illustrated schematically by Fig. 2.7. In this method, an ultrasonic wave of initial intensity I_0 propagates through a suspension over a defined path length x, resulting in a transmitted intensity I_x. The total attenuation coefficient α is then obtained from the exponential decay of sound intensity, as expressed by Eq. 2.7. The measured attenuation arises from multiple coexisting mechanisms such as viscoinertial, thermal, scattering and intrinsic absorption losses, which collectively govern the overall energy dissipation in the system.

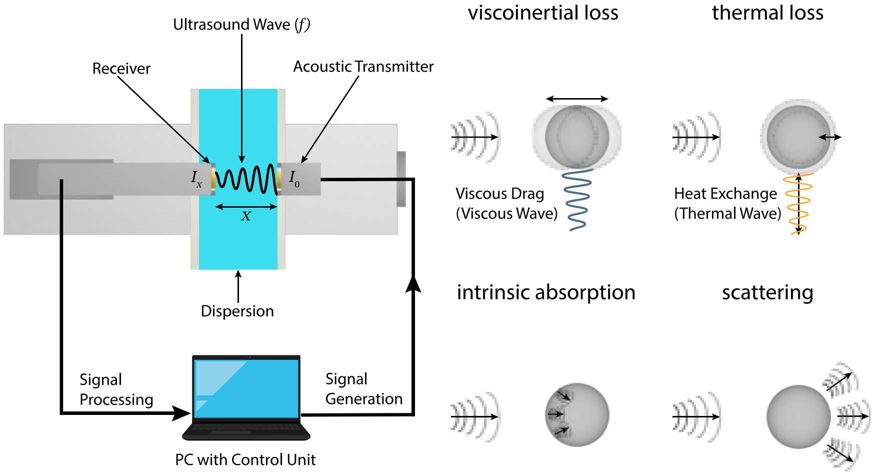

Fig. 2.7: Schematic representation of acoustic attenuation spectroscopy (AAS). **Left:** Experimental setup showing the propagation of an ultrasonic wave of initial intensity I_0, which propagates through a suspension over a known path length x, with the transmitted intensity I_x detected by a receiver. **Right:** Illustration of the main mechanisms contributing to the total attenuation coefficient α, including viscoinertial, thermal, scattering and intrinsic absorption losses.

The experimental development of ultrasonic spectroscopy dates back to the mid-twentieth century, with early contributions from Pellam and Galt[73], followed by Pinkerton[74]. These foundational studies led to the construction of the first ultrasonic spectrometers,[75,76] which allowed for precise attenuation measurements.

Interpretation of an attenuation spectrum depends especially on the particle concentration. In dilute dispersions, particle interactions are negligible, so each particle contributes independently to the measured signal. The total spectrum is therefore a sum of single-particle responses, creating a linear relationship between the size distribution and the data and reducing the evaluation to a linear inversion problem. In concentrated dispersions, hydrodynamic coupling and multiple scattering break this linearity; recovering reliable size information demands more advanced theoretical models that capture collective effects. [67,77]

While acoustic attenuation spectroscopy offers real-time, non-invasive access even to highly loaded systems, its accuracy hinges on precise knowledge of material parameters, and broad, polydisperse size distributions further complicate the inversion. The treatment of both concentration regimes, together with strategies to mitigate these practical limitations, is presented in later sections.

2.3.1.1 Dilute Dispersions

The theoretical foundation of acoustic attenuation in dilute suspensions was established through the work of Epstein and Carhart,[78] who developed an analytical approach for sound propagation in emulsions. This approach was subsequently extended by Allegra and Hawley [79] to include elastic and highly viscous particles, along with experimental validation. Their formulation, commonly known as the Epstein-Carhart-Allegra-Hawley (ECAH) theory, remains the most widely used model for predicting attenuation in monodisperse (i.e. particles of uniform diameter), spherical and dilute dispersions, where particle–particle interactions are negligible. The ECAH theory is a rather complex single-scattering theory based on the assumption of isolated, non-interacting particles and therefore predicts a linear dependence of sound attenuation on particle concentration. In principle, the theory is applicable across all frequencies. However, in the LWR and in the case of very dilute systems the attenuation coefficient can be considerably simplified and separated into the different loss mechanisms. Under these assumptions the expression for the viscoinertial loss α_{vis} is:[80,81]

$$\alpha_{\mathrm{vis}} = \frac{\varphi}{2}\frac{\Omega_{\mathrm{d}}}{c_{\mathrm{m}}\rho_{\mathrm{m}}}\frac{(\rho_{\mathrm{p}}-\rho_{\mathrm{m}})^2}{(\rho_{\mathrm{p}}+\rho_{\mathrm{m}}\Omega_{\mathrm{i}})^2+\left(\frac{\Omega_{\mathrm{d}}}{\omega}\right)^2} \tag{2.11}$$

with the dissipative Ω_{d} and inertial Ω_{i} drag coefficients:

$$\Omega_{\mathrm{d}} = \frac{9\eta}{2a^2}\left(1+\sqrt{\frac{a^2\omega\rho_{\mathrm{m}}}{2\eta}}\right) \tag{2.12}$$

$$\Omega_{\mathrm{i}} = \frac{1}{2}\left(1+\frac{9}{2}\sqrt{\frac{2\eta}{a^2\omega\rho_{\mathrm{m}}}}\right) \tag{2.13}$$

where, φ is the particle volume fraction, a the particle radius, c_{m} and ρ_{m} the sound speed and density of the suspending medium, ρ_{p} the particle density, η the dynamic viscosity of the medium and $\omega = 2\pi f$ the angular frequency.

Under the conditions described above, the following expression for the thermal attenuation α_{th} is obtained by ECAH theory:[79,80]

$$\alpha_{\mathrm{th}} = \frac{3\varphi c_{\mathrm{m}} T\rho_{\mathrm{m}}\tau_{\mathrm{m}}}{2a^2}\left(\frac{\beta_{\mathrm{m}}}{\rho_{\mathrm{m}}C_{\mathrm{p}}^{\mathrm{m}}}-\frac{\beta_{\mathrm{p}}}{\rho_{\mathrm{p}}C_{\mathrm{p}}^{\mathrm{p}}}\right)^2 \mathrm{Re}(H) \tag{2.14}$$

with the interfacial heat transfer coefficient H defined as:

$$H = \left[\frac{1}{1-iZ_{\mathrm{m}}}-\frac{\tau_{\mathrm{m}}}{\tau_{\mathrm{p}}}\frac{\tan Z_{\mathrm{p}}}{\tan Z_{\mathrm{p}}-Z_{\mathrm{p}}}\right]^{-1} \tag{2.15}$$

where

$$Z_{\mathrm{m}} = (1+i)\sqrt{\frac{a^2\omega\rho_{\mathrm{m}}C_{p}^{\mathrm{m}}}{2\tau_{\mathrm{m}}}} \tag{2.16}$$

$$Z_{\mathrm{p}} = (1+i)\sqrt{\frac{a^2\omega\rho_{\mathrm{p}}C_{p}^{\mathrm{p}}}{2\tau_{\mathrm{p}}}} \tag{2.17}$$

Here T is the absolute temperature, τ_{m} and τ_{p} are the thermal conductivity of the medium and particles, respectively, β_{m} and β_{p} are the volumetric thermal-expansion coefficients and $C_{\mathrm{p}}^{\mathrm{m}}$ and $C_{\mathrm{p}}^{\mathrm{p}}$ are the isobaric specific-heat capacities.

The form of the scattering attenuation α_{sc}, valid under the above assumptions, is:[12,79]

$$\alpha_{\mathrm{sc}} = \frac{\varphi\omega^4a^3}{2c_{\mathrm{m}}^4}\left[\left(\frac{1}{3}\left(1-\frac{\rho_{\mathrm{m}}c_{\mathrm{m}}^2}{\rho_{\mathrm{p}}c_{p}^2}\right)\right)^2+\left(\frac{\rho_{\mathrm{p}}-\rho_{\mathrm{m}}}{2\rho_{\mathrm{p}}+\rho_{\mathrm{m}}}\right)^2\right] \tag{2.18}$$

where c_p is the sound speed within the particles.

In case of the intrinsic absorption α_int within the LWR, McClement and Coupland [82] derived a simple expression for monodisperse, spherical and dilute dispersions:

$$\alpha_\mathrm{int} = (1-\varphi)\alpha_\mathrm{m} + \varphi\alpha_\mathrm{p} \tag{2.19}$$

where α_m and α_p are the intrinsic absorption coefficients of the medium and the particle material, respectively.

2.3.1.2 Concentrated Dispersions

In concentrated colloidal dispersions, particle-particle interactions become significant, altering the mechanisms governing acoustic attenuation. Unlike dilute systems, where the attenuation spectrum primarily results from single-particle contributions, concentrated dispersions require additional theoretical considerations. The transition from dilute to concentrated conditions is not merely a matter of increasing volume fraction; rather, it fundamentally changes how acoustic waves propagate through the system, necessitating more sophisticated modelling approaches.[83]

When ultrasound propagates through a fluid containing particles, three types of waves are generated at each particle: compressional waves (i.e., classical sound waves), viscous (transverse) waves and thermal waves. Compressional waves can travel relatively far through the medium, whereas viscous and thermal waves decay rapidly and propagate only over short distances. For this reason, the latter are neglected in models for dilute dispersions.

The spatial extent of viscous and thermal wave propagation is described by the corresponding penetration depths. These represent the distances over which the wave amplitudes decrease by a factor of 1/*e*. The viscous penetration depth δ_η and the thermal penetration depth δ_th are given by the following expressions:

$$\delta_\eta = \sqrt{\frac{2\eta}{\omega\rho_\mathrm{m}}} \tag{2.20}$$

$$\delta_\mathrm{th} = \sqrt{\frac{2\tau_\mathrm{m}}{\omega\rho_\mathrm{m}C_\mathrm{p}^\mathrm{m}}} \tag{2.21}$$

Both penetration depths are strongly frequency-dependent and become shorter at higher frequencies. As the particle concentration increases, the average distance between particles may become smaller than the viscous or thermal penetration depth. Under such conditions, the assumption of isolated scattering breaks down. The incident wave at a given particle then consists not only of the original excitation but also of the waves scattered by neighbouring particles. This mutual interaction leads to multiple scattering, where already-scattered waves are scattered again. As a result, attenuation is no longer linearly related to concentration and nonlinear effects emerge that the theory for dilute dispersions cannot account for.

Theoretical approaches for the description of the nonlinear acoustic attenuation in concentrated colloidal dispersions are based on two distinct modelling philosophies: scattering models and coupled-phase models.

Scattering models focus on wave–particle interactions at the microscopic level and extend single particle theories by incorporating the effects of multiple scattering. These models calculate the coherent wave propagation through the medium by summing contributions from all particles, accounting for the modifications of the local wave field caused by surrounding particles. Classic multiple scattering formulations such as those by Lloyd and Berry [84] and Waterman and Truell [85,86] rely on scattering coefficients derived from models like ECAH and are valid primarily for monodisperse systems. Efforts to incorporate polydispersity through either averaged scattering coefficients [87] or summations over particle size distributions [88] have been proposed, although neither approach is rigorously derived from multiple scattering theory. Although multiple scattering theory provides a physically consistent framework applicable in principle across the full frequency spectrum, it is constrained mathematically to spherical particles and yields closed-form analytical solutions only in limiting cases. As such, its ability to accurately describe particle interactions at high concentrations remains limited and the interpretation of results becomes increasingly model-dependent as the system complexity increases.

Core-shell models or effective medium theories, commonly formulated as self-consistent effective medium approximations within scattering theory, are designed to capture the interparticle interactions that arise in concentrated dispersions due to the spatial overlap of thermal and viscous wave fields. In these models, each particle with radius a is surrounded by a concentric spherical shell of fluid extending to radius b, which represents its immediate local environment (see Fig. 2.8). This shell is embedded in a surrounding effective medium whose properties approximate those of the bulk suspension. By applying boundary conditions at the shell interface, the model accounts for the averaged influence of neighbouring particles on the acoustic field while retaining a wave-mechanical description at the particle scale.

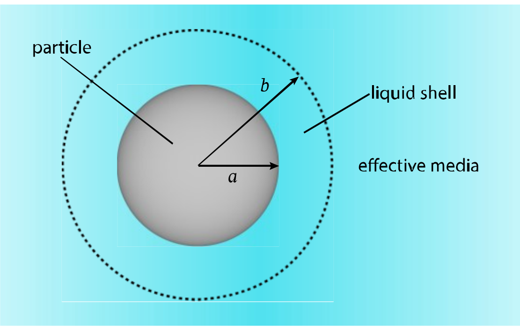

Fig. 2.8: Schematic illustration of the core–shell model in effective medium theory. Each particle of radius a is surrounded by a concentric fluid shell extending to radius b.

Early implementations, such as the model proposed by Hemar et al.[89], focused on thermal wave interactions. Later McClements et al. [90,91] extended the approach to include viscous losses. A more advanced formulation was proposed by Hipp et al.[92], which incorporates scattering contributions from compressional, thermal, and shear wave modes. While core-shell models have demonstrated strong agreement with experimental results in monodisperse systems, they suffer from conceptual and practical limitations in polydisperse media, most notably in defining an appropriate shell radius and the properties of the surrounding effective medium.

In contrast to scattering models, coupled-phase models treat the dispersion as two interacting continuous media: one representing the suspended particles and the other the surrounding fluid. Instead of modelling individual particle interactions, these models describe the system using volume-averaged conservation laws for mass, momentum and energy, which are applied separately to each phase. The two phases are connected through coupling terms that account for momentum exchange due to viscous drag and where applicable, heat transfer between the particles and the fluid. These models are only suitable for the long-wavelength regime, where individual scattering effects are less dominant and wave–particle interactions can be averaged over the suspension. Early models such as those by Harker and Temple [93] and later extensions by Evans and Attenborough,[94] have progressively incorporated more realistic drag and thermal transfer terms, drawing from hydrodynamic models like Vand [95] and Happel [96]. While originally restricted to monodisperse suspensions, several extensions to polydisperse systems have been proposed.[97–99] Nonetheless, coupled-phase models remain limited in their range of validity, particularly for higher frequencies or large particles where wavelength-to-particle-radius ratios fall outside the long-wavelength assumption.

For the evaluation of acoustic attenuation spectra in this work, the model developed by Dukhin and Goetz [12] was used. This model is based on a coupled-phase framework and describes the suspension as two interacting continuous phases governed by volume-averaged conservation equations. Viscoinertial losses are treated using a generalized Happel cell model,[100] which accounts for hydrodynamic drag in concentrated systems.[97] Thermal losses are implemented through a core-shell formulation that captures the overlapping of thermal diffusion layers and uses effective thermophysical properties of the dispersion.[101] Intrinsic attenuation is calculated as a volume-weighted average of the contributions from the particle and fluid phases, with corrections that account for differences in density and sound velocity between the two materials.[67] Scattering contributions are computed using classical elastic theory,[85] assuming linear superposition and negligible multiple scattering. The combined model enables the extraction of volume-weighted particle size distributions from undiluted, polydisperse samples under long-wavelength conditions, although in practice reliable interpretation is typically limited to bimodal distributions.

2.3.2 Reference Methods

Acoustic attenuation spectroscopy (AAS) offers clear advantages for particle size characterization, particularly in highly concentrated or optically opaque dispersions. However, it remains less established than conventional optical techniques. In this work, AAS results are compared with those obtained from two widely used optical methods: dynamic light scattering (DLS) and laser diffraction spectroscopy (LDS). Both techniques infer particle size distributions based on the interaction of light with dispersed particles and are routinely employed in the characterization of colloidal and particulate systems.

They provide complementary insights based on distinct physical principles. Although DLS and LDS have limitations, particularly in systems that are highly concentrated or strongly polydisperse where multiple and dependent scattering can compromise accuracy, they are supported by standardized protocols and a long history of reliable application. Their inclusion in this study serves both to benchmark the AAS results and to identify potential systematic deviations. The following sections provide a detailed discussion of the principles, strengths and limitations of DLS and LDS.

2.3.2.1 Dynamic Light Scattering

Dynamic light scattering (DLS), also known as photon correlation spectroscopy (PCS) or quasi-elastic light scattering (QELS), is a widely used technique to determine the size of particles in colloidal dispersions. First introduced in the 1960s,[102] DLS has since become a standard method in nanoparticle characterization across fields such as materials science, chemistry and biophysics.

The method is based on analysing the Brownian motion of particles by observing fluctuations in scattered laser light intensity. When a coherent laser beam illuminates a sample, the suspended particles scatter light in all directions. This scattered light interferes constructively and destructively, forming a dynamic speckle pattern of bright and dark regions. As particles move, this pattern fluctuates in time. Smaller particles, which diffuse more rapidly, cause faster fluctuations, whereas larger ones produce slower variations. The timescale of these fluctuations contains direct information about particle diffusivity and, consequently, particle size (see Fig. 2.9).[103]

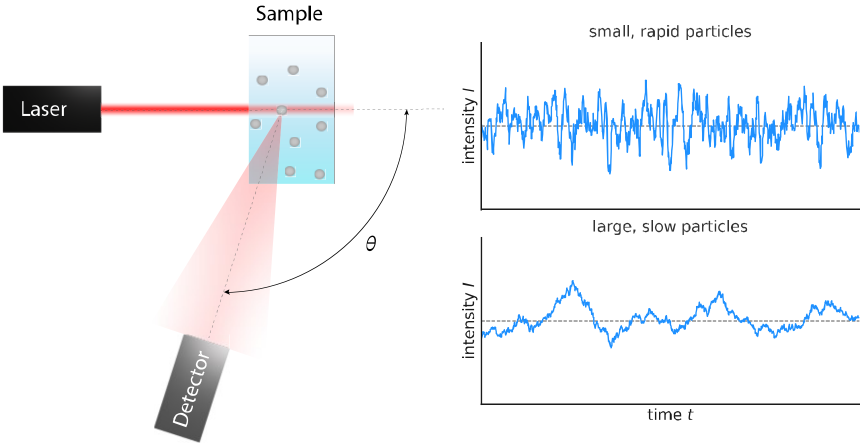

Fig. 2.9: Schematic representation of the principle of dynamic light scattering (DLS). **Left:** A coherent laser beam passes through a colloidal sample, and scattered light at a defined angle θ is collected by a photodetector. **Right:** The detector records temporal fluctuations of the scattered intensity $I(t)$, originating from particle Brownian motion.

Because of its sensitivity to such motion, DLS is not only used for particle sizing but also for the determination of the molar mass,[104] studying aggregation processes,[105] monitoring phase transitions [106] and investigating gelation processes [107] in colloidal or polymeric systems.

There are three main detection configurations used in DLS: direct (or self-beating), homodyne and heterodyne detection. These configurations differ in whether a reference beam is combined with the scattered light and if so, whether the reference has the same or a shifted frequency. In the direct or self-beating configuration, only the scattered light is detected. The signal results from interference between scattered waves originating from different particles. This is the most common configuration in commercial systems and is often loosely referred to as homodyne detection. In a stricter sense, homodyne detection involves the deliberate addition of a reference beam with the same frequency as the incident laser. This increases signal sensitivity and coherence, which can help in tracking small particle displacements. Heterodyne detection, on the other hand, combines the scattered light with a reference beam of slightly shifted frequency. This introduces a beat frequency at the detector and allows access to drift velocities and flow profiles in addition to Brownian motion. Heterodyne setups are more complex and less frequently used in standard particle sizing applications.[10]

To extract information about particle size from the temporal fluctuations in scattered light, DLS relies on statistical analysis.[108] The quantity of physical interest is the translational diffusion coefficient D, which characterizes how fast particles move due to Brownian motion. This diffusion coefficient is related to the measured decay rate $\mathit{\Gamma}$ of the correlation function by:

$$\mathit{\Gamma} = Dq^2 \tag{2.22}$$

Here, q is the scattering vector, which depends on the experimental geometry:

$$q = \frac{4\pi n}{\lambda} \sin\left(\frac{\theta}{2}\right) \tag{2.23}$$

where n is the refractive index of the solvent, λ is the laser wavelength in vacuum and θ is the scattering angle. Once the diffusion coefficient is known, the hydrodynamic radius a_h of the particle can be calculated using the Stokes–Einstein equation [109]:

$$\mathrm{D} = \frac{k_\mathrm{B} T}{6\pi\eta a_\mathrm{h}} \tag{2.24}$$

In this expression, k_B is Boltzmann's constant, T is the absolute temperature and η is the viscosity of the liquid medium. The result corresponds to the radius of a sphere diffusing at the same rate as the particle under investigation.

The intensity of scattered light fluctuates over time due to the random motion of particles. These fluctuations are quantified by the intensity autocorrelation function $g_2(\tau)$, which describes how similar the detected intensity at time t is to the intensity at a later time $t + \tau$. It is defined as:

$$g_2(\tau) = \frac{\langle I(t) I(t+\tau) \rangle}{\langle I(t) \rangle^2} \tag{2.25}$$

where, $I(t)$ is the scattered light intensity, τ is the delay time and $\langle \cdot \rangle$ denotes a time average. This function describes how strongly the intensity at a given time correlates with that at a later time. The faster the particles move, the more quickly the speckle pattern decorrelates and the faster $g_2(\tau)$ decays.

To connect this measured intensity signal to the underlying particle dynamics, a second quantity is introduced: the field correlation function $g_1(\tau)$. Although the light field itself is not measured directly, its statistical behaviour governs the observed intensity correlations. For monodisperse particles undergoing Brownian motion, this function decays exponentially:

$$g_1(\tau) = e^{-\Gamma\tau} \tag{2.26}$$

The link between $g_2(\tau)$ and $g_1(\tau)$ is given by the Siegert relation:[110]

$$g_2(\tau) = 1 + \beta |g_1(\tau)|^2 \tag{2.27}$$

This relation is valid under two conditions: first, that each photon is scattered only once before detection (single scattering), and second, that the scattered light results from a large number of randomly moving particles, which causes the overall signal to follow Gaussian statistics. These assumptions are typically met in dilute systems.

Substituting Eq. 2.26 into Eq. 2.27 yields the final form commonly used to fit experimental data:[108]

$$g_2(\tau) = 1 + \beta e^{-2\Gamma\tau} \tag{2.28}$$

Here, β is an instrument-specific coherence factor that depends on the optical setup and detector geometry. This expression allows the decay rate Γ to be extracted, which can then be used to determine the particle diffusion coefficient and, ultimately, the particle size.

The accuracy of DLS depends on preserving the ideal measurement conditions described above. Depending on the particle size and concentration, multiple scattering may occur, meaning that light is scattered more than once before it reaches the detector. This process violates the single-scattering assumption required for the Siegert relation and can lead to distortions in the measured correlation function. To reduce these effects, two approaches are commonly used: backscattering and cross-correlation techniques. Backscattering minimizes the optical path length by detecting scattered light at angles close to 180°, thereby reducing the likelihood of multiple scattering [111,112]. Cross-correlation techniques go further by employing two spatially separated detectors that record independent scattering signals from the same sample volume.[113–115] Only those fluctuations that appear simultaneously in both detectors are evaluated, as these are most likely due to single scattering. The amplitude of the cross-correlation function scales with the square of the single-scattering fraction, allowing reliable measurements even in turbid samples. Although this approach improves data quality, it requires precise optical alignment and more advanced instrumentation.

The reliable detection of particles larger than 1 µm becomes increasingly difficult due to sedimentation.[116] The magnitude of this effect depends on the density difference between the particles and the surrounding medium. When gravitational settling dominates over Brownian diffusion, particle motion is no longer random, potentially distorting the measured size distribution. Sedimentation effects become particularly significant in polydisperse systems, where gravitational settling and diffusion are interdependent processes.[117]Moreover, sedimentation can lead to a shift in the apparent size distribution within the measurement region, potentially affecting the accuracy of the results.

Modern DLS systems perform digital photon counting and calculate the autocorrelation function in real time. Since the derived particle size depends on temperature and viscosity through the Stokes–Einstein relation, it is essential to control the temperature of the sample with high precision, often to within ±0.3 °C.[103]

2.3.2.2 Laser Diffraction Spectroscopy

Laser diffraction spectroscopy (LDS) offers a fast, optics-based method to quantify particle size distributions in both liquid and dry particulate systems. It belongs to the class of static light scattering methods and is based on measuring the angular distribution of light scattered by particles illuminated by a monochromatic laser beam. The fundamental principle relates particle size to scattering angle. Large particles scatter light predominantly at small angles, while smaller particles produce more diffuse patterns extending to higher angles. By recording the intensity of scattered light across a defined angular range, particle size distributions can be determined using appropriate optical models. The technique is especially valued in colloid science for its speed, broad size range and reproducibility.[118,119]

Early commercial LDS instruments were initially developed for micrometre-sized particles, a regime in which scattering is dominated by diffraction and application of the Fraunhofer approximation is generally sufficient. Fraunhofer diffraction theory [120] describes how light scatters in the far field when it encounters an opaque object. Theoretically, the resulting diffraction pattern corresponds to the Fourier transform of the object's two-dimensional projection and therefore reflects characteristics related to both size and shape. However, in practical laser diffraction analysis, the Fraunhofer model is manly applied under the simplifying assumption of spherical particle geometry. The inversion of scattering data yields an equivalent spherical diameter distribution, without resolving shape-specific features of the pattern. The Fraunhofer theory remains valid when particles are significantly larger than the wavelength of light and strongly scattering, conditions under which edge diffraction dominates.[121] For smaller or partially transparent particles, however, this model fails to account for refraction or absorption. The Mie theory,[122] provides a rigorous model for spherical particles of arbitrary size and refractive index. It describes scattering as a combination of diffraction, refraction and reflection and is applicable across the full colloidal size range. Its implementation in particle sizing requires the complex refractive indices of both the particles and the medium. While Mie calculations are more demanding in terms of computation and can be numerically unstable for very large particles, modern processing capabilities have made them standard in commercial instruments. Fraunhofer-based analysis is used primarily when particle size is very large and optical properties are unknown.[118]

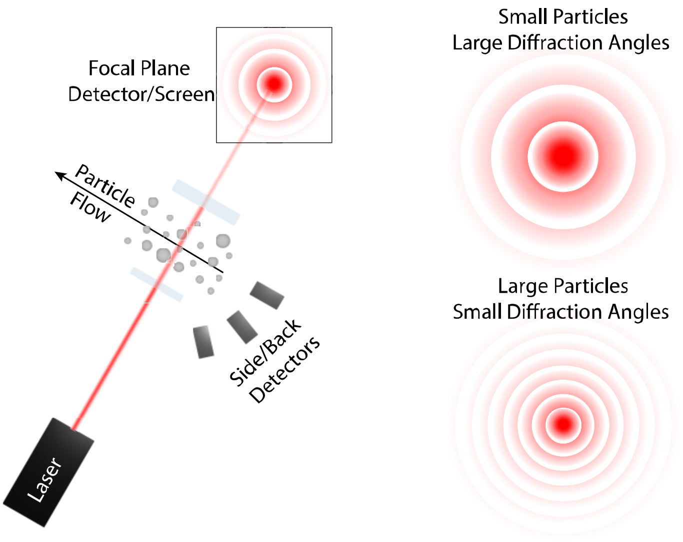

Fig. 2.10: Schematic representation of the principle of laser diffraction spectroscopy (LDS). **Left:** Optical setup showing a monochromatic laser beam passing through a dispersed particle system, with scattered light detected at various angles. **Right:** Corresponding angular intensity patterns for small and large particles.

In a typical experiment, a laser beam passes through a sample containing dispersed particles. The scattered light is collected by an array of detectors positioned at various angles relative to the incident beam. These detectors are often arranged in concentric or semi-circular geometries to resolve a broad angular range [119]. The collected intensity pattern represents a superposition of all individual particle scattering contributions. For spherical particles, the resulting pattern consists of concentric rings who's spacing and contrast are directly related to particle size. This behaviour is illustrated in Fig. 2.10, which shows the optical configuration of a standard laser diffraction apparatus on the left-hand side and the diffraction patterns of individual particles on the right. The upper right quadrant illustrates the pattern produced by a small particle, characterised by a broad angular distribution and wide ring spacing. In contrast, the lower right quadrant shows the narrow, high-intensity pattern typical of large particles, where most scattering is confined to small angles.[123]

Laser diffraction systems convert the angular intensity distribution into a particle size distribution by fitting theoretical scattering curves to the observed data. These curves are typically based on Mie theory. The inversion process assumes spherical particles and yields a volume-weighted distribution. While this assumption introduces systematic error for non-spherical particles, it remains acceptable in many practical cases where anisotropy is moderate or unknown. However, researchers should be aware that highly elongated or irregularly shaped colloids may yield size distributions that reflect equivalent spherical diameters rather than true geometric dimensions.[118,123]

Modern instruments often employ multiple laser wavelengths and extended-angle detection to enhance performance. The use of blue lasers [124] or light-emitting diodes (LED's) [125] increases scattering from small particles due to the shorter wavelength and corresponding stronger interaction with submicron matter. High-angle and backscattering detectors are now incorporated in instruments designed to access the lower nanometre size range. In addition, polarization-based techniques such as polarization intensity differential scattering (PIDS) have been developed to increase sensitivity to very fine particles.[119,126] These enhancements enable the detection of colloids with diameters as small as approximately 40 nm, although measurement accuracy and resolution are not uniform across the full-size range.

Sample preparation and experimental conditions are critical for obtaining reliable results. Multiple scattering is a major concern in concentrated colloidal suspensions, as photons scattered more than once before reaching the detector distort the angular intensity profile and can lead to overestimation of particle size. To avoid this, measurements must be performed at appropriate dilution levels, where single scattering dominates and the optical transmission remains within a suitable range. An exact concentration threshold cannot be universally defined, but practical guidance based on particle size exists. For particles around 1 μm in diameter, an obscurance of approximately 5 % (corresponding to a transmission of about 95 %) is typically suitable to ensure single scattering conditions. In contrast, for larger particles near 100 μm, higher obscurance values up to 25 % (equivalent to roughly 75 % transmission) may still yield reliable results. Suitable dispersants are chosen to stabilise the suspension and to minimise background scattering. Ultrasound and other dispersion techniques are often used to break up agglomerates and ensure that individual particles are measured.[118]

An accurate size determination also requires precise knowledge of the refractive index. For Mie-based analysis, both the real and imaginary components of the refractive index must be supplied. Errors in these values can lead to systematic deviations in the resulting size distribution, especially for transparent or weakly scattering particles. Although the instrument software often provides databases of common materials, custom refractive indices may be required for novel or composite systems. Sensitivity analyses can be used to assess the effect of index variations on measurement outcome, providing additional confidence in the result.[118,123]

Laser diffraction spectroscopy is well suited for rapid and reproducible size measurements. A single analysis typically requires less than a minute and evaluates a statistically significant number of particles, resulting in low measurement variance. Despite its strengths, laser diffraction has limitations. Its assumption of spherical geometry reduces accuracy for highly anisotropic particles. Its ensemble nature makes it less sensitive to minor populations unless they represent a substantial volume fraction. Detection of very small particles remains challenging due to inherently weak scattering and the difficulty of separating signal from noise. [118]

3 Aim and Outline of the Thesis

This thesis aims to advance the understanding of stability mechanisms in concentrated dispersions by employing acoustic techniques including colloidal vibration potential (CVI) and the acoustic attenuation spectroscopy (AAS). These methods are suited for the determination of the zeta potential and particle size distribution (PSD) in concentrated systems.

The experimental material concept of this work is based on a set of aqueous polymer dispersions differing in chemical composition, particle size and interfacial properties, including polyvinyl chloride (PVC), styrene-butadiene rubber (SBR), polytetrafluoroethylene (PTFE), polyurethane (PU) and polymethyl methacrylate-*co*-butyl acrylate (PBAMM). These systems were selected to cover a broad range of physical and interfacial characteristics relevant to acoustic and electrokinetic behaviour. PTFE, for example, exhibits high density, stiffness, and low interfacial polarity, whereas SBR is a soft, low-density elastomer. PU and PBAMM are likewise soft but more polar dispersions. PVC, serving as the primary reference system, combines intermediate mechanical and interfacial properties, making it well suited for systematic comparisons across different measurement techniques. Together, these dispersions provide a representative basis for evaluating theoretical models and measurement methods under realistic, industrially relevant conditions.

The thesis first examines the impact of surface conductivity on zeta potential determination using standard models like Helmholtz-Smoluchowski and Henry theory where surface conductivity is typically ignored (Chapter 4). This analysis was carried out on the complete set of polymer dispersions introduced above (PVC, SBR, PTFE, PU, and PBAMM), in order to validate the applicability of standard electrokinetic models across a diverse set of dispersion systems. The results reveal that neglecting the surface conductivity even in standard models can lead to errors of up to 100 % with increasing particle volume fraction. By accounting for surface conductivity using the Dukhin number, the CVI results align closely with electrophoretic light scattering (ELS) measurements across a wide range of volume fractions.

Based on this, Chapter 5 focuses the accurate determination of zeta potential in diluted and concentrated colloidal dispersions by addressing the relaxation effect using advanced models. The analysis focuses on PVC, SBR, PU and PBAMM dispersions, which were selected because they allowed stable determination of the Dukhin number. It highlights the determination of Dukhin numbers via conductivity measurements of the dispersion and dispersion medium individually, enabling a comprehensive evaluation of the surface conductivity contributions from both the stagnant and diffuse layers. For the first time, advanced CVI theory is shown to accurately account for surface conductivity effects across a wide range of particle volume fractions, delivering results that closely correspond with ELS measurements analysed using the Dukhin-Semenikhin theory or a modified Ohshima-Healy-White theory.

Chapter 6 considers the challenge of accurately determining particle size distribution (PSD) of polymer latex dispersions using acoustic attenuation spectroscopy (AAS), addressing the critical influence of intrinsic absorption on the attenuation spectrum. The full set of aqueous dispersions

(PVC, PTFE, PU, PBAMM, and SBR) was examined to assess how intrinsic particle absorption varies in magnitude and material dependence. The intrinsic particle absorption was modelled using the Dukhin and Goetz coupled phase model. The findings reveal that accounting for intrinsic particle absorption in the AAS model significantly improves PSD accuracy, especially for the median particle diameters. However, accurately determining PSD width remains a challenge.

Further, Chapter 7 investigates colloidal stability of concentrated dispersions using acoustic attenuation. Two polyvinyl chloride dispersions, differing in particle size and polymerization method, are examined to assess the influence of surfactant type and coverage on the critical coagulation concentration (CCC). The results show that higher surfactant coverage increases CCC due to stronger electrostatic repulsion and underscore the utility of acoustic attenuation for analysing concentrated, opaque dispersions, offering valuable insights for the optimization of colloidal formulations.

Finaly, the dissertation concludes with a discussion (Chapter 8) and summary (Chapter 9) of the key contributions and findings, highlighting their significance for the advancement of colloid science.

4 Impact of Surface Conductivity on the Zeta Potential Determination of Concentrated Aqueous Polymer Dispersions Using Electroacoustics and Electrokinetic Standard Models

Matthias Frangenberg[a,b], Annette M. Schmidt[b], Jan Wilkens[a*]

[a] Faculty of Applied Natural Sciences, TH Köln – University of Applied Sciences, Cologne, Germany
[b] Department of Chemistry, Institute of Physical Chemistry, University of Cologne, Cologne, Germany
* E-Mail: jan.wilkens@th-koeln.de; Phone: +49 214-32831-4614; Address: Campusplatz 1, 51379 Leverkusen, Germany

Reproduced from Ref [1] with permission from *Colloid and Polymer Science*; Springer.

Abstract

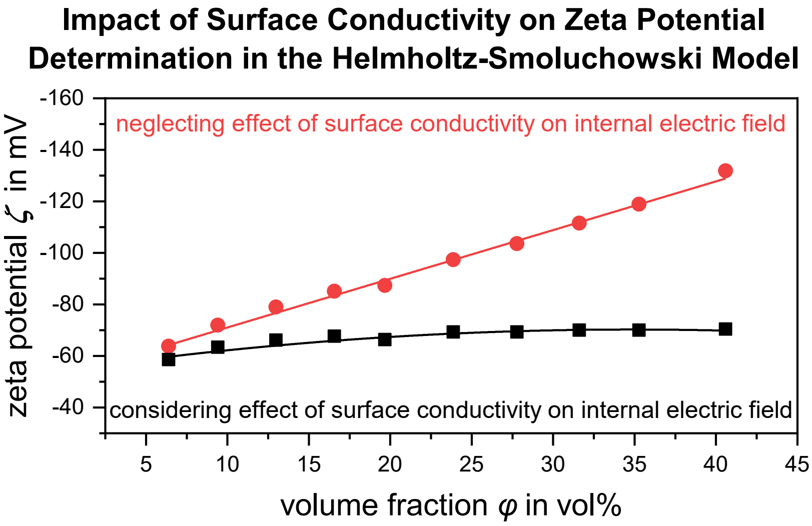

Surface conductivity can have a significant impact on the determination of the zeta potential, but it is normally not accounted for when applying the Helmholtz-Smoluchowski or Henry models. In this study, we investigate concentrated polymer dispersions using electroacoustics and both standard models. We also pay particular attention to the influence of surface conductivity, which is characterized by conductivity measurements of the dispersion and dispersion medium. The Dukhin number as a measure of surface conductivity is calculated according to Maxwell-Wagner-O'Konski theory. Zeta potentials were determined by means of colloid vibration current (CVI) and electrophoretic light scattering (ELS) methods. It has been found that neglecting surface conductivity in standard electrokinetic models can lead to large measurement errors of up to 100 % with increasing particle volume fraction. In this study, the surface conductivity is now correctly taken into account by using the conductivities of the dispersion and the dispersion medium. Alternatively, this influence can also be considered using the Dukhin number. The zeta potentials

resulting from the CVI measurement are then in excellent agreement with ELS reference measurements over a wide volume fraction range.

4.1 Introduction

The zeta potential is one of the crucial parameters for the characterisation of the electrostatic interaction in charged colloidal dispersions. Optical methods such as electrophoretic light scattering (ELS) are commonly employed to measure zeta potential, but their use is limited to diluted samples [2,3]. As an alternative, electroacoustics has also enabled characterization of electrokinetic properties of colloidal dispersions [2,4]. Electroacoustic phenomena can occur if the colloidal particles and the dispersion medium have a density contrast. The application of an acoustic field causes the particles and medium to move relative to each other due to inertia effects. This motion also affects the counter-ions that are located in the diffuse layer around the particle, resulting in a perturbation of the charge distribution and thus creating a dipole moment. The polarization of the diffuse layer can be measured as a colloid vibration current (CVI) or a colloid vibration potential (CVP) signal. The electrokinetic sonic amplitude (ESA) phenomenon, on the other hand, is the inverse of the CVI and CVP phenomenon, with the driving force being an electric field instead of a hydrodynamic field and the measured quantity being a sound amplitude. This study is primarily concerned with the CVI phenomenon. Further information on the ESA and the CVP phenomenon can be found in a review by Hunter [5] and in the article by Marlow et al. [6], respectively. Recently, a review on the measurement of zeta potential by electroacoustic methods has been published, providing a comprehensive survey of the latest findings [7].

The typical result of electrokinetic studies is the static or dynamic electrophoretic mobility, which is a measure for the motion of particles in the dispersion medium. These parameters depend in particular on the zeta potential. The relationship between these quantities can be described by various theories [8]. They differ primarily in the consideration of various effects that influence the motion of particles. This involves that certain limits of validity have to be taken into account when applying these theories. The Helmholtz-Smoluchowski (HS) theory is widely known and applicable to particles of any shape and size [9]. However, it is only valid when the thickness of the diffuse layer is small compared to the particle size. If this condition is not met, the Henry theory should be applied, which is valid for low to moderate zeta potentials [10]. However, both theories neglect surface conductivity and polarization effects of the electrical double layer, which can have a significant effect on electrophoretic mobility, particularly at high zeta potentials. In this case, advanced theories should be employed in order to avoid inaccuracies [8]. Despite these drawbacks, HS and Henry theory are often used for the evaluation of electroacoustic phenomena due to their simplicity, so that a detailed study and comparison with the ELS method is of particular practical value.

Nevertheless, an investigation of the surface conductivity is useful, as it can have an influence on the effective electric field strength within the dispersion. A suitable parameter is the dimensionless Dukhin number, which can be determined by conductivity measurements [11–16] or frequency-dependent studies of dielectric properties [17–22]. This study focuses on conductivity measurements of the dispersion and the dispersion medium. Several theories are known to calculate the Dukhin number using these values, including the Maxwell-Wagner-O'Konski (MWO) theory [23–25]. A detailed overview can be found in the publication by Van der Put and Bijsterbosch [12].

While electroacoustic methods have been extensively used for the investigation of inorganic materials like ceramics and metal oxides [6], only few research paper are known for polymer dispersions. Most of them are focused on low particle volume fractions [26–33]. To our knowledge, only the publications by Ishikawa et al. [34], Hozumi and Furusawa [35] and Rasmusson [36] deal with particle volume fractions above 10 vol%. The reasons are not clear, but the underrepresentation of polymer latices in electroacoustic research may be attributed to the weak measuring signal due to the rather low-density contrast. However, recent studies have shown that modern instruments can provide reliable results even for density differences of less than 0.01 g/L [34]. Therefore, it is worthwhile to clarify the capability of electroacoustic measurement methods for the characterisation of polymer dispersions.

In this study, we determine the zeta potential of highly concentrated polymer dispersions using electroacoustic methods. The zeta potential is calculated from the measured CVI signal by means of the HS and Henry theories. The influence of the surface conductivity on the effective electric field strength is considered by the Dukhin number. For this purpose, the conductivity of the dispersion and the dispersion medium is measured. As an electrokinetic consistency test, the zeta potential is also determined by ELS measurements on diluted samples.

4.2 Theory

Typically, particles dispersed in an aqueous medium have a charged surface. These charges generate an electrical potential that is subsequently screened by counter-ions located in the Helmholtz layer and in the diffuse layer surrounding the particle. This arrangement is called electrical double layer (EDL). Application of an external driving field can cause particles, ions and liquid within the EDL to move relative to each other, resulting in a perturbation of the equilibrium state. At the slip plane, the velocity of the dispersion medium relative to the particle is zero and the corresponding potential is called zeta potential. Its value depends on several influence factors, e.g. valence and concentration of electrolytes in the dispersion medium. In the absence of co-ion adsorption, the absolute zeta potential decreases as ionic strength increases.

Furthermore, the disturbance of the equilibrium state can lead to a polarization of the EDL. Due to the EDL structure, there is a local excess concentration of counter-ions near the particle surface. Thus, the applied external field leads to an excess conductivity compared to the conductivity in the bulk medium K_{m}. This quantity depends on the particle surface area and the surface conductivity K^{σ}. Typically, the particle itself is not conductive and behaves as an electrical insulator (dielectric). Therefore, it decreases the conductivity of the dispersion K_{s}. The extent of this effect depends on the particle volume and the medium conductivity K_{m}. A measure for the balance of both effects is the dimensionless Dukhin number Du given in Eq. 4.1, which also includes the particle radius a.

Like zeta potential, Du is not a constant particle property, as it depends on the ionic strength of the dispersion medium. It is also worth mentioning that the EDL can contribute to the surface conductivity both below and beyond the slip plane [8,37]. These contributions are known as stagnant layer and diffuse layer conductivity, respectively. Therefore, the method for determining the Dukhin number should be able to account for both.

$$Du = \frac{K^{\sigma}}{K_{\mathrm{m}} a} \tag{4.1}$$

There are several external driving forces that can be used to generate a tangential fluid motion near a charged particle surface. One of the most frequently applied electrokinetic methods is electrophoresis. In this case, the charged particles are accelerated by an external electric field of strength E_{ext}. The resulting particle velocity υ_{p} depends, among others, on the zeta potential ζ. The relation between these quantities can be described with the simple but very popular HS equation [9]:

$$\mu = \frac{|\upsilon_{\mathrm{p}}|}{|E_{\mathrm{ext}}|} = \frac{\varepsilon_0 \varepsilon_{\mathrm{m}} \zeta}{\eta} \tag{4.2}$$

where μ is the electrophoretic mobility, ε_0 the vacuum permittivity, ε_{m} the relative permittivity of the medium, and η the dynamic viscosity. This equation is only valid for particles with a thin diffuse ion layer compared to the particle radius a, i.e. $\varkappa a \gg 1$, where $\varkappa$ is the Debye-Hückel parameter:

$$\varkappa = \sqrt{\frac{N_{\mathrm{A}} e^2}{\varepsilon_0 \varepsilon_{\mathrm{m}} k_{\mathrm{B}} T} \sum_{i=1}^{N} z_i^2 c_i} \tag{4.3}$$

with Avogadro constant N_{A}, elementary charge e, Boltzmann constant k_{B}, thermodynamic temperature T, charge number z_i and concentration c_i (medium contains $i = 1$ to N ionic species).

If the thickness of the diffuse layer is not thin compared to the particle radius, the retardation effect of the hydrated electrolyte ions on the electrophoretic mobility is more accurately characterised by the Henry function $f_{\mathrm{H}}(\varkappa a)$, shown in Eq. 4.4 [10]. This function can be calculated using the simple approximation Eq. 4.5 derived by Ohshima [38]:

$$\mu = \frac{\varepsilon_0 \varepsilon_{\mathrm{m}} \zeta}{\eta} f_{\mathrm{H}}(\varkappa a) \tag{4.4}$$

$$f_{\mathrm{H}}(\varkappa a) = \frac{2}{3}\left[1 + \frac{1}{2}\left(1 + \frac{2.5}{\varkappa a(1+2\exp(-\varkappa a))}\right)^{-3}\right] \tag{4.5}$$

Very often $\varkappa$ cannot be calculated according to Eq. 4.3, since the exact composition of the dispersion medium is unknown. Instead, it is approximated utilizing the conductivity of the dispersion medium K_{m} and Eq. 4.6 [2]. In this case, the average value of the presumed electrolyte should be used for the effective diffusion coefficient D_{eff}.

$$\varkappa \approx \left(\sqrt{\frac{\varepsilon_{\mathrm{m}} \cdot \varepsilon_0 \cdot D_{\mathrm{eff}}}{K_{\mathrm{m}}}}\right)^{-1} \tag{4.6}$$

The diffusion coefficient $D_{\pm}$ of cations (+) and anions (-) can be calculated according to the Nernst-Einstein equation, where $\Lambda_{\pm}^{0}$ is the limiting molar conductivity of electrolyte ions at infinite dilution:

$$D_{\pm} = \frac{k_{\mathrm{B}} T \Lambda_{\pm}^{0}}{z_{\pm}^{2} N_{\mathrm{A}} e^{2}} \tag{4.7}$$

It is important to note that the HS and Henry theories neglect surface conductivity and EDL polarization (relaxation effect), which become relevant at high zeta potentials (especially for $|\zeta| >$ 50 mV). Furthermore, Eq. 4.2 and 4.4 are only valid for dilute dispersions as they take the external field strength E_{ext} into account. This condition is usually fulfilled in electrophoretic light scattering (ELS) experiments. However, we have to consider that with increasing particle concentration, the field strength within the dispersion E_{int} deviates from the external field E_{ext} because particles normally behave as electrical insulators. Moreover, the surface conductivity can also exert an influence on the internal electric field. A simple relationship between the internal electric field E_{int} and the external electric field $E_{\mathrm{ext}}$with the conductivity of the dispersion medium K_{m} and the dispersion K_{s} is shown in the Eq. 4.8 [39]. It should be noted that K_{s} also considers the surface conductivity of the particles.

$$\frac{|\boldsymbol{E}_{\mathrm{int}}|}{|\boldsymbol{E}_{\mathrm{ext}}|} = \frac{K_{\mathrm{m}}}{K_{\mathrm{s}}} \tag{4.8}$$

This relationship provides the opportunity to extend the HS equation to concentrated systems [40,41].

$$\mu = \frac{|\boldsymbol{v}_{\mathrm{p}}|}{|\boldsymbol{E}_{\mathrm{int}}|} = \frac{\varepsilon_0 \varepsilon_{\mathrm{m}} \zeta}{\eta} \frac{K_{\mathrm{s}}}{K_{\mathrm{m}}} \tag{4.9}$$

Eq. 4.8 can likewise be applied to the Henry equation 4.4:

$$\mu = \frac{\varepsilon_0 \varepsilon_{\mathrm{m}} \zeta}{\eta} f_{\mathrm{H}}(\kappa a) \frac{K_{\mathrm{s}}}{K_{\mathrm{m}}} \tag{4.10}$$

Eq. 4.9 and 4.10 are becoming important for electrokinetic investigations at high solid contents, like in electroacoustics. At this point, it is worth mentioning that usual electrophoretic measurements involve stationary electrophoretic mobility, whereas electroacoustic measurements involve dynamic electrophoretic mobility. The concept of dynamic electrophoretic mobility μ_{d} was originally introduced by O'Brien [42]. It relates electroacoustic parameters to relevant colloidal parameters, such as the zeta potential ζ. Dukhin and co-workers applied this concept to concentrated dispersions and to the CVI phenomenon [43–45]. In the case of the HS model framework, they obtained the following relationship:

$$\mu_{\mathrm{d}} = \frac{CVI_{\omega\rightarrow 0}}{\Delta P} \frac{\rho_{\mathrm{s}}}{\rho_{\mathrm{p}} - \rho_{\mathrm{s}}} \frac{1}{\varphi} \frac{1}{F(Z_{\mathrm{T}}, Z_{\mathrm{s}}) A(\omega)} = \frac{\varepsilon_0 \varepsilon_{\mathrm{m}} \zeta}{\eta} \frac{K_{\mathrm{s}}}{K_{\mathrm{m}}} \tag{4.11}$$

Here, $CVI_{\omega\rightarrow 0}$ is the measured colloidal vibration current amplitude at low frequency, ΔP the pressure difference, $A(\omega)$ is an instrument constant which is determined by calibration and $F(Z_{\mathrm{T}}, Z_{\mathrm{s}})$ a function of the acoustic impendence of the instrument transducer Z_{T} and dispersion Z_{s}. For non-porous particles, the density of the dispersion ρ_{s} depends on the density of particles ρ_{p} and medium ρ_{m} and on the volume fraction of the particles φ as follows:

$$\rho_s = \varphi \rho_p + (1-\varphi)\rho_m \tag{4.12}$$

Eq. 4.11 is only valid for particles with a small thickness of the diffuse ion layer ($\kappa a \gg 1$) and neglects EDL polarization effects due to surface conductivity ($Du \ll 1$). Additionally, the low frequency limit given by Eq. 4.13 and 4.14 must be observed, since the CVI signal may depend on the frequency of the ultrasonic wave ω. This can be neglected if ω is much lower than the frequency of the hydrodynamic relaxation ω_{hd} and the frequency of the electrodynamic relaxation ω_{MW} (Maxwell-Wagner frequency).

$$\omega \ll \omega_{hd} = \frac{\eta}{\rho_m a^2} \tag{4.13}$$

$$\omega \ll \omega_{MW} = \frac{K_m}{\varepsilon_0 \varepsilon_m} = \kappa^2 D_{eff} \tag{4.14}$$

As already mentioned, the relative conductivity $K_s K_m^{-1}$ in Eq. 4.11 accounts for the influence of the nonconducting particles and the surface conductivity on the effective electric field within the dispersion. Therefore, the relative conductivity must be known in order to correctly determine the zeta potential using CVI measurements. For this purpose, we have taken a closer look at three different approaches that are valid at the low-frequency limit mentioned above.

Approach 1:

Eq. 4.15 describes the volume fraction dependence of the relative conductivity $K_s K_m^{-1}$ for particles which have no surface conductivity ($Du = 0$) [23,24]:

$$\frac{K_s}{K_m} = \frac{1-\varphi}{1+0.5\varphi} \tag{4.15}$$

In this case, there is no need to measure the relative conductivity. Only the volume fraction φ of the nonconducting particles needs to be known. Due to its simplicity and convenience for the user, this formula is implemented by default in the software of the measuring device employed in this study. Therefore, determined zeta potentials have to be recalculated if the relative conductivity according to approaches 2 or 3 is to be used. For more details, refer to the supporting information.

Approach 2:

The relative conductivity can be directly calculated using measured conductivities of the dispersion K_s and the medium K_m. However, the measurement of the conductivity of the dispersion medium K_m can be quite tedious because particles must be separated thoroughly. This task can become increasingly difficult with decreasing particle size and low-density contrast between particles and dispersion medium.

Nevertheless, one should bear in mind that the EDLs of individual particles might overlap at high particle volume fraction. This can also occur if the particles are separated by centrifugation. As a consequence, charge regulation in the interfacial area might be affected having an impact on the conductivity of the dispersion and dispersion medium, respectively. Accordingly, the measured conductivity data should be critically examined for systematic trends when the volume fractions increase.

Approach 3:

The MWO theory describes the effect of surface conductivity on the relationship between K_s and K_m [23–25]. In Eq. 4.16, the volume fraction φ is involved as well as the Dukhin number *Du*.

$$\frac{K_\mathrm{s}}{K_\mathrm{m}} = \frac{1+Du-\varphi(1-2Du)}{1+Du+0.5\varphi(1-2Du)} \tag{4.16}$$

An appropriate way to determine *Du* is to measure K_s and K_m for at least two dispersions with sufficiently different particle volume fractions. Using Eq. 4.16, *Du* can then be calculated by least square fit. Compared to approach 2, the advantage is that the relative conductivity can be calculated using Eq. 4.16 for any other volume fraction once *Du* is known for the investigated system and influences of the EDL overlap are small. Furthermore, *Du* is needed for calculations according to the advanced CVI theory, which takes the relaxation effect into account. This topic will be the subject of a forthcoming study.

4.3 Experimental

4.3.1 Materials

The following polymer latices were examined in this study (the sample identifier is based on the material and the particle diameter d_{50} in microns, i.e. material@d_{50}): Three polyvinyl chloride (PVC) dispersions from Westlake Vinnolit GmbH & Co. KG (PVC@0.20, produced by emulsion polymerisation; PVC@0.78 and PVC@2.10, both produced by micro suspension polymerisation), one styrene-butadiene rubber dispersion of type Taktene S 62 F (SBR@0.23) from Arlanxeo Switzerland S.A., two polytetrafluoroethylene dispersions of type PFA 6900 GZ (PTFE@0.21) and PFA 6910 GZ (PTFE@0.08) from 3M Dyneon GmbH, one polyurethane dispersion (PU@0.07; synthesized as part of an unpublished master's thesis of Christina Gassner at Heinrich Heine University Düsseldorf in 2021) and one polymethyl methacrylate-*co*-butyl acrylate dispersion (PBAMM@0.10; synthesized as part of an unpublished master's thesis of Sven Kroß at TH Köln in 2021).

4.3.2 Sample Preparation

In general, a 150 mL dispersion of the required volume fraction was prepared by diluting the highly concentrated stock dispersion. In case of deviations to the original pH value, the pH value in the diluted dispersion was adjusted by adding appropriate amounts of HCl or NaOH. Since the volumes of 0.1 mol·L^{-1} NaOH and HCl added were considered negligible, their exact amounts were not recorded. The additions were performed using an Eppendorf Research plus G single-channel pipette, which had a variable volume range of either 10 – 100 µL or 20 – 200 µL. NaOH or HCl was added up to three times, and typically, greater volumes were necessary for samples with lower particle volume fractions (i.e., higher dilutions). As the preceding treatment of most samples was not known, we did not use nitrogen blanketing to avoid carbon dioxide absorption. Due to partly limited sample quantities, different dilution procedures were followed, as described below.

In case of the PVC samples (PVC@0.20, PVC@0.78, PVC@2.09) and the PTFE samples (PTFE@0.08, PTFE@0.21), the particles were separated from the dispersion medium in an RC 5B Plus centrifuge from Sorvall with an SLA-3000 rotor (6×400 mL) at 10,000 rpm (≈17,500 RCF) and a run time of 2-6 h at 4 °C. The supernatant was then used as diluent for the stock dispersion. Therefore, the chemical equilibrium between the particle surface and the dispersion medium is maintained and any influence of the diluent on the electrical double layer can be ruled out. This procedure is called equilibrium dilution [2]. Notably, for these samples no pH adjustment was necessary. In all other cases we refer to non-equilibrium dilution.

The original sample SBR@0.23 was dialyzed against deionized water with a 200,000 MWCO membrane for 10 days to obtain the stock dispersion. The water was changed twice every day. Thereafter, it was assumed that only a negligible amount of electrolyte was present in the dispersion medium. Subsequently, the samples were diluted with a 2 $\mathrm{mol{\cdot}L^{-1}}$ KCl solution and deionized water adjusting a concentration of 10 $\mathrm{mmol{\cdot}L^{-1}}$ KCl in the dispersion medium.

All other samples were not pre-treated due to limited sample quantity. Instead, they were directly diluted and adjusted to a concentration of 10 $\mathrm{mmol{\cdot}L^{-1}}$ KCl in the dispersion medium using deionized water and a 2 $\mathrm{mol{\cdot}L^{-1}}$ KCl solution. Since these stock solutions may contain some electrolyte, it cannot be excluded that slight differences in electrolyte concentration have occurred in the dilution series.

Furthermore, minor pH adjustments were necessary for samples with non-equilibrium dilution. Nevertheless, following the described protocol the maximum deviation in the concentration of monovalent electrolytes, influenced by pH adjustments, should be maintained below 5 %.

4.3.3 Determination of Particle Density

Densities were determined with a 50 mL glass pycnometer, which was tempered at 25 °C in a water bath and calibrated with deionized water before each measurement. To determine the particle density ρ_p, the density of the original, undiluted dispersion ρ_s was measured. The density of water at 25 °C (0.997 g/L) was used as the density of the dispersion medium ρ_m. A sample of the dispersion was dried to constant weight at 80 °C to determine the particle mass fraction w. It was assumed that the dry residue consisted only of polymer. Finally, the particle density ρ_p was calculated with the following equation, assuming that the particles are not porous:

$$\rho_\mathrm{p} = \frac{\rho_\mathrm{s}\rho_\mathrm{m}w}{\rho_\mathrm{m}-\rho_\mathrm{s}(1-w)} \tag{4.17}$$

4.3.4 Measurement of pH Values

The pH was determined concurrently with the colloidal vibration current measurements using a 9615S-10D electrode from Horiba. This electrode was connected to the DT-1202 CVI measurement device from Dispersion Technology. Calibration of the pH electrode was performed at room temperature using a three-point calibration method. Buffer solutions with pH values of 4.01, 7.00, and 9.21 from Mettler Toledo were utilized for this calibration.

4.3.5 Determination of Conductivity Data and Dukhin Number

For the calculation of Dukhin number Du, the relative conductivity $K_s K_m^{-1}$ has to be estimated at different particle volume fractions. Prior to the measurement of the conductivity in the dispersion medium K_m, the particles have to be removed with a centrifuge. For this purpose, 35 mL of each sample was centrifuged for 2-8 h at 4 °C, and 25,000 RPM (≈130,000 RCF) in an Optima XPN-90 ultracentrifuge of Beckman Coulter with rotor SW 28 (6×35 mL). The measurement of conductivities K_s and K_m were performed with the conductivity electrode of the CVI measurement device DT-1202 from Dispersion Technology at room temperature. Each measurement was repeated three times and the results were averaged.

The measured conductivities of the dispersion medium K_m were also used to calculate the Debye-Hückel parameter κ according to Eq. 4.6, as the compositions of the electrolyte were unknown in the CVI measurements. The data obtained at various particle volume fractions were averaged.

4.3.6 Determination of Zeta Potential by CVI

CVI measurements were performed with DT-1202 from Dispersion Technology (software version: 12 m56030) at room temperature using a sonic frequency of 3 MHz and the "more precise" setup mode, which enhances the signal to noise ratio. To prevent settling and inhomogeneity, the samples were circulated with a peristaltic pump during measurement.

Each sample underwent three repetitions of measurement, with the results being averaged. Subsequently, the mass fraction was determined in triplicate. Measurement of the ion vibration current (IVI) was omitted because only dispersions with a particle volume fraction of more than 2.5 vol% were investigated. Therefore, the measured total vibration current (TVI) is essentially determined by the CVI and not affected by the IVI.

4.3.7 Determination of Zeta Potential with ELS

ELS measurements were performed with ZetaSizer Nano ZS from Malvern Panalytical. While the equilibration time was set to 180 s and the number of runs to 50, attenuation, measuring position and voltage were selected automatically by the software. All measurements were performed at 25 °C using a wavelength of 633 nm and folded capillary cells DTS 1070. The samples were diluted according to the protocol described in Chapter 4.3.2. The pH values were adjusted to the same values as for the CVI measurements using slight amounts of NaOH or HCl solution, again using the same protocol as described in Chapter 4.3.2. To reveal multiple light scattering effects, measurements were performed at least at five different particle volume fractions. The volume fractions studied were approximately between 0.1 and 0.001 vol%. Only values with nearly constant zeta potentials were averaged.

4.3.8 Determination of Particle Size

With exception of the samples PVC@0.78 and PVC@2.09, particle size distribution (PSD) was determined by dynamic light scattering (DLS) at 25 °C in polymethylmethacrylate macro cuvettes using ZetaSizer Nano ZS from Malvern Panalytical at a wavelength of 633 nm. The signal was detected using backscatter detection at an angle of 173° and each single measurement was obtained from 15 sub-runs. The attenuator and the measuring position was set automatically. For the refractive indices of the dispersed particles, the values in Tab. 4.1 are used and the absorbance was set to 0.01. For the dispersion medium, a dynamic viscosity of 0.8872 mPa·s and a refractive index of 1.334 were assumed. All samples were diluted according to the protocol described in Chapter 4.3.2. and measurements were performed at least at five different particle volume fractions in the range of approx. 0.1 to 0.001 vol%. Only almost constant particle sizes were averaged in order to exclude errors resulting from multiple scattering effects.

Tab. 4.1: Refractive indices used for the measurement of particle size.

sample	PVC [46]	SBR [47]	PBAMM [48]	PU [49]	PTFE [50]
refractive index *n*	1.540	1.534	1.489	1.485	1.350

In the case of samples PVC@0.78 and PVC@2.08, PSD was determined by laser diffraction spectroscopy (LDS) with MasterSizer 2000 and sampling unit Hydro 2000MU from Malvern Panalytical. The stirring speed was set to 1100 rpm. Sample was added to deionized water until laser obscuration reached a value between 10 and 20 %. All samples were measured in triplicate at room temperature at wavelengths of 633 nm and 433 nm, the results were averaged by the measuring instrument software. The same parameters for refractive index and absorbance were used as for the DLS measurements.

4.4 Results and Discussion

In this section, we present the results of our study in detail. Due to the numerous parameters that are considered, certain symbols are used that specifically address the various aspects examined. A list of symbols with a brief description can be found in Tab. 4.2 Detailed explanations are provided in the subsequent sections.

Tab. 4.2: Reference table of symbols.

Symbol *	Description
K_s	Measured conductivity in the dispersion
K_m	Measured conductivity in the dispersion medium
$\varkappa a_\mathrm{CVI}$	Ratio of Debye-Hückel parameter $\varkappa$ (calculated on basis of Eq. 4.6 and the conductivity of the dispersion medium) and particle radius a; used for the interpretation of CVI data
$\varkappa a_\mathrm{ELS}$	Ratio of Debye-Hückel parameter $\varkappa$ (calculated on basis of Eq. 4.3 and the electrolyte concentration of the dispersion medium) and particle radius a; used for the interpretation of ELS data
Du	Dukhin number calculated from the conductivity data of the dispersion and dispersion medium using MWO theory (Eq. 4.16), reflecting surface conductivity in both diffuse and stagnant layer
$\zeta^\mathrm{HS}_\mathrm{CVI}$	Zeta potential calculated from CVI data using Helmholtz-Smoluchowski theory and Eq. 4.9
$\zeta^\mathrm{HS}_\mathrm{ELS}$	Zeta potential calculated from ELS data using Helmholtz-Smoluchowski theory and Eq. 4.2
$\zeta^\mathrm{H}_\mathrm{CVI}$	Zeta potential calculated from CVI data using Henry theory and Eq. 4.10
$\zeta^\mathrm{H}_\mathrm{ELS}$	Zeta potential calculated from ELS data using Henry theory and Eq. 4.4

* The superscript indicates the evaluation method for the determination of the zeta potential: Helmholtz-Smoluchowski theory (HS) and Henry theory (H). The subscript refers to the measurement method used: colloid vibration current (CVI) and electrophoretic light scattering (ELS).

4.4.1 Evaluation of Sample Preparation and Estimation of Dukhin Number

Inappropriate dilution of the samples can change the ionic strength of the dispersion medium resulting in an impact on the electrical double layer and therefore on dispersion properties. As shown below, these effects can be well characterized by measuring conductivities of the dispersion and the dispersion medium. This also offers the opportunity to determine the Dukhin number Du.

Changes in the ionic strength directly influence the Debye-Hückel parameter $\varkappa$ (cf. Eq. 4.3), whose reciprocal value is a measure of the thickness of the diffuse layer. The ratio of the particle radius a to this reciprocal is of particular importance for the application and interpretation of electrokinetic methods. Hence, it is advisable to record the $\varkappa a$ values in the individual measurements and compare them with each other.

In the case of the CVI measurements, the composition of the electrolyte and thus the ionic strength remained unknown. Therefore, $\varkappa$ was calculated based on the conductivity of the dispersion medium using Eq. 4.6. The data obtained at various particle volume fractions were averaged and are listed in Tab. 4.3 in the column labelled κa_{CVI}.

For ELS measurements, substantial sample dilution is required, resulting in the electrolyte concentration being primarily influenced by the diluent. Except for the PVC and PTFE samples, κ was determined using Eq. 4.3 and the target concentration of 10 mmol·L^{-1} KCl in the dispersion medium. However, the PVC and PTFE samples were diluted with their supernatant so that the κa_{CVI} values can be adopted. The characteristic κa values obtained for the ELS measurements are presented in Tab. 4.3 in the column labelled κa_{ELS}.

4.4.1.1 Equilibrium Dilution of Polymer Dispersions

Equilibrium dilution is best suited to exclude influences of the dispersion medium on the zeta potential and the Dukhin number. This can be achieved by dilution with pure dispersion medium after removing the particles. To verify the success of equilibrium dilution, the conductivities of the diluted and undiluted dispersion medium can be compared as shown below.

All PVC samples were diluted with their respective centrifugate. As a representative example, the results obtained for sample PVC@0.20 are depicted in Fig. 4.1. The success of equilibrium dilution can be evidenced by the almost uniform dispersion conductivities K_{m} in the supernatant of each sample (cf. dots in Fig. 4.1). This behaviour is also observed with all other PVC samples (for details see supporting information, Fig. 4.8 A and B). Determination of relative conductivity $K_{\mathrm{s}}K_{\mathrm{m}}^{-1}$ is necessary for calculation of Dukhin number Du. The trend of the experimentally determined $K_{\mathrm{s}} \cdot K_{\mathrm{m}}^{-1}$ values (cf. squares in Fig. 4.1) of all PVC samples can be clearly described by fitting with MWO theory (cf. solid line in Fig. 4.1). The values thus obtained for Du significantly deviate from zero indicating pronounced surface conductivity for these samples (see Tab. 4.3).

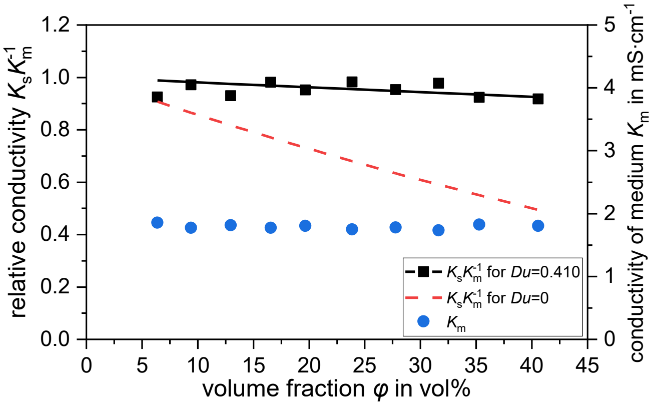

Fig. 4.1: Conductivity of media and relative conductivity of PVC@0.20 sample. Measured relative conductivities $K_{\mathrm{s}}K_{\mathrm{m}}^{-1}$ are plotted as squares. The solid line refers to the fit of $K_{\mathrm{s}}K_{\mathrm{m}}^{-1}$ according to MWO theory. For comparison, the course of $K_{\mathrm{s}}K_{\mathrm{m}}^{-1}$ for Du=0 has been plotted as a red dashed line. Conductivities of the medium K_{m} are shown as blue dots on the secondary y axis.

The PTFE samples, which were diluted with their respective centrifugate, also exhibit equilibrium dilution as can be seen from consistent medium conductivities (see Fig. 4.2 and supporting information, Fig. 4.8 C). Nevertheless, the relative conductivity values $K_{\mathrm{s}}K_{\mathrm{m}}^{-1}$ do not comply with MWO theory because the extrapolated trend of $K_{\mathrm{s}}K_{\mathrm{m}}^{-1}$ does not intersect the y axis at a value of one as expected. Consequently, the *Du* number cannot be determined using MWO theory. This behaviour is quite surprising and was not observed for any other sample in this study. The reason is not yet clear, but it is conspicuous that the PTFE samples are the only samples stabilized with non-ionic surfactants according to the product data sheet. Remarkably, previous work by Bárány and Dukhin [13] also reported difficulties in describing the relative conductivity of particle dispersions stabilized with non-ionic polymers, which have similar stabilization mechanisms compared to non-ionic surfactants. While their results showed an unexpected behaviour in slope, the observed intercepts on the *y* axis were always one. However, it can be supposed that the observed relative conductivities of the PTFE samples may be attributed to the adsorption of non-ionic surfactants.

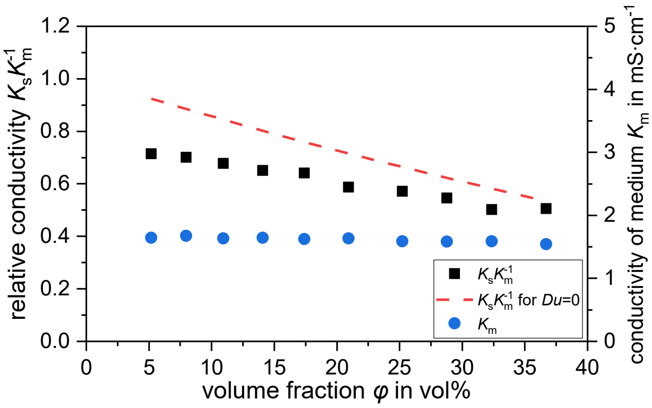

Fig. 4.2: Conductivity of media and relative conductivity of PTFE@0.21 sample at pH value of 9.3. Measured relative conductivities $K_s K_m^{-1}$ are plotted as squares. For comparison, the course of $K_s K_m^{-1}$ for $Du = 0$ has been plotted as a dashed line. Conductivities of the medium K_m are shown as dots on the secondary y axis. The sample was diluted with its supernatant to maintain an equilibrium dilution, so the electrolyte concentration is unknown.

4.4.1.2 Non-Equilibrium Dilution of Polymer Dispersions

The SBR@0.23 sample underwent dialysis prior to dilution, effectively removing most ions from the dispersion. Adequate amounts of KCl were then added to achieve a constant electrolyte concentration in the stock dispersion and the diluted samples. The sample exhibited almost behaviour of equilibrium dilution, as only a slight decrease in K_m was observed with increasing particle volume fraction (cf. Fig. 4.3)

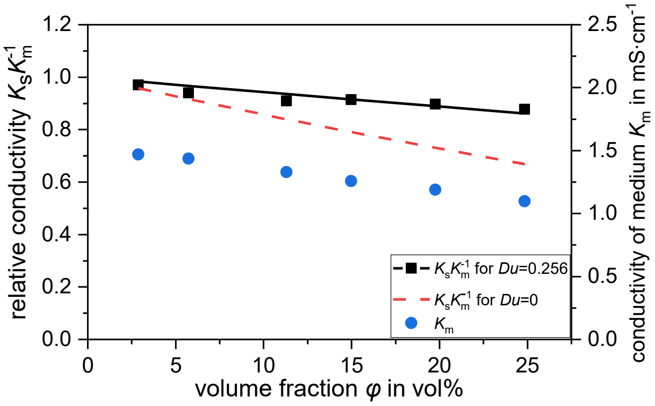

Fig. 4.3: Conductivity of media and relative conductivity of SBR@0.23 sample at pH value of 8.9. Measured relative conductivities $K_\mathrm{s}K_\mathrm{m}^{-1}$ are plotted as squares. The solid black line refers to the fit of $K_\mathrm{s}K_\mathrm{m}^{-1}$ according to MWO theory. For comparison, the course of $K_\mathrm{s}K_\mathrm{m}^{-1}$ for $Du = 0$ has been plotted as a dashed line. Conductivities of the medium K_m are shown as dots on the secondary y axis. The original sample was dialyzed against deionized water, and then diluted to achieve a 10 mmol·L^{-1} KCl concentration in the dispersion medium.

Only limited sample quantities were available for the PBAMM and PU dispersions. Therefore, they were used as received and diluted in such a way that a constant KCl concentration was achieved in the dispersion medium (see Chapter 4.3.2.). The assumption that the original ion concentration in the dispersion medium of the stock solution was almost negligible failed, since the samples show a pronounced increase in K_m with increasing φ (see supporting information, Fig. 4.8 D and E). This is likely caused by a higher ionic strength in the stock solution compared to the added electrolyte solution.

The presence of a noticeable trend in K_m with variation of φ indicates distinct non-equilibrium dilution for the PBAMM and PU samples. However, the relative conductivities $K_\mathrm{s}K_\mathrm{m}^{-1}$ are barely affected, and the values can be fitted quite well according to MWO theory because variations in K_m are partly displayed in K_s as well. The fit procedure gives the *Du* number of SBR, PBAMM and PU. All values significantly deviate from zero, indicating pronounced surface conductivity in these polymer dispersions (see Tab. 4.3).

Tab. 4.3: Dukhin number *Du*, κa value, pH value and mean zeta potential of CVI and ELS measurements *

sample	pH	*Du*	κa_{CVI}	κa_{ELS}	$\zeta^{\mathrm{HS}}_{\mathrm{CVI}}$ [mV]	$\zeta^{\mathrm{HS}}_{\mathrm{ELS}}$ [mV]	$\zeta^{\mathrm{H}}_{\mathrm{CVI}}$ [mV]	$\zeta^{\mathrm{H}}_{\mathrm{ELS}}$ [mV]
PVC@0.20	9.0	0.410	36.3	36.3	-67.5	-67.9	-71.8	-72.3
	±0.1		±0.3	±0.3	±1.7	±9.3	±1.8	±9.9
PVC@0.78	6.8	0.254	216.5	216.5	-69.7	-70.8	-70.5	-71.6
	±0.1		±9.4	±9.4	±3.8	±6.5	±3.9	±6.6
PVC@2.09	9.6	0.283	234.5	234.5	-91.7	-89.6	-92.7	-90.5
	±0.1		±2.9	±2.9	±2.3	±4.1	±2.3	±4.2
PTFE@0.08	9.8	—	22.4	22.4	-13.2	-14.8	-14.5	-16.3
	±0.0		±0.9	±0.9	±1.2	±0.3	±1.3	±0.3
PTFE@0.21	9.3	—	36.2	36.2	-19.8	-21.0	-22.1	-22.4
	±0.3		±0.4	±0.4	±1.0	±5.7	±1.1	±6.1
SBR@0.23	8.9	0.256	34.3	38.3	-78.4	-74.9	-83.7	-79.5
	±0.1		±1.7		±1.0	±2.2	±1.1	±2.4
PU@0.07	8.8	0.348	13.5	11.4	-38.7	-44.1	-44.7	-51.9
	±0.4		±2.4		±2.5	±3.6	±2.9	±1.3
PBAMM@0.10	8.6	0.114	31.9	16.3	-52.7	-54.5	-56.5	-61.7
	±0.1		±8.1		±2.8	±2.3	±3.0	±2.6

* Superscript HS indicates evaluation according to Helmholtz-Smoluchowski theory and superscript H indicates Henry theory

4.4.2 Zeta Potentials Determined by CVI and ELS Measuring Methods

The electrophoretic mobility is one of the primary results obtained in electrokinetic experiments of charged particles. We used Eq. 4.2 and 4.9 to calculate the zeta potential within the framework of the HS theory. Since this theory is only valid for thin EDL compared to the particle radius, corresponding zeta potentials were also determined by means of the Henry theory using the κa values and Eq. 4.4 and 4.10, respectively. Although both theories do not take surface conductivity into account, we will show in the following section that it can have a severe impact in the zeta potential determination at higher solids content.

4.4.2.1 Equilibrium Dilution of Polymer Dispersions

PVC@0.20 was selected for comparison of the three approaches presented in the theoretical section, as it is the sample with the highest Dukhin number determined. The results using the HS theory for the individual CVI measurements are shown in Fig. 4.4. The first approach (●), which is generally employed by the used measuring device, does not consider the influence of surface conductivity on the internal electric field strength E_{int}, unlike the second (▲) and third (■) approaches. In case of PVC@0.20, this first approach shows an increase in absolute zeta potential with increasing particle volume fraction. On the other hand, the second and third approaches result in nearly identical, constant zeta potentials, which basically do not depend on particle volume fraction. At low particle volume fractions, the discrepancy between the first approach and the other approaches is small, but increases almost linearly with increasing particle volume fraction. The zeta potential at the highest investigated particle volume fraction is -127.6 mV in the first approach, while in the second and third approaches, the calculated zeta potential is about -68 mV, indicating a deviation of nearly 100 %. This emphasizes the importance of considering the influence of surface conductivity on the internal electric field strength E_{int}, especially for high particle volume fractions. For this purpose, the approaches 2 and 3 have proven to be very suitable. On the other hand, an increase in the absolute value of the zeta potential determined according to the first approach may indicate the presence of surface conductivity and should then be examined more closely. Furthermore, this feature also offers another opportunity for a rough estimation of the Dukhin number, as described in the supporting information.

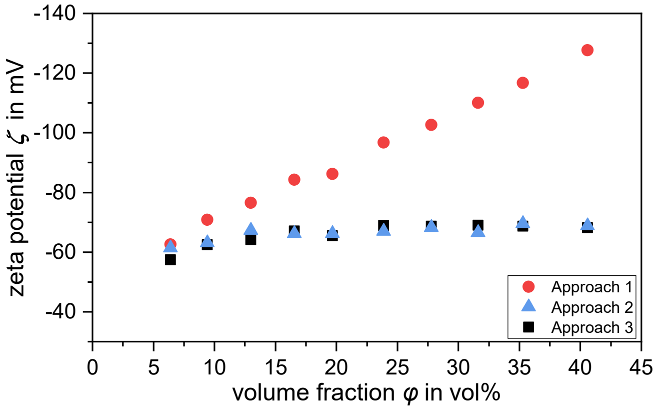

Fig. 4.4: Comparison of the three approaches for calculating the zeta potential according to HS model, as discussed in the theory section, using PVC@0.20 dispersion as an example. First approach ●, second approach ▲, third approach ■. The pH value is 9.0, and the sample was diluted with its supernatant to maintain an equilibrium dilution, so the electrolyte concentration is unknown.

Fig. 4.5 shows the findings for all PVC samples tested. All zeta potential results are evaluated according to the third approach with the use of the HS theory. Over a wide range of volume fraction, the values remain almost constant within the measurement accuracy. This is quite surprising, especially as the analysed solids contents ranged up to 40 vol%. Dukhin and Reisel have recently shown for a silica dispersion that EDL overlap leads to a significant increase in zeta potential [51]. However, the polymer dispersions investigated in this study do not exhibit comparable behaviour and the influence of EDL overlap is assumed to be low. It should also be mentioned that the magnitude of the zeta potentials measured at low particle volume fractions decreased significantly for the samples PVC@0.20 and PVC@0.78. Therefore, these measurements were considered as outliers due to measurement inaccuracy (unfilled data points) and were excluded from the calculation of the mean value.

As can be seen from the κa values, the determined thickness of the EDL is very low. Only the sample PVC@0.20 shows a slight increase in zeta potential when the Henry theory is applied. Nevertheless, it should be noted that the zeta potentials of all three samples calculated with these standard models are quite high (>50 mV). Consequently, it is to be expected that effects due to EDL polarisation (relaxation effect) are already present. The extent of this influence will be analysed in detail in a forthcoming study.

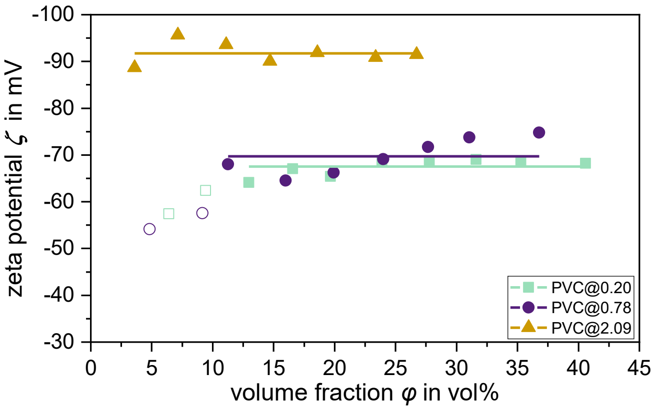

Fig. 4.5: Zeta potentials at different particle volume fractions of different sized PVC dispersions calculated according to the third approach and the HS theory. The displayed lines correspond to the mean values. Filled data points were considered for the calculation of the mean value; unfilled data points were neglected. The pH values of the samples were 9.0, 6.8, and 9.6 respectively for PVC@0.20, PVC@0.78, and PVC@2.09. All samples were diluted with their respective centrifugate to maintain an equilibrium dilution, so the electrolyte concentrations are unknown.

It was shown in Chapter 4.4.1.1 that it was not possible to determine *Du* for the PTFE samples with the MWO theory. This in turn means that the third approach cannot be applied. Nevertheless, reasonable zeta potentials can be determined using the second approach (see Fig. 4.6), which is based on the relative conductivity $K_\mathrm{s}K_\mathrm{m}^{-1}$. Variations in the values are rather small and tolerable, so that the influence of a possible EDL overlap at high volume fractions is again regarded as low. Although the relative conductivities do not obey the MWO theory in this case, these results underline that they are a very good parameter to describe the effect of the internal electric field strength $\boldsymbol{E}_\mathrm{int}$ in electrophoretic measurements.

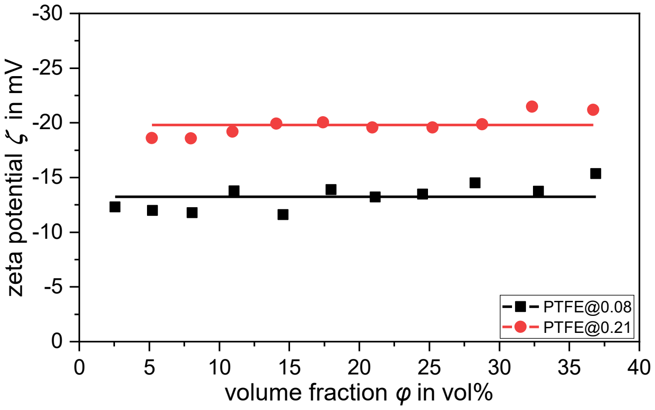

Fig. 4.6: Zeta potentials at different particle volume fractions of different sized PTFE dispersions calculated according to the second approach and the HS theory. Displayed lines correspond to the mean values. The pH values of the samples were 9.8 and 9.3 respectively for PTFE@0.08 and PTFE@0.21. Both samples were diluted with their supernatant to maintain an equilibrium dilution, so the electrolyte concentrations are unknown.

Since zeta potential is a specific parameter for a charged surface under certain conditions, experimentally determined values should not dependent on the measurement method used. This quality check was called electrokinetic consistency test by Lyklema [52] or integrated electro surface investigation by Dukhin and Derjaguin [37]. The mean values of the zeta potentials determined with the CVI method for the different PVC and PTFE samples agree very well with the values determined by the ELS method (see Tab. 4.3), as the observed deviations are within typical error limits usually expected for zeta potential measurements, i.e. approximately 10 % [53]. This applies both to the values calculated using HS theory and Henry theory. Thus, these results also strongly underline the reliability of the values obtained by the CVI measurement method when the influence of surface conductivity is correctly taken into account.

4.4.2.2 Non-Equilibrium Dilution of Polymer Dispersions

As already mentioned, it was not possible to dilute the samples of several polymer dispersions investigated in this study with their centrifugate. Instead, the samples were prepared with a diluted electrolyte solution. Nevertheless, the characterization with the CVI method succeeds and both the second and third approach show similar and relatively consistent zeta potentials over a broad range of volume fractions (see Fig. 4.7). Only the PU and PBAMM dispersions reveal a slight trend in the zeta potential values. This is probably due to the quite pronounced non-equilibrium dilution, as can be seen from the conductivities of the dispersion medium (cf. Fig. 4.8 D and E in the supporting information). The plausibility of the CVI results can be checked again by comparison with the ELS data (refer to Tab. 4.3). The overall agreement of the values is still very good. This indicates that the CVI method proves to be quite robust even in the case of difficulties with the measurement protocol.

The $\varkappa a$ values show that the retardation effect only has a small impact. Therefore, the zeta potentials according to the Henry theory are only slightly higher than those according to the HS theory. However, the magnitude of the zeta potentials again suggests that the relaxation effect should be taken into account to improve reliability, at least for SBR@0.23.

We have already pointed out that sample SBR@0.23 was diluted approximately under equilibrium condition, as indicated by the conductivity data of the dispersion medium K_m. Interestingly, the corresponding $\varkappa a_\mathrm{CVI}$ and $\varkappa a_\mathrm{ELS}$ values are also in excellent agreement with each other. This implies that Eq. 4.6 can be used for a reliable approximation of the Debye-Hückel parameter if Eq. 4.3 is not applicable.

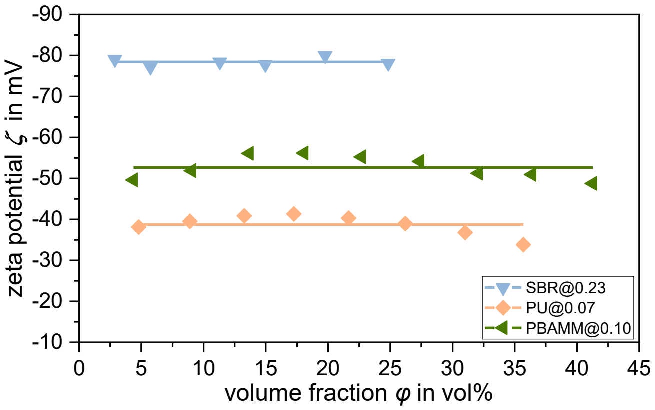

Fig. 4.7: Zeta potentials at different particle volume fractions of different polymer dispersions calculated according to the third approach and the HS theory. Displayed lines correspond to the mean values. The pH values of the samples were 8.9 for SBR@0.23, 8.8 for PU@0.07, and 8.6 for PBAMM@0.10. SBR@0.23 was dialyzed and then diluted to achieve a 10 mmol L^{-1} KCl concentration in the dispersion medium. The PU and PBAMM samples were directly diluted to achieve a final KCl concentration of 10 mmol L^{-1} in the dispersion medium; however, the original ion concentration was assumed to be negligibly low, which was not the case.

Only few studies are available in which the zeta potential of polymer dispersions was investigated using electroacoustic methods. Most of them have been focused on particle volume fractions below 10 vol%. Therefore, it is not surprising that they did not report about the influence of surface conductivity on zeta potential determination because this impact becomes evident primarily at high particle volume fractions. However, in the study by Ishikawa et al. [34] several polyacrylate latices were examined up to a concentration of approx. 27 vol% using the CVI method in a 10 mmol·L^{-1} NaCl solution. The main focus of their study was to examine the influence of particle volume fraction on the CVI signal, rather than exploring the relationship between zeta potential and volume fraction. For this purpose, they used a procedure comparable to our approach 1 and were able to understand the dependence of the CVI signal on the volume fraction. This in turn means that the polyacrylate samples examined by Ishikawa et al. showed negligible surface conductivities. The very good agreement of the zeta potentials determined with the CVI and ELS methods also supports this conclusion.

In the study by Rasmusson [36], among others, the dynamic electrophoretic mobility of a polystyrene dispersion was investigated up to a particle volume fraction of 18 vol%. It was found that the experimental data showed a much lower volume fraction dependence than calculated with various models. Possibly, these models do not consider the surface conductivity of the particles in an adequate way. As can be seen from Eq. 4.9, the volume fraction dependence of the dynamic electrophoretic mobility is accounted for by the relative conductivity $K_s K_m^{-1}$ in this study. By means of Eq. 4.16 it becomes clear that this influence decreases with increasing Dukhin number *Du*. Therefore, the polystyrene dispersion studied by Rasmusson presumably exhibited considerable surface conductivity.

Hozumi and Furusawa [35] studied various polystyrene latices with solid contents above 10 vol% using the CVP method. They observed an unexpected decrease in the absolute zeta potential with increasing particle volume fraction, contrary to the findings in this study. Based on conductivity measurements of the dispersions, they attributed this phenomenon to interparticle surface conductivity caused by an overlap of hairy layers on the particle surfaces. However, this parameter is not considered in the theory applied by Hozumi and Furusawa to determine the zeta potential, which is essentially based on a Levine cell model [54]. They also showed, using silica reference measurements, that this model becomes inaccurate above a volume fraction of about 20 vol%. On the other hand, the theory applied in this study utilizes a Kuwabara cell model [55] for hydrodynamic parameters and a Shilov-Zharkikh cell model [56] for electrokinetic parameters. It takes into account the surface conductivity with the help of the multiplier $K_\mathrm{s}K_\mathrm{m}^{-1}$, which is not used in the Levine cell model [57]. This may be one of the main reasons why such large differences in the volume fraction dependence of the zeta potential were observed compared to our study.

4.5 Conclusion

In this study, we investigated the zeta potential of aqueous polymer dispersions using the colloidal vibration current (CVI) measurement method at high particle concentration as well as the electrokinetic light scattering (ELS) measurement method in the diluted state. The analysis of the CVI and ELS data was conducted by means of the standard models of Helmholtz-Smoluchowski (HS) and Henry, both neglecting surface conductivity effects such as the polarization of the electrical double layer. However, our study has revealed that surface conductivity can have an extraordinary influence on the accuracy of the zeta potential determination, especially at high particle volume fractions.

The specific investigation of polymer dispersions in this study addresses a notable gap in the literature. While electroacoustic methods have been extensively applied in the investigation of inorganic materials, research on polymer dispersions is limited. Previous studies have mainly focused on low particle volume fractions [26–33] and have therefore not fully explored the capabilities of electroacoustic methods. Only few publications [34–36] have dealt with polymer dispersions with solids contents above 10 vol%. Since all polymer dispersions investigated in our study exhibit significant surface conductivity, a distinctive aspect of our research is the examination of its influence on the zeta potential determination, especially in the field of electroacoustics.

As the volume fraction of particles increases, non-conductive particles (dielectrics) diminish the effective internal field strength in electrokinetic experiments, while surface conductivity counteracts this effect. The second factor can be characterised by means of the dimensionless Dukhin number. This parameter was determined in our study on the basis of the Maxwell-Wagner-O'Konski theory [23–25] using conductivity data from the dispersion (K_s) and the dispersion medium (K_m). Moreover, we have demonstrated that the relative conductivity $K_\mathrm{s}K_\mathrm{m}^{-1}$ correctly accounts for the influence of the particle volume fraction and the surface conductivity on the zeta potential determination within the framework of both standard models.

We have found that neglecting the surface conductivity can lead to measurement errors of up to 100 %, especially for high particle volume fractions and dispersions with high Dukhin number. If necessary, the most reliable results are obtained by equilibrium dilution. Although some measurements in our study do not meet this condition, the zeta potential values determined by CVI measurement show remarkable consistency with the values obtained by ELS method when the surface conductivity is correctly taken into account. Since some of the investigated polymer dispersions also exhibit high zeta potentials, the influence of the polarization effect on the CVI measurement will be investigated in detail in future research work.

4.6 Supporting Information

4.6.1 Calculation of the Zeta Potential According to the Different Approaches

As highlighted in the main article, the study utilizes the DT-1202 device to determine the zeta potential. This device employs Eq. 4.18 as default, which we have designated as the first approach for calculating the zeta potential ζ_{A1} based on the Helmholtz-Smoluchowski model [40].

$$\frac{CVI_{\omega\to 0}}{\Delta P} = \frac{\varepsilon_0 \varepsilon_m \zeta_{A1}}{\eta} \frac{1-\varphi}{1+0.5\varphi} \frac{\rho_p - \rho_s}{\rho_s} \varphi F(Z_T, Z_s) A(\omega) \tag{4.18}$$

To determine the zeta potential using the second and third approach, we performed a recalculation of the zeta potential ζ_{A1} obtained from the first approach. The zeta potential according to the second approach (ζ_{A2}) was calculated using Eq. 4.19, while Eq. 4.20 was used for the zeta potential referring to the third approach (ζ_{A3}).

$$\zeta_{A2} = \zeta_{A1} \frac{1-\varphi}{1+0.5\varphi} \frac{K_m}{K_s} \tag{4.19}$$

$$\zeta_{A3} = \zeta_{A1} \frac{1-\varphi}{1+0.5\varphi} \frac{1+Du+0.5\varphi(1-2Du)}{1+Du-\varphi(1-2Du)} \tag{4.20}$$

Particle Densities and Particle Size Distributions

Tab. 4.4 shows all particle densities determined by glass pycnometer at 25°C using Eq. 4.17 in the main article. In addition, the volume-weighted particle size distribution data are presented for all analysed samples.

Tab. 4.4: Measured particle densities analysed at 25 °C

sample	density ρ $[\mathrm{g\cdot cm^{-3}}]$	d_{10} $[\mu\mathrm{m}]$	d_{50} $[\mu\mathrm{m}]$	d_{90} $[\mu\mathrm{m}]$	d_{mean} $[\mu\mathrm{m}]$
PVC@0.20	1.41	0.129	0.202	0.314	0.212
PVC@0.78	1.39	0.354	0.783	1.377	0.834
PVC@2.09	1.41	1.057	2.086	4.223	2.416
PTFE@0.08	2.00	0.058	0.080	0.118	0.084
PTFE@0.21	2.00	0.144	0.212	0.308	0.219
SBR@0.23	0.94	0.063	0.233	0.575	0.270
PU@0.07	1.16	0.045	0.069	0.127	0.079
PBAMM@0.10	1.10	0.069	0.099	0.155	0.105

4.6.2 Estimation of Dukhin Number

Fig. 4.8 presents supplementary data regarding the estimation of relative conductivities $K_s K_m^{-1}$ and bulk medium conductivities K_m, which were not presented in the main article. A comprehensive discussion on the fundamental meaning and interpretation can be found in the main article.

As stated in the main article, the zeta potentials increase when using the first approach (i.e. ζ_{A1}) for particles with surface conductivity. Since the zeta potential is a material property, it should be constant with increasing particle volume fraction in an otherwise fixed system. This feature can be utilized to approximately determine the Dukhin number. For this purpose, the Dukhin number (for distinction Du_{A3}) in Eq. 4.20 (third approach) is adjusted by least square refinement until an average zeta potential ζ_{A3} with minimal standard deviation is achieved. In order to receive consistent results, measurements at low particle concentrations ($\lesssim$ 7 vol%) were neglected. In contrast, the Dukhin numbers determined in the main article were based on relative conductivities $K_s K_m^{-1}$ and are denoted by Du. The corresponding zeta potentials are referred to as ζ_{CVI}^{HS}.

Tab. 4.5 provides a comparison of the Dukhin numbers Du and Du_{A3} and zeta potentials ζ_{CVI}^{HS} and ζ_{A3}. While some significant differences are observed in the different Dukhin numbers, the overall trend remains consistent. Analysis of the zeta potentials shows that, except for PVC@0.78, the mean zeta potentials are relatively similar. In general, the zeta potentials obtained from Du are closer to the ELS results, suggesting that the determination of Dukhin number by relative conductivity measurements is more reliable. And, of course, one should bear in mind that other factors can also contribute to an increase in the zeta potential as the particle concentration increases, such as the overlapping of the EDL [51]. Accordingly, it is necessary to interpret the measurement data with great caution. However, the alternative method described here in the supporting information is a pragmatic way to approximate the Dukhin number if conductivity data of dispersion and medium are not available.

Tab. 4.5: Comparison of different Dukhin numbers and zeta potentials

material	Du	Du_{A3}	ζ_{CVI}^{HS} [mV]	ζ_{A3} [mV]	ζ_{ELS}^{HS} [mV]
PVC@0.20	0.410	0.553	-67.5±1.7	-62.5±1.2	-67.9±9.3
PVC@0.78	0.254	0.582	-69.7±3.8	-58.1±2.0	-70.8±6.5
PVC@2.09	0.283	0.256	-91.7±2.3	-92.8±2.3	-89.6±4.1
SBR@0.23	0.256	0.279	-78.4±1.0	-78.0±1.9	-74.9±2.2
PU@0.07	0.348	0.106	-38.7±2.5	-46.7±1.2	-44.1±3.6
PBAMM@0.10	0.114	0.050	-52.7±2.8	-57.6±1.4	-54.5±2.3

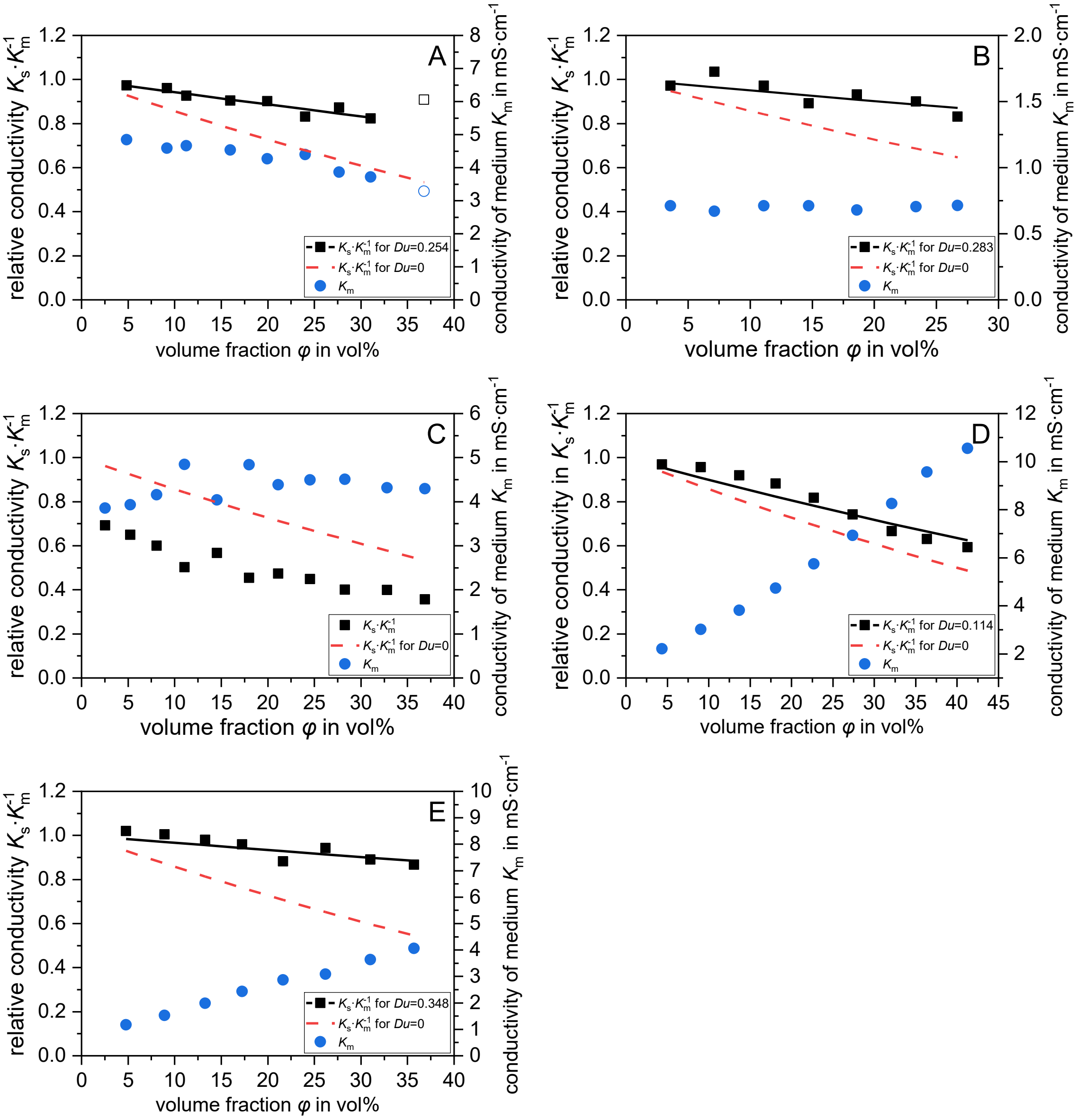

Fig. 4.8: Conductivity of media and relative conductivity of samples, which were not presented in the main article. Where A is PVC@0.78 (pH value of 6.8), B is PVC@2.09 (pH value of 9.6), C is PTFE@0.08 (pH value of 9.8), D is PBAMM@0.10 (pH value of 8.6) and E is PU@0.07 (pH value of 8.8). Measured relative conductivities $K_s K_m^{-1}$ are plotted as black squares. The black solid line refers to the fit of $K_s K_m^{-1}$ according to MWO theory. For comparison, the course of $K_s K_m^{-1}$ for $Du = 0$ has been plotted as a red dashed line. Conductivities of the medium K_m are shown as blue dots on the secondary y axis.

Acknowledgments

This project has received fundings by the German Ministry of Education and Research (BMBF) as part of the funding program “Forschung an Fachhochschulen” under contract number13FH142PX6. We are also very grateful for valuable discussions and financial and material support provided by Westlake Vinnolit GmbH &Co. KG. Furthermore, we would like to thank A. S. Dukhin of Dispersion Technology Inc., Bedford Hills, NY, USA for fruitful discussions. No human and/or animal studies were used in this article, and all authors are fully aware that nothing in this article violates ethics. The authors declare no competing interests

4.7 References

[1] Frangenberg, M.; Schmidt, A. M.; Wilkens, J. Impact of surface conductivity on the zeta potential determination of concentrated aqueous polymer dispersions using electroacoustics and electrokinetic standard models. *Colloid Polym. Sci.* **2024**, *302*, 1801–1813. DOI: 10.1007/s00396-024-05301-7.

[2] International Organization for Standardization. *Colloidal systems - Methods for zeta-potential determination - Part 1: Electroacoustic and electrokinetic phenomena*, 2012, *19.120* (ISO 13099-1:2012-06).

[3] International Organization for Standardization. *Colloidal systems - Methods for zeta-potential determination - Part 2: Optical methods*, 2012, *19.120* (ISO 13099-2:2012-06).

[4] International Organization for Standardization. *Colloidal systems - Methods for zeta potential determination - Part 3: Acoustic methods*, 2014, *19.120* (13099-3:2014-07).

[5] Hunter, R. J. Recent developments in the electroacoustic characterisation of colloidal suspensions and emulsions. *Colloids Surf., A* **1998**, *141*, 37–66. DOI: 10.1016/S0927-7757(98)00202-7.

[6] Marlow, B. J.; Fairhurst, D.; Pendse, H. P. Colloid vibration potential and the electrokinetic characterization of concentrated colloids. *Langmuir* **1988**, *4*, 611–626. DOI: 10.1021/la00081a021.

[7] Mohammadi-Jam, S.; Waters, K. E.; Greenwood, R. W. A review of zeta potential measurements using electroacoustics. *Adv. Colloid Interface Sci.* **2022**, *309*, 102778. DOI: 10.1016/j.cis.2022.102778.

[8] Delgado, A. V.; González-Caballero, F.; Hunter, R. J.; Koopal, L. K.; Lyklema, J. Measurement and interpretation of electrokinetic phenomena. *J. Colloid Interface Sci.* **2007**, *309*, 194–224. DOI: 10.1016/j.jcis.2006.12.075.

[9] Smoluchowski, M. v. Elektrische Endosmose und Strömungsströme. In *Handbuch der Elektrizität und des Magnetismus*; Graetz, L., Ed.; Johann Ambrosius: Barth, Leipzig, 1921; pp 366–428.

[10] Henry, D. C. The Cataphoresis of Suspended Particles. Part I. The Equation of Cataphoresis. *Proc. R. Soc. London, Ser. A* **1931**, *133*, 106–129. DOI: 10.1098/rspa.1931.0133.

[11] Midmore, B.; O'Brien, R. The conductivity of concentrated suspensions at low frequencies. *J. Colloid Interface Sci.* **1988**, *123*, 486–493. DOI: 10.1016/0021-9797(88)90270-6.

[12] Van Der Put, A.G; Bijsterbosch, B. Electrical conductivity of dilute and concentrated aqueous dispersions of monodisperse polystyrene particles. Influence of surface conductance and double-layer polarization. *J. Colloid Interface Sci.* **1980**, *75*, 512–524. DOI: 10.1016/0021-9797(80)90474-9.

[13] Bárány, S.; Dukhin, S. Effect of adsorbed polymers on the surface conductivity of dispersed particles. *Colloids Surf., A* **2001**, *192*, 307–316. DOI: 10.1016/S0927-7757(01)00731-2.

[14] O'Brien, R.; Perrins, W. The electrical conductivity of a porous plug. *J. Colloid Interface Sci.* **1984**, *99*, 20–31. DOI: 10.1016/0021-9797(84)90081-X.

[15] Minor, M.; van der Linde, A. J.; van Leeuwen, H. P.; Lyklema, J. Streaming potentials and conductivities of porous silica plugs. *Colloids Surf., A* **1998**, *142*, 165–173. DOI: 10.1016/S0927-7757(98)00365-3.

[16] Löbbus, M.; van Leeuwen, H. P.; Lyklema, J. Streaming potentials and conductivities of latex plugs. Influence of the valency of the counterion. *Colloids Surf., A* **2000**, *161*, 103–113. DOI: 10.1016/S0927-7757(99)00329-5.

[17] Hughes, M. P.; Morgan, H.; Flynn, M. F. The Dielectrophoretic Behavior of Submicron Latex Spheres: Influence of Surface Conductance. *J. Colloid Interface Sci.* **1999**, *220*, 454–457. DOI: 10.1006/jcis.1999.6542.

[18] Midmore, B.; Hunter, R.; O'Brien, R. The dielectric response of concentrated latices. *J. Colloid Interface Sci.* **1987**, *120*, 210–217. DOI: 10.1016/0021-9797(87)90342-0.

[19] Jiménez, M. L.; Arroyo, F. J.; Carrique, F.; Delgado, A. V. Surface conductivity of colloidal particles: experimental assessment of its contributions. *J. Colloid Interface Sci.* **2007**, *316*, 836–843. DOI: 10.1016/j.jcis.2007.07.016.

[20] Kijlstra, J.; van Leeuwen, H. P.; Lyklema, J. Low-frequency dielectric relaxation of hematite and silica sols. *Langmuir* **1993**, *9*, 1625–1633. DOI: 10.1021/la00031a005.

[21] Minor, M.; van Leeuwen, H. P.; Lyklema, J. Low-Frequency Dielectric Response of Polystyrene Latex Dispersions. *J. Colloid Interface Sci.* **1998**, *206*, 397–406. DOI: 10.1006/jcis.1998.5619.

[22] Roldán-Toro, R.; Solier, J. D. Wide-frequency-range dielectric response of polystyrene latex dispersions. *J. Colloid Interface Sci.* **2004**, *274*, 76–88. DOI: 10.1016/j.jcis.2004.02.068.

[23] Maxwell, J. C. *A treatise on electricity and magnetism vol.1*; Oxford University Press: Oxford, 1873.

[24] Wagner, K. W. Erklärung der dielektrischen Nachwirkungsvorgänge auf Grund Maxwellscher Vorstellungen. *Archiv f. Elektrotechnik* **1914**, *2*, 371–387. DOI: 10.1007/bf01657322.

[25] O'Konski, C. T. Electric Properties of Macromolecules. V. Theory of Ionic Polarization in Polyelectrolytes. *J. Phys. Chem.* **1960**, *64*, 605–619. DOI: 10.1021/j100834a023.

[26] James, R. O.; Texter, J.; Scales, P. J. Frequency dependence of electroacoustic (electrophoretic) mobilities. *Langmuir* **1991**, *7*, 1993–1997. DOI: 10.1021/la00058a002.

[27] Klingbiel, R. T.; Coll, H.; James, R. O.; Texter, J. Electrokinetic sonic amplitude of colloidal poly(methyl methacrylate) and Ludox®-TM. *Colloids Surf.* **1992**, *68*, 103–109. DOI: 10.1016/0166-6622(92)80151-Q.

[28] Gibb; Hunter. Dynamic Mobility of Colloidal Particles with Thick Double Layers. *J. Colloid Interface Sci.* **2000**, *224*, 99–111. DOI: 10.1006/jcis.1999.6676.

[29] Goetz, R. J.; El-Aasser, M. S. Effects of dispersion concentration on the electroacoustic potentials of o/w miniemulsions. *J. Colloid Interface Sci.* **1992**, *150*, 436–452. DOI: 10.1016/0021-9797(92)90213-6.

[30] Hunter, R. J.; Midmore, B. R.; Zhang, H. Zeta Potential of Highly Charged Thin Double-Layer Systems. *J. Colloid Interface Sci.* **2001**, *237*, 147–149. DOI: 10.1006/jcis.2001.7423.

[31] Shubin, V. E.; Hunter, R. J.; O'Brien, R. W. Electroacoustic and Dielectric Study of Surface Conduction. *J. Colloid Interface Sci.* **1993**, *159*, 174–183. DOI: 10.1006/jcis.1993.1309.

[32] Dahlsten, P.; Próchniak, P.; Kosmulski, M.; Rosenholm, J. B. Electrokinetic behavior of melamine–formaldehyde latex particles at moderate electrolyte concentration. *J. Colloid Interface Sci.* **2009**, *339*, 409–415. DOI: 10.1016/j.jcis.2009.07.029.

[33] Kosmulski, M.; Dahlsten, P.; Próchniak, P.; Rosenholm, J. B. High ionic strength electrokinetics of melamine–formaldehyde latex. *J. Colloid Interface Sci.* **2006**, *301*, 538–541. DOI: 10.1016/j.jcis.2006.05.052.

[34] Ishikawa, Y.; Aoki, N.; Ohshima, H. Characterization of latex particles for aqueous polymeric coating by electroacoustic method. *Colloids Surf., B* **2005**, *46*, 147–151. DOI: 10.1016/j.colsurfb.2005.10.005.

[35] Hozumi, Y.; Furusawa, K. Electrokinetic study on concentrated suspensions using colloid vibration potential measurements. *Colloid Polym. Sci.* **1990**, *268*, 469–475. DOI: 10.1007/bf01411006.

[36] Rasmusson, M. Volume Fraction Effects in Electroacoustic Measurements. *J. Colloid Interface Sci.* **2001**, *240*, 432–447. DOI: 10.1006/jcis.2001.7559.

[37] Dukhin, S. S.; Derjaguin, B. V. *Surface and Colloid Science*; J. Wiley & Sons: New York, 1974.

[38] Ohshima, H. A Simple Expression for Henry's Function for the Retardation Effect in Electrophoresis of Spherical Colloidal Particles. *J. Colloid Interface Sci.* **1994**, *168*, 269–271. DOI: 10.1006/jcis.1994.1419.

[39] Dukhin, S. S. Non-equilibrium electric surface phenomena. *Adv. Colloid Interface Sci.* **1993**, *44*, 1–134. DOI: 10.1016/0001-8686(93)80021-3.

[40] Dukhin, A. S.; Goetz, P. J. *Characterization of Liquids, Dispersions, Emulsions, and Porous Materials Using Ultrasound*, Third edition; Elsevier: Amsterdam, Oxford, Cambridge, MA, 2017.

[41] Kruyt, H. R., Ed. *Colloid science: Volume 1: Irreversible systems*; Elsevier: New York [etc.], 1952.

[42] O'Brien, R. W. Electro-acoustic effects in a dilute suspension of spherical particles. *J. Fluid Mech.* **1988**, *190*, 71. DOI: 10.1017/S0022112088001211.

[43] Dukhin, A. S.; Shilov, V. N.; Ohshima, H.; Goetz, P. J. Electroacoustic Phenomena in Concentrated Dispersions: New Theory and CVI Experiment. *Langmuir* **1999**, *15*, 6692–6706. DOI: 10.1021/la990317g.

[44] Dukhin, A. S.; Shilov, V.; Borkovskaya, Y. Dynamic Electrophoretic Mobility in Concentrated Dispersed Systems. Cell Model. *Langmuir* **1999**, *15*, 3452–3457. DOI: 10.1021/la981382d.

[45] Ohshima, H.; Dukhin, A. S. Colloid Vibration Potential in a Concentrated Suspension of Spherical Colloidal Particles. *J. Colloid Interface Sci.* **1999**, *212*, 449–452. DOI: 10.1006/jcis.1998.6059.

[46] Zhang, X.; Qiu, J.; Li, X.; Zhao, J.; Liu, L. Complex refractive indices measurements of polymers in visible and near-infrared bands. *Applied optics* **2020**, *59*, 2337–2344. DOI: 10.1364/AO.383831.

[47] Khan, H. U.; Gupta, V. K.; Yamin, M. Specific Refractive Index Increments of Polybutadiene, Styrene-Butadiene Rubber, Crepe Rubber, Polystyrene, Polymethyl Methacrylate, and Styrene-Methyl Methacrylate in Various Solvents and Variation of Refractive Index Increment with Molecular Weight. *Journal of Macromolecular Science: Part A - Chemistry* **1983**, *20*, 503–513. DOI: 10.1080/00222338308060797.

[48] Sultanova, N. G.; Kasarova, S. N.; Nikolov, I. D. Characterization of optical properties of optical polymers. *Opt Quant Electron* **2013**, *45*, 221–232. DOI: 10.1007/s11082-012-9616-6.

[49] Bauer, J.; Gutke, M.; Heinrich, F.; Edling, M.; Stoycheva, V.; Kaltenbach, A.; Burkhardt, M.; Gruenefeld, M.; Gamp, M.; Gerhard, C.*; et al.* Novel UV-transparent 2-component polyurethane resin for chip-on-board LED micro lenses. *Opt. Mater. Express* **2020**, *10*, 2085. DOI: 10.1364/OME.393844.

[50] French, R. H.; Rodriguez-Parada, J. M.; Yang, M. K.; Derryberry, R. A.; Lemon, M. F.; Brown, M. J.; Haeger, C. R.; Samuels, S. L.; Romano, E. C.; Richardson, R. E. Optical properties of materials for concentrator photovoltaic systems. In *2009 34th IEEE Photovoltaic Specialists Conference (PVSC)*; IEEE, 2009; pp 394–399.

[51] Dukhin, A. S.; Reisel, A. Overlapping double layers in electrokinetics of concentrated dispersions. *J. Colloid Interface Sci.* **2022**, *609*, 764–774. DOI: 10.1016/j.jcis.2021.11.092.

[52] Lyklema, J. *Fundamentals of Interface and Colloid Science: Solid-Liquid Interfaces*; Academic Press: Burlington, 1995.

[53] Lowry, G. V.; Hill, R. J.; Harper, S.; Rawle, A. F.; Hendren, C. O.; Klaessig, F.; Nobbmann, U.; Sayre, P.; Rumble, J. Guidance to improve the scientific value of zeta-potential measurements in nanoEHS. *Environ. Sci.: Nano* **2016**, *3*, 953–965. DOI: 10.1039/C6EN00136J.

[54] Levine, S.; Neale, G.; Epstein, N. The prediction of electrokinetic phenomena within multiparticle systems. *J. Colloid Interface Sci.* **1976**, *57*, 424–437. DOI: 10.1016/0021-9797(76)90221-6.

[55] Kuwabara, S. The Forces experienced by Randomly Distributed Parallel Circular Cylinders or Spheres in a Viscous Flow at Small Reynolds Numbers. *J. Phys. Soc. Jpn.* **1959**, *14*, 527–532. DOI: 10.1143/JPSJ.14.527.

[56] Shilov, V. N.; Zharkikh, N. I.; Borkovskaya, Y. B. Theory of non-equilibrium electrical surface phenomena in concentrated disperse systems. 1: Application of the method of thermodynamics of irreversble processes to the cellular model of a concentrated dispersion. *Colloid J.* **1981**, *43*, 434–438.

[57] Dukhin, A. S.; Goetz, P. J. Acoustic and electroacoustic spectroscopy for characterizing concentrated dispersions and emulsions. *Adv. Colloid Interface Sci.* **2001**, *92*, 73–132. DOI: 10.1016/S0001-8686(00)00035-X.

5 New Experimental Approach for the Proper Consideration of Stagnant and Diffuse Layer Conductivity in the Zeta Potential Determination

Matthias Frangenberg[a,b], Annette M. Schmidt[b], Jan Wilkens[a,*]

[a] Faculty of Applied Natural Sciences, TH Köln – University of Applied Sciences, D-51379 Leverkusen, Germany
[b] Department of Chemistry, Institute of Physical Chemistry, University of Cologne, D-50939 Cologne, Germany
* E-Mail: jan.wilkens@th-koeln.de; Phone: +49 214-32831-4614; Address: Campusplatz 1, D-51379 Leverkusen, Germany

Reproduced from Ref [1] with permission from *Langmuir*; ACS.

Abstract

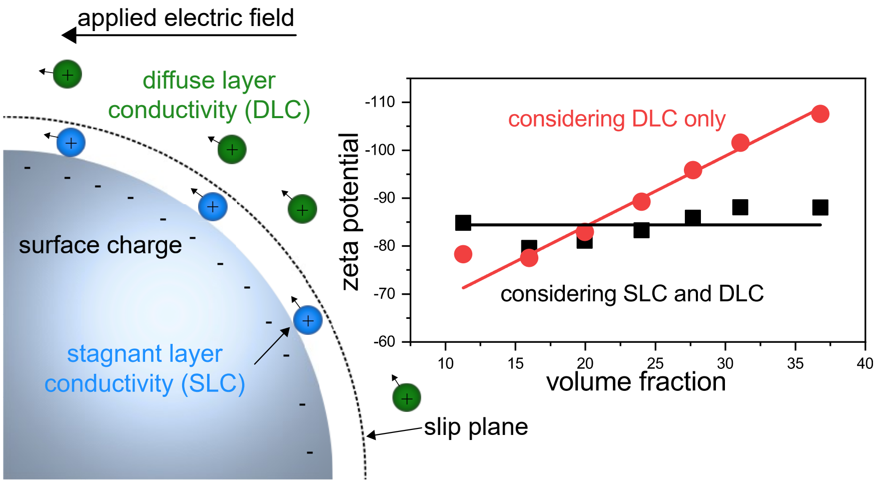

Accurate determination of the zeta potential in colloidal dispersions often requires consideration of the relaxation effect, which is associated with the polarization of the electrical double layer and the surface conductivity. In this study, we pursue a new approach that combines conductivity measurements of the dispersion and dispersion medium with the electroacoustic and electrophoretic zeta potential determination. The conductivity data are analysed with the Maxwell-Wagner-O'Konski theory, providing the Dukhin number. Zeta potentials of highly concentrated polymer dispersions were determined using the colloid vibration current (CVI) method and compared with those obtained by electrophoretic light scattering (ELS) in diluted dispersions. In both cases, the relaxation effect was now taken into account on the basis of the experimentally determined Dukhin number.

The evaluation of the Dukhin numbers revealed significant surface conductivity for all investigated polymer dispersions. In addition, it was often found that not only the diffuse layer but also the stagnant layer contributes considerably to the surface conductivity. Proper consideration of both effects is essential for the reliable determination of the zeta potential, as otherwise inconsistencies

can be observed in the evaluated data. Moreover, we have validated for the first time that the advanced CVI theory takes the effect of surface conductivity properly into account for a wide range of particle volume fractions. These values agree well with those obtained by the ELS method using the Dukhin-Semenikhin theory or a modified theory of Ohshima, Healy and White. This study thus shows that the Dukhin number can serve as a key parameter to reliably connect conductivity, electrophoretic and electroacoustic experiments.

5.1 Introduction

The zeta potential is an important parameter that provides valuable insight into the electrical properties of charged interfaces, i.e., the constitution of the electrical double layer (EDL). It depends on the nature of the particles and the dispersion medium, e.g., the pH value, ionic strength and chemical composition. A well-established method for its determination is electrophoretic light scattering (ELS). Usually, measurements are performed with diluted dispersions to avoid errors due to multiple light scattering.

Advances in measurement technology and theoretical foundations have made it possible to use electroacoustic method as an alternative for the determination of the zeta potential in concentrated systems. Electroacoustic methods exist in two implementations depending on the driving force moving the particles: electrokinetic sonic amplitude (ESA) and colloid vibration current (CVI) setups [2,3]. There are commercial devices available that are based either on the ESA or CVI method. Both, electrophoretic and electroacoustic methods nowadays reach high level of maturity, which is reflected in the existence of International Standards [4–6].

An experimentally measured output of ELS studies is the electrophoretic mobility. The corresponding equivalent in electroacoustics is the so-called dynamic electrophoretic mobility. These quantities are closely related to the zeta potential and can be converted into each other using various theories. Standard theories such as the Debye-Hückel [7], the Henry [8] or the Helmholtz-Smoluchowski theory [9] are easy to use, but their application is subject to several restrictions. For example, they are only valid if the ratio of the particle radius to the reciprocal Debye-Hückel parameter, which is a characteristic length of the EDL, is within a certain range. Moreover, the zeta potential must be quite low, as these theories disregard the relaxation effect, i.e. the impact of surface conductivity and polarization of the EDL on the electrophoretic mobility. Advanced theories attempt to address these limitations. However, they require knowledge of more input parameters than the classical ones. This may explain why the relaxation effect is often neglected in zeta potential determination.

A comprehensive overview concerning the influence and consideration of the surface conductivity and the polarization of the EDL can be found in various review articles, for example [10–12], and in an IUPAC Technical Report [13]. Surface conductivity arises from ions that are located in both parts of the EDL, namely in the diffuse layer and in the hydrodynamically immobile stagnant layer behind the slip plane. Several studies deal with the contribution of both conductivities on zeta potential determination [14–36]. Although the potential impact of stagnant layer conductivity (SLC) is now well known, many publications focus solely on the contribution of the diffuse layer or neglect the surface conductivity completely. This may lead to an underestimation of the zeta potential. Therefore, it is recommended to check the boundary conditions and carefully choose an appropriate theory for the conversion of the primary measurement signal into zeta potential [13].

Surface conductivity cannot be measured directly, but various investigation methods can be used to estimate this quantity or at least give an indication of its presence. The authors of the IUPAC Technical Report recommend, for example, to measure the electrophoretic mobility as a function of the electrolyte concentration. Significant surface conductivity can then be recognized by an extremum at low electrolyte concentrations. They also refer to the possibility of determining the Stern potential by means of particle charge titration and comparing it with the measured zeta potential. Deviations between these values then indicate that the surface conductivity was not correctly taken into account in the calculation of the zeta potential. [13] Moreover, the impact of surface conductivity is also reflected in the electrical conductivity of a dispersion. Several theories have been developed in the past to describe this relationship, e.g. by Maxwell, Wagner and O'Konski (MWO) [37–39], Ohshima [40] or Carrique et al. [41,42]. International Standards therefore recommend to measure the electrical conductivity of the dispersion and the dispersion medium at different volume fractions of dispersed particles. From these data, the Dukhin number, which is a measure of the surface conductivity contribution to electrokinetic phenomena, can then be extracted using the MWO theory. [4,43] This procedure offers some advantages. First, the Dukhin number determined in this way covers the contributions of both stagnant and diffuse layer. Second, this parameter can be directly used in the evaluation of electrophoretic and electroacoustic measurement data by applying certain advanced theories, but to the best of our knowledge this approach has not yet been carried out.

Among the advanced theories, the analytical expression of Ohshima, Healy and White (OHW theory) [44] is broadly recognized, as it leads to exact solutions although it does not use numerical methods. However, it should be noted that this theory only takes into account the diffuse layer conductivity (DLC) and cannot process an experimentally determined Dukhin number. The full Dukhin-Semenikhin theory (DS theory) [45,46], on the other hand, does not have these limitations, but requires knowledge of the Stern potential and ion diffusion in the stagnant layer, which makes its practical application a bit more difficult. Dukhin and Semenikhin also developed a simplified version of their theory [46,47] that eliminates these special requirements. However, both versions of DS theory have rarely been applied so far [48–57], and there is a lack of studies demonstrating their performance when using the experimentally determined Dukhin number.

Over the last decades, electroacoustics has proven to be a reliable tool for determining the zeta potential of inorganic dispersions, even at high particles volume fractions [58]. However, only a few studies have so far examined the electroacoustic behaviour of polymer dispersion [1,20,59–68]. In-depth investigations of polymer latices would therefore be useful to better understand the capabilities and limitations of this measurement method. Due to this knowledge gap, one aim of the present study is a detailed investigation of the applicability and requirements of electroacoustic measuring methods for determining zeta potential of concentrated polymer dispersions.

We have already reported our findings using the Helmholtz-Smoluchowski and Henry frameworks in a recent publication [1]. In this study, we focus on the correct consideration of the relaxation effect and the surface conductivity. We present a new experimental approach that combines the Dukhin number determined by MWO theory with the electroacoustic and electrophoretic determination of the zeta potential.

The zeta potentials of concentrated polymer dispersions are determined using the CVI method in combination with the advanced CVI theory, which is capable of using the Dukhin number to account for the relaxation effect. Consequently, contributions of both diffuse layer and stagnant layer are reflected in the calculated zeta potential. In order to perform an "electrokinetic consistency test", measurements of the zeta potential are also carried out on diluted samples using the ELS method. On the one hand, we evaluate these data with an analytical expression derived by Ohshima, Healy and White that considers the relaxation effect only on the basis of the surface conductivity in the diffuse layer. We have additionally modified this expression to consider the influence of surface conductivity by using the Dukhin number. On the other hand, we also apply the Dukhin-Semenikhin theory in the full and simplified version, which takes both SLC and DLC into account if the Dukhin number is properly determined. This allows a comprehensive comparison of the two experimental approaches and the evaluation theories used. In addition, we obtain information on the significance of the surface conductivity contribution in the stagnant layer.

5.2 Theory

5.2.1 Electrical Double Layer and Zeta Potential

The electrokinetic behaviour of charged colloidal particles dispersed in an electrolyte solution is strongly affected by the distribution of these ions in the vicinity of the particle. This arrangement is called electrical double layer (EDL) and various models can be used to describe its structure in varying degrees of complexity. The Gouy-Chapman-Stern model is rather simple and is often adopted for describing many electrokinetic phenomena. It postulates formation of two layers at the electrically charged particle interface. The inner layer, called the Stern layer, consists of a compact layer of adsorbed ions that are strongly bound to the interface. The outer, diffuse layer encompasses the ions that are distributed diffusely within the dispersion medium due to thermal motion. Compared to the bulk medium, the diffuse layer and the Stern layer have an excess electric charge with sign that is opposite to the sign of the surface charge. This allows the entire EDL structure to be neutral.

An external electric field or mechanical force can provoke a tangential flow of the dispersion medium relative to the charged surface. The velocity decreases to zero at a certain distance from the surface, which is referred to as the hydrodynamic slip or shear plane. The layer that extends from the surface to the slip plane is known as the stagnant layer. Although it is hydrodynamically immobile, the electrolyte ions in this layer can still conduct electricity. It is worth mentioning that the stagnant layer and the Stern layer do not necessarily coincide [13].

The electric potential of the charged interface in EDL is called surface potential ψ_0 and that of the external boundary of the Stern layer is referred to as Stern potential ψ_d. The electric potential at the slip plane in the EDL is defined as the zeta potential ζ. Its value depends on the chemical composition of the charged interface, as well as the electrolyte content and chemical composition of the dispersion medium. Typically, it decreases with increasing electrolyte concentration due to the compression of the diffuse layer.

5.2.2 Surface Conductivity

The total ion concentration in the EDL is higher than in the bulk medium, resulting in an excess electric conductivity known as surface conductivity K^σ. It contributes together with the conductivity of the dispersion medium K_m to the total conductivity of the dispersion K_s.

The significance of surface conductivity K^σ compared to the medium conductivity K_m can be expressed by the dimensionless Dukhin number Du, where a is the particle radius:

$$Du = \frac{K^\sigma}{K_\mathrm{m} a} \tag{5.1}$$

It is also important to note that the surface conductivity contains contributions of ions in the diffuse layer ($K^{\sigma\mathrm{d}}$) as well as mobile ions in the stagnant layer ($K^{\sigma\mathrm{s}}$). Therefore, the surface conductivity and the Dukhin number must be expressed by the sum of both contributions [13]:

$$K^\sigma = K^{\sigma\mathrm{d}} + K^{\sigma\mathrm{s}} \tag{5.2}$$

$$Du = Du^\mathrm{d} + Du^\mathrm{s} = Du^\mathrm{d+s} \tag{5.3}$$

The diffuse layer conductivity $K^{\sigma\mathrm{d}}$ is also known as Bikerman surface conductivity and can be calculated for a symmetrical z-z electrolyte in case of $\kappa a \gg 1$ using Eq. 5.4 [13]. It should be noted that this calculation requires knowledge of the correct zeta potential.

$$K^{\sigma\mathrm{d}} = \frac{2e^2 N_\mathrm{A} z^2 c}{k_\mathrm{B} T \kappa}\left[D_+\left(\mathrm{e}^{-ze\zeta/2k_\mathrm{B}T} - 1\right)\left(1 + \frac{3m_+}{z^2}\right) + D_-\left(\mathrm{e}^{-ze\zeta/2k_\mathrm{B}T} - 1\right)\left(1 + \frac{3m_-}{z^2}\right)\right] \tag{5.4}$$

Here, $D_\pm$ is the diffusion coefficient of cations (+) and anions (-). It can be calculated according to the Nernst-Einstein relation.

$$D_\pm = \frac{k_\mathrm{B} T \Lambda_\pm^0}{z_\pm^2 N_\mathrm{A} e^2} \tag{5.5}$$

$m_\pm$ is the dimensionless ion mobility of the electrolyte ions

$$m_\pm = \frac{2}{3}\left(\frac{k_\mathrm{B} T}{e}\right)^2 \frac{\varepsilon_\mathrm{m}\varepsilon_0}{\eta D_\pm} \tag{5.6}$$

and κ is the Debye-Hückel parameter

$$\kappa = \sqrt{\frac{N_\mathrm{A} e^2}{\varepsilon_0 \varepsilon_\mathrm{m} k_\mathrm{B} T} \sum_{i=1}^{N} z_i^2 c_i} \tag{5.7}$$

where e is the elementary charge, N_A is the Avogadro constant, z_i is the valence and c_i is the concentration of the electrolyte ions, k_B is the Boltzmann constant, T is the thermodynamic temperature and $\Lambda_\pm^0$ is the limiting molar conductivity of electrolyte ions at infinite dilution.

Often $\varkappa$ cannot be calculated according to Eq. 5.7, since the exact composition of the dispersion medium is unknown. Therefore, its value can be approximated utilizing the conductivity of the dispersion medium K_m and Eq. 5.8 [4]. For the effective diffusion coefficient D_eff, the average value of the presumed electrolyte should be used. This parameter also accounts for the greatest uncertainty in this equation due to unknown electrolyte composition. However, D_eff usually falls within a predictable range, as the diffusion coefficients of most ions in aqueous solutions at room temperature typically span from $0.6 \cdot 10^{-9}\ \mathrm{m^2 \cdot s^{-1}}$ to $2 \cdot 10^{-9}\ \mathrm{m^2 \cdot s^{-1}}$. The square root of D_eff further reduces the uncertainty in the estimation of the Debye-Hückel parameter according to Eq. 5.8. [2]

$$\varkappa \approx \sqrt{\frac{K_\mathrm{m}}{\varepsilon_\mathrm{m}\varepsilon_0 D_\mathrm{eff}}} \tag{5.8}$$

Finally, to ease the calculation of $K^{\sigma\mathrm{d}}$ or Du^d, a simplification is often made. Assuming $m_+ = m_- = m$, one obtains [13]:

$$Du^\mathrm{d} = \frac{2}{\varkappa a}\left(1 + \frac{3m}{z^2}\right)\left[\cosh\left(\frac{ze\zeta}{2k_\mathrm{B}T}\right) - 1\right] \tag{5.9}$$

This equation can be approximated well for large zeta potentials (say $\zeta > 50$ mV) as follows:

$$Du^\mathrm{d} = \frac{2}{\varkappa a}\left(1 + \frac{3m}{z^2}\right)\left[0.5\exp\left(\frac{ze\zeta}{2k_\mathrm{B}T}\right) - 1\right] \tag{5.10}$$

As already mentioned, the Bikerman theory only accounts for the diffuse layer conductivity (DLC), i.e. $K^{\sigma\mathrm{d}}$. The second contribution to the surface conductivity is provided by the stagnant layer conductivity (SLC), i.e. $K^{\sigma\mathrm{s}}$. A direct measurement of this parameter is not yet possible. Therefore, it is usually determined by means of Eq. 5.2 when K^σ and $K^{\sigma\mathrm{d}}$ are known. Accordingly, K^σ or Du has to be measured.

5.2.3 Experimental Determination of the Dukhin Number

For a detailed characterisation of the surface conductivity, it is useful to know the Dukhin number Du. According to the recommendation in International Standard ISO 13099, Part 1, Appendix B.3[4], Du can easily be determined using conductivity measurements. This procedure includes measurement of the conductivities of the dispersion (K_s) and the dispersion medium (K_m). Such measurements should be performed at various particle volume fractions φ. The relative conductivity $K_\mathrm{s}K_\mathrm{m}^{-1}$ of a dispersion of non-conducting spherical particles can be described by the MWO theory [37–39] and, finally, Du can be calculated by least-squares fit using Eq. 5.11.

$$\frac{K_\mathrm{s}}{K_\mathrm{m}} = \frac{1 + Du - \varphi(1 - 2Du)}{1 + Du + 0.5\varphi(1 - 2Du)} \tag{5.11}$$

The Dukhin number determined experimentally in this way reflects the surface conductivity in both diffuse and stagnant layer. For the sake of distinction, we designate it with $Du^{\mathrm{d+s}}$. The contribution of the diffuse layer alone (Du^d) can be calculated using Eq. 5.9. Finally, the contribution of the stagnant layer (Du^{s}) can be determined by subtracting Du^{d} from $Du^{\mathrm{d+s}}$ according to Eq. 5.3.

5.2.4 Advanced Zeta Potential Theory for CVI Method

O'Brien introduced the concept of the dynamic electrophoretic mobility μ_{d} in the context of electroacoustic measurements, whose basic expressions are given in Eqs. 5.12 and 5.13 [69]. It relates measured electroacoustic parameters to relevant colloidal parameters, including the zeta potential ζ. Based on this pioneering concept, A. Dukhin and colleagues developed an advanced zeta potential theory specifically for CVI measurements [2,70]. Their approach extends O'Brien's framework by considering alternative cell models to account for the effects of particle-particle interactions in concentrated dispersions on the dynamic electrophoretic mobility μ_{d} [71–73].

$$\mu_{\mathrm{d}} = \frac{CVI}{\Delta P}\frac{\rho_{\mathrm{s}}}{\rho_{\mathrm{p}}-\rho_{\mathrm{s}}}\frac{1}{\varphi}\frac{1}{F(Z_{\mathrm{T}},Z_{\mathrm{s}})A(\omega)} \tag{5.12}$$

$$\mu_{\mathrm{d}} = \frac{2}{3}\frac{\varepsilon_0\varepsilon_{\mathrm{m}}\zeta}{\eta}G(s,\varphi)\big(1+F(Du,\omega',\varphi)\big) \tag{5.13}$$

In Eq. 5.12, CVI is the measured colloidal vibration current amplitude, ΔP is the pressure difference, $A(\omega)$ is an instrument constant that is determined by calibration and $F(Z_T,Z_{\mathrm{s}})$ is a function of the acoustic impedance of the instrument transducer Z_T and dispersion Z_{s}. The equation also accounts for the densities of the dispersion ρ_{s} and the particles ρ_{p}, as well as the volume fraction of the particles φ.

Eq. 5.13 introduces the factor $G(s,\varphi)$ to consider inertial effects and the factor $F(Du,\omega',\varphi)$ to describe electrodynamic effects (s and ω' are factors depending on the angular frequency ω). In the advanced CVI theory, O'Brien's original approach was adapted by refining these functions. The factor $F(Du,\omega',\varphi)$ also accounts for the Dukhin number and accordingly for the effects of surface conductivity and EDL polarisation [74]. Therefore, accurate determination of the Dukhin number, which considers both the conductivity contributions beyond and behind the slip plane, is of particular importance in order to obtain reliable values for the zeta potential ζ.

The advanced CVI theory is applicable in cases of a thin EDL (i.e. $\varkappa a \gg 1$). In-depth information on this sophisticated theory and the extensive calculation of the factors $G(s,\varphi)$ and $F(Du,\omega',\varphi)$ can be found in [2], Chapter 5.4.

5.2.5 Advanced Zeta Potential Theory for ELS Method

The renowned theory developed by O'Brien and White [75] for electrophoresis includes the effect of surface conductivity and EDL polarization. It uses numerical calculations for the zeta potential of a spherical colloidal particle and is applicable for any range of zeta potential, arbitrary $\varkappa a$ values and different electrolyte valences. However, it should be noted that this theory only accounts for the diffuse layer conductivity $K^{\sigma\mathrm{d}}$, but not for the surface conductivity of the stagnant layer $K^{\sigma\mathrm{s}}$. Mangelsdorf and White [76] later extended the theory of O'Brien and White to consider the effect of SLC as well. They used a dynamic Stern layer model, which refers to the adsorption of ions and their mobilities within the stagnant layer. This theory is valid just like the theory of O'Brien and

White for arbitrary κa values. It requires information about several parameters that describe the characteristics of the dynamic Stern layer. These input parameters can be determined, for example, by a combined analysis of electrophoretic and dielectric dispersion data [18].

5.2.5.1 Theory of Ohshima, Healy and White

As an alternative to numerical methods, several analytical expressions have been derived that approximate the relationship between the electrophoretic mobility and the zeta potential of a spherical hard particle. Usually, boundary conditions concerning the product of the Debye-Hückel parameter κ and the particle radius a have to be considered. For example, Ohshima, Healy and White (OHW) derived Eq. 5.14 for a symmetrical z-z electrolyte. It is valid for $\kappa a \geq 10$ with a relative error of less than 1 %, regardless of the value of the zeta potential [44].

$$\mu = \mathrm{sign}(\zeta)\frac{\varepsilon_\mathrm{m}\varepsilon_0}{\eta}\left(\mathrm{abs}(\zeta)\frac{2F}{1+F}\frac{k_\mathrm{B}T}{ze}H\right) + \mathrm{sign}(\zeta)\frac{2\varepsilon_\mathrm{m}\varepsilon_0 k_\mathrm{B}T}{3\eta e}\left(\frac{1}{\kappa a}\left(-18\left(t+\frac{t^3}{9}\right)K + \frac{15F}{1+F}\left(t+\frac{7t^2}{20}+\frac{t^3}{9}\right) - 6(1+ 3m_\mathrm{CO})\left(1-\exp\left(-\frac{\zeta}{2}\right)\right)G + \frac{12F}{(1+F)^2}H + \frac{9\zeta}{1+F}(m_\mathrm{CO}G + m_\mathrm{C}H) - \frac{36F}{1+F}\left(m_\mathrm{CO}G^2 + \frac{m_\mathrm{C}}{1+F}H^2\right)\right)\right) \tag{5.14}$$

Here, m_C and m_CO are the dimensionless ion mobilities of the counterion and co-ion, respectively. Eqs. 5.15 to 5.20 provide the values for the dimensionless zeta potential ζ as well as the individual functions F, G, H, K, and t.

$$\zeta = \frac{ze|\zeta|}{k_\mathrm{B}T} \tag{5.15}$$

$$F = \frac{2}{\kappa a}(1+3m_\mathrm{C})\left(\exp\left(\frac{\zeta}{2}\right)-1\right) \tag{5.16}$$

$$G = \ln\left(\frac{1+\exp\left(-\frac{\zeta}{2}\right)}{2}\right) \tag{5.17}$$

$$H = \ln\left(\frac{1+\exp\left(\frac{\zeta}{2}\right)}{2}\right) \tag{5.18}$$

$$K = 1 - \frac{25}{3(\kappa a+10)}\exp\left(-\frac{\kappa a}{6(\kappa a-6)}\zeta\right) \tag{5.19}$$

$$t = \tanh\left(\frac{\zeta}{4}\right) \tag{5.20}$$

When using this analytical expression to calculate the zeta potential, it is important to note that it only accounts for the surface conductivity of the diffuse layer $K^{\sigma\mathrm{d}}$ (i.e. DLC). Errors in zeta potential determination are to be expected if SLC is significant. We have therefore looked for a way to introduce the Dukhin number into the OHW theory. The combination of Eq. 5.10 with Eq. 5.16 gives Eq. 5.21, which initially takes Du^d into account. However, it also offers the possibility to consider the SLC contribution to the surface conductivity in the OHW theory on a trial basis if $Du^\mathrm{d+s}$ values are used for the Dukhin number instead of Du^d.

$$F = 2Du^\mathrm{d} + \frac{2}{\kappa a}(1+3m_\mathrm{C}) \tag{5.21}$$

5.2.5.2 Theory of Dukhin and Semenikhin

For comparison with the OHW and advanced CVI theory, we can use the approximate Eq. 5.22 of S. Dukhin and Semenikhin (DS theory), which is valid for symmetrical z-z electrolytes [4,45,46]. Moncho et al. showed that the relative error is low if $\varkappa a$ is larger than 25-50 [48]. It should be noted that this $\varkappa a$ limit is somewhat higher than that of the OHW theory.

$$\mu = \frac{3}{2}\frac{\eta e}{\varepsilon_\mathrm{m}\varepsilon_0 k_\mathrm{B}T}\mu = \frac{3}{2}\,\zeta - \frac{3}{2}\,\frac{\zeta(4(1+3m)\sinh^2(\zeta/4)+2g_1)+(2(1+3m)\sinh(\zeta/2)-3m\zeta+2g_2)4\ln(\cosh(\zeta/4))}{\varkappa a+8(1+3m)\sinh^2(\zeta/4)-24m\ln(\cosh(\zeta/4))+4g_1} \tag{5.22}$$

with

$$g_1 = p\left(\cosh\left(\frac{\psi_\mathrm{d}}{2}\right) - \cosh\left(\frac{\zeta}{2}\right)\right) \tag{5.23}$$

$$g_2 = p\left(\sinh(\psi_\mathrm{d}/2) - \sinh(\zeta/2)\right) \tag{5.24}$$

$$\zeta = \frac{ze\zeta}{k_\mathrm{B}T} \tag{5.25}$$

$$\psi_\mathrm{d} = \frac{ze\psi_\mathrm{d}}{k_\mathrm{B}T} \tag{5.26}$$

The ion diffusion coefficient in the boundary layer $D_\pm^\mathrm{s}$ might be lower than its value in the bulk medium $D_\pm$. This influence is therefore taken into account by the parameter p:

$$p = \frac{D_\pm^\mathrm{s}}{D_\pm} \tag{5.27}$$

Eq. 5.22 considers both the dimensionless Stern potential ψ_d and the dimensionless zeta potential ζ. The relationship between these variables can be established using the parameter p and the Dukhin number $Du^\mathrm{d+s}$, which covers both DLC and SLC. As can easily be seen, the first product term in the bracket of Eq. 5.28 corresponds to Du^d (cf. Eq. 5.9) and the second to Du^s.

$$Du^\mathrm{d+s} = \frac{2}{\varkappa a}\left((1+3m)\left(\cosh\left(\frac{\zeta}{2}\right)-1\right) + p\left(\cosh\left(\frac{\psi_\mathrm{d}}{2}\right) - \cosh\left(\frac{\zeta}{2}\right)\right)\right) \tag{5.28}$$

The DS theory also provides a simplification of Eq. 5.22, which is shown in Eq. 5.29. It is valid for $\psi_\mathrm{d} > 1.5$ [46,47]. In this case, knowledge of the parameter p is not a prerequisite for calculating the zeta potential. For correct consideration of the surface conductivity, the Dukhin number $Du^\mathrm{d+s}$ should again be used in Eq. 5.29. Please note that, unlike in the original equation (e.g. equation 3.8.13 in [46]), we have divided by the absolute value of the dimensionless zeta potential $|\zeta|$. As we will show in Chapter 5.4.2.2, this is necessary to obtain the correct solution in the case of negative electrophoretic mobilities.

$$\mu = \frac{\varepsilon_\mathrm{m}\varepsilon_0}{\eta}\zeta\left(1 - \frac{Du\left(1+(4\ln(\cosh(\zeta/4))/|\zeta|)\right)}{1+2Du}\right) \tag{5.29}$$

5.3 Experimental

5.3.1 Materials and Characteristic Dispersion Parameters

We examined a variety of polymer latices in this study. Each sample identifier comprises the material and particle diameter d_{50} in microns, i.e. material@d_{50}. Three polyvinyl chloride (PVC) dispersions from Westlake Vinnolit GmbH & Co. KG were used: PVC@0.20, produced by emulsion polymerisation; PVC@0.78 and PVC@2.10, both produced by microsuspension polymerisation. A styrene-butadiene rubber, Taktene S 62 F (SBR@0.23), was supplied by Arlanxeo Switzerland S.A. Furthermore, a polyurethane dispersion (PU@0.07; synthesized as part of an unpublished master's thesis of Christina Gassner at Heinrich Heine University Düsseldorf in 2021) and a polymethyl methacrylate-co-butyl acrylate dispersion (PBAMM@0.1; synthesized as part of an unpublished master's thesis of Sven Kroß at TH Köln in 2021) were included in this study.

The particle densities were measured using a pycnometer and pH values were determined using a calibrated 9615S-10D electrode from Horiba. Particle size distributions (PSD) were determined by dynamic light scattering or laser diffraction spectroscopy, depending on the particle size. For detailed information regarding these measurements, refer to our recent publication [1]. The resulting dispersion characteristics are summarized in Tab. 5.1 and Tab. 5.4 in the Supporting Information.

5.3.2 Sample Preparation

The samples have to be diluted in steps for most measurements. We used equilibrium supernatant for conducting “equilibrium dilution” [4]. This supernatant was extracted by centrifugation. Therefore, the chemical equilibrium between the particle surface and the dispersion medium is maintained. However, supernatant was not available in some cases. We then used a solution that approximately resembles the dispersion medium. These would be “non-equilibrium dilutions”. Different dilution protocols were used depending on the available sample quantity and the applied measurement technique. The detailed procedure can be found in [1], but the most important aspects will be briefly outlined here for better understanding.

5.3.2.1 CVI Method

All PVC samples were diluted with their equilibrium supernatant achieving true equilibrium dilution. The SBR sample was first dialyzed and then diluted with the appropriate amount of electrolyte solution to achieve a nominal concentration of $10\,\mathrm{mmol{\cdot}L^{-1}}$ KCl in the dispersion medium. All other samples were directly diluted to have a nominal electrolyte concentration of $10\,\mathrm{mmol{\cdot}L^{-1}}$ KCl in the dispersion medium (cf. Tab. 5.1), neglecting the unknown initial electrolyte background. These samples may therefore deviate from equilibrium dilution.

5.3.2.2 ELS Method

In the case of PVC samples, the equilibrium supernatant was used for dilution, same as for CVI measurements. All other samples were diluted using a 10 mmol·L^{-1} KCl solution. The degree of dilution of the stock dispersion is so pronounced that the influence of the original electrolyte background can be neglected.

Tab. 5.1: Summary of relevant sample characteristics [a]

Sample	Diluent/target concentration	ρ_p [g·cm^{-3}]	d_{50} [µm]	K_m [mS·cm^{-1}]	pH value
PVC@0.20	supernatant	1.41	0.202	1.78±0.03	9.0±0.1
PVC@0.78	supernatant	1.39	0.783	4.24±0.37	6.8±0.1
PVC@2.09	supernatant	1.41	2.086	0.69±0.02	9.6±0.1
SBR@0.23	10 mmol·L^{-1} KCl	0.94	0.233	1.27±0.13	8.9±0.1
PU@0.07	10 mmol·L^{-1} KCl	1.10	0.069	2.17±0.76	8.8±0.4
PBAMM@0.10	10 mmol·L^{-1} KCl	1.16	0.099	6.09±2.93	8.6±0.1

[a] The particle densities ρ_p were analysed at 25 °C and the particle size data d_{50} are based on a volume weighted particle size distribution. All particles were removed with a centrifuge prior to the measurement of the electrical conductivity K_m of the dispersion medium. For further details, refer to [126]. Calculated standard deviations are absolute values from triplicate measurements.

5.3.3 Determination of the Dukhin Number

In order to determine the Dukhin number Du, the relative conductivities $K_\mathrm{s}K_\mathrm{m}^{-1}$ were determined at different particle volume fractions. The corresponding conductivities of the dispersion (K_s) and the dispersion medium (K_m) were measured using the conductivity electrode of the CVI measurement device DT-1202 from Dispersion Technology at 3 MHz and room temperature. Measurements were performed in triplicate and the results were averaged. Then we applied Maxwell-Wagner-O'Konski (MWO) theory, as described in Chapter 5.2.3. The value of the Dukhin number Du can be computed by least-squares fit using Eq. 5.11 and fixing the correct limiting behaviour $K_\mathrm{s}K_\mathrm{m}^{-1} \rightarrow 1$ at vanishing volume fractions. For the sake of distinction, we designate the corresponding values with $Du^{\mathrm{d+s}}$ reflecting that surface conductivity is considered in both the stagnant and diffuse layer. The electrolyte concentrations of all samples were above the isoconductive point, as the relative conductivities $K_\mathrm{s}K_\mathrm{m}^{-1}$ were less than one and the resulting $Du^{\mathrm{d+s}}$ values were below 0.5. More details about the experimental procedure and the results can be found in [1].

5.3.4 Determination of Zeta Potential by CVI Method

CVI measurements were performed using a DT-1202 device from Dispersion Technology Inc at room temperature. Frequency of ultrasound was 3 MHz. We ignored contribution of ions (so-called Ion Vibration Current) because it was negligible comparing to the contribution of charged particles. To prevent settling and inhomogeneity, the samples were circulated with a peristaltic pump during measurement. Each sample was measured 3 times, with the results being averaged.

The determination of the zeta potential with the advanced CVI theory requires the Debye-Hückel parameter $\varkappa$ and the Dukhin number. Since the composition of the dispersion medium was not known, we used a method described in ISO Standard 13099, Part 1 [4]. Consequently, the value of the parameter $\varkappa$ was calculated with Eq. 5.8 using the conductivity data K_m of the dispersion medium given in Tab. 5.1. For the effective diffusion coefficient D_eff, a value of $1.994 \cdot 10^{-9} \cdot \mathrm{m}^2 \cdot \mathrm{s}^{-1}$ was used, which corresponds to potassium chloride.

The software of DT-1202 has an option for calculating the Dukhin number automatically when extracting the zeta potential value from measured CVI. It employs essentially the Bikerman approach. Therefore, it only takes into account diffuse layer conductivity, when working in automatic mode. However, the latest software version (12 m56060) now also offers the option to enter the *Du* value manually. This allows the use of a Dukhin number that correctly reflects both contributions to the surface conductivity, from diffuse and from stagnant layer.

To investigate the dependence of the zeta potential on the electrolyte concentration, KCl solutions of varying concentrations were added to the stock dispersion of the PVC@0.20 sample. A particle volume fraction of approx. 11.3 vol% was adjusted and the actual values were determined by analysing the dry residue. The electrolyte content of the stock dispersion was not known but was diluted during sample preparation. The respective $Du^\mathrm{d+s}$ values were determined from the relative conductivities $K_\mathrm{s}K_\mathrm{m}^{-1}$ using Eq. 5.11. For details on the calculation of the zeta potential according to Henry's theory, we refer to our previous publication [1].

5.3.5 Determination of Zeta Potential by ELS Method

ELS measurements were performed using a ZetaSizer Nano ZS device from Malvern Panalytical. The equilibration time was set to 180 s and the number of runs to 50. The attenuation, measuring position and voltage were selected automatically by the software (version: 7.13). All measurements were performed at 25 °C using a wavelength of 633 nm and folded capillary cells DTS 1070. The samples were diluted according to the protocol described in Chapter 5.3.2.The pH values were adjusted to the same values as for the CVI measurements using 0.1 mol·L^{-1} NaOH or HCl solution. To reveal multiple light scattering effects, measurements were performed at least at five different particle volume fractions. The volume fractions studied were approximately between 0.1 and 0.001 vol%.

The measured electrophoretic mobilities were converted into zeta potentials using Eq. 5.14. For most samples, the required $\varkappa$ values were calculated according to Eq. 5.7, assuming a concentration of 10 mmol·L^{-1} KCl (cf. Tab. 5.1) as justified by the dilution procedure. In case of the PVC samples, the approximated $\varkappa$ values of the CVI measurements have to be used because information about the electrolyte composition were missing. For comparison, the ELS measurement results were also evaluated with Eqs. 5.22 and 5.29 using the experimentally determined Dukhin numbers $Du^\mathrm{d+s}$. In all cases, only values with almost identical zeta potentials were averaged (inappropriate particle concentrations were easily recognised by significantly deviating values, which would also increase the determined standard deviations).

5.4 Results and Discussion

A systematic of symbols is used for the detailed presentation of our results, as summarized in Tab. 5.2 with a brief description. Detailed explanations are given in the subsequent sections.

Tab. 5.2: Reference table of symbols

Symbol [a)]	Description
$Du^{\mathrm{d+s}}$	Dukhin number calculated according to Eq. 5.11 using conductivity data and MWO theory, reflecting surface conductivity in both diffuse and stagnant layer
Du^{d}	Dukhin number calculated according to Eq. 5.9 using $\zeta^{\mathrm{d+s}}_{\mathrm{CVI}}$ and κa_{CVI}, reflecting surface conductivity in the diffuse layer only
$Du^{\mathrm{d}}_{\mathrm{DT}}$	Dukhin number calculated automatically by DT-1202 software using conductivity of the dispersion K_{s}, reflecting surface conductivity in the diffuse layer only
Du^{s}	Dukhin number calculated by subtracting Du^{d} from $Du^{\mathrm{d+s}}$, reflecting surface conductivity in the stagnant layer only
$\zeta^{\mathrm{d}}_{\mathrm{CVI}}$	Zeta potential calculated according to Eqs. 5.12 and 5.13 from CVI data for $Du^{\mathrm{d}}_{\mathrm{DT}}$, reflecting surface conductivity of diffuse layer only
$\zeta^{\mathrm{d+s}}_{\mathrm{CVI}}$	Zeta potential calculated according to Eqs. 5.12 and 5.13 from CVI data for $Du^{\mathrm{d+s}}$, reflecting surface conductivity in both diffuse and stagnant layer
$\zeta^{\mathrm{d}}_{\mathrm{ELS}}$	Zeta potential calculated according to Eq. 5.14 under consideration of Eq. 5.16 from ELS data, reflecting surface conductivity of diffuse layer only (original OHW theory)
$\zeta^{\mathrm{d+s}}_{\mathrm{ELS1}}$	Zeta potential calculated according to Eq. 5.14 under consideration of Eq. 5.21 from ELS data for $Du^{\mathrm{d+s}}$, reflecting surface conductivity in both diffuse and stagnant layer (modified OHW theory)
$\zeta^{\mathrm{d+s}}_{\mathrm{ELS2}}$	Zeta potential calculated according to Eqs. 5.22-5.28 from ELS data for $Du^{\mathrm{d+s}}$, reflecting surface conductivity in both diffuse and stagnant layer (full DS theory)
κa_{CVI}	Product of Debye-Hückel parameter κ (calculated on basis of Eq. 5.8 and the conductivity of the dispersion medium K_{m}) and particle radius a; used for the interpretation of CVI data (for details refer to [1])
κa_{ELS}	Product of Debye-Hückel parameter κ (calculated on basis of Eq. 5.7 and the electrolyte concentration of the dispersion medium) and particle radius a; used for the interpretation of ELS data (for details refer to [1])

[a] The superscript indicates the considered contributions of surface conductivity in the diffuse layer (d) and the stagnant layer (s). The subscript refers to the measurement method used, i.e. CVI for colloid vibration current data, ELS for electrophoretic light scattering data.

5.4.1 Estimation of κa Values

In this study, we used two different dilution protocols based on the available sample quantities. In the case of equilibrium dilution, the stock dispersion was diluted with equilibrium supernatant extracted by centrifugation. This method ensured that the composition and the ionic strength of the dispersion medium did not change during the dilution process. Accordingly, the structure of the EDL was preserved and all related parameters remained constant.

In the case of non-equilibrium dilution, we added electrolyte solution with composition that might deviate from the composition of the original dispersion. We tried to match both compositions, but some deviations still remained. If the two compositions differ significantly, certain impacts on the ionic strength and electrokinetic parameters are to be expected. Information regarding the effects of the dilution can be obtained from the conductivity measurements of the dispersion medium. These are reported and discussed in detail in our recent publication [1]. For a better understanding of the results in this study, we classify the various dispersion samples in terms of their dilution behaviour using the κa values.

The electrolyte composition is not known for the CVI measurements, as the original dispersant was not analysed. We have therefore calculated κ using Eq. 5.8 and the conductivity of the dispersion medium K_m. The data at various particle volume fractions were averaged and are shown in Tab. 5.3 in the column labelled κa_CVI. In the case of ELS measurements, the samples were diluted to such an extent that Eq. 5.7 with the target concentration listed in Tab. 5.1 can be used for κ determination. The corresponding κa values are presented in Tab. 5.3 in the column labelled κa_ELS. However, the PVC samples were diluted with their supernatant, so that the κa_CVI values were adopted in these cases.

Tab. 5.3: Compilation of κa values, zeta potentials ζ and Dukhin numbers Du [a)]

material	κa_CVI [b)]	κa_ELS [b)]	$\zeta^\mathrm{d+s}_\mathrm{CVI}$ [mV]	$\zeta^\mathrm{d}_\mathrm{ELS}$ [mV]	$\zeta^\mathrm{d+s}_\mathrm{ELS1}$ [mV]	$\zeta^\mathrm{d+s}_\mathrm{ELS2}$ [mV]	$Du^\mathrm{d+s}$ [b)]	Du^d	$\frac{Du^\mathrm{s}}{Du^\mathrm{d}}$
PVC@0.20	36.3 ±0.3	36.3 ±0.3	-87.1 ±1.5	-83.2 ±11.4	-102.2 ±14.0	-102.5 ±14.0	0.410	0.152	1.70
PVC@0.78	216.5 ±9.4	216.5 ±9.4	-84.4 ±3.3	-73.6 ±6.8	-93.7 ±8.7	-93.3 ±8.6	0.254	0.024	9.58
PVC@2.09	234.5 ±2.9	234.5 ±2.9	-111.4 ±3.6	-94.4 ±4.4	-123.7 ±5.7	-123.5 ±5.7	0.283	0.044	5.43
SBR@0.23	34.3 ±1.7	38.3	-97.5 ±2.6	-95.8 ±2.9	-102.1 ±3.0	-100.7 ±3.0	0.256	0.214	0.20

[a)] The subscript refers to the measurement technique used (the number in the subscript indicates solutions obtained using different evaluation models: 1 refers to the modified OHW theory and 2 to the DS theory) and the superscript to the surface conductivity contribution considered. $Du^\mathrm{d+s}$ is determined experimentally on the basis of MWO theory and covers both the contribution of the diffuse layer (Du^d) and that of the stagnant layer (Du^s). Du^d is calculated according to Eq. 5.9 on the basis of the $\zeta^\mathrm{d+s}_\mathrm{CVI}$ values and Du^s as the difference of $Du^\mathrm{d+s}$ and Du^d. Calculated standard deviations are absolute values from triplicate measurements.

[b)] Values determined in our recent publication. For further details, refer to [1].

All PVC samples show genuine equilibrium dilution, indicated by the low standard deviations of the κa_CVI values (<5 %). These samples cover a broad spectrum of particle sizes, ranging from 0.20 to 2.09 µm. In particular, PVC@0.78 and PVC@2.09 have a very thin double layer, as κa values are greater than 200.

The SBR@0.23 sample also has a relatively low standard deviation for the κa_CVI value (approx. 5 %), which is almost comparable to those of the PVC samples. Moreover, it agrees very well with the κa_ELS value. These findings indicate only minor changes in the ionic strength within the dilution series and are also a hint for the reliability of the approximation Eq. 5.8. Thus, a well-defined electrolyte concentration can be set and maintained within the dilution series after the original electrolyte background has been eliminated by dialysis, meaning that almost equilibrium dilution is achieved.

In contrast, the samples PU@0.07 and PBAMM@0.10 show clear signs of non-equilibrium dilution, as indicated by the relatively high standard deviation of the κa_{CVI} values (>15 %). Since this also affected the quality of the further investigations, their results are only listed and discussed in the Supporting Information (Chapter 5.6.4).

5.4.2 Zeta Potential Determination and Dukhin Number

In this study, we use CVI and ELS measurements to determine the zeta potential of polymer dispersions. In a previous publication, we analysed the data within the framework of the Helmholtz-Smoluchowski and Henry model [1]. In this section, we now present the results obtained with more advanced models that consider the relaxation effect and surface conductivity. The characterization of particle surface conductivity is carried out by means of the Dukhin number, which relates the surface conductivity to that of the dispersion medium. We determined this parameter on the basis of electrical conductivity data using the MWO theory. In addition, we also applied the Bikerman theory to carry out a more detailed analysis of the individual contributions to the surface conductivity.

Since the method of sample dilution can influence electrokinetic properties, we focus here on the samples in which equilibrium dilution was present or almost achieved. This is especially true for all PVC dispersions and the styrene-butadiene rubber SBR@0.23. As already mentioned, the samples PU@0.07 and PBAMM@0.10 revealed noticeable effects of non-equilibrium dilution. This is also reflected in their electrokinetic results, which, however, do not show any fundamental differences or new findings compared to the other samples. For the sake of completeness and with regard to our previous publication, we have collated the results of these two samples in the Supporting Information (Chapter 5.6.4).

In the following two sections, the basic investigation approach is explained in detail using the sample PVC@0.20. We will then discuss the differences and peculiarities of the other samples.

5.4.2.1 Discussion of Sample PVC@0.20 for the CVI Method

In accordance with the IUPAC recommendations [13], we have investigated the dependence of the zeta potential on the electrolyte (KCl) concentration using the sample PVC@0.20 as an example. Among others, the measured CVI signals were analysed using the Henry theory, as described in our previous publication [1]. The results are shown in Fig. 5.1 (●) and listed in the Supporting Information (Chapter 5.6.2.2).

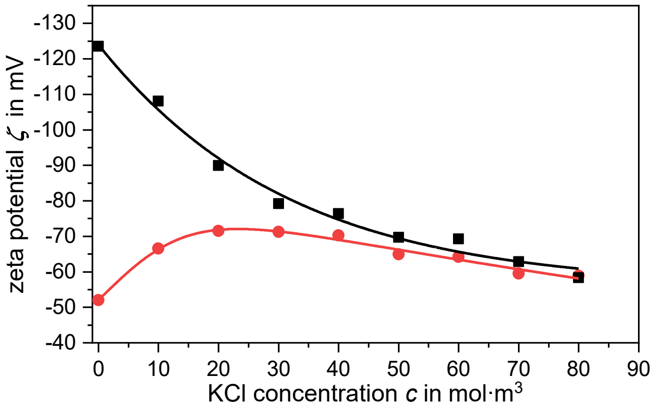

Fig. 5.1: Zeta potential ζ determined with CVI method as a function of KCl concentration c for sample PVC@0.20 at a particle volume fraction of approx. $\varphi = 0.113$. The zeta potentials are shown on the primary y-axis, where ■ refers to ζ using the advanced zeta potential theory and $Du^{\mathrm{d+s}}$ values and ● refers to ζ using the Henry theory. The pH values of the samples were 8.2. Solid lines are a guide to the eye.

Fig. 5.1 clearly shows a pronounced extremum at an electrolyte concentration of approximately 20 mmol·L^{-1}, indicating a significant impact of surface conductivity on the electrokinetic measurement. The zeta potential shows values of up to -71.5 mV at quite low electrolyte concentrations. Such high values in magnitude also suggest that a mere consideration of the retardation effect, as described by the Henry theory, is no longer sufficient for a reliable evaluation. Consequently, subsequent zeta potential calculations were conducted using the advanced CVI theory, which accounts for both the relaxation effect and the surface conductivity of the particles. However, this approach requires knowledge of the Dukhin number.

Fig. 5.2 shows the zeta potentials and the corresponding Dukhin numbers as a function of the particle volume fraction. Similar plots can be found for all other dispersions investigated in the Supporting Information (Fig. 5.5), and essential parameters are provided in Tab. 5.3.

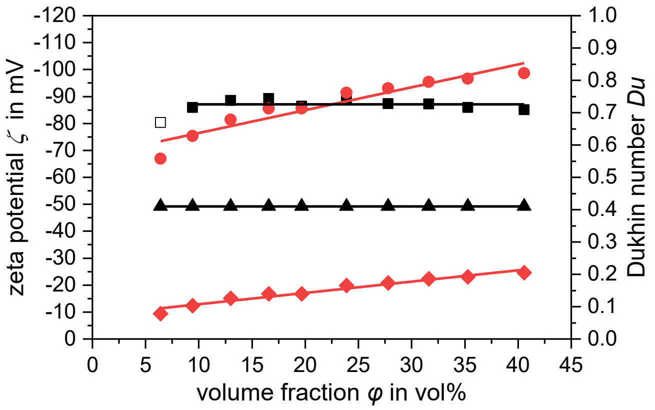

Fig. 5.2: Zeta potential ζ determined with CVI method as a function of particle volume fraction φ for sample PVC@0.20. The zeta potentials are shown on the primary y-axis, where ■ refers to ζ using Dukhin number $Du^{\mathrm{d+s}}$ and ● refers to ζ using $Du^{\mathrm{d}}_{\mathrm{DT}}$ values estimated by the CVI software on the basis of the measured dispersion conductivity. The corresponding Dukhin numbers are shown on the secondary y-axis, where ◆ represents $Du^{\mathrm{d}}_{\mathrm{DT}}$ estimated by the CVI software and ▲ $Du^{\mathrm{d+s}}$. Filled data points (■) were considered for the calculation of the average zeta potential value $\zeta^{\mathrm{d+s}}_{\mathrm{CVI}}$ (shown as black solid line and listed in Tab. 5.3), whereas unfilled data points (□) were neglected. The pH values of the samples were 9.0. The electrolyte concentrations were unknown, as the samples were diluted with their supernatant to maintain equilibrium dilution.

The Dukhin number is mandatory for the calculation of the zeta potential based on the advanced CVI theory. The software of the CVI device used offers the option to calculate this value iteratively from the measured conductivity of the dispersion K_s with an approach following Bikerman's theory. This means that these values only account for the contribution of surface conductivity within the diffuse layer, i.e. $Du^\mathrm{d}_\mathrm{DT}$. Fig. 5.2 shows that the Dukhin numbers (◆) determined in this way are relatively low and rise slightly with increasing volume fraction. On the other hand, the magnitude of the corresponding zeta potentials $\zeta^\mathrm{d}_\mathrm{CVI}$ (●) increases strongly from -67 mV to -99 mV. This behaviour is unsatisfactory, as it contradicts the expectations for equilibrium dilution of the measured samples.

As an alternative, the Dukhin number can be determined experimentally, e.g. using the measured conductivity of the dispersion medium K_m and the dispersion K_s. Several theories are known, which relates the relative conductivity $K_\mathrm{s}K_\mathrm{m}^{-1}$ of a dispersion of non-conducting spherical particles to the Dukhin number and the volume fraction φ. We tested some of them to ensure that we were using a well-suited theory for our data analysis. The results are presented in Chapter 5.6.2.3 in the Supporting Information. It turned out that the evaluation with the MWO theory (cf. Eq. 5.11) provides a reliable Dukhin number (▲ in Fig. 5.2). For clear distinction, we denote these values with $Du^\mathrm{d+s}$. This method gives a value of 0.410 for PVC@0.20, which is also the highest value of all dispersions studied. It was likewise found that $Du^\mathrm{d+s}$ is significantly higher than the $Du^\mathrm{d}_\mathrm{DT}$ values determined by the software. This is mainly due to the fact that the method based on MWO theory also considers stagnant layer conductivity (i.e. Du^s, calculated as the difference between $Du^\mathrm{d+s}$ and Du^d according to Eq. 5.3). Moreover, the contribution of SLC to the total surface conductivity of this dispersion is larger than that of DLC ($Du^\mathrm{s}/Du^\mathrm{d}=1.70$, where Du^d is calculated according to the Bikerman theory using Eq. 5.9 and the $\zeta^\mathrm{d+s}_\mathrm{CVI}$ value). The software of the CVI device offers the option to enter the Dukhin number manually and to include it in the calculation of the zeta potential. Using the experimentally determined Dukhin number $Du^\mathrm{d+s}$, the resulting zeta potentials (■) are almost constant above a volume fraction of approximately 10 vol%. Hence, they fulfil an essential plausibility criterion, because the zeta potential is a unique characteristic of a charged interface under given conditions [13]. Moreover, the corresponding mean value $\zeta^\mathrm{d+s}_\mathrm{CVI}$ (-87.1 mV) is very reasonable, as a comparison with the results of the ELS method will show.

The particle volume fractions investigated in the CVI experiment are partly very high, so that the EDLs of individual particles might overlap. This could have an impact on the charge regulation in the interfacial area and consequently on the determined zeta potentials. In this case, the magnitude of the zeta potentials would rise according to a recent study of A. Dukhin and Reisel [77]. Due to the uniform $\zeta^\mathrm{d+s}_\mathrm{CVI}$ values obtained in our study for equilibrium dilution, the influence of EDL overlap is considered to be small.

The plausibility of the advanced CVI theory can also be tested by analysing the zeta potentials measured at different electrolyte concentrations. As the diffuse layer is compressed with increasing ionic strength, the potential at the slip plane decreases. Therefore, the concentration-dependent extremum of the zeta potential should no longer be present if the effect of surface conductivity is properly taken into account. This is indeed observed, as shown in Fig. 5.1 (■), where the absolute values of the zeta potentials decrease monotonically.

The corresponding Dukhin numbers are presented in Fig. 5.3. It was found that the determined $Du^{\mathrm{d+s}}$ values are well above 0.5 at low KCl concentrations. Or in other words, the dilution of the stock dispersion results in an overall electrolyte content below the isoconductive point, which has a major influence on the zeta potentials determined (see Fig. 5.1). As the KCl concentration increases, the conductivity of the dispersion medium K_{m} also increases. Consequently, the Dukhin number decreases according to Eq. 5.1 and the influence of the surface conductivity K^{σ} on the zeta potential determination diminishes. The evaluations with the Henry and the advanced CVI theory therefore lead to comparable results at high KCl concentrations (see Fig. 5.1).

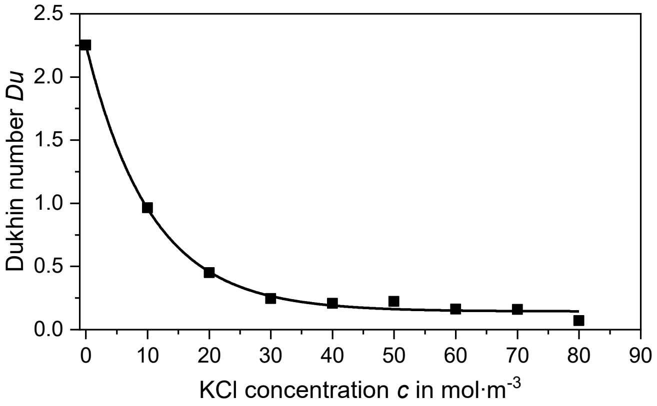

Fig. 5.3: Dukhin number $Du^{\mathrm{d+s}}$ (■) as a function of electrolyte concentration c for sample PVC@0.20 at a particle volume fraction of approx. $\varphi = 0.113$. The Dukhin numbers were estimated from the relative conductivities $K_{\mathrm{s}} \cdot K_{\mathrm{m}}^{-1}$ on the basis of Eq. 5.11 in the main article. The pH values of the samples were 8.2. The solid line is a guide to the eye.

5.4.2.2 Discussion of Sample PVC@0.20 for the ELS method

To check the plausibility of the CVI results, we followed Lyklema's recommendation and performed an "electrokinetic consistency test", i.e. the zeta potential was determined based on a different electrokinetic property in the same given dispersion medium [78]. For this purpose, we employed the ELS method. The determined κa value is 36.3. Thus, the condition of a thin diffuse layer is met, which is required when applying many models. Accordingly, the measured electrophoretic mobility can be evaluated using Eqs. 5.14-5.20 by Ohshima, Healy and White. The value obtained for $\zeta_{\mathrm{ELS}}^{\mathrm{d}}$ is -83.2 mV, which is nearly identical to $\zeta_{\mathrm{CVI}}^{\mathrm{d+s}}$ at -87.1 mV. At first glance, this finding seems plausible, since Delgado et al. pointed out that SLC significantly affects electrokinetic studies only when $Du^{\mathrm{s}}/Du^{\mathrm{d}}$ exceeds 2-5 [13]. However, PVC@0.20 is close to this condition with a value of 1.70 and it should be noticed that the contribution of SLC to the surface conductivity is already considerable.

For comparison, we have also determined the zeta potential using a modification of the OHW theory, i.e. we have included Eq. 5.21 instead of Eq. 5.16 in the calculation. This allows the influence of the SLC to be taken into account in the OHW theory if the determined $Du^{\mathrm{d+s}}$ value is employed instead of Du^{d} for the Dukhin number. The value calculated in this way is -102.2 mV (cf. $\zeta_{\mathrm{ELS1}}^{\mathrm{d+s}}$ in Tab. 5.3) and is somewhat higher in magnitude than the $\zeta_{\mathrm{CVI}}^{\mathrm{d+s}}$ value. In order to recognise incorrect assumptions when modifying the OHW theory, it is useful to calculate the zeta potentials additionally by means of the DS theory, which has rarely been applied in the past [48–57]. In the following, we will explain the main features of this approach in detail.

Eq. 5.22 describes the relation between the electrophoretic mobility μ obtained from ELS measurement and the Stern and zeta potential. The parameter p is also required, which describes the ratio of the ion diffusion coefficient in the boundary layer to that in the bulk medium. The influence of these parameters on the Dukhin number is given by Eq. 5.28. The zeta potential was calculated in former studies on the basis of Eq. 5.22 and experimentally determined values of the electrophoretic mobility and the Stern potential. A plausible value of 0.85 for the parameter p was additionally adopted, as suggested by Moncho et al. for polystyrene particles [48]. In a new alternative approach, we have now used the Dukhin number instead of the Stern potential. Based on the experimentally determined values for μ and $Du^{\mathrm{d+s}}$, it is possible to solve the system of Eqs 5.22-5.28 numerically and obtain values for the Stern and zeta potential.

In principle, we obtain two solution sets: a plausible one with the correct sign for both potentials and an incorrect one, where the Stern potential has the opposite sign to the electrophoretic mobility and the zeta potential. In addition, the zeta potentials in both solutions differ considerably. The correct zeta potential is listed in Tab. 5.3 in the column labelled $\zeta_{\mathrm{ELS2}}^{\mathrm{d+s}}$. For comparison, all other results can be found in the Supporting Information in Tab. 5.7.

Before we take a closer look at the individual results, it makes sense to determine the influence of the approximately estimated parameter p and take it into account in the discussion. For this purpose, we varied this parameter in a range from 0.55 to 1.0. The associated zeta and Stern potentials are also listed in the Supporting Information in Tab. 5.5. We found that the values for the Stern potential ψ_{d} lie within a range of -135.5 to -152.2 mV. Obviously, the variation of the parameter p has a distinct influence on the Stern potential, meaning that an exact value cannot be reliably determined in our study. The differences, however, are so small that at least the order of magnitude of the Stern potential can be estimated. Remarkably, the zeta potential remains practically unaffected by the variation of the parameter p, as we found a uniform value -102.5 mV. This finding is of great importance as it allows the determination of the zeta potential even without precise knowledge of the parameter p.

Eq. 5.29 is a simplified approximation of Eq. 5.22, with the advantage that the parameter p no longer needs to be known [46,47]. To check the accuracy and reliability of this straightforward formula, we also calculated the zeta potential using the experimentally determined Dukhin number $Du^{\mathrm{d+s}}$. The Stern potential can subsequently be determined by means of Eq. 5.28, again assuming $p = 0.85$. In this way, we obtained a value of -100.2 mV for the zeta potential and a value of -140.4 mV for the Stern potential (cf. Tab. 5.7 in the Supporting Information). These values are in excellent agreement with the results of Eq. 5.22. This finding is also confirmed for the other polymer samples investigated in this study. It can therefore be concluded that Eq 5.29 offers a very good and simple alternative to Eq. 5.22. However, in the case of negative electrophoretic mobilities, it is essential for

Eq. 5.29 to divide by the absolute value of the dimensionless zeta potential. Otherwise, the second incorrect value for the zeta potential is calculated, as determined when solving Eq. 5.22. The excellent agreement of the results obtained with Eqs. 5.22 and 5.29 also proves that the knowledge of the parameter p is not necessary for the determination of the zeta potential if the Dukhin number is determined experimentally.

The close agreement between $\zeta^{\mathrm{d+s}}_{\mathrm{ELS1}}$ (-102.2 mV) and $\zeta^{\mathrm{d+s}}_{\mathrm{ELS2}}$ (-102.5 mV) underscores the reliability of both approximation formula. These values are higher in magnitude than the $\zeta^{\mathrm{d}}_{\mathrm{ELS}}$ value (-83.2 mV), as was to be expected due to the contribution of the SLC to the surface conductivity. In this context, the comparison with the CVI method is also of particular interest. The $\zeta^{\mathrm{d+s}}_{\mathrm{CVI}}$ value (-87.1 mV) is only slightly higher in magnitude than the $\zeta^{\mathrm{d}}_{\mathrm{ELS}}$ value. Although the differences to $\zeta^{\mathrm{d+s}}_{\mathrm{ELS1}}$ and $\zeta^{\mathrm{d+s}}_{\mathrm{ELS2}}$ is noticeable, it should be recognized that all these methods adequately account for the contribution of the SLC. Thus, they provide more reliable zeta potentials than the original OHW approach if SLC is significant.

Our results reveal that PVC@0.20 contains highly charged particles with high surface potential. For this reason, relaxation effects are likely to occur. Consequently, the magnitude of the zeta potential is significantly higher than the value calculated according to the Henry theory (see Tab. 5.7 in the Supporting Information) if the surface conductivity is taken into account correctly.

5.4.2.3 Discussion of Samples PVC@0.78 and PVC@2.09

The comparison of the results from PVC@2.09 and PVC@0.78 reveals some similarities (see Tab. 5.3 and Fig. 5.4). In contrast to PVC@0.20, these samples are characterised by large particle sizes with very thin diffuse layers ($\kappa a > 200$). The $Du^{\mathrm{d+s}}$ values show that the effect of the surface conductivity in relation the dispersion conductivity is not as pronounced as for PVC@0.20. However, it should be noticed that the SLC contribution to the total surface conductivity is dominant for PVC@0.78 and PVC@2.09, with PVC@0.78 having the highest value of all dispersions studied ($Du^{\mathrm{s}}/Du^{\mathrm{d}} = 9.58$).

As already explained for PVC@0.20, the high SLC contribution causes distinct differences in the various zeta potentials, listed in Tab. 5.3. Again, reliable zeta potentials can only be determined if both contributions of the surface conductivity are correctly taken into account by the Dukhin number. The use of $Du^{\mathrm{d+s}}$ in the CVI method leads to consistent zeta potentials over a wide volume fraction range (cf. Fig. 5.4). The corresponding average value $\zeta^{\mathrm{d+s}}_{\mathrm{CVI}}$ again matches the values from the modified OHW and DS theory quite well, but always tends to be lower in magnitude. On the other hand, the values for $\zeta^{\mathrm{d+s}}_{\mathrm{ELS1}}$ and $\zeta^{\mathrm{d+s}}_{\mathrm{ELS2}}$ show excellent agreement with only negligible differences. It is particularly important to note that neglecting the contribution of SLC in the original OHW theory leads to $\zeta^{\mathrm{d}}_{\mathrm{ELS}}$ values, which are considerably lower in magnitude. In this respect, it can again be stated that the consideration of the $Du^{\mathrm{d+s}}$ values in the other theories significantly increases the reliability of the determined zeta potential.

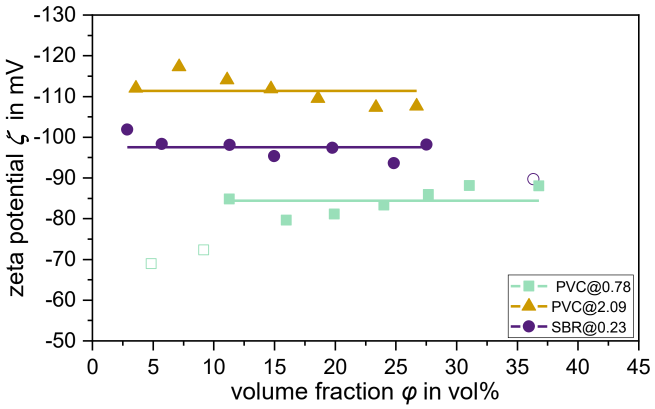

Fig. 5.4: Zeta potential ζ measured by CVI method as a function of particle volume fraction φ for samples PVC@0.78, PVC@2.09 and SBR@0.23. The Dukhin number $Du^{\mathrm{d+s}}$ determined experimentally on the basis of the MWO theory was used. Filled data points were considered for the calculation of the average zeta potential value $\zeta_{\mathrm{CVI}}^{\mathrm{d+s}}$ (shown as solid line and listed in Tab. 5.3), whereas unfilled data points were neglected. The pH values of the samples were 6.8 for PVC@0.78, 9.6 for PVC@2.09 and 8.9 for SBR@0.23. The electrolyte concentrations of the PVC samples were unknown, as the samples were diluted with their supernatant to maintain equilibrium dilution. SBR@0.23 was first dialyzed and then diluted to achieve a KCl concentration of 10 mmol L^{-1} in the dispersion medium.

5.4.2.4 Discussion of Sample SBR@0.23

As explained in Chapter 5.4.1 the κa values of SBR@0.23 changed only slightly upon dilution, suggesting that almost equilibrium dilution was achieved. This is also reflected in the zeta potentials measured with the CVI method as a function of the particle volume fraction. Fig. 5.4 shows that SBR@0.23 exhibits consistent zeta potentials with only minor fluctuations over a wide range of particle concentrations.

It was found that the effect of surface conductivity is also relevant for SBR@0.23 ($Du^{\mathrm{d+s}} = 0.256$). However, the analysis of the Dukhin numbers indicates that the contribution of the SLC can be neglected ($Du^{\mathrm{s}}/Du^{\mathrm{d}} = 0.20$). The major contribution of the DLC is also reflected in the determined zeta potentials, as $\zeta_{\mathrm{ELS}}^{\mathrm{d}}$ (-95.8 mV) and $\zeta_{\mathrm{CVI}}^{\mathrm{d+s}}$ (-97.5 mV) are in excellent agreement, with only $\zeta_{\mathrm{ELS1}}^{\mathrm{d+s}}$ (-102.1 mV) and $\zeta_{\mathrm{ELS2}}^{\mathrm{d+s}}$ (-100.7 mV) being slightly higher in magnitude. This is an important result because $\zeta_{\mathrm{ELS}}^{\mathrm{d}}$ is based on the original OHW theory [44], which is regarded as a reliable alternative to the generally accepted reference theory of O'Brien and White [75] for the case of negligible SLC. Similar observations were reported for polystyrene particles when the ELS method was used in combination with the standard electrokinetic model assuming a constant surface charge density and diffuse layer conductivity only. It was shown that the calculated zeta potentials reliably describe the measured electrophoretic mobilities even at very low electrolyte concentrations. [79,80]

Consequently, it can be concluded that not only the modified OHW theory, but also the advanced CVI theory and the DS theory correctly account for the DLC when the thickness of the diffuse layer is sufficiently thin. This in turn implies that the differences observed for the PVC samples between $\zeta_{\mathrm{CVI}}^{\mathrm{d+s}}$ on the one hand and $\zeta_{\mathrm{ELS1}}^{\mathrm{d+s}}$ and $\zeta_{\mathrm{ELS2}}^{\mathrm{d+s}}$ on the other hand are probably due to a slightly different consideration of SLC in the underlying theories. Based on our results, however, it is hardly possible to decide which values are more accurate. In this respect, further investigations using alternative electrokinetic methods would be helpful, as they could provide additional information.

5.5 Conclusions

Zeta potentials of polymer dispersions were determined for a wide range of solids content by electroacoustic measurement of the colloid vibration current (CVI). They were compared with values determined by electrophoretic light scattering (ELS) in diluted dispersion in order to perform an "electrokinetic consistency test" [78]. When evaluating the primary ELS measurement results, we used the full and a simplified version of the Dukhin-Semenikhin (DS) theory [45–47] as well as the original and a modified version of the Ohshima-Healy-White (OHW) [44] theory. Our modification now allows the Dukhin number to be taken into account. The advanced CVI theory [2,70] was applied to the CVI data, which particularly enables the measurement of dispersions with high volume fractions. In a previous publication [70], the dependence on volume fraction has already been validated. In this study, we verify for the first time the proper consideration of surface conductivity in the advanced CVI theory. We also pursue a new approach that combines conductivity measurements of the dispersion and dispersion medium with the electroacoustic and electrophoretic zeta potential determination. Moreover, a detailed analysis of the conductivity within the stagnant layer (SLC) and in the diffuse layer (DLC) is given, as both can play an important role for the surface conductivity.

The Dukhin number was used as a measure for the contribution of SLC and DLC to electrokinetic and electroacoustic effects. The experimental determination was carried out by measuring the conductivities of the dispersion and the dispersion medium at different particle volume fractions, as described in a recent publication [1]. Preferably, the solids content of the dispersions should be adjusted by equilibrium dilution with supernatant in order to avoid effects on the properties of the electrical double layer. The evaluation of these data was based on the Maxwell-Wagner-O'Konski (MWO) theory [37–39]. As a result, the Dukhin number $Du^{\mathrm{d+s}}$ is obtained, which reflects the contribution of both the stagnant (Du^{s}) and the diffuse layer (Du^{d}) to the surface conductivity. The contribution of the diffuse layer alone can be estimated by means of the Bikerman theory [13]. Comparison of these two values of Dukhin number yields information on the surface conductivity in the stagnant layer.

Our study reveals that the surface conductivity is of significant importance for all investigated polymer dispersions. It has been found that this effect must be correctly taken into account in the CVI measurement in order to determine zeta potential values that are not influenced by the volume fraction. Furthermore, the analysis of the Dukhin numbers proved that in many cases not only the DLC but also the SLC contributes considerably to the surface conductivity. Neglecting the SLC contribution can result in zeta potential values whose magnitudes are considerably lower than the correct values.

We have demonstrated for the first time that reliable zeta potential values can be obtained for a wide volume fraction range using the CVI method in combination with the advanced CVI theory. These values agree well with those obtained by the ELS method. As expected, significant deviations to the original OHW theory are only observed for samples with a much higher conductivity in the stagnant than in the diffuse layer, since this proven theory does not account for SLC. This limitation can be overcome by employing the rarely used DS theory or the modified OHW theory for analysing the ELS data. These approaches provide reasonable zeta potentials with values that are only slightly higher in magnitude than those obtained with the advanced CVI theory.

Moreover, our study reveals that the knowledge of the parameter p, which accounts for differences in the ion diffusion coefficients in the stagnant layer compared to the bulk medium, is not a prerequisite for the zeta potential determination when using the full DS theory. However, this requires knowledge of the Dukhin number as an essential input parameter. We also find an excellent agreement between the full and the simplified version of the DS theory. This is a very useful result as it shows the possibility of simplifying the calculation procedure for the zeta potential.

In summary, these results highlight the benefits of conductivity measurements of the dispersion and the dispersion medium for electrokinetic investigations. The common link between these methods is the Dukhin number $Du^{\mathrm{d+s}}$, which can be determined experimentally in a simple and reliable way. This parameter allows the influence of both the SLC and the DLC to be correctly taken into account when determining the zeta potential.

5.6 Supporting Information

5.6.1 Particle Size Distribution of the Investigated Samples

The particle size distributions (PSD) of most samples were determined using dynamic light scattering at 25°C with a ZetaSizer Nano ZS from Malvern Panalytical (633 nm wavelength and backscatter detection at 173°). Measurements were conducted in polymethyl methacrylate macro cuvettes, with each measurement comprising 15 sub-runs. Samples were diluted according to the protocol described in Chapter 5.3.2.2 of the main article. They were measured at different particle volume fractions to ensure that multiple light scattering is discovered. The PSDs of samples PVC@0.78 and PVC@2.09 were determined using laser diffraction spectroscopy with a MasterSizer 2000 (633 nm and 433 nm wavelength) from Malvern Panalytical. The measurements were carried out in triplicate. Median size and standard deviation are the necessary input parameters of a lognormal particle size distribution in the DT-1202 CVI software. More details can be found in our recent publication [1].

Tab. 5.4: Characteristic data for the volume-weighted particle size distribution

sample	d_{10} [μm]	d_{50} [μm]	d_{90} [μm]	d_{mean} [μm]	standard deviation
PVC@0.20	0.129	0.202	0.314	0.212	0.160
PVC@0.78	0.354	0.783	1.377	0.834	0.136
PVC@2.09	1.057	2.086	4.223	2.416	0.255
SBR@0.23	0.063	0.233	0.575	0.270	0.327
PU@0.07	0.045	0.069	0.127	0.079	0.220
PBAMM@0.10	0.069	0.099	0.155	0.105	0.163

5.6.2 Dukhin Numbers and Zeta Potentials Determined Using the Advanced CVI Theory

5.6.2.1 Dependency on Volume Fraction

Individual Dukhin numbers and the corresponding zeta potentials determined with the CVI measuring method are compared in Fig. 5.5 as a function of volume fraction φ. On the one hand, the particle surface conductivity is characterized by the experimentally determined Dukhin number $Du^{\mathrm{d+s}}$, which is based on the Maxwell-Wagner-O'Konski (MWO) theory and reflects surface conductivity in both diffuse and stagnant layer. On the other hand, the approach of the CVI software is used, which iteratively determines the Dukhin number $Du^{\mathrm{d}}_{\mathrm{DT}}$ on the basis of the measured dispersion conductivity K_{s} following the Bikerman theory. Therefore, it reflects surface conductivity in the diffuse layer only. The comparison contains all samples that are not included in the main article.

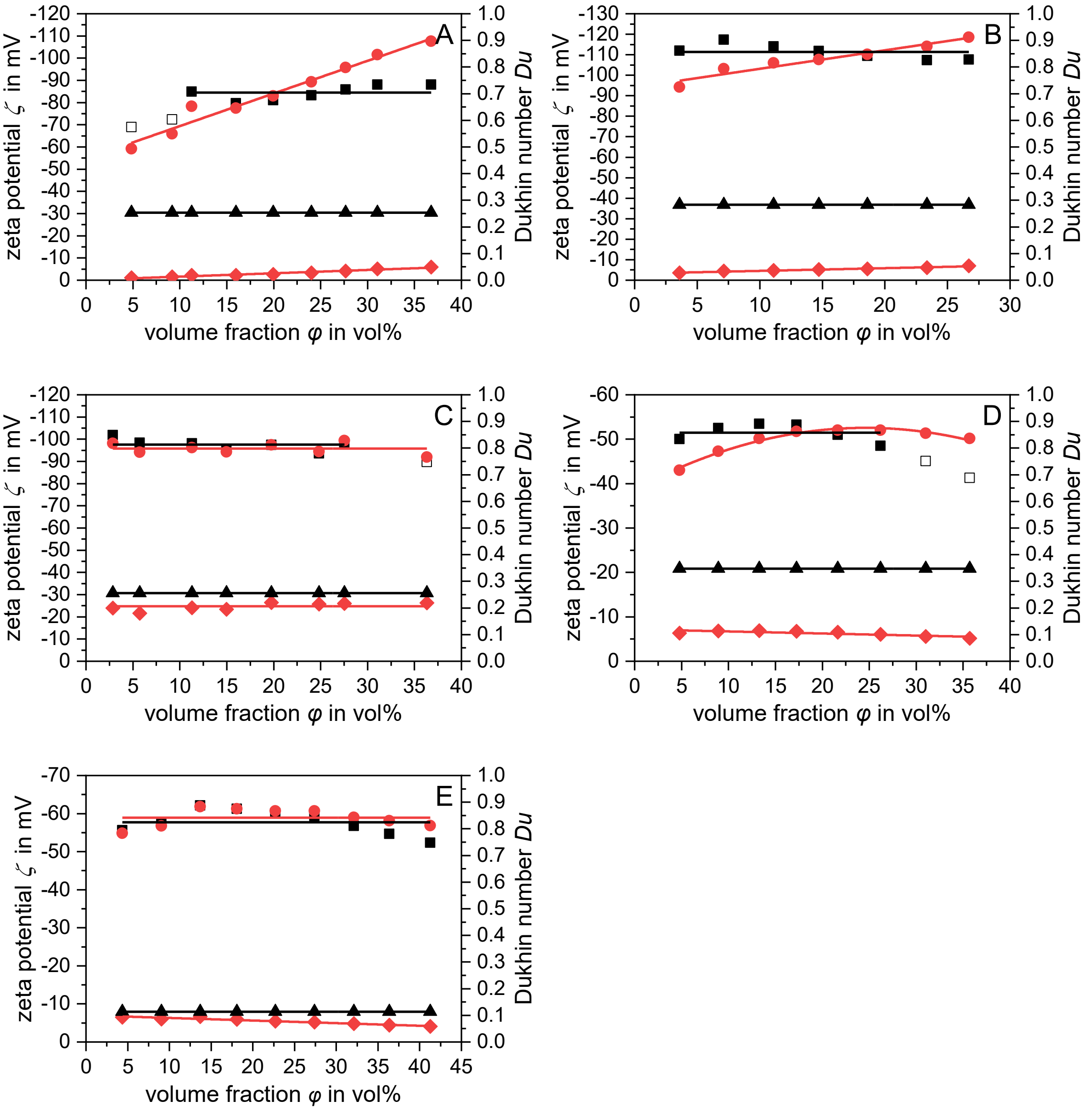

Fig. 5.5: Zeta potential ζ determined with the CVI method as a function of particle volume fraction φ, where A is PVC@0.78, B is PVC@2.09, C is SBR@0.23, D is PU@0.07 and E is PBAMM@0.10. The zeta potentials are shown on the primary y-axis, where ■ refers to ζ using Dukhin number $Du^{\mathrm{d+s}}$ and ● refers to ζ using $Du^{\mathrm{d}}_{\mathrm{DT}}$ values estimated by the CVI software on the basis of the measured dispersion conductivity. The corresponding Dukhin numbers are shown on the secondary y-axis, where ◆ represents $Du^{\mathrm{d}}_{\mathrm{DT}}$ estimated by the CVI software and ▲ $Du^{\mathrm{d+s}}$. Filled data points (■) were considered for the calculation of the average zeta potential value $\zeta^{\mathrm{d+s}}_{\mathrm{CVI}}$ (shown as black solid line and listed in Tab. 5.3 of the main article and Tab. 5.9), whereas unfilled data points (□) were neglected.

5.6.2.2 Dependency on Electrolyte Concentration

We have investigated the dependence of the zeta potential on the electrolyte concentration using the sample PVC@0.20 and the CVI method. The stock dispersion was diluted with KCl solutions of varying concentrations to a particle volume fraction φ of approx. 11.3 vol%. All relevant data and results are summarised in Tab. 5.5.

Tab. 5.5: Dependence of the zeta potential ζ on the KCl concentration c for PVC@0.20 [a)]

c [mmol·L^{-1}]	κa	K_m [S·m^{-1}]	$Du^\mathrm{d+s}$	$\zeta_\mathrm{CVI,H}$ [mV]	$\zeta_\mathrm{CVI}^\mathrm{d+s}$ [mV]
0	17.1	0.0397	2.230	-52.0	-123.5
10	33.5	0.1520	0.960	-66.5	-108.1
20	43.2	0.2533	0.449	-71.5	-89.9
30	53.8	0.3930	0.245	-71.3	-79.2
40	60.1	0.4900	0.206	-70.2	-76.4
50	66.3	0.5963	0.224	-64.9	-69.7
60	73.2	0.7267	0.161	-64.2	-69.2
70	78.4	0.8337	0.160	-59.5	-62.9
80	83.9	0.9550	0.071	-58.9	-58.3

[a)] Measurement of the electrical conductivity of the dispersion medium (K_m) is required for calculating the Debye-Hückel parameter κ using Eq. 5.8. The Dukhin number $Du^\mathrm{d+s}$ is determined using Eq. 5.11. The subscript of the zeta potentials refers to the measurement technique used for the determination of the electrophoretic mobility μ (CVI: colloid vibration current) and the superscript to the surface conductivity contribution considered (d+s: surface conductivity in both diffuse and stagnant layer). The subscript H indicates zeta potentials calculated according to the Henry theory, thus neglecting surface conductivity. The pH values of the samples were approx. 8.2.

5.6.2.3 Determination of the Dukhin Number using Alternative Theories

Accurate determination of the zeta potential in colloidal dispersions often requires consideration of the relaxation effect, which is associated with the polarization of the electrical double layer and the surface conductivity. In this study, we have investigated the particle surface conductivity by means of the Dukhin number Du, which is a measure for the significance of the surface conductivity K^σ compared to the medium conductivity K_m. This parameter is also mandatory for the zeta potential determination using the advanced CVI, the Dukhin-Semenikhin and a modification of the Ohshima-Healy-White theory to account for the influence of the surface conductivity.

The Dukhin number can be determined experimentally, e.g. by measuring the conductivity of the dispersion medium K_m and the dispersion K_s at different particle volume fractions φ. Several theories are known, which relate the relative conductivity $K_\mathrm{s}K_\mathrm{m}^{-1}$ of a dispersion of non-conducting spherical particles to the Dukhin number and the volume fraction. A good overview can be found in the publication by Van der Put and Bijsterbosch [81]. We tested the Henry-Booth or Bruggeman theory (HB-B; Eq. 5.30) and the Dukhin-Semenikhin theory (DS; Eq. 5.31). The obtained Dukhin numbers were compared with those resulting from the Maxwell-Wagner-O'Konski theory (MWO; Eq. 5.11 in the main article). As described in Chapter 5.3.3 of the main article, the Dukhin number can be computed by least-squares fit using the cited equations. The results are shown in Tab 5.6.

$$\left(\frac{K_\mathrm{S}}{K_\mathrm{m}}\right)^{\frac{1}{3}} = \frac{1}{1-\varphi}\left[\frac{\frac{K_\mathrm{S}}{K_\mathrm{m}} - 2Du_\mathrm{HB-B}^\mathrm{d+s}}{1-2Du_\mathrm{HB-B}^\mathrm{d+s}}\right] \tag{5.30}$$

$$\left(\frac{K_\mathrm{S}}{K_\mathrm{m}}\right)^{\frac{4}{3}} = \frac{1}{1-\varphi}\left[\frac{\frac{K_\mathrm{S}}{K_\mathrm{m}} - Du_\mathrm{DS}^\mathrm{d+s}}{1-Du_\mathrm{DS}^\mathrm{d+s}}\right]^2 \tag{5.31}$$

The least squares fits yielded very good results for all theories and do not indicate a preference for one theory. However, considerable discrepancies can be observed between the Dukhin numbers determined. While the *Du* values of the MWO and the HB-B theory are quite similar, there are major differences to the values of the DS theory. Since PVC@0.20 has the largest Dukhin number of all dispersion studied, we selected this sample to investigate the influence of the different Dukhin numbers on the zeta potential determination.

Tab. 5.6: Dukhin number calculated on the basis of various theories [a)]

material	Maxwell-Wagner-O'Konski $Du_\mathrm{MWO}^\mathrm{d+s}$	Henry-Booth and Bruggeman $Du_\mathrm{HB-B}^\mathrm{d+s}$	Dukhin-Semenikhin $Du_\mathrm{DS}^\mathrm{d+s}$
PVC@0.20	0.410	0.390	0.662
PVC@0.78	0.254	0.251	0.349
PVC@2.09	0.283	0.251	0.345
SBR@0.23	0.256	0.255	0.346
PU@0.07	0.348	0.329	0.512
PBAMM@0.10	0.114	0.107	0.136

[a)] *Du* in dependence of the volume fraction φ using the above mentioned equations. The $K_\mathrm{s}K_\mathrm{m}^{-1}$ values were determined in our recent publication. For further details, refer to [1].

Zeta potentials of sample PVC@0.20 were determined with the CVI measuring method and are shown in Fig. 5.6 as a function of the volume fraction φ. Obviously, the magnitude of the zeta potentials, which are determined with the Dukhin number $Du_\mathrm{DS}^\mathrm{d+s}$ according to the Dukhin-Semenikhin theory (●), decreases significantly from -96.5 mV to -78.3 mV with increasing volume fraction. This behaviour is unsatisfactory, as it contradicts the expectations for equilibrium dilution of the measured samples. In contrast, the zeta potentials, which are calculated with the Dukhin number $Du_\mathrm{MWO}^\mathrm{d+s}$ according to the Maxwell-Wagner-O'Konski theory (■), are almost constant above a volume fraction of approximately 10 vol%. The same applies to the Dukhin number $Du_\mathrm{HB-B}^\mathrm{d+s}$, which is based on the Henry-Booth or Bruggeman theory (▲). Hence, both theories fulfil an essential plausibility criterion, because the zeta potential is a unique characteristic of a charged interface under given conditions [13].

The comparison of the zeta potentials as a function of the volume fraction clearly shows that the Dukhin numbers determined by means of both the MWO and the HB-B theory lead to very plausible results, especially compared to the DS theory. Due to the similarity of the results, there is no preference for one of the two theories. We therefore decided to follow the recommendations of International Standard ISO 13099, Part 1, and analysed the relative conductivities in this study using the MWO theory [4].

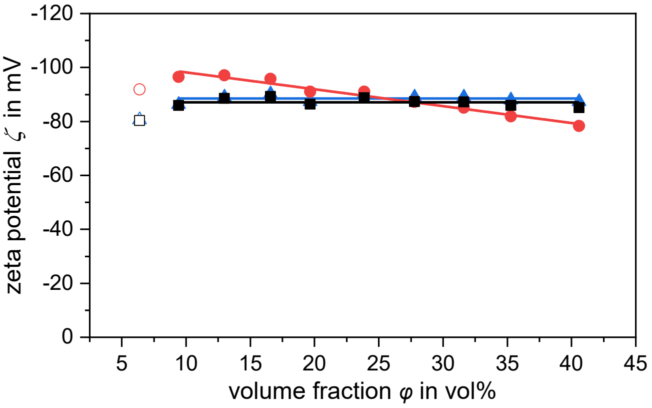

Fig. 5.6: Zeta potential ζ determined with the CVI method as a function of particle volume fraction φ for sample PVC@0.20, where ■ refers to ζ using Dukhin number $Du^{\mathrm{d+s}}_{\mathrm{MWO}} = 0.410$, ▲ refers to ζ using Dukhin number $Du^{\mathrm{d+s}}_{\mathrm{HB-B}} = 0.390$ and ● refers to ζ using Dukhin number $Du^{\mathrm{d+s}}_{\mathrm{DS}} = 0.662$. The pH values of the samples were 9.0. The electrolyte concentrations were unknown, as the samples were diluted with their supernatant to maintain equilibrium dilution. Solid lines in the case of $Du^{\mathrm{d+s}}_{\mathrm{MWO}}$ and $Du^{\mathrm{d+s}}_{\mathrm{HB-B}}$ represent the average zeta potential values. The solid line in case of $Du^{\mathrm{d+s}}_{\mathrm{DS}}$ corresponds to a linear fit and is only a guide to the eye. Filled data points were considered for the calculation of the solid lines, whereas unfilled data points were neglected.

5.6.3 Compilation of Results Obtained with the Henry and Dukhin-Semenikhin Theory

5.6.3.1 Zeta and Stern Potentials Determined Using the Henry and Dukhin-Semenikhin Theory

The determination of the zeta and the Stern potential using the Dukhin-Semenikhin theory (DS theory) is described in detail in the main article. In this section, we essentially present the other, alternative results.

Tab. 5.7: Comparison of different zeta potentials ζ and Stern potentials ψ_d a)

material	μ $\left[\frac{\mu\mathrm{m}\cdot\mathrm{cm}}{\mathrm{V}\cdot\mathrm{s}}\right]$	$\zeta_\mathrm{CVI,H}$ b) [mV]	$\zeta_\mathrm{ELS,H}$ b) [mV]	$\zeta^\mathrm{d+s}_\mathrm{ELS2}$ c) [mV]	$\psi^\mathrm{d+s}_\mathrm{d,ELS2}$ c) [mV]	$\zeta^\mathrm{d+s}_\mathrm{ELS3}$ d) [mV]	$\psi^\mathrm{d+s}_\mathrm{d,ELS3}$ d) [mV]	$\zeta^\mathrm{d+s}_\mathrm{ELS4}$ e) [mV]	$\psi^\mathrm{d+s}_\mathrm{d,ELS4}$ e) [mV]
PVC@0.20	-5.320	-71.8	-72.3	-102.5	-139.6	-80.8	145.8	-100.2	-140.4
PVC@0.78	-5.554	-70.5	-71.6	-93.3	-213.1	-79.9	214.0	-93.0	-213.2
PVC@2.09	-7.024	-92.7	-90.5	-123.5	-220.4	-100.9	222.5	-123.1	-220.4
SBR@0.23	-5.871	-83.7	-79.5	-100.7	-114.7	-85.8	121.8	-98.9	-115.8
PU@0.07	-3.308	-44.7	-51.9	-59.3	-85.6	-50.3	89.0	-57.1	-86.5
PBAMM@0.10	-4.276	-56.5	-61.7	-63.2	-45.6	-59.4	49.8	-62.1	-46.8

a) The subscript refers to the measurement technique used for the determination of the electrophoretic mobility μ (CVI: colloid vibration current; ELS: electrophoretic light scattering; H indicates zeta potentials calculated according to Henry theory, neglecting surface conductivity) and the superscript to the surface conductivity contribution considered (d+s: surface conductivity in both diffuse and stagnant layer). The number in the subscript indicates different solutions obtained using the Dukhin-Semenikhin theory (DS theory).

b) Zeta potentials calculated according to the Henry theory, as determined in our recent publication. For further details, refer to [1].

c) Correct solution of the system of Eqs. 5.22-5.28 (the zeta and Stern potentials have the same sign as the electrophoretic mobility).

d) Incorrect second solution of the system of Eqs. 5.22-5.28 (the zeta potential has the same sign as the electrophoretic mobility, whereas the Stern potential has the opposite sign).

e) Correct solution using the simplified Eq. 5.29 for the zeta potential. The Stern potential was subsequently calculated using Eq. 5.28.

It can be clearly seen that the values with index 2 (full DS theory) and 4 (simplified DS theory) correspond very well with each other. As explained in the main article, they represent plausible results. The values with the index 3 are the alternative solutions of the system of Eqs. 5.22-5.28 (full DS theory). Since the Stern potentials have the opposite sign to the measured electrophoretic mobilities, these solution sets must be regarded as implausible.

5.6.3.2 Influence of the Parameter *p* on the Determination of the Zeta and Stern Potential

The determination of the zeta and the Stern potential using the full Dukhin-Semenikhin theory (DS theory) is described in detail in the main article. In this section, we present the results for PVC@0.20 obtained by varying the parameter *p*.

Tab. 5.8: Zeta potentials ζ and Stern potentials ψ_d for PVC@0.20, determined using the DS theory [a)]

material	p	$\zeta^{\mathrm{d+s}}_{\mathrm{ELS5}}$ [b)] [mV]	$\psi^{\mathrm{d+s}}_{\mathrm{d,ELS5}}$ [b)] [mV]
PVC@0.20	0.55	-102.5	-152.2
PVC@0.20	0.70	-102.5	-144.9
PVC@0.20	0.85	-102.5	-139.6
PVC@0.20	1.00	-102.6	-135.5

[a)] The subscript refers to the measurement technique used for the determination of the electrophoretic mobility μ (ELS: electrophoretic light scattering) and the superscript to the surface conductivity contribution considered (d+s: surface conductivity in both diffuse and stagnant layer). The number in the subscript is used to distinguish it from the other results.

[b)] Correct solution of the system of Eqs. 5.22-5.28 (the zeta and Stern potentials have the same sign as the electrophoretic mobility).

The data in Tab. 5.8 clearly show that the Stern potential is strongly influenced by the variation of the parameter *p*. The zeta potential, on the other hand, remains practically unaffected by this variation (deviations only occur in the first decimal place). This result is of great importance as it allows the determination of the zeta potential even without precise knowledge of the parameter *p*.

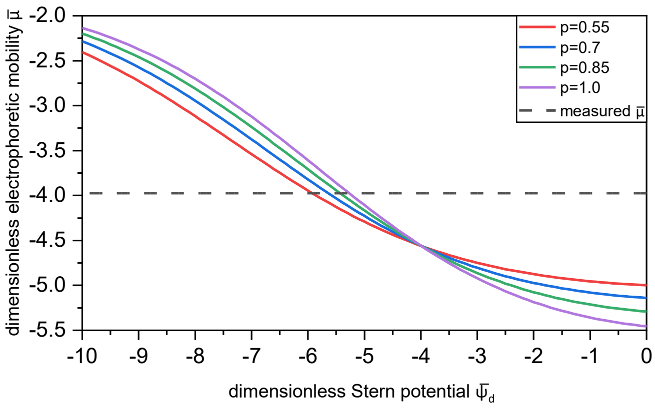

Fig. 5.7: Plot of the dimensionless electrophoretic mobility $\bar{\mu}$ as a function of the dimensionless Stern potential $\overline{\psi_\mathrm{d}}$ for a given dimensionless zeta potential $\bar{\zeta}$ with a value of -3.991, which corresponds to $\zeta = -102.5$ mV. The parameter *p* is varied between 0.55 and 1.0. The associated, experimentally determined dimensionless electrophoretic mobility has a value of -3.973, which corresponds to $\mu = -5.320$ (μm·cm)/(V·s), and is shown in the diagram as a grey, dashed line.

The strong dependence of the Stern potential on the parameter *p* is also visualised in Fig. 5.7, again using the parameter of the sample PVC@0.20. The intersections of the curves with the measured dimensionless electrophoretic mobility (grey, dashed line) characterise possible values for the dimensionless Stern potential.

5.6.4 Results and Discussion of the Samples PU@0.07 and PBAMM@0.10

All results for the samples PU@0.07 and PBAMM@0.10 are compiled in Tab. 5.9. Details on the determination are provided in the main article.

Tab. 5.9: Compilation of κa values, zeta potentials ζ and Dukhin numbers Du [a]

material	κa_{CVI} [b]	κa_{ELS} [b]	$\zeta^{\text{d+s}}_{\text{CVI}}$ [mV]	$\zeta^{\text{d}}_{\text{ELS}}$ [mV]	$\zeta^{\text{d+s}}_{\text{ELS1}}$ [mV]	$\zeta^{\text{d+s}}_{\text{ELS2}}$ [mV]	$Du^{\text{d+s}}$ [b]	Du^{d}	$\frac{Du^{\text{s}}}{Du^{\text{d}}}$
PU@0.07	13.5 ±2.4	11.4	-51.4 ±2.0	-54.8 ±1.4	-60.1 ±1.5	-59.3 ±1.5	0.348	0.122	1.85
PBAMM@0.10	31.9 ±8.1	16.3	-57.7 ±3.2	-72.4 ±3.1	-68.8 ±2.9	-63.2 ±2.7	0.114	0.067	0.70

[a] The subscript refers to the measurement technique used (the number in the subscript indicates solutions obtained using different evaluation models: 1 refers to the modified OHW theory and 2 to the DS theory) and the superscript to the surface conductivity contribution considered. $Du^{\text{d+s}}$ is determined experimentally on the basis of MWO theory and covers both the contribution of the diffuse layer (Du^{d}) and that of the stagnant layer (Du^{s}). Du^{d} is calculated according to Eq. 5.9 on the basis of the $\zeta^{\text{d+s}}_{\text{CVI}}$ values and Du^{s} as the difference of $Du^{\text{d+s}}$ and Du^{d}. Calculated standard deviations are absolute values.

[b] Value determined in our recent publication. For further details, refer to [1].

5.6.4.1 Estimation of κa Values

In contrast to the other samples of the study, PU@0.07 and PBAMM@0.10 show clear signs of non-equilibrium dilution, as can be seen from the differences in the zeta potentials in Fig. 5.5. This is also indicated by the relatively high standard deviation of the κa_{CVI} values (>15 %). However, the κa_{CVI} and κa_{ELS} values of PU@0.07 are close to each other, suggesting that the electrolyte content could have a comparable impact on the electrical double layer in both cases. This is not expected for PBAMM@0.10, as the κa_{CVI} and κa_{ELS} values differ considerably. It should also be noted that PU@0.07 has the lowest κa value of all polymer dispersions investigated in this study. With a value of just over 10, it is no longer possible to consider the thickness of the diffuse layer to be very small compared to the particle size.

5.6.4.2 Zeta Potential Determination and Dukhin Number

Limited sample quantities were available for the dispersions PU@0.07 and PBAMM@0.10. Therefore, sample dilution was performed as described in Chapter 5.3.2 of the main article with an electrolyte solution of known concentration, neglecting the original electrolyte content. This led to non-equilibrium dilution effects, which must be considered in the discussion of the following results.

In the case of PU@0.07, we found quite similar values for $\zeta^{\text{d}}_{\text{ELS}}$ (-54.8 mV), $\zeta^{\text{d+s}}_{\text{CVI}}$ (-51.4 mV), $\zeta^{\text{d+s}}_{\text{ELS1}}$, (-60.1 mV) and $\zeta^{\text{d+s}}_{\text{ELS2}}$ (-59.3 mV). This seems a bit surprising, since the contribution of the SLC is noticeable compared to that of the SLC ($Du^{\text{s}}/Du^{\text{d}} = 1.85$). However, in addition to the effects due to non-equilibrium dilution, we have to bear in mind that the thickness of the diffuse layer for this sample is already quite large in relation to the particle size ($\kappa a = 11.4$). Therefore, the validity of the evaluation methods may no longer be strictly given and $\zeta^{\text{d+s}}_{\text{CVI}}$ and $\zeta^{\text{d+s}}_{\text{ELS2}}$ values should only be considered with caution. The zeta potentials obtained using the original and the modified OHW theory, on the other hand, are very reliable as they are valid for $\kappa a \geq 10$. Due to the relatively low zeta potential and a rather low contribution of DLC to the surface conductivity, $\zeta_{\text{ELS,H}}$ (-51.9 mV) and $\zeta^{\text{d}}_{\text{ELS}}$ (-54.8 mV) differ only slightly from each other. However, the modified OHW theory allows the SLC contribution to be taken into account. This results in a higher and more realistic value for $\zeta^{\text{d+s}}_{\text{ELS1}}$ (-60.1 mV).

The situation is a little different for PBAMM@0.10. The κa values show that the electrolyte concentration decreases significantly upon dilution. This pronounced non-equilibrium dilution has a considerable influence on the thickness of the diffuse layer. It is much larger at low particle volume fractions ($\kappa a_{\mathrm{ELS}} = 16.3$) compared to high ones ($\kappa a_{\mathrm{CVI}} = 31.9$). Consequently, the compression of the diffuse layer causes a decrease in the zeta potential. Hence, it is reasonable that the magnitude of the zeta potential obtained with the CVI method ($\zeta^{\mathrm{d+s}}_{\mathrm{CVI}} = -57.7\,\mathrm{mV}$) is significantly lower than that determined by the ELS method ($\zeta^{\mathrm{d}}_{\mathrm{ELS}} = -72.4\,\mathrm{mV}$ and $\zeta^{\mathrm{d+s}}_{\mathrm{ELS1}} = -68.8\,\mathrm{mV}$). Due to the moderate contribution of SLC to the surface conductivity ($Du^{\mathrm{s}}/Du^{\mathrm{d}} = 0.70$), the values of the original and the modified OHW theory should be quite similar. In fact, the differences are small and can probably be attributed to the non-equilibrium dilution, which also affects the determination of the $Du^{\mathrm{d+s}}$ number. Moreover, the violation of the validity criterion of the DS theory becomes obvious from the implausible calculated potentials (cf. Tab 5.7), since the absolute value of the Stern potential ($\psi^{\mathrm{d+s}}_{\mathrm{d,ELS2}} = -45.6\,\mathrm{mV}$) is much lower than that of the zeta potential ($\zeta^{\mathrm{d+s}}_{\mathrm{ELS2}} = -63.2\,\mathrm{mV}$).

Fig. 5.8 finally depicts the zeta potentials measured by the CVI method as a function of the particle volume fraction, taking into account the $Du^{\mathrm{d+s}}$ values. Obviously, the values for PU@0.07 and PBAMM@0.10 show a slight but systematic trend, which is presumably due to the noticeable non-equilibrium dilution. Some values are therefore neglected in the calculation of the average zeta potential value $\zeta^{\mathrm{d+s}}_{\mathrm{CVI}}$. However, this effect is rather small so that the results are still quite reliable.

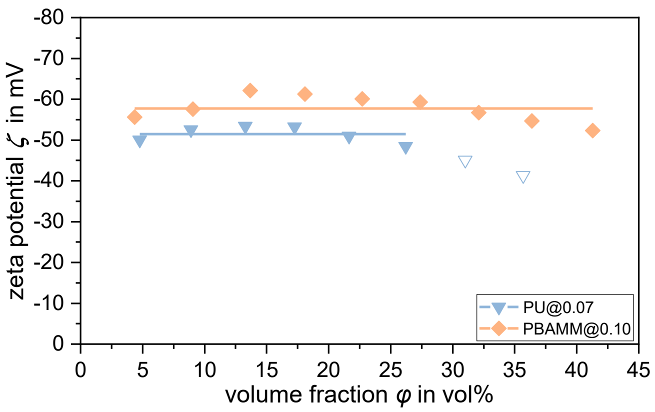

Fig. 5.8: Zeta potential ζ measured by CVI method as a function of particle volume fraction φ for samples PU@0.07 and PBAMM@0.10. The Dukhin number $Du^{\mathrm{d+s}}$ determined experimentally on the basis of the MWO theory was used. Filled data points were considered for the calculation of the average zeta potential value $\zeta^{\mathrm{d+s}}_{\mathrm{CVI}}$ (shown as solid line and listed in Tab. 5.9), whereas unfilled data points were neglected. The pH values of the samples were 8.8 for PU@0.07 and 8.6 for PBAMM@0.10. The PU and PBAMM samples were directly diluted to achieve a nominal KCl concentration of 10 mmol L^{-1} in the dispersion medium, neglecting the original electrolyte content.

Acknowledgments

We would like to express our gratitude to A. S. Dukhin of Dispersion Technology Inc., Bedford Hills, NY, USA for many valuable discussions and software support for the DT-1202 measuring device. We are also very grateful to S. Voigt of TH Köln for measuring the zeta potentials as a function of electrolyte concentration. This project has received fundings from the German Ministry of Education and Research (BMBF) as part of the funding program “Forschung an Fachhochschulen” under contract number 13FH142PX6. We are also very grateful for valuable discussions and financial and material support provided by Westlake Vinnolit GmbH & Co. KG. The authors declare no competing interests. Data that support the findings of this study are available from the corresponding author upon reasonable request.

5.7 References

[1] Frangenberg, M.; Schmidt, A. M.; Wilkens, J. Impact of surface conductivity on the zeta potential determination of concentrated aqueous polymer dispersions using electroacoustics and electrokinetic standard models. *Colloid Polym. Sci.* **2024**, *302*, 1801–1813. DOI: 10.1007/s00396-024-05301-7.

[2] Dukhin, A. S.; Goetz, P. J., Eds. *Characterization of Liquids, Dispersions, Emulsions, and Porous Materials Using Ultrasound*, Third edition; Elsevier: Amsterdam, Oxford, Cambridge, MA, 2017.

[3] Hunter, R. J. Recent developments in the electroacoustic characterisation of colloidal suspensions and emulsions. *Colloids Surf., A* **1998**, *141*, 37–66. DOI: 10.1016/S0927-7757(98)00202-7.

[4] International Organization for Standardization. *Colloidal systems - Methods for zeta-potential determination - Part 1: Electroacoustic and electrokinetic phenomena*, 2012, *19.120* (ISO 13099-1:2012-06).

[5] International Organization for Standardization. *Colloidal systems - Methods for zeta-potential determination - Part 2: Optical methods*, 2012, *19.120* (ISO 13099-2:2012-06).

[6] International Organization for Standardization. *Colloidal systems - Methods for zeta potential determination - Part 3: Acoustic methods*, 2014, *19.120* (13099-3:2014-07).

[7] Hückel, E. Die Kataphorese der Kugel. *Phys. Z.* **1924**, *25*, 204–210.

[8] Henry, D. C. The Cataphoresis of Suspended Particles. Part I. The Equation of Cataphoresis. *Proc. R. Soc. London, Ser. A* **1931**, *133*, 106–129. DOI: 10.1098/rspa.1931.0133.

[9] Smoluchowski, M. v. Elektrische Endosmose und Strömungsströme. In *Handbuch der Elektrizität und des Magnetismus*; Graetz, L., Ed.; Johann Ambrosius: Barth, Leipzig, 1921; pp 366–428.

[10] Lyklema, J.; Minor, M. On surface conduction and its role in electrokinetics. *Colloids Surf., A* **1998**, *140*, 33–41. DOI: 10.1016/S0927-7757(97)00266-5.

[11] Hidalgo-Álvarez, R.; Martín, A.; Fernández, A.; Bastos, D.; Martínez, F.; las Nieves, F. de. Electrokinetic properties, colloidal stability and aggregation kinetics of polymer colloids. *Adv. Colloid Interface Sci.* **1996**, *67*, 1–118. DOI: 10.1016/0001-8686(96)00297-7.

[12] Hunter, R. J. The significance of stagnant layer conduction in electrokinetics. *Adv. Colloid Interface Sci.* **2003**, *100-102*, 153–167. DOI: 10.1016/S0001-8686(02)00060-X.

[13] Delgado, A. V.; González-Caballero, F.; Hunter, R. J.; Koopal, L. K.; Lyklema, J. Measurement and interpretation of electrokinetic phenomena. *J. Colloid Interface Sci.* **2007**, *309*, 194–224. DOI: 10.1016/j.jcis.2006.12.075.

[14] Minor, M.; van der Linde, A. J.; van Leeuwen, H. P.; Lyklema, J. Streaming potentials and conductivities of porous silica plugs. *Colloids Surf., A* **1998**, *142*, 165–173. DOI: 10.1016/S0927-7757(98)00365-3.

[15] Löbbus, M.; van Leeuwen, H. P.; Lyklema, J. Streaming potentials and conductivities of latex plugs. Influence of the valency of the counterion. *Colloids Surf., A* **2000**, *161*, 103–113. DOI: 10.1016/S0927-7757(99)00329-5.

[16] Hughes, M. P.; Morgan, H.; Flynn, M. F. The Dielectrophoretic Behavior of Submicron Latex Spheres: Influence of Surface Conductance. *J. Colloid Interface Sci.* **1999**, *220*, 454–457. DOI: 10.1006/jcis.1999.6542.

[17] Midmore, B.; Hunter, R.; O'Brien, R. The dielectric response of concentrated latices. *J. Colloid Interface Sci.* **1987**, *120*, 210–217. DOI: 10.1016/0021-9797(87)90342-0.

[18] Jiménez, M. L.; Arroyo, F. J.; Carrique, F.; Delgado, A. V. Surface conductivity of colloidal particles: experimental assessment of its contributions. *J. Colloid Interface Sci.* **2007**, *316*, 836–843. DOI: 10.1016/j.jcis.2007.07.016.

[19] Minor, M.; van Leeuwen, H. P.; Lyklema, J. Low-Frequency Dielectric Response of Polystyrene Latex Dispersions. *J. Colloid Interface Sci.* **1998**, *206*, 397–406. DOI: 10.1006/jcis.1998.5619.

[20] Shubin, V. E.; Hunter, R. J.; O'Brien, R. W. Electroacoustic and Dielectric Study of Surface Conduction. *J. Colloid Interface Sci.* **1993**, *159*, 174–183. DOI: 10.1006/jcis.1993.1309.

[21] Bouhaik, I. S.; Leroy, P.; Ollivier, P.; Azaroual, M.; Mercury, L. Influence of surface conductivity on the apparent zeta potential of TiO2 nanoparticles: application to the modeling of their aggregation kinetics. *J. Colloid Interface Sci.* **2013**, *406*, 75–85. DOI: 10.1016/j.jcis.2013.05.034.

[22] Djerdjev, A. M.; Beattie, J. K.; Hunter, R. J. Stagnant Layer Conduction in Surfactant-Stabilized Hexadecane Emulsion Systems Measured by Electroacoustics. *Aust. J. Chem.* **2003**, *56*, 1081. DOI: 10.1071/CH03013.

[23] Gómez-Merino, A. I.; Rubio-Hernández, F. J.; Velázquez-Navarro, J. F.; Aguiar, J. Estimation of Ion Diffusion Coefficients at the Stagnant Layer Using TiO 2 Aqueous Suspension Zeta Potential Data. *Soft Mater.* **2015**, *13*, 127–137. DOI: 10.1080/1539445X.2015.1017769.

[24] Jiménez, M. L.; Arroyo, F. J.; Carrique, F.; Kaatze, U.; Delgado, A. V. Determination of stagnant layer conductivity in polystyrene suspensions: temperature effects. *J. Colloid Interface Sci.* **2005**, *281*, 503–509. DOI: 10.1016/j.jcis.2004.08.093.

[25] Leroy, P.; Devau, N.; Revil, A.; Bizi, M. Influence of surface conductivity on the apparent zeta potential of amorphous silica nanoparticles. *J. Colloid Interface Sci.* **2013**, *410*, 81–93. DOI: 10.1016/j.jcis.2013.08.012.

[26] Leroy, P.; Tournassat, C.; Bizi, M. Influence of surface conductivity on the apparent zeta potential of TiO2 nanoparticles. *J. Colloid Interface Sci.* **2011**, *356*, 442–453. DOI: 10.1016/j.jcis.2011.01.016.

[27] Li, S.; Leroy, P.; Heberling, F.; Devau, N.; Jougnot, D.; Chiaberge, C. Influence of surface conductivity on the apparent zeta potential of calcite. *J. Colloid Interface Sci.* **2016**, *468*, 262–275. DOI: 10.1016/j.jcis.2016.01.075.

[28] Löbbus, M.; Sonnfeld, J.; van Leeuwen, H. P.; Vogelsberger, W.; Lyklema, J. An Improved Method for Calculating Zeta-Potentials from Measurements of the Electrokinetic Sonic Amplitude. *J. Colloid Interface Sci.* **2000**, *229*, 174–183. DOI: 10.1006/jcis.2000.6980.

[29] Minor, M.; Wal, A.; Lyklema, J. Dielectric Spectroscopy of Model Colloids, and the Role of Conduction Behind the Plane of Shear. *Pelizzetti, E. (eds) Fine Particles Science and Technology. NATO ASI Series, vol 12*; Springer: Dordrecht, 1996; pp 225–238.

[30] O'Brien, R. W.; Rowlands, W. N. Measuring the Surface Conductance of Kaolinite Particles. *J. Colloid Interface Sci.* **1993**, *159*, 471–476. DOI: 10.1006/jcis.1993.1348.

[31] O'Brien, R. W.; Wade, T. A.; Carasso, M. L.; Hunter, R. J.; Rowlands, W. N.; Beattie, J. K. Electroacoustic Determination of Droplet Size and Zeta Potential in Concentrated Emulsions. In *Particle size distribution III: Assessment and characterization*; Provder, T., Ed.; American Chemical Society: Washington, DC, 1998; pp 311–319.

[32] Pochapski, D. J.; Carvalho Dos Santos, C.; Leite, G. W.; Pulcinelli, S. H.; Santilli, C. V. Zeta Potential and Colloidal Stability Predictions for Inorganic Nanoparticle Dispersions: Effects of Experimental Conditions and Electrokinetic Models on the Interpretation of Results. *Langmuir* **2021**, *37*, 13379–13389. DOI: 10.1021/acs.langmuir.1c02056.

[33] Rasmusson, M.; Rowlands, W.; O'Brien, R. W.; Hunter, R. J. The Dynamic Mobility and Dielectric Response of Sodium Bentonite. *J. Colloid Interface Sci.* **1997**, *189*, 92–100. DOI: 10.1006/jcis.1997.4793.

[34] Rowlands, W. N.; O'Brien, R. W. The Dynamic Mobility and Dielectric Response of Kaolinite Particles. *J. Colloid Interface Sci.* **1995**, *175*, 190–200. DOI: 10.1006/jcis.1995.1445.

[35] Sonnefeld, J.; Löbbus, M.; Vogelsberger, W. Determination of electric double layer parameters for spherical silica particles under application of the triple layer model using surface charge density data and results of electrokinetic sonic amplitude measurements. *J. Colloid Interface Sci.* **2001**, *195*, 215–225. DOI: 10.1016/S0927-7757(01)00845-7.

[36] Spanos, N.; Tsevis, A.; Koutsoukos, P. G.; Minor, M.; van der Linde, A. J.; Lyklema, J. Electro-kinetic measurements on plugs of doped titania. *Colloids Surf., A* **1998**, *141*, 101–109. DOI: 10.1016/S0927-7757(98)00206-4.

[37] Maxwell, J. C. *A treatise on electricity and magnetism vol.1*; Oxford University Press: Oxford, 1873.

[38] Wagner, K. W. Erklärung der dielektrischen Nachwirkungsvorgänge auf Grund Maxwellscher Vorstellungen. *Archiv f. Elektrotechnik* **1914**, *2*, 371–387. DOI: 10.1007/bf01657322.

[39] O'Konski, C. T. Electric Properties of Macromolecules. V. Theory of Ionic Polarization in Polyelectrolytes. *J. Phys. Chem.* **1960**, *64*, 605–619. DOI: 10.1021/j100834a023.

[40] Ohshima, H. Electrical Conductivity of a Concentrated Suspension of Spherical Colloidal Particles. *J. Colloid Interface Sci.* **1999**, *212*, 443–448. DOI: 10.1006/jcis.1998.6048.

[41] Carrique, F.; Arroyo, F. J.; Delgado, A. V. Electrokinetics of Concentrated Suspensions of Spherical Colloidal Particles: Effect of a Dynamic Stern Layer on Electrophoresis and DC Conductivity. *J. Colloid Interface Sci.* **2001**, *243*, 351–361. DOI: 10.1006/jcis.2001.7903.

[42] Carrique, F.; Cuquejo, J.; Arroyo, F. J.; Jiménez, M. L.; Delgado, A. V. Influence of cell-model boundary conditions on the conductivity and electrophoretic mobility of concentrated suspensions. *Adv. Colloid Interface Sci.* **2005**, *118*, 43–50. DOI: 10.1016/j.cis.2005.04.001.

[43] Dukhin, S. S. Electrochemical characterization of the surface of a small particle and nonequilibrium electric surface phenomena. *Adv. Colloid Interface Sci.* **1995**, *61*, 17–49. DOI: 10.1016/0001-8686(95)00258-R.

[44] Ohshima, H.; Healy, T. W.; White, L. R. Approximate analytic expressions for the electrophoretic mobility of spherical colloidal particles and the conductivity of their dilute suspensions. *J. Chem. Soc., Faraday Trans. 2* **1983**, *79*, 1613. DOI: 10.1039/f29837901613.

[45] Dukhin, S. S.; Derjaguin, B. V. *Surface and Colloid Science*; J. Wiley & Sons: New York, 1974.

[46] Dukhin, S. S. Non-equilibrium electric surface phenomena. *Adv. Colloid Interface Sci.* **1993**, *44*, 1–134. DOI: 10.1016/0001-8686(93)80021-3.

[47] Dukhin, S. S.; Derjaguin, B. V. *Electrophoresis (on russian)*; Nauka: Moskva, 1976.

[48] Moncho, A.; Martínez-López, F.; Hidalgo-Álvarez, R. Comparative study of theories of conversion of electrophoretic mobility into ζ-potential. *Colloids Surf., A* **2001**, *192*, 215–226. DOI: 10.1016/S0927-7757(01)00726-9.

[49] Chabalgoity-Rodríguez, A.; Martín-Rodríguez, A.; Galisteo-González, F.; Hidalgo-Alvarez, R. Electrophoretic mobility, primary electroviscous effect and colloid stability of highly charged polystyrene latexes. *Progr. Colloid Polym. Sci.* **1991**, *84*, 416–424. DOI: 10.1007/BFb0116015.

[50] Hidalgo-Alvarez, R.; Moleon, J. A.; De Las Nieves, F. J; Bijsterbosch, B. H. Effect of anomalous surface conductance on ζ-potential determination of positively charged polystyrene microspheres. *J. Colloid Interface Sci.* **1992**, *149*, 23–26. DOI: 10.1016/0021-9797(92)90386-Z.

[51] Galisteo-González, F.; Moleón-Baca, J. A.; Hidalgo-Alvarez, R. On the structure of electrical double layer of IgG immobilized on polystyrene microspheres. *J. Biomater. Sci., Polym. Ed.* **1993**, *4*, 631–641. DOI: 10.1163/156856293X00267.

[52] Fernández-Barbero, A.; Martín-Rodríguez, A.; Callejas-Fernández, J.; Hidalgo-Alvarez, R. On the Calculation of Electrokinetic Potential and Hamaker Constant of Model Colloids. *J. Colloid Interface Sci.* **1994**, *162*, 257–260. DOI: 10.1006/jcis.1994.1035.

[53] Rubio-Hernández, F. J. Effect of Liquid Composition on the Double Layer of Polystyrene Model Colloids. *J. Non-Equilib. Thermodyn.* **1996**, *21*, 30–40. DOI: 10.1515/jnet.1996.21.1.30.

[54] Unzueta, E.; Forcada, J.; Hidalgo-Alvarez, R. Colloidal and electrokinetic behaviour of poly(methyl methacrylate-co-butyl acrylate) latex particles. *Polymer* **1997**, *38*, 6097–6102. DOI: 10.1016/S0032-3861(97)00185-7.

[55] Peula-García, J. M.; Hidalgo-Alvarez, R.; las Nieves, F. J. de. Colloid stability and electrokinetic characterization of polymer colloids prepared by different methods. *Colloids Surf., A* **1997**, *127*, 19–24. DOI: 10.1016/S0927-7757(96)03890-3.

[56] Bárány, S. Complex electrosurface investigations of dispersed microphases. *Adv. Colloid Interface Sci.* **1998**, *75*, 45–78. DOI: 10.1016/S0001-8686(97)00043-2.

[57] Bárány, S. On the use of the Smoluchowski equation in the calculation of the electrokinetic potential. *Magyar Kemiai Folyoirat, Kemiai Kozlemenyek* **2005**, *111*, 105–109.

[58] Mohammadi-Jam, S.; Waters, K. E.; Greenwood, R. W. A review of zeta potential measurements using electroacoustics. *Adv. Colloid Interface Sci.* **2022**, *309*, 102778. DOI: 10.1016/j.cis.2022.102778.

[59] James, R. O.; Texter, J.; Scales, P. J. Frequency dependence of electroacoustic (electrophoretic) mobilities. *Langmuir* **1991**, *7*, 1993–1997. DOI: 10.1021/la00058a002.

[60] Klingbiel, R. T.; Coll, H.; James, R. O.; Texter, J. Electrokinetic sonic amplitude of colloidal poly(methyl methacrylate) and Ludox®-TM. *Colloids Surf.* **1992**, *68*, 103–109. DOI: 10.1016/0166-6622(92)80151-Q.

[61] Gibb; Hunter. Dynamic Mobility of Colloidal Particles with Thick Double Layers. *J. Colloid Interface Sci.* **2000**, *224*, 99–111. DOI: 10.1006/jcis.1999.6676.

[62] Goetz, R. J.; El-Aasser, M. S. Effects of dispersion concentration on the electroacoustic potentials of o/w miniemulsions. *J. Colloid Interface Sci.* **1992**, *150*, 436–452. DOI: 10.1016/0021-9797(92)90213-6.

[63] Hunter, R. J.; Midmore, B. R.; Zhang, H. Zeta Potential of Highly Charged Thin Double-Layer Systems. *J. Colloid Interface Sci.* **2001**, *237*, 147–149. DOI: 10.1006/jcis.2001.7423.

[64] Dahlsten, P.; Próchniak, P.; Kosmulski, M.; Rosenholm, J. B. Electrokinetic behavior of melamine–formaldehyde latex particles at moderate electrolyte concentration. *J. Colloid Interface Sci.* **2009**, *339*, 409–415. DOI: 10.1016/j.jcis.2009.07.029.

[65] Kosmulski, M.; Dahlsten, P.; Próchniak, P.; Rosenholm, J. B. High ionic strength electrokinetics of melamine–formaldehyde latex. *J. Colloid Interface Sci.* **2006**, *301*, 538–541. DOI: 10.1016/j.jcis.2006.05.052.

[66] Ishikawa, Y.; Aoki, N.; Ohshima, H. Characterization of latex particles for aqueous polymeric coating by electroacoustic method. *Colloids Surf., B* **2005**, *46*, 147–151. DOI: 10.1016/j.colsurfb.2005.10.005.

[67] Hozumi, Y.; Furusawa, K. Electrokinetic study on concentrated suspensions using colloid vibration potential measurements. *Colloid Polym. Sci.* **1990**, *268*, 469–475. DOI: 10.1007/bf01411006.

[68] Rasmusson, M. Volume Fraction Effects in Electroacoustic Measurements. *J. Colloid Interface Sci.* **2001**, *240*, 432–447. DOI: 10.1006/jcis.2001.7559.

[69] O'Brien, R. W. Electro-acoustic effects in a dilute suspension of spherical particles. *J. Fluid Mech.* **1988**, *190*, 71. DOI: 10.1017/S0022112088001211.

[70] Dukhin, A. S.; Goetz, P. J. Acoustic and electroacoustic spectroscopy for characterizing concentrated dispersions and emulsions. *Adv. Colloid Interface Sci.* **2001**, *92*, 73–132. DOI: 10.1016/S0001-8686(00)00035-X.

[71] Dukhin, A. S.; Shilov, V. N.; Ohshima, H.; Goetz, P. J. Electroacoustic Phenomena in Concentrated Dispersions: New Theory and CVI Experiment. *Langmuir* **1999**, *15*, 6692–6706. DOI: 10.1021/la990317g.

[72] Dukhin, A. S.; Shilov, V.; Borkovskaya, Y. Dynamic Electrophoretic Mobility in Concentrated Dispersed Systems. Cell Model. *Langmuir* **1999**, *15*, 3452–3457. DOI: 10.1021/la981382d.

[73] Dukhin, A. S.; Ohshima, H.; Shilov, V. N.; Goetz, P. J. Electroacoustics for Concentrated Dispersions. *Langmuir* **1999**, *15*, 3445–3451. DOI: 10.1021/la9813836.

[74] Dukhin, A. S.; Shilov, V. N.; Ohshima, H.; Goetz, P. J. Electroacoustic Phenomena in Concentrated Dispersions: Effect of the Surface Conductivity. *Langmuir* **2000**, *16*, 2615–2620. DOI: 10.1021/la991305y.

[75] O'Brien, R. W.; White, L. R. Electrophoretic mobility of a spherical colloidal particle. *J. Chem. Soc., Faraday Trans. 2* **1978**, *74*, 1607. DOI: 10.1039/f29787401607.

[76] Mangelsdorf, C. S.; White, L. R. Effects of stern-layer conductance on electrokinetic transport properties of colloidal particles. *J. Chem. Soc., Faraday Trans.* **1990**, *86*, 2859. DOI: 10.1039/ft9908602859.

[77] Dukhin, A. S.; Reisel, A. Overlapping double layers in electrokinetics of concentrated dispersions. *J. Colloid Interface Sci.* **2022**, *609*, 764–774. DOI: 10.1016/j.jcis.2021.11.092.

[78] Lyklema, J. *Fundamentals of Interface and Colloid Science: Solid-Liquid Interfaces*; Academic Press: Burlington, 1995.

[79] Kobayashi, M. Electrophoretic mobility of latex spheres in the presence of divalent ions: experiments and modeling. *Colloid Polym. Sci.* **2008**, *286*, 935–940. DOI: 10.1007/s00396-008-1851-9.

[80] Chassagne, C.; Ibanez, M. Electrophoretic mobility of latex nanospheres in electrolytes: Experimental challenges. *Pure Appl. Chem.* **2012**, *85*, 41–51. DOI: 10.1351/PAC-CON-12-02-12.

[81] Van Der Put, A.G; Bijsterbosch, B. Electrical conductivity of dilute and concentrated aqueous dispersions of monodisperse polystyrene particles. Influence of surface conductance and double-layer polarization. *J. Colloid Interface Sci.* **1980**, *75*, 512–524. DOI: 10.1016/0021-9797(80)90474-9.

6 Determination of Particle Size Distribution from Concentrated Latices Using Acoustic Attenuation Apectroscopy – Importance of Intrinsic Attenuation

Matthias Frangenberg[a,b], Annette M. Schmidt[b], Jan Wilkens[a*]

[a] Faculty of Applied Natural Sciences, TH Köln, Cologne, Germany

[b] Department of Chemistry, Institute of Physical Chemistry, University of Cologne, Cologne, Germany

* E-Mail: jan.wilkens@th-koeln.de; Phone: +49 214-32831-4614; Address: Campusplatz 1, 51379 Leverkusen, Germany

Abstract

Hypothesis: Determining the particle size distribution of polymer latex dispersions using acoustic attenuation spectroscopy (AAS) is challenging due to the significant contribution of intrinsic absorption to the attenuation spectrum. This study aims to address this challenge by modelling the intrinsic absorption of various aqueous latex systems and assessing its impact on particle size distribution determination.

Experiments: In this study, we investigated various aqueous latex systems. To model intrinsic absorption, we initially examined the effects of viscoinertial, thermal, and scattering losses using the coupled phase model developed by Dukhin and Goetz, applied across different particle volume fractions. To carry out this modelling, we first determined the particle size distribution using reference methods such as dynamic light scattering and laser diffraction spectroscopy. Additionally, several thermophysical input parameters were required. We experimentally determined the density and coefficient of thermal expansion of the particles using a pycnometer. The heat capacity of the particles was measured with differential scanning calorimetry. The speed of sound in the particles was determined in parallel with measuring the sound attenuation spectrum using an acoustic spectrometer. Finally, the thermal conductivity of the particle material, along with all thermophysical input parameters of the dispersion medium (water), were estimated based on a comprehensive review of the relevant literature.

Findings: This study highlights the significant role of intrinsic particle absorption in determining the particle size distribution (PSD) of polymer latex dispersions using acoustic attenuation spectroscopy. Incorporating intrinsic particle absorption into the AAS model greatly improved PSD accuracy. The AAS method provided consistent median particle diameters for various polymer latices (PVC, PTFE, SBR, PU), closely aligning with dynamic light scattering or laser diffraction spectroscopy. However, accurately determining the PSD width remains challenging, with high variability across different particle volume fractions. Despite this, AAS shows potential for approximate PSD of concentrated polymer latices over a broad range of concentration, which is sufficient for many practical applications.

6.1 Introduction

Polymer latexes are widely used in industries such as paints, coatings, adhesives, and pharmaceuticals due to their versatile properties, including high adhesion, customizable viscosity, and excellent film-forming capabilities. Despite their widespread use, the characterization of polymer latexes, especially in their concentrated forms, poses significant scientific challenges. Traditional particle sizing methodologies like Dynamic Light Scattering (DLS), Laser Diffraction Spectroscopy (LDS) or various forms of microscopy, often fall short as they are predominantly suited for analysing diluted dispersions.

In recent times, Acoustic Attenuation Spectroscopy (AAS) has gained prominence in colloid science as a revolutionary technique for examining concentrated, opaque dispersions [1]. AAS operates by measuring the frequency-dependent attenuation of ultrasound waves as they pass through a dispersion, providing rapid, online measurement capabilities and a non-destructive approach to particle analysis. Despite its potential, AAS faces challenges in accurately interpreting data, primarily due to the complex interplay of various attenuation mechanisms. To address this, a comprehensive set of thermophysical parameters is essential for precise analysis of the ultrasonic spectra [2,3].

The complexity of interpreting AAS data varies with the nature of the particles under examination. For rigid, submicron inorganic particles, the process is relatively straightforward, focusing primarily on viscoinertial effects that influence sound attenuation. Essential thermophysical parameters in these instances like media viscosity, particle and media density, intrinsic media absorption and particle volume fraction, are generally straightforward to determine. Contrastingly, for larger particles that cause ultrasound scattering, additional factors become crucial, including the sound velocities of both particle and medium [1,4].

The analysis becomes particularly intricate when dealing with low density or soft particles, like latices or emulsions. In these cases, thermal losses and intrinsic absorption play a significant role in sound attenuation. Accurately interpreting these thermal losses necessitates detailed knowledge of thermal conductivity, heat capacity and thermal expansion for both the particles and the dispersion medium. Moreover, intrinsic absorption, which pertains to the molecular-level dissipation of acoustic energy within a material, must be quantified individually for each substance. While this process is relatively straightforward for emulsions, where the dispersed phase is easily analysed, it becomes markedly more challenging for latex particles due to the near-impossibility of independently assessing the material composition of the latex particle phase. This obstacle uniquely complicates the use of AAS for particle sizing in latex dispersions, distinguishing them from other colloidal systems [1,5].

In light of these challenges, our study introduces an approach to model the intrinsic particle absorption in various aqueous latex dispersions. We started by collecting all the necessary thermophysical parameters through direct measurements and reviewing existing literature. Next, we used optical measurement techniques on highly diluted dispersions to accurately determine the

Particle Size Distributions (PSD) for each sample. Utilizing this PSD data and employing the coupled phase model by Dukhin and Goetz [1,4–6], we simulated the viscoinertial, thermal and scattering attenuations for different particle volume fractions within each dispersion. At the core of our approach was the comparison of these simulations with the measured total attenuation, enabling us to isolate the residual attenuation. We posited that this residual could be ascribed solely to the intrinsic absorption of the particles, a characteristic that should remain constant across varying particle volume fractions in the dispersion. To test the robustness and accuracy of our methodology, we reintegrated the calculated intrinsic particle absorption spectra into the Dukhin and Goetz model in a reverse application, thereby validating our approach.

6.2 Theory

The core principle of the Acoustic Attenuation Spectroscopy (AAS) technique revolves around determining the total attenuation coefficient α. This coefficient is essential quantifying the total reduction in sound energy amplitude as it propagates through a sample. It is calculated using:

$$\alpha = -\frac{1}{x} ln\left(\frac{I_0}{I_x}\right) \tag{6.1}$$

in this context I_0 represents the initial sound intensity, while I_x denotes the sound intensity after traveling a distance x through a sample [2].

The attenuation coefficient α and the sound velocity c are related to the real and imaginary parts of the complex wave number k:

$$k = \frac{2\pi f}{c} + \alpha i \tag{6.2}$$

where f is the ultrasonic frequency and i the imaginary number [6]. Common models and theories used to determine particle size distribution from acoustic spectra are based on the assumption that the particles are much smaller than the wavelength of the applied sound. Which is called long wave regime (LWR) and can be expressed by the following term:

$$ka = \frac{2\pi a}{\lambda} \ll 1 \tag{6.3}$$

here a denotes the particle radius and λ the wave length. The LWR is of great importance for AAS, as the sound attenuation in this frequency range is most sensitive to the size and concentration of the dispersed particles. In contrast, in the regime of shorter wavelengths within the scale of particle dimensions, dissipation becomes negligible, while scattering, especially through diffraction, is dominant.[1]

6.2.1 Loss Mechanisms

The measured total ultrasonic attenuation coefficient α in the LWR includes primary viscoinertial loss α_{vis}, thermal loss α_{th}, elastic scattering α_{sc} and intrinsic absorption α_{int} of the dispersion. Within the LWR, these mechanisms can be considered separately, allowing α to be expressed as the sum of these partial attenuations:

$$\alpha = \alpha_{\text{vis}} + \alpha_{\text{th}} + \alpha_{\text{sc}} + \alpha_{\text{int}} \tag{6.4}$$

The viscoinertial losses α_{vis} are hydrodynamic in their nature and arise from the relative motion between particles and the surrounding medium in a sound wave's pressure field. The extent of the particle movement and the delay in following pressure variation depend on the density contrast with the medium. When the particle has the same density as the surrounding fluid, it oscillates in phase with it. As the density difference between the particle and the surrounding medium increases, the particle's relative oscillation intensifies. This increased oscillation leads to viscous friction with the continuous phase and exerts considerable hydrodynamic drag on the particle, decreasing the total energy of the particle's oscillation.

Thermal losses α_{th} represent a thermodynamic phenomenon that results from the exchange of heat between particles and their surrounding medium. This heat exchange primarily arises due to friction caused by viscoinertial losses, which generates heat at the surfaces of the particles, creating a temperature gradient. To balance this gradient, heat begins to transfer within the medium and particle, contributing to an overall loss of energy.

In the case of scattering α_{sc}, reflection, refraction and diffraction occur when sound interacts with particles, resulting in a partial redirection of the sound energy. As a result, the energy decreases along the original direction of propagation and some of the sound energy does not reach the receiving transducer of the measuring device. It is important to note that scattering losses, unlike viscous loss, thermal loss and intrinsic absorption, do not dissipate sound energy.

The intrinsic absorption α_{int} refers to the attenuation of acoustic energy resulting from the interaction between sound waves and the individual material of particles and the surrounding medium. This loss is independent of the size of the dispersed phase.

In the existing literature, additional loss mechanisms have been discussed. However, the structural loss mechanism α_{st} stands out to be the only one of practical significance [1,7]. This mechanism occurs when particles are interconnected and form a network like structure. Oscillation of interconnecting bonds results in additional energy dissipation. For the dispersions investigated in our study, it is assumed that no network structures were present. Therefore, this loss mechanism was not taken into account.

Tab. 6.1: Required thermophysical input parameter for Dukhin and Goetz coupled phase model [1]. These parameters are essential for accurately calculating viscoinertial α_{vis}, thermal α_{th} scattering α_{sc} and intrinsic α_{int} losses

sample	particle	medium	unit	required for calculation of
density ρ	ρ_{p}	ρ_{m}	$\mathrm{g{\cdot}cm^{-3}}$	$\alpha_{\mathrm{vis}}, \alpha_{\mathrm{th}}, \alpha_{\mathrm{sc}}$
dynamic viscosity η		η_{m}	$\mathrm{Pa{\cdot}s}$	$\alpha_{\mathrm{vis}}, \alpha_{\mathrm{th}}$
specific heat capacity C_{p}	$C_{\mathrm{p}}^{\mathrm{p}}$	$C_{\mathrm{p}}^{\mathrm{m}}$	$\mathrm{J{\cdot}g^{-1}{\cdot}K^{-1}}$	α_{th}
thermal conductivity τ	τ_{p}	τ_{m}	$\mathrm{mW{\cdot}cm^{-1}{\cdot}K^{-1}}$	α_{th}
thermal expansion β	β_{p}	β_{m}	$\mathrm{K^{-1}}$	α_{th}
sound velocity c	c_{p}	c_{m}	$\mathrm{m{\cdot}s^{-1}}$	α_{sc}
scattering coefficient C_{sc}	$C_{\mathrm{sc,p}}$			α_{sc}
intrinsic absorption α_{int}	α_{p}	α_{m}	$\mathrm{dB{\cdot}cm^{-1}}$	α_{int}

In this study, we employed the coupled phase model of Dukhin and Goetz [1,4,5], which is suited for modelling the PSD of concentrated dispersions within the LWR. This model requires the knowledge of a range of thermophysical parameters for accurately calculating the different loss mechanisms. These parameters are detailed in Tab. 6.1.

6.2.2 Intrinsic Absorption

Recognizing the significant role of intrinsic absorption in this study, we will provide a more detailed exploration of this loss mechanism. Eq. 6.5 is showing how the intrinsic absorption is calculated according the coupled phase model of Dukhin and Goetz [5,8]. It incorporates the approach of Allegra and Hawley [9] to account for intrinsic losses in the dilute case, and the methodology of McClements [10] for the complex wavenumber to extend the expression to concentrated systems.

$$\alpha_{\mathrm{int}} = \frac{(1-\varphi)\frac{\alpha_{\mathrm{m}}}{c_{\mathrm{m}}} + \varphi\frac{\rho_{\mathrm{m}}\alpha_{\mathrm{p}}}{\rho_{\mathrm{p}}c_{\mathrm{p}}}}{\sqrt{\frac{1-\varphi}{c_{\mathrm{m}}^2} + \frac{\varphi\rho_{\mathrm{m}}}{\rho_{\mathrm{p}}c_{\mathrm{p}}^2}}}\sqrt{\frac{\rho_{\mathrm{s}}}{\rho_{\mathrm{m}}}} \tag{6.5}$$

with

$$\rho_{\mathrm{s}} = \rho_{\mathrm{p}}\varphi + \rho_{\mathrm{m}}(1-\varphi) \tag{6.6}$$

where φ represents the particle volume fraction, ρ_{s} denotes the density of the dispersion, and α_{m}, c_{m}, and ρ_{m} correspond to the attenuation, sound velocity, and density of the medium, respectively. Similarly, α_{p}, c_{p}, and ρ_{p} refer to the attenuation, sound velocity and density of the particle.

As our study focuses on modelling the intrinsic absorption of the dispersed polymer particles α_{p}. We calculated viscoinertial α_{vis}, thermal α_{th}, and scattering α_{sc} losses using the measuring device's software, which applies the Dukhin and Goetz coupled phase model [1,4,5]. This modelled attenuation α_{mod} was subtracted from the total measured attenuation α_{meas}, assuming the remaining, residual attenuation α_{res} to be solely due to intrinsic absorption α_{int}.

$$\alpha_{\mathrm{int}} \approx \alpha_{\mathrm{res}} = \alpha_{\mathrm{meas}} - \alpha_{\mathrm{mod}} = \alpha_{\mathrm{meas}} - \alpha_{\mathrm{vis}} - \alpha_{\mathrm{th}} - \alpha_{\mathrm{sc}} \tag{6.7}$$

Subsequently, the intrinsic absorption of the particles α_{p} was calculated using Eq. 6.5. For the intrinsic absorption of the medium α_{m}, which in this case was water, we referred to literature values (refer to Chapter 6.4.1). To accurately predict a reasonable particle attenuation spectrum, the procedure was applied to the same latex dispersion at several different particle volume fractions φ and measurement frequencies f.

At this point, it should be mentioned that in this publication the attenuation coefficient is expressed as absolute attenuation coefficient α which means that the total attenuation coefficient α is divided by the ultrasonic frequency f [11].

$$\alpha = \alpha/f \tag{6.8}$$

This approach offers significant benefits in representing the attenuation spectrum. As, the area beneath the curve in this representation correlates directly with the particle volume fraction, providing a clear and proportional relationship.

The intrinsic absorption within polymers involves a complex interplay of physical mechanisms that dissipate acoustic energy, each linked to the material's inherent properties and its interaction with acoustic waves. The primary sources of attenuation are hysteretic behaviour and scattering [12].

Hysteretic attenuation, results from the viscoelastic nature of polymers, which exhibit a delayed response to cyclic stresses. This delay in response causes irreversible molecular rearrangements and energy loss, especially pronounced near the glass transition temperature, where polymers transition between glassy and rubbery states. [13,14]

Acoustic scattering is another significant factor contributing to intrinsic absorption in polymers. This phenomenon occurs when there are heterogeneities within the polymer material. Variations in acoustic impedance caused by these heterogeneities lead to the scattering of sound waves. Such inhomogeneities can arise from crystallites within the polymers [13] or from composites of different materials incorporated into the polymer [15,16]. The degree of scattering attenuation is influenced by the frequency of the sound waves and the average size of these heterogeneities.

The frequency dependent behaviour of the intrinsic absorption of polymers is in the majority of literature [12,17–19] described by a single longitudinal attenuation constant C_0:

$$\alpha_{\mathrm{p}}(f) = C_0 \tag{6.9}$$

However, most studies have conducted single frequency measurements and/or measurements within relatively low frequency ranges. Specifically, for the materials analysed in this study, no references were found for measurements conducted above 10 MHz. Only a few studies involving different materials [5,17] considered a frequency range comparable to this study (3 to 99.5 MHz).

In this study, as well as in others [5,9], deviations from the expected behaviour described by Eq. 6.9 have been observed. Consequently, similar to previous research [20], a second-order polynomial function was used to describe the intrinsic absorption of the particles. (see Eq. 6.10)

$$\alpha_{\mathrm{p}}(f) = C_0 + C_1 f + C_2 f^2 \tag{6.10}$$

6.3 Experimental

6.3.1 Materials

In this study, we examined an array of polymer latices, each identified by its material and mean particle diameter (d_{50} in microns). The selection included three polyvinyl chloride (PVC) dispersions, namely E 75 HV (PVC@0.20), M 68 FW (PVC@0.78) and P 70 HT (PVC@2.10), all supplied by Westlake Vinnolit GmbH & Co. KG. Additionally, a styrene-butadiene rubber dispersion, Taktene S 62 F (SBR@0.23), was provided by Arlanxeo Switzerland S.A. We also analysed two polytetrafluoroethylene (PTFE) dispersions PFA 6900 GZ (PTFE@0.21) and PFA 6910 GZ (PTFE@0.08) from 3M Dyneon GmbH. The study also incorporated a polyurethane dispersion (PU@0.07), synthesized as part of Christina Gassner's unpublished master's thesis at Heinrich Heine University Düsseldorf in 2021, and a polymethyl methacrylate-co-butyl acrylate dispersion (PBAMM@0.10), synthesized by Sven Kroß for his unpublished master's thesis at TH Köln in 2021.

6.3.2 Measurement of Particle Density

To calculate the particle density ρ_{p}, we first determined the density of the undiluted dispersion ρ_{s} using a 50 mL glass pycnometer. This pycnometer was set to 25 °C in a water bath and calibrated with deionized water before each use. We used the density of water at 25 °C (0.997 g/L) as the density of the dispersion medium ρ_{m}. The particle mass fraction w was determined by drying a dispersion sample at 80 °C to constant weight, presuming the residue to be composed of pure particle phase. Subsequently, the particle density ρ_{p} was calculated using the following equation:

$$\rho_{\mathrm{p}} = \frac{\rho_{\mathrm{s}}\rho_{\mathrm{m}}w}{\rho_{\mathrm{m}} - \rho_{\mathrm{s}}(1-w)} \tag{6.11}$$

6.3.2.1 Estimation of Particle Thermal Expansion

To estimate the coefficient of thermal expansion, we measured the particle density ρ_{p}, of all samples at three different temperatures: 20 °C, 25 °C, and 30 °C. To ensure the accuracy and reliability of our measurements, the density determination for each temperature was repeated three times.

The thermal expansion coefficient of the particle β_{p} was then calculated by analysing the slope of the particle density change with temperature at constant pressure $\left(\frac{\partial \rho_{\mathrm{p}}}{\partial T}\right)_P$. This analysis was conducted using Eq. 6.12, with the specific particle density ρ_{p} measured at 25 °C.

$$\beta_{\mathrm{p}} = -\frac{1}{\rho_{\mathrm{p}}}\left(\frac{\partial \rho_{\mathrm{p}}}{\partial T}\right)_P \tag{6.12}$$

6.3.3 Measurement of Heat Capacity

In this study, the heat capacity of the sample was measured using a Q2000 differential scanning calorimeter (DSC) from TA Instruments. Initially, a small volume (10 to 20 μL) of the stock dispersion was placed in a pre-weighed aluminium pan and dried at 100 °C. Post-drying, the dry substance's mass was recorded, and the sample was then loaded into the DSC. The heat capacity determination involved two heating and cooling cycles between -30 and 130 °C at a rate of 10 $K \cdot min^{-1}$. The heat capacity value reported in Tab. 6.3 corresponds to the findings from the second heating cycle, specifically at 25 °C.

6.3.4 Measurement of Acoustic Attenuation

The AAS measurements were conducted using the DT-1202 tone burst instrument from Dispersion Technology Inc at room temperature. The attenuation was measured across 18 different frequencies, ranging from 3 to 99.5 MHz, using the "more precise" setup mode to enhance the signal-to-noise ratio. Each sample underwent three repeated measurements, with the results subsequently averaged. To ensure homogeneity and prevent settling, the samples were continuously circulated using a peristaltic pump during the measurement process. Following these measurements, the mass fraction for each sample was determined in triplicate.

6.3.4.1 Sample Preparation

Acknowledging that changes in pH value and electrolyte concentration can significantly affect dispersion stability and consequently influence the PSD, this study employed a careful sample preparation protocol.

Typically, a 150 mL dispersion at the desired volume fraction was prepared by diluting the concentrated stock dispersion. The pH value of the diluted dispersion was adjusted, if necessary, to match the original pH, using either 0.1 $mol \cdot L^{-1}$ HCl or 0.1 $mol \cdot L^{-1}$ NaOH.

For the PVC (PVC@0.20, PVC@0.78, PVC@2.09) and PTFE (PTFE@0.08, PTFE@0.21) samples, a centrifugation process was employed. Particles were separated from the dispersion medium using an RC 5B Plus centrifuge from Sorvall with an SLA-3000 rotor at 10,000 rpm for 2-6 hours at 4 °C. The supernatant obtained was then used as a diluent.

For the SBR@0.23 sample, dialysis against deionized water was conducted over 10 days using a 200,000 MWCO membrane, changing the water twice daily. This ensured minimal electrolyte presence in the dispersion medium. The samples were then diluted with a 2 $mol \cdot L^{-1}$ KCl solution and deionized water to a final concentration of 10 $mmol \cdot L^{-1}$ KCl.

Other samples, due to limited quantities, were directly diluted to a concentration of 10 $mmol \cdot L^{-1}$ KCl in the dispersion medium using deionized water and a 2 $mol \cdot L^{-1}$ KCl solution.

Despite these efforts, slight variations in electrolyte concentration in the dilution series might have persisted.

6.3.4.2 Data Evaluation

For analysing the attenuation spectra, we used the DT-1202 software, which incorporates the coupled phase model by Dukhin and Goetz. A critical aspect of this software is that its applicability is limited to particle systems that fulfil LWR conditions. Consequently, when employing the full frequency range of the measuring device (1-100 MHz), the particle size of the sample to be analysed should be less than 10 μm. The process of determining particle size distributions involved fitting the obtained attenuation curves from the spectra with theoretical curves, based on either a monomodal or bimodal lognormal distribution. However, in this particular study, our analysis was confined to the monomodal case.

6.3.5 Measurement of Suspension Sound Velocity

The determination of sound velocity of the dispersion c_s in this study was also conducted using the DT-1202 measuring device. This measurement was performed at a frequency of 10 MHz and was carried out in parallel with the measurement of acoustic attenuation.

6.3.5.1 Estimation of Particle Material Sound Velocity

The sound velocity of the particle material was deduced through a regression analysis, involving the examined sound velocities of the suspension at varying particle volume fractions φ, the sound velocity of water as medium sound velocity ($c_\mathrm{m} = 1498\ \mathrm{m{\cdot}s^{-1}}$) and the so-called Wood equation [21]:

$$c_\mathrm{s} = \sqrt{\frac{c_\mathrm{m}^2}{\frac{\rho_\mathrm{s}}{\rho_\mathrm{m}}\left(1-\varphi+\varphi\frac{\rho_\mathrm{m} c_\mathrm{m}^2}{\rho_\mathrm{p} c_\mathrm{p}^2}\right)}} \tag{6.13}$$

where the variables c_s, c_m, and c_p represent the sound velocities in the dispersion, dispersion medium, and particles, respectively.

The Wood equation offers a straightforward theoretical framework for interpreting the propagation of sound through a mixture of particles suspended in a dispersing medium. However, its accuracy is generally constrained to scenarios involving dilute suspensions and low frequency ranges. In concentrated colloidal systems, where particle interactions are more significant, the Wood equation's applicability diminishes.

In order to reduce the effects of particle interactions on the sound velocity calculations of the particle material c_p, a critical volume fraction φ_cr, was defined (Eq. 6.14). Sound velocity measurements that exceeded this critical threshold were disregarded in the estimation process. The equation for φ_cr is:

$$\varphi_\mathrm{cr} = \frac{\pi}{6}\frac{1}{\left(1+\frac{10}{\varkappa d_{50}}\right)^3} \tag{6.14}$$

In this context, the Debye-Hückel parameter $\varkappa$ is estimated based on the conductivity of the dispersion medium K_m, as shown in Eq. 6.15. Here, ε_0 represents the vacuum permittivity, and ε_m the medium's relative permittivity. The effective diffusion coefficient D_eff was set at $1.994{\cdot}10^{-9}{\cdot}\mathrm{m}^2{\cdot}\mathrm{s}^{-1}$, aligning with the properties of potassium chloride. The approximation is given by:

$$\varkappa \approx \left(\sqrt{\frac{\varepsilon_{\mathrm{m}}\varepsilon_0 D_{\mathrm{eff}}}{K_{\mathrm{m}}}}\right)^{-1} \tag{6.15}$$

This methodology ensures the analysis includes only those particle volume fractions that maintain a minimum separation distance equivalent to ten times the Debye length k^{-1}.

6.3.6 Measurement of Refence PSD

The reference PSD of most samples, except for PVC@0.78 and PVC@2.09, was analysed using dynamic light scattering (DLS) with a ZetaSizer Nano ZS from Malvern Panalytical. Measurements were conducted at 25 °C, with all samples thermostated for 2 minutes, in polymethylmethacrylate cuvettes, utilizing a 633 nm wavelength laser. Backscatter detection was employed at a 173° angle, with each measurement consisting of 15 sub-runs. Both the attenuator and measurement position were auto-adjusted. The refractive indices of the particles were obtained from Tab. 6.2, with absorbance set to 0.01. The dispersion medium, water, was assumed to have a dynamic viscosity of 0.8872 mPa·s and a refractive index of 1.334. Samples were diluted according to the protocol described in Chapter 6.3.2.4 and measured at five different volume fractions ranging from about 0.1 to 0.001 vol%. Averaging was performed only for nearly identical particle size results to minimize multiple scattering errors. Measurement quality was verified using Cumulant Fit and Multimodal Fit Error, ensuring values below the manufacturer's threshold of 0.005 in all cases.

Tab. 6.2: Refractive indices used for determining particle size distribution in various polymer latices.

sample	PU [22]	SBR [23]	PTFE [24]	PVC [25]
refractive index n	1.491	1.530	1.356	1.531

For PVC@0.78 and PVC@2.08, PSD was determined via laser diffraction spectroscopy (LDS) using a MasterSizer 2000 and Hydro 2000MU sampling unit from Malvern Panalytical. The stirring speed was maintained at 1100 rpm, and the samples were added to deionized water until laser obscuration was between 10 and 20 %. Measurements were taken in triplicate at room temperature using 633 nm and 433 nm wavelengths, with the results averaged by the instrument's software. The refractive index and absorbance settings for LDS were identical to those used in DLS measurements.

6.4 Results and Discussion

This section presents our study's results, including by an in-depth discussion interpreting these findings within the context of existing research and theoretical frameworks.

We begin with the determined thermophysical input parameters in Chapter 6.4.1, which form the foundation of our study. Using these input parameters, along with the reference PSD data, we calculated the model attenuation α_{mod} according to the coupled phase model by Dukhin and Goetz. As already described in the theory section, the intrinsic absorption of the different analysed polymers α_{p} can be estimated by knowledge of the measured attenuation α_{meas} and the model attenuation α_{mod}, assuming that any residual attenuation α_{res} can be attributed to the intrinsic absorption α_{int} (see Chapter 6.2.2). The results of the intrinsic absorption of the different analysed polymers α_{p} are discussed in Chapter 6.4.2.

Chapter 6.4.3 presents and discusses the different attenuation mechanisms that arise when the determined intrinsic particle absorption α_p is taken into account in the particle sizing model, assuming the PSD of the reference method. This is exemplified by measurements with a particle volume fraction of approximately 20 vol.%.

In Chapter 6.4.4, the PSD results of the AAS method at different particle volume fractions are compared with those of the reference method. In this section, the PSDs are obtained by fitting the attenuation spectra with the experimentally determined thermophysical parameters and the intrinsic absorption. As these parameters have to be determined individually for each sample, the procedure is highly time-consuming.

Therefore, in the final Chapter 6.4.5, we examine the AAS PSD results obtained when uniform input parameters are assumed for the three different PVC dispersions. This approach aims to streamline the analysis by using averaged input parameters, which simulate the scenario where literature data is used.

6.4.1 Thermophysical Input Parameter

Accurate thermophysical input parameters are fundamental to the successful application of acoustic attenuation spectroscopy for determining particle size distribution, as they influence the modelling of the various attenuation mechanisms. Given AAS's sensitivity to these parameters, any deviations can significantly impact the accuracy of the results. This section presents the required thermophysical parameters for the simulation of the viscoinertial α_vis, thermal α_th and scattering losses α_sc using in the Dukhin and Goetz coupled phase model.

The parameters for the dispersion medium, water, were obtained from the DT 1202 measuring device software, detailing the following values at 25 °C: density ρ_m =0.997 g·cm^{-3}, viscosity η_m = 0.8904 mPa·s, heat conductivity τ_m =6.06 mW·cm^{-1}·K^{-1}, specific heat capacity C_p^m = 4.180 J·g^{-1}·K^{-1}, volumetric thermal expansion coefficient β_m =2.57·10^{-4} K^{-1} acoustic velocity c_m = 1497 m·s^{-1} and the intrinsic medium absorption of $\alpha_\mathrm{m}(f) = f \cdot 0.002\ \ \mathrm{dB \cdot cm \cdot MHz^{-2}}$.

In contrast, the thermophysical parameters of the different particles were ascertained predominantly through experimental methods, with thermal conductivity being the only parameter determined through literature review. These findings are summarized in Tab.6 3. A detailed discussion of each measurement and its analysis exceeds the intended scope of this paper. However, a presentation is available in the Supporting Information.

Tab. 6.3: Thermophysical parameters for different particles used in the study: density ρ_p, thermal conductivity τ_p, specific heat capacity C_p^p, thermal expansion coefficient β_p and sound velocity c_p. These parameters are essential for modeling attenuation mechanisms in AAS.

sample	ρ_p [g·cm^{-3}]	τ_p [mW·cm^{-1}·K^{-1}]	C_p^p [J·g^{-1}·K^{-1}]	β_p [·10^{-4}·K^{-1}]	c_p [m·s^{-1}]
PU@0.07	1.158	2.10 [26]	1.692	6.5	1836
SBR@0.23	0.937	2.08 [27]	2.069	5.0	1540
PTFE@0.08	2.003	2.35 [28]	1.157	4.0	1266
PTFE@0.21	2.027	2.35 [28]	1.257	3.6	1298
PVC@0.20[a]	1.408	1.92 [29]	1.078	1.7	2026
PVC@0.78[a]	1.385	1.92 [29]	0.945	2.1	2000
PVC@2.09[a]	1.409	1.92 [29]	1.184	1.8	2135
PVC[a,b]	1.401	1.92	1.069	1.9	2054

[a] For all PVC samples a scattering coefficient $C_\mathrm{sc,p}$ of 0.7 was assumed, while scattering losses were disregarded for all other samples ($C_\mathrm{sc,p} = 0$). [b] Values correspond to the mean value of all analysed PVC samples.

A comparison of the values determined in this study with other literature values is only meaningful to a limited extent, as no values for the particular samples examined in this study were found in the literature. Nevertheless, values for comparable samples could still be found. These are generally in a comparable order of magnitude to the values determined here. Which are summarized in the Tab. 6.10 in the supporting information.

The study by Babick et al. [30] on oil in water emulsions highlights the different impact of thermophysical input parameters' precision. The analysis, accounting for a ±5 % deviation in input parameters, identifies particle and medium density as the most influential factors, potentially altering outcomes by up to 26 %. In contrast, the effect of thermal conductivity is minimal, impacting the median particle size by a maximum of 2.3 %. Given their substantial effect on PSD results, parameters of high influence should ideally be validated experimentally. Conversely, for low-impact parameters, relying on values obtained from the literature can be adequately precise. This rationale supports the methodology of the present study, which relies only on literature values for particle thermal conductivity τ_p.

As the scattering losses for small particles are minimal and negligible, they were only considered in this study for all PVC as an example. A scattering coefficient $C_\mathrm{sc,p}$ of 0.7 was assumed for these samples, while all other samples were assigned a scattering coefficient of zero ($C_\mathrm{sc,p} = 0$), whereby scattering effects were not taken into account. Further details are discussed in Chapter 6.4.3.

6.4.2 Intrinsic Particle Absorption

The intrinsic absorption of the different particles α_p was determined as described in the theory section (Chapter 6.2.2). The model attenuation α_mod, was calculated using the "predict mode" function of the DT-1202 measuring device. The following figures display the calculated intrinsic particle absorption of the different polymers, measured at various wavelengths and particle volume fractions.

Tab. 6.4 summarizes the coefficients for describing intrinsic particle absorption using Eq. 6.10, including the minimum particle volume fraction φ_{min}. Measurements at particle volume fractions below φ_{min} had to be excluded from the fitting procedure and are not shown in this section's figures. At these low particle volume fractions, the calculated intrinsic particle absorption deviated significantly compared to higher volume fractions. However, since intrinsic particle absorption is considered a material property, it should be in general independent of the particle volume fraction. It is assumed that at low particle volume fractions, measurement errors are comparable in magnitude to the intrinsic particle absorption themselves.

Due to the intrinsic particle absorption being determined at different particle volume fractions but measured at identical frequencies, slight variations were observed between the measurements at different fractions. This resulted in a noticeable spread of data points in the diagrams. However, these deviations appear to be generally random, which is why all measurement points shown in the diagrams, were included in the fit using Eq. 6.10.

For the polyurethane dispersion investigated in this study, the observed behaviour of the intrinsic absorption closely aligns with the expected behaviour predicted by Eq. 6.9 (see Fig. 6.1). Minor deviations are noted only at very high frequencies ($f > 70$ MHz), which can be accurately described using Eq. 6.10.

Jarzynski et al. [13] determined an intrinsic particle absorption of 3.75 dB·cm^{-1}·MHz^{-1} for a polyether-based and 4.55 dB·cm^{-1}·MHz^{-1} for a polybutadiene-based polyurethane in a single frequency investigation at 2 MHz. In this study, however, a polyester-based polyurethane was analysed. Based on the results of Jarzynski et al., it can be assumed that the polyol used in the polyurethane synthesis has a significant influence on the intrinsic absorption. Therefore, the calculated intrinsic absorption (refer to Fig. 6.1 and Tab. 6.4) is considered to be within in a plausible order of magnitude.

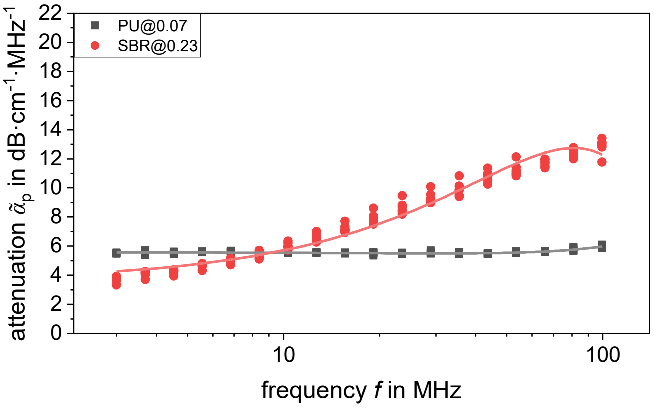

Fig. 6.1: Intrinsic particle absorption of PU@0.07 and SBR@0.23 latices. The lines correspond to a second order polynomial fit. More details about the fitted parameters can be found in Tab. 6.4.

In our study, the styrene-butadiene rubber (SBR) exhibited behaviour significantly deviating from that described by Eq. 6.9. Instead of a constant value, a continuous increase in intrinsic absorption with increasing frequency was observed (see Fig. 6.1). As SBR is a material that generally has little or no crystallinity [31,32], the observed attenuation cannot be explained by scattering phenomena caused by crystallites. Instead, we assume that this is due to the significantly more elastic viscoelastic behaviour of SBR, which is characteristic of rubbery materials [33], compared to other polymers. Unlike the polyurethane sample, this behaviour is poorly described by Eq. 6.10, particularly at frequencies above 81 MHz. Therefore, in the subsequent analysis, only frequencies below 81 MHz were considered for the determination of the particle size distribution (PSD).

In the study by Wada et al. [34], the acoustic attenuation of SBR is analysed across a temperature range of 0 to 50 °C and at frequencies of 1, 3, and 5 MHz. From the graphically presented data, an attenuation coefficient of C_0 of approximately 13.7 dB·cm^{-1}·MHz^{-1} at 25 °C can be derived. This value is significantly higher than the values observed here. In contrast, the study by Faghihi et al. [35] measured an acoustic attenuation of approximately 1.6 dB·cm^{-1}·MHz^{-1} at 3.8 MHz, which is significantly lower than the values measured in this study.

Interestingly, in the study by Dukhin et al. [5], which deals with the determination of the particle size distribution of neoprene rubber using AAS, plausible results were only obtained when a single intrinsic absorption coefficient C_1 of 0.15 dB·cm^{-1}·MHz^{-2} was assumed. This suggests that a strong increase in intrinsic absorption with increasing frequency may be expected for rubber-like materials. In addition, the attenuation determined by Dukhin et al. is of a similar order of magnitude to that of the styrene-butadiene rubber measured here.

Tab. 6.4: Summary of the coefficients C_0, C_1 and C_2 used to describe the intrinsic particle absorption for various polymer latices using a second-order polynomial function (see Eq. 6.10). The table also includes Information about the minimum particle volume fraction φ_{min}used in the fitting process.

sample	C_0 [dB·cm^{-1}·MHz^{-1}]	C_1 [dB·cm^{-1}·MHz^{-2}]	C_2 [dB·cm^{-1}·MHz^{-3}]	φ_{min} [vol%]
PU@0.07	5.591	-5.981·10^{-3}	9.892·10^{-5}	17.3
SBR@0.23	3.598	2.251·10^{-1}	-1.385·10^{-3}	11.3
PTFE@0.08	5.541	1.472·10^{-1}	-7.978·10^{-4}	14.6
PTFE@0.21	6.928	2.137·10^{-1}	-9.923·10^{-4}	17.4
PVC@0.20	2.816	-3.423·10^{-3}	7.852·10^{-5}	22.7
PVC@0.78	2.459	-1.153·10^{-3}	1.610·10^{-4}	11.3
PVC@2.09	3.688	-1.424·10^{-2}	3.638·10^{-4}	11.1
PVC[a]	2.838	-6.745·10^{-3}	2.302·10^{-4}	11.1

[a] Values are obtained when the mean value of all three analysed PVC samples from Tab. 6.3 is used and then the measuring points of all samples are taken into account when fitting the intrinsic particle attenuation.

The observed behaviour of the two PTFE samples in this study diverges significantly from that predicted by Eq. 6.9 (refer to Fig. 6.2). Similar to the intrinsic particle absorption observed in the SBR@0.23 sample, there is an observable increase in attenuation with rising frequency, which can be fitted with Eq. 6.10. Given PTFE's high crystallinity (ranging from 41% to 98% [36]) and the potential for scattering phenomena caused by crystallites, the notable increase in attenuation at higher frequencies might be attributed to these effects. However, we did not find references corroborating this increase in attenuation with frequency, likely due to prior measurements being conducted at substantially lower frequencies.

Hung and Goldstein [37] reported an attenuation coefficient C_0 of 8.04 dB·cm^{-1}·MHz^{-1} measured between 1 and 10 MHz at room temperature, which closely matches the values obtained for the PTFE@0.21 sample in the same frequency range. Conversely, Ono [12] documented a much higher attenuation of 14.71 dB·cm^{-1}·MHz^{-1} at 1 MHz, which exceeds our measurements in this frequency range. It is important to note that our PTFE samples also contain amounts of perfluoro(propyl vinyl ether) (PPVE), according to the manufacturing information. The exact influence of PPVE on the intrinsic absorption behaviour remains unclear. However, this discrepancy could explain why the intrinsic absorption differs significantly between the two samples, despite being supposedly an identical material.

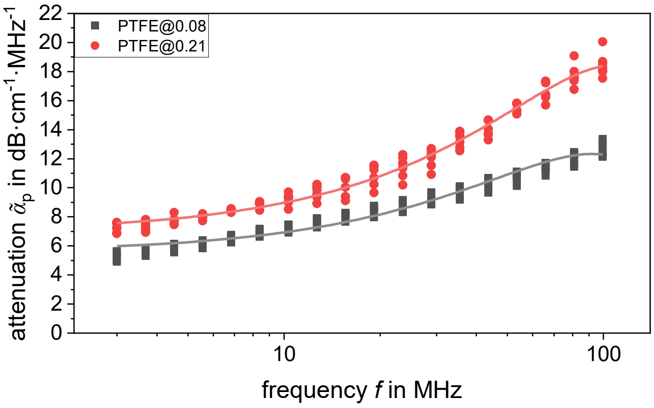

Fig. 6.2: Intrinsic particle absorption for different sized PTFE latices (PTFE@0.08, PTFE@0.21). The lines correspond to a second order polynomial fit. More details about the fitted parameters can be found in Tab. 6.4.

In the case of the PVC dispersions, the intrinsic absorption behaviour is similar to that of the PU@0.08 sample. Here, the intrinsic absorption can be described over a wide frequency range using a constant. However, an increase in attenuation with increasing frequency can be observed from frequencies above 40 MHz. This trend is consistent for all PVC samples studied, where the intrinsic adsorption behaviour can be accurately described using Eq. 6.10.

The PVC dispersions PVC@0.20 and PVC@0.78 exhibit almost identical intrinsic absorption behaviours, indicating consistent characteristics between these samples. Conversely, the PVC@2.09 sample shows the same general pattern but at a slightly higher level overall, corresponding to an upward shift of the curve.

Overall, PVC had the highest number of reference sources for intrinsic particle absorption among all the polymers analysed. However, the reported behaviour was always consistent with Eq. 6.9, which is likely due to the fact that none of these studies conducted measurements above 10 MHz. For example, Pouet and Rasolafsaon [38] measured an intrinsic absorption coefficient C_0 of approximately 1.85 dB·cm^{-1}·MHz^{-1} for measurements between 1 and 5 MHz. Wypych [39] reported an intrinsic absorption of 2.24 dB·cm^{-1}·MHz^{-1} at 5 MHz. Similarly, Ono [12] measured an intrinsic absorption coefficient C_0 of 2.24 dB·cm^{-1}·MHz^{-1} for measurements between 1 and 10 MHz. Sinha and Buckley [14] documented an intrinsic absorption of 4.05 dB·cm^{-1}·MHz^{-1} at 2 MHz, and Deutsch et al. [40] reported an intrinsic absorption of 4.32 dB·cm^{-1}·MHz^{-1} measured at 1.46 MHz and 20 °C. In summary, the values measured in this study fall within the range of the different reference sources.

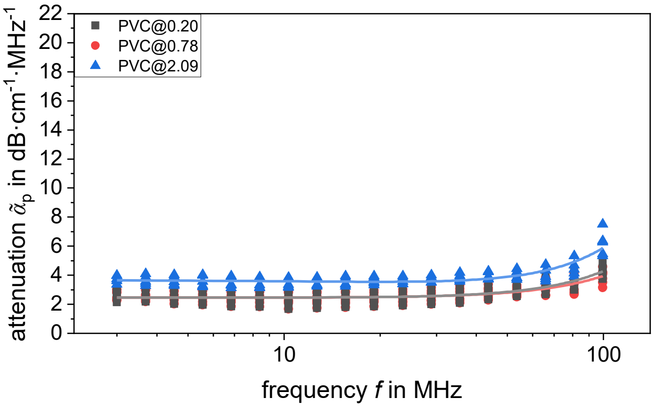

Fig. 6.3: Intrinsic particle absorption for different sized PVC latices (PVC@0.20, PVC@0.78, PVC@2.09). The lines correspond to a second order polynomial fit. More details about the fitted parameters can be found in Tab. 6.4.

6.4.3 Investigation of Various Loss Mechanisms

In this section, we examine the various loss mechanisms that contribute to the overall attenuation spectrum as calculated using the Dukhin-Goetz model. For these calculations, we used the particle size distributions of the reference methods provided in Tab. 6.6. We also compare these calculated spectra with the measured attenuation data. This analysis focuses on dispersions with relatively high particle volume fractions of approximately 20 vol%, the exact particle volume fractions are detailed in Tab. 6.5.

Due to conciseness remaining, not all spectra of the analysed materials are presented in this section; however, the omitted figures are available in the Supporting Information. Tab. 6.5 lists the different attenuation contributions at frequencies of 6.8 and 65.9 MHz, facilitating quick traceability of the discussion. All input parameters used in the model, except for intrinsic particle absorption, are documented in Chapter 6.4.1. The intrinsic particle absorption parameters are detailed in Chapter 6.4.2.

By examining the different attenuation mechanisms, we can identify which mechanisms dominate for each material under consideration. In general, our results show that intrinsic absorption usually accounts for the largest attenuation contribution of the modelled attenuation spectrum for all investigated polymers unlike in other studies [9,41]. Therefore, neglecting intrinsic particle absorption can lead to significant misinterpretations of PSD.

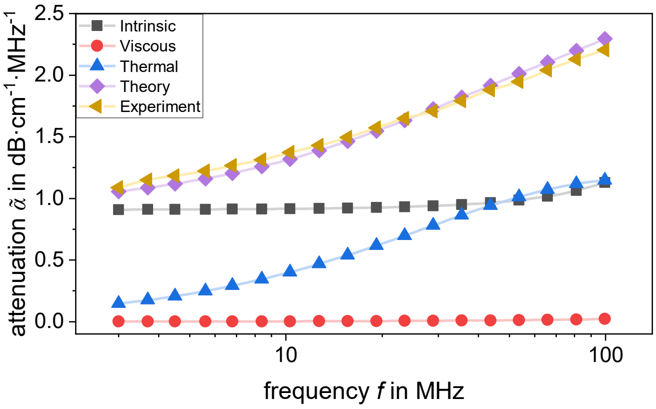

Fig. 6.4: Presentation of the attenuation spectra of the PU@0.07 sample with a particle volume fraction of 21.7 vol%. Plot includes the contributions from different attenuation mechanisms: intrinsic absorption α_{int} (Intrinsic), viscoinertial α_{vis} (Viscous) and thermal α_{th} (Thermal) losses. The sum of these mechanisms is labelled as Theory and the experimentally measured spectrum is labelled as Experiment.

For PU@0.07 (Fig. 6.4) and SBR@0.23 (Fig. 6.21), the observed behaviour aligns with findings reported in several studies [5,30,42], indicating that thermal attenuation predominates over viscoinertial losses in dispersions containing low density contrast such as emulsions or latices. Conversely, for higher-density polymers like PTFE (Fig. 6.22 and 6.23) and PVC (Fig. 6.5, 6.6 and 6.24), this is no longer true. In these cases, viscoinertial losses significantly exceed thermal losses in the spectrum (refer to Tab. 6.5).

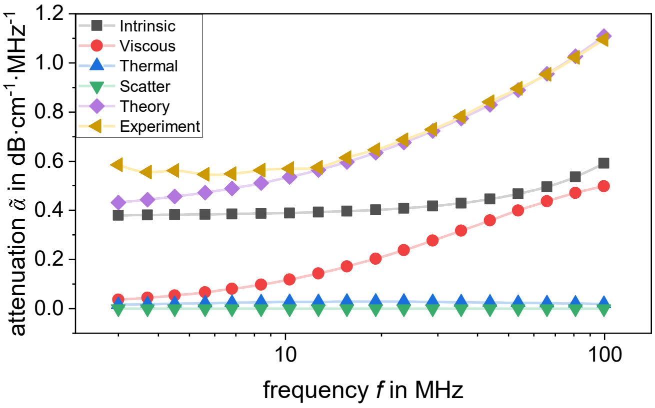

Fig. 6.5: Presentation of the attenuation spectrum of the PVC@0.20 sample with a particle volume fraction of 22.7 vol%. Plot includes the contributions from different attenuation mechanisms: intrinsic absorption α_{int} (Intrinsic), viscoinertial α_{vis} (Viscous) thermal α_{th} (Thermal) and scattering α_{sc} (Scatter) losses. The sum of these mechanisms is labelled as Theory and the experimentally measured spectrum is labelled as Experiment.

In general, with the exception of PVC@0.20, the agreement between the model calculations and experimental results is very good. However, for the PVC@0.20 sample, significantly higher attenuations were measured in the frequency range from 3 to 12.7 MHz than the model predicted. Similar behaviour was observed by Storti et al. [43], who also reported discrepancies between the model and the experimental data for a PVC latex in the lower-frequency portion of the spectrum, specifically from 1 to 20 MHz. This mismatch has been attributed to intrinsic relaxation phenomena or hindered movements of the polymer chains causing additional attenuation at low frequencies [17,44]. Also multiple scattering of thermal and viscous waves or particle clustering were also considered [17,45], but are less likely as the effect was also observed in dilute systems [17].

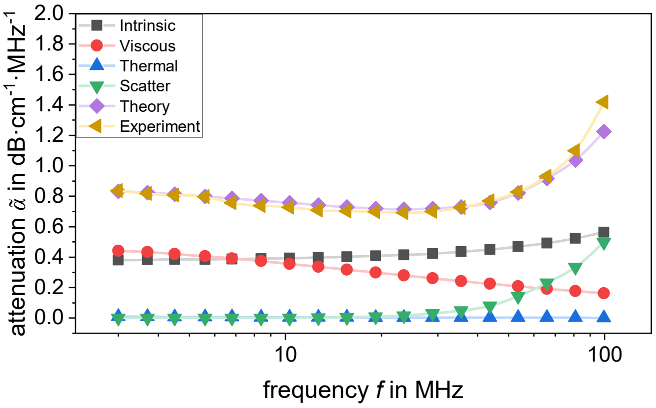

Fig. 6.6: Presentation of the attenuation spectrum of the PVC@2.09 sample with a particle volume fraction of 18.6 vol%. Plot includes the contributions from different attenuation mechanisms: intrinsic absorption α_{int} (Intrinsic), viscoinertial α_{vis} (Viscous) thermal α_{th} (Thermal) and scattering α_{sc} (Scatter) losses. The sum of these mechanisms is labeled as Theory and the experimentally measured spectrum is labeled as Experiment.

The behaviour observed in this study does not entirely align with the general statement by Dukhin and Goetz [46] regarding scattering losses, which stated significant contributions from particles larger than 3 µm at frequencies above 10 MHz. Our results show significant scattering contributions for the PVC@2.09 sample (see Fig. 6.6) at frequencies above 28.9 MHz, despite the particle having a d_{50} value of less than 3 µm. Besides particle size, the particle volume fraction also significantly influences scattering behaviour. Therefore, it is useful to consider scattering losses for particles with d_{50} values greater than 1 µm, especially at high particle volume fractions. In contrast, no significant scattering contribution (<1 %) is observed for PVC@0.20 (Fig. 6.5) and PVC@0.78 (Fig. 6.24). Thus, as mentioned in Chapter 6.4.1, scattering losses were neglected for all other analysed dispersions consisting of similarly sized or smaller particles.

Tab. 6.5: Detailed composition of the different attenuation loss mechanisms of the theoretically fitted spectrum at 6.8 and 65.9 MHz in dB·cm^{-1}·MHz^{-1}. The table also includes the analysed particle volume fractions φ in vol%.

sample	φ	@6.8 MHz				@65.9 MHz			
		α_{int}	α_{vis}	α_{th}	α_{sc}	α_{int}	α_{vis}	α_{th}	α_{sc}
PU@0.07	21.7	0.9118	0.0015	0.2913	-	1.0177	0.0145	1.0721	-
SBR@0.23	19.8	1.0403	0.0039	0.4331	-	2.6255	0.0104	0.3549	-
PTFE@0.08	21.1	0.9338	0.0707	0.0815	-	1.785	0.6566	0.2432	-
PTFE@0.21	20.9	1.2856	0.5048	0.2267	-	2.6042	2.5944	0.1518	-
PVC@0.20	22.7	0.3849	0.0803	0.0239	0	0.4958	0.4369	0.0224	0.0001
PVC@0.78	19.9	0.3029	0.4509	0.0700	0	0.4780	0.3499	0.0253	0.0066
PVC@2.09	18.6	0.3877	0.3916	0.0064	0.0004	0.4922	0.1921	0.0021	0.2308

6.4.4 Analysis of Particle Size Distribution

In this section, we discuss the results of the PSD determined using AAS at different particle volume fractions. The calculations were performed using the Dukhin and Goetz model with the software provided by the AAS measuring device. The necessary input parameters, except for the intrinsic particle attenuation, are documented in Chapter 6.4.1, while the intrinsic particle attenuation is detailed in Chapter 6.4.2.

In addition to the median of the particle diameter (d_{50}), the distribution width is crucial for evaluating a particle size distribution. One common metric for this evaluation is the span, calculated using Eq. 6.16. The span is determined by the difference between the d_{90} and d_{10} values, divided by the particle diameter median d_{50}. The values d_{90} and d_{10} represent the particle diameters at which 90 % and 10 % of the sample's cumulative distribution are smaller, respectively.

$$\text{span} = \frac{d_{90}-d_{10}}{d_{50}} \tag{6.16}$$

In the diagrams presented in this section, the d_{50} value is always plotted against the analysed particle volume fraction in the left-hand diagrams, while the span is plotted against the particle volume fraction in the right-hand diagrams. For comparison with the reference method, mean values were determined from the d_{50} and span values measured at different particle volume fractions. Unfilled data points were excluded when calculating the mean value. These mean values are depicted as lines in the diagrams and are also included in Tab. 6.6, along with the standard deviation. When calculating the mean values of the AAS method, care was taken to ensure that comparable d_{50} values were averaged. This was not the case with the span values, which exhibited significant variations, except for the PU@0.07 sample. Therefore, the span was averaged over the measurements at the same particle volume fractions as the d_{50} values.

Tab. 6.6 additionally shows the averaged d_{50} and span values of the different reference methods. The PSDs determined during an AAS measurement correspond to a weight basis. These are compared in Tab. 6.6 with the PSDs on a volume basis, which were determined using the reference methods of Dynamic Light Scattering (DLS) and laser diffraction spectroscopy (LDS). Assuming that the disperse phase and the continuous phase each have uniform and identical densities, the volume-weighted and mass-weighted particle size distributions coincide.

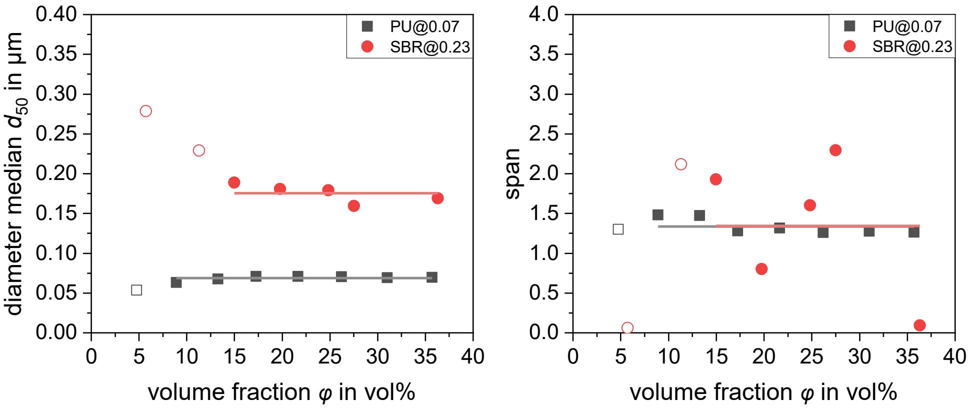

Fig. 6.7: Particle diameter median and span of PU@0.07 and SBR@0.23. The left diagram shows the diameter median d_{50} and the right diagram shows the span as a function of the particle volume fraction. Mean values are shown in the form of lines. Unfilled data points were not taken into account when calculating the mean value.

As shown in Fig. 6.7, the d_{50} and span values for the PU@0.07 dispersion remained very consistent, except for one measurement at approximately 5 vol%. Additionally, the average median particle diameter using the AAS method was identical to the DLS reference measurement at 0.069 µm (refer to Tab. 6.6). While the span values were 1.335 for the AAS measurement and 1.290 for the DLS measurement, these results are nearly identical. The excellent agreement between the AAS and DLS PSD data for the PU@0.07 sample indicates that the approach presented in this study for determining intrinsic particle absorption can provide very plausible values. However, this high consistency was not observed for the other samples analysed in this study, particularly with regard to the PSD span.

Tab. 6.6: Volume weighted particle size distribution data.

sample	d_{50}^{AAS} [µm]	span$^{\mathrm{AAS}}$	d_{50}^{REF} [µm]	span$^{\mathrm{REF}}$
PU@0.07	0.069±0.003	1.335±0.099	0.069±0.005	1.290±0.087
SBR@0.23	0.175±0.011	1.343±0.890	0.233±0.054	2.064±0.141
PTFE@0.08	0.081±0.005	1.058±0.454	0.080±0.006	0.800±0.183
PTFE@0.21	0.195±0.006	1.020±0.136	0.212±0.007	0.764±0.045
PVC@0.20	0.214±0.010	1.178±0.743	0.202±0.006	0.911±0.068
PVC@0.78	0.898±0.101	1.241±0.644	0.783±0.040	1.195±0.290
PVC@2.09	2.388±0.159	1.946±0.273	2.086±0.053	1.529±0.162

For the SBR@0.23 sample, consistent d_{50} values were only measured at a particle volume fraction above 15 vol% (refer to Fig. 6.7). The average d_{50} value was 0.175 µm, with an average span of 1.343. Both of these values were lower than the Dynamic Light Scattering (DLS) reference values, which were 0.233 µm for d_{50} and 2.064 for the span. Additionally, the AAS method showed significant fluctuations in span, resulting in a standard deviation of 0.890 (66 % of the mean value). This result is surprising because the comparison between the experimental data and the theoretical calculations based on the reference Particle Size Distribution (PSD) in the previous section showed good agreement at 19.8 vol% (see Fig. 6.21). This discrepancy may be due to the sensitivity of the particle size determination algorithm to measurement deviations.

Discrepancies observed between different particle measurement methods can be attributed to their inherent differences in sensitivity to particle size and shape, concentration and the physical interactions they measure. Dynamic Light Scattering (DLS) determines the hydrodynamic diameter by measuring time-dependent fluctuations in scattered light intensity caused by the Brownian motion of particles. Laser Diffraction Spectroscopy (LDS) infers the volume-equivalent sphere diameter based on the angular distribution of scattered light. AAS, as previously described, measures the attenuation of ultrasonic waves as they pass through a suspension, determining the acoustic particle diameter. Each method relies on distinct physical principles and interaction mechanisms between the particles and the measurement system.

In several studies, AAS was compared with other particle measurement methods [3,6,17,42,43,45,47–50]. Although the PSDs did not coincide, the results were generally in good agreement in many of the studies [3,6,42,43,45,49]. Deviations of the AAS PSD from those obtained by transmission electron microscopy (TEM) or scanning electron microscopy (SEM) were often justified by the number-based PSD [42] and the extensive sample preparation required for TEM [45,47] and SEM [49] methods. Deviations from the DLS are often attributed to dilution effects [47], the sensitivity of DLS to larger particles [50] or the fact that the hydrodynamic diameter in case of DLS may contain parts of the particle environment [45], such as surfactants, etc. The discrepancies between LDS were explained due to uncertainties related to assumptions about refractive indices and particle shape as well as the influence of dilution on the PSD [3]. On the other hand, factors contributing to differences in AAS PSD include non-linear attenuation effects especially at higher concentrations [3], assumption of many acoustic properties [42], sensitivity to particle aggregation [3] and influence of acoustic attenuation by particles of different shapes [51].

In the case of the SBR@0.23 sample, the AAS PSD result was smaller than the DLS PSD result. This aligns with the findings of Ocepek et al. [48], who demonstrated that AAS provided more accurate PSD compared to DLS. The DLS method struggled with detecting smaller secondary particles. Transmission Electron Microscopy (TEM) confirmed the presence of these secondary particles but was limited by the effects of sample preparation, often resulting in larger PSD outcomes. Mende et al. [50] observed a similar issue, where DLS was unable to accurately measure smaller particle sizes. This discrepancy was attributed to the sensitivity of DLS to larger agglomerates, which skewed the PSD results. TEM imaging further illustrated the presence of very fine particles (50 nm and smaller) alongside some larger agglomerated particles, affecting the volume distribution but not the number distribution. In the paper by Adjadj et al. [17], a significantly smaller particle size is also measured using AAS compared to DLS, which is not discussed further. This suggests that AAS may be more sensitive to small particles than the DLS method.

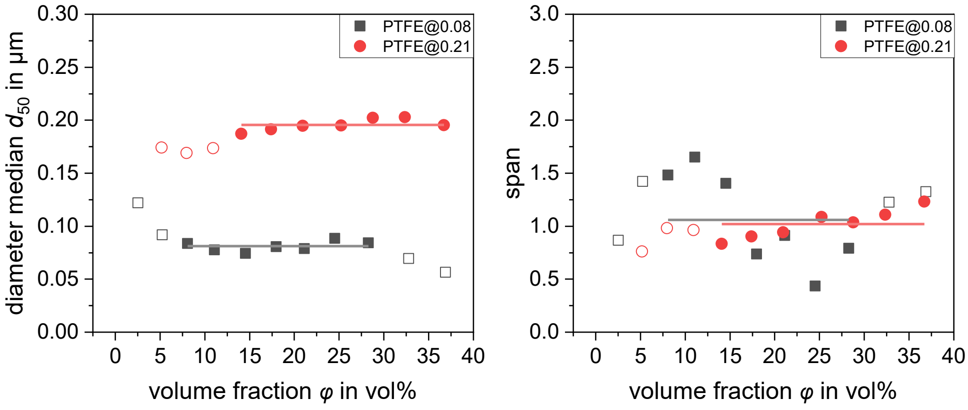

Fig. 6.8: Particle diameter median and span of different PTFE samples (PTFE@0.08 and PTFE@0.21). The left diagram shows the diameter median d_{50} and the right diagram shows the span as a function of the particle volume fraction. Mean values are shown in the form of lines. Unfilled data points were not taken into account when calculating the mean value.

For the PTFE@0.08 sample, very constant d_{50} values were determined between 8 and 28 vol%, which averaged at 0.081 µm corresponding very well with the d_{50} value of the DLS method at 0.080 µm. The span, which averages a value of 1.058 for the AAS measurement, is slightly larger than for the DLS measurement (0.800). However, again no clear trend can be recognised for the span, which is why there is a large standard deviation (refer to Tab. 6.6 and Fig. 6.8). With the PTFE@0.21 sample, a very constant d_{50} value of 0.195 µm is determined between approx. 14 vol% and 37 vol% (see Fig. 6.8), which is only marginally smaller than the value of 0.202 µm for the DLS measurement. The span is similar to that of the PTFE@0.080 sample and the value of 1.020 is higher than the DLS measurement of 0.764. Overall, however, there is a relatively uniform span compared to many other AAS measurements.

We found three studies by Hipp et al. [42,43,52] in which PTFE dispersions were also analysed using AAS. In two of these studies, only individual particle volume fractions (1.11 wt% [42] and 1.05 wt% [43]) were analysed using the well-known Epstein/Carhart [53] and Allegra/Hawley [9] (ECAH) Theory, which is only suitable for dilute systems. Therefore, intrinsic particle attenuation was neglected in both studies. Nevertheless, the results were in good agreement with reference measurements. The most recent study by Hipp et al. [52] investigates a PTFE sample with a $d_{50} \approx 0.2\ \mu m$ up to approx. 15 vol% with an alternative coupled phase model for predicting acoustic attenuation and particle size distributions in concentrated suspensions. This model, different from the one used in our study, was able to predict relatively consistent PSD data. However, a slight increase of the d_{50} value with increasing particle volume fraction (0.2 µm up to 0.25 µm), as well as some fluctuations in PSD width, similar to the trends observed in the PTFE@0.21, are also notable. Unfortunately, the study does not provide detailed information on the thermophysical input parameters used, making it unclear whether or how the intrinsic particle absorption was accounted for.

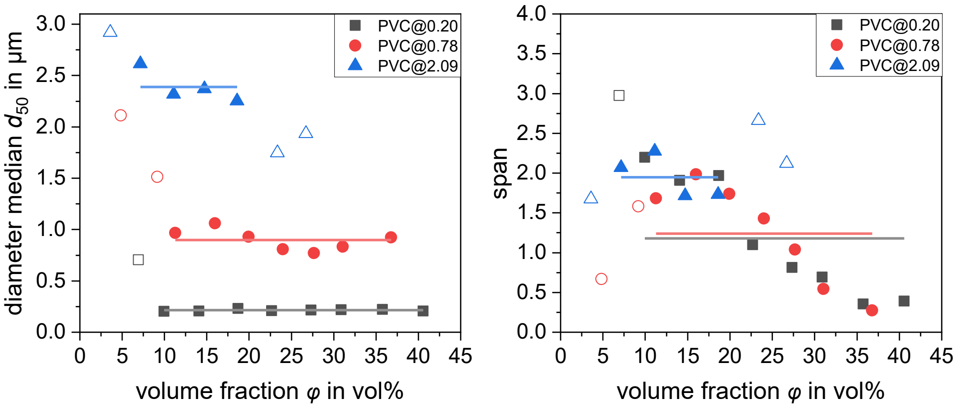

Fig. 6.9: Particle diameter median and span of different PVC samples (PVC@0.20, PVC@0.78 and PVC@2.09). The left diagram shows the diameter median d_{50} and the right diagram shows the span as a function of the particle volume fraction. Mean values are shown in the form of lines. Unfilled data points were not taken into account when calculating the mean value.

In the case of the PVC@0.20 sample, very consistent d_{50} averages of 0.214 µm were measured across a wide range of concentrations, from approximately 10 vol% up to 40 vol% (refer to Fig. 6.9). This matches closely with the d_{50} value from the DLS reference measurement, which averaged 0.202 µm. However, the span of the PSD did not remain constant. Instead, it exhibited an almost linear decrease with increasing particle volume fraction over the entire measured concentration range. A similar trend was observed for the PVC@0.78 µm sample. Here, the d_{50} values also remained stable at concentrations above 11 vol%, averaging 0.898 μm. Conversely, the span showed a constant decline between approximately 15 vol% and 35 vol%.

Overall, this behaviour is very implausible, as it suggests that the width of particle size distribution decrease with increasing particle volume fraction. This contradicts most other studies [6,46,52], where PSD analysis at different particle volume fractions using AAS typically showed larger particle sizes at higher particle concentrations. This discrepancy is often attributed to the formation of agglomerates [46] or the use of inadequate models that fail to predict attenuation accurately at such high particle volume fractions [6].

For the PVC@2.09 sample, the d_{50} values were relatively constant between approximately 7 and 19 vol%, averaging 2.388 μm. Although there is no downward trend in this range, there is also no constant span value, resulting in a large standard deviation (see Tab. 6.6 and Fig. 6.9). It is notable that for both the PVC@0.78 and PVC@2.09 samples, the reference PSDs, which were measured using LDS instead of DLS, are consistently slightly smaller than the AAS results. In contrast, the opposite trend is observed for some samples measured using DLS. Several sources have observed this trend with DLS [17,48,50], suggesting a potential systematic bias based on the measurement method. However, no such systematic deviation was reported for LDS, which was only compared with the AAS method at different particle concentrations in one study known to us [3].

We are aware of only one study, in which PVC dispersions were analysed using the AAS method. In the already mentioned paper by Hipp et al. [43], three PVC dispersions of different sizes were examined. However, only individual concentrations of approximately 5 vol% were analysed using the ECAH theory without considering intrinsic particle absorption.

The PSD determination procedure described in this paper, which uses the Dukhin-Goetz model, generally provides consistent d_{50} values across a wide range of particle volume fractions, sizes, and different polymeric materials. These d_{50} values typically align with reference methods such as DLS and LDS. Despite a good agreement between the theoretical and measured attenuation spectra for all samples in Chapter 6.4.3, significant fluctuations and unexpected trends in the span values, particularly for PVC samples, highlight potential limitations of this approach. Consequently, even very small measurement fluctuations may have a relatively large influence on the PSD span determined by the algorithm.

A critical aspect of the presented methodology in this paper is the inevitable use of an alternative PSD measuring method to determine the intrinsic particle absorption. This introduces a potential source of error, as it must be assumed that the AAS method inherently produces slightly different PSD results. Therefore, an incorrect intrinsic particle absorption might have been assumed, leading to deviations in span values.

To simplify the analysis of the experimental data, a log-normal distribution was used to fit the AAS data in this study. This method assumes a specific median and standard deviation, which can lead to incorrect estimations of the proportion of small or large particles. This is particularly problematic for polydisperse systems, where the complexity of the distribution may not be fully captured, resulting in oversimplified interpretations, especially when evaluating metrics such as span. However, the reference particle size measurements detected only monomodal particle size distributions.

In the next section, the impact of using sets of generalized standard data, generated by averaging all thermophysical input parameters and intrinsic particle absorption for one material, on the PSD determination process will be analysed. This analysis will assess whether the determined intrinsic particle absorption of a material can be applied to other samples of the same material with varying particle sizes.

6.4.5 Impact of Averaged Input Parameters on PSD Determination

In the previous section, the input parameters were determined individually for each sample, a procedure that is very time-consuming. Additionally, the particle size distribution from a reference method was used to calculate the intrinsic particle absorption. Any residual attenuation, which could not be described using the Dukhin-Goetz model under the assumption of the reference PSD, was attributed to intrinsic particle absorption. This approach inherently resulted in the findings being comparable to the reference measurement.

To evaluate the robustness of the procedure presented in this paper, this section focusses on averaged input parameters for an individual material. The PVC dispersions were chosen because they are the material that covers the widest particle size range in this paper. The thermophysical input parameters used can be found in Tab. 6.3 under the PVC column. The coefficients required to describe the intrinsic particle absorption according to Eq. 6.10 are listed in Tab. 6.4 in the PVC column using these input parameters, the PSDs were determined for all particle volume fractions analysed. A representation of the data and the data fit for determining intrinsic particle absorption can be found in the supporting information in Fig. 6.24. Fig. 6.10 shows the d_{50} values and the range of the PSD using the averaged input parameters as a function of the particle volume fraction. Tab. 6.6 summarizes the averaged d_{50} and span values and compares them with the reference method.

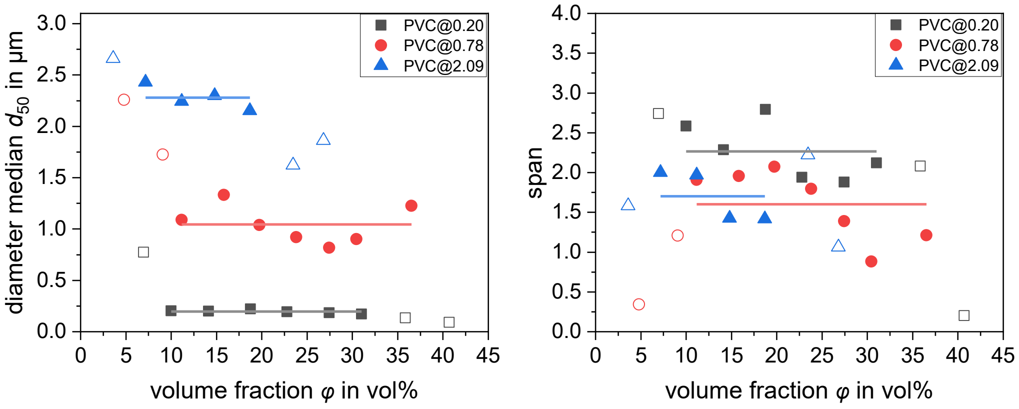

Fig. 6.10: The d_{50} particle diameter and particle distribution span at different particle volume fractions of different PVC dispersions calculation is based on the mean thermophysical parameters and intrinsic particle absorption of all PVC samples in this study. The displayed lines correspond to the mean values. Unfilled data points were not taken into account when calculating the mean value.

As shown in Fig. 6.10, the use of averaged input parameters for the PVC@0.20 sample resulted in very consistent d_{50} values between approximately 10 and 31 vol%, averaging 0.195 µm (see Tab. 6.6). Compared to measurements with individual input data, the d_{50} values are slightly lower and more constant over a limited concentration range. In terms of span, which has a mean value of 2.267, the pronounced downward trend with increasing particle concentration is no longer observed, and the span is significantly larger than that in the DLS reference PSD measurement (0.911).

For the PVC@0.70 sample, the d_{50} values are very constant between 11 and 37 vol%. However, the averaged d_{50} values of 1.046 µm are generally higher than those obtained with non-averaged input parameters, where the value was 0.898 µm. This results in a significant deviation from the d_{50} values of the LDS measurements, where the average d_{50} value was 0.783 µm. The span, averaging 1.601, is similar to that of the PVC@0.20 sample, but the use of averaged input parameters results in a less pronounced downward trend and more uniform span values overall (standard deviation = 0.446). Here, the span is also larger than in the LDS reference measurement (1.195), though the effect is less pronounced than with the PVC@0.20 sample.

The smallest changes in the PSD due to the use of averaged input parameters were observed in the PVC@2.09 sample. The d_{50} values are quite consistent between 7 and 19 vol%, averaging 2.281 µm, which is only slightly lower than without standardized input parameters (2.388 µm). The span has an average value of 1.703, also slightly lower than the measurement without averaged input parameters. Because the d_{50} and span values are slightly smaller, the overall results are somewhat closer to those of the LDS reference measurements (refer to Tab. 6.6). This is initially surprising but is likely due to the fact that the values were not averaged over the entire analysed range.

Tab. 6.7: Volume weighted particle size distribution data of PVC when average values of thermophysical parameters are used

sample	d_{50}^{AAS} [µm]	span^{AAS}	d_{50}^{REF} [µm]	span^{REF}
PVC@0.20*	0.195±0.017	2.267±0.363	0.202±0.006	0.911±0.068
PVC@0.78*	1.046±0.184	1.601±0.446	0.783±0.040	1.195±0.290
PVC@2.09*	2.281±0.116	1.703±0.325	2.086±0.053	1.529±0.162

The consistent d_{50} values indicate that even with averaged input parameters, the median particle diameter for PVC can be sufficiently determined over a wide range of particle concentrations. Although these values sometimes deviate from the reference measurements, the deviations are within an acceptable range expected when comparing different particle measurement methods [17,42,45,47,50]. While the use of averaged input parameters resulted in somewhat more uniform span values, there is still significant fluctuation across different particle concentrations. Altogether, the method presented in this paper is not suitable to determine precise PSD, however it is suitable for approximate PSD of concentrated polymer latices over a broad range of concentration. This level of accuracy is more than sufficient for many practical applications, such as quality control in polymerization [43,54] and milling [50,55] processes, or monitoring the stability [56] of colloidal suspensions. However, this approach is only successful if the material has similar intrinsic attenuations. For example, the PTFE samples examined in this study would not be suitable for this approach due to the significant differences in intrinsic attenuation (see Fig. 6.2).

6.5 Conclusion

This study investigates the crucial role of intrinsic particle absorption in determining the particle size distribution (PSD) of polymer latex dispersions using acoustic attenuation spectroscopy (AAS). Historically, challenges in determining intrinsic absorption have hindered research in this field, especially for concentrated polymer latex dispersions where conventional methods like dynamic light scattering (DLS) and laser diffraction spectroscopy (LDS) are ineffective. Our new approach to determine intrinsic absorption for various aqueous latex systems, provides significant insights and advances in this area.

At the core of our approach is the coupled phase model developed by Dukhin and Goetz, which accounts for viscoinertial, thermal and scattering losses in the attenuation spectrum. This model requires a comprehensive set of thermophysical parameters, which we obtained through direct measurements and literature review. Key parameters such as density, thermal expansion coefficient, heat capacity and sound velocity were measured for each sample, whereas intrinsic absorption was inferred indirectly by difference from the measured and calculated spectra (see Eq. 6.7), resulting in a significant improvement in the accuracy of the determined PSD.

Our results highlight the substantial impact of intrinsic absorption on the total attenuation spectrum. The analysis of different polymer latexes (PVC, PTFE, SBR, PU) demonstrated that intrinsic absorption strongly depends on the material. While some systems showed increasing frequency-dependent attenuation, others remained almost constant over a wide range. This underlines that intrinsic absorption is a material-specific property and must be determined individually for reliable modelling.

Incorporating intrinsic absorption into the model significantly improved the accuracy of PSD determination. This was particularly evident when comparing the AAS results to those obtained using reference methods. For instance, the polyurethane (PU) sample showed remarkable consistency between the AAS and DLS results, where both approaches yielded nearly identical median diameters and span values. This consistency validates our methodology and underscores the importance of accounting for intrinsic absorption.

It should be noted that, even with our approach, accurately determining the PSD span remains challenging. Most of our samples showed high variability in span values for different particle volume fractions. This indicates that while the AAS method is suitable for determining mean particle size (d_{50}), but further improvements are necessary to accurately capture the distribution width or span. Discrepancies were observed in the PVC@0.20 sample, where the measured attenuation was significantly higher than the model predictions at lower frequencies. This suggests that additional attenuation mechanisms, such as intrinsic relaxation phenomena or hindered movements of polymer chains, may contribute. Such complexities highlight the need for further refinement in modelling techniques and parameter acquisition.

Consequently, although our approach does not yield high resolution of the PSDs, it provides sufficiently robust particle size estimates to support practical applications where approximate distributions are acceptable, such as in process control, material processing or stability evaluation.

6.6 Supporting Information

6.6.1 Thermal Expansion

This section includes illustrations of the results used to determine the coefficient of thermal expansion. As described in the main text, the thermal expansion coefficient of the polymer particles was determined by measuring the particle density at three different temperatures (20 °C, 25 °C and 30 °C). Each measurement was repeated three times to ensure accuracy. The coefficient was calculated by analysing the slope of the density change with temperature, which is documented in Tab. 6.8.

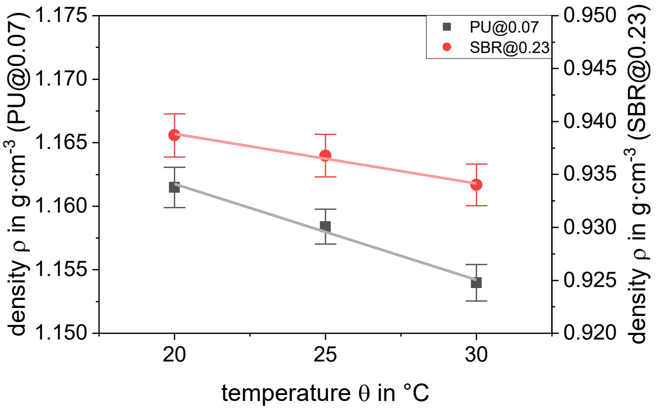

Fig. 6.11: Measured particle density at 20 °C, 25 °C and 30 °C of PU@0.07 and SBR@0.23 latices. The lines correspond to linear curve fits.

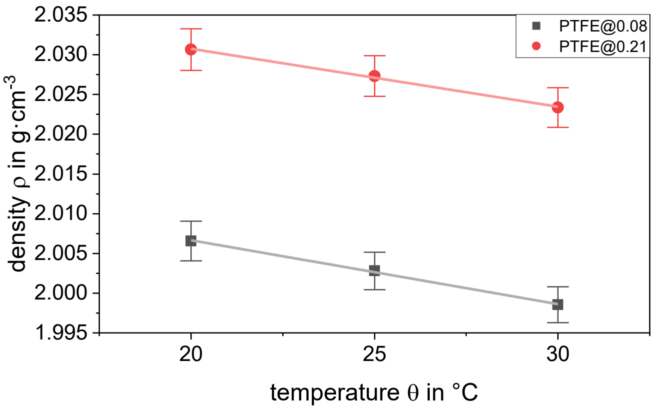

Fig. 6.12: Measured particle density at 20 °C, 25 °C, and 30 °C for different sized PTFE latices (PTFE@0.08, PTFE@0.21). The lines correspond to linear curve fits.

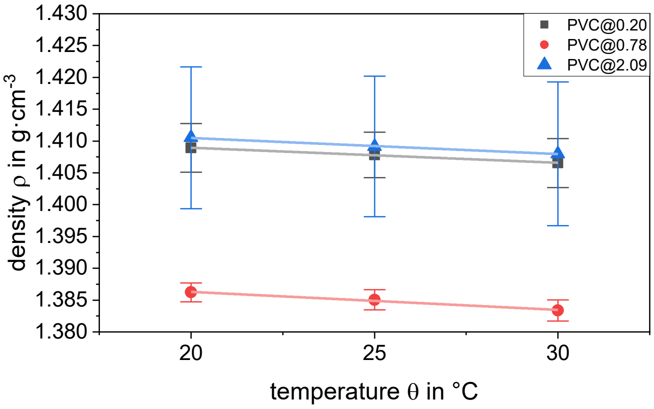

Fig. 6.13: Measured particle density at 20 °C, 25 °C, and 30 °C for different sized PVC latices (PVC@0.20, PVC@0.78, PVC@2.09). The lines correspond to linear curve fits. The considerable higher measurement fluctuation observed for the PVC@2.09 dispersion is attributed to its comparatively low particle volume fraction.

Tab. 6.8: Analysed slope of the density change with temperature for the different, including the corresponding coefficient of determination R^2 values.

sample	$\left(\frac{\partial \rho_\mathrm{p}}{\partial T}\right)_P$ [mg·cm^{-3}·K^{-1}]	R^2
PU@0.07	-0.7503	0.9895
SBR@0.23	-0.4678	0.9893
PTFE@0.08	-0.8021	0.9987
PTFE@0.21	-0.7283	0.9974
PVC@0.20	-0.2367	0.9985
PVC@0.78	-0.2849	0.9886
PVC@2.09	-0.2526	0.9974

6.6.2 Heat Capacity

This section includes illustrations of the measured heat capacity of the polymer dispersions between -30 °C and 130 °C. The measurements were conducted in two heating and cooling cycles. The figures presented here show the results from the second heating cycle.

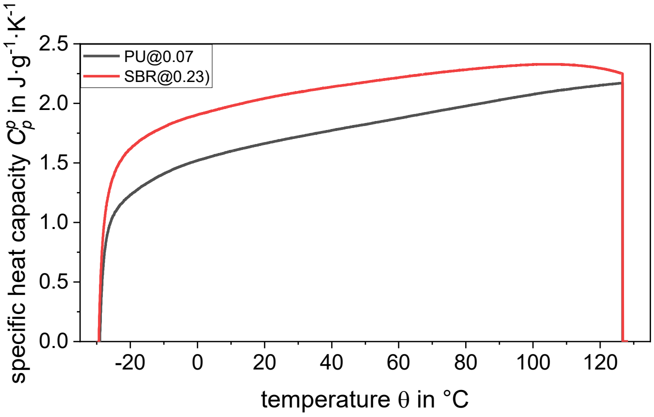

Fig. 6.14: Measured heat capacity between -30 °C and 130 °C of PU@0.07 and SBR@0.23 latices determined with DSC.

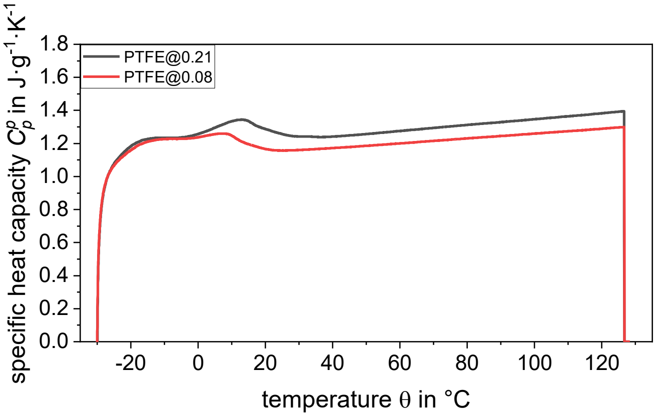

Fig. 6.15: Measured heat capacity between -30 °C and 130 °C for different sized PTFE latices (PTFE@0.08, PTFE@0.21) determined with DSC.

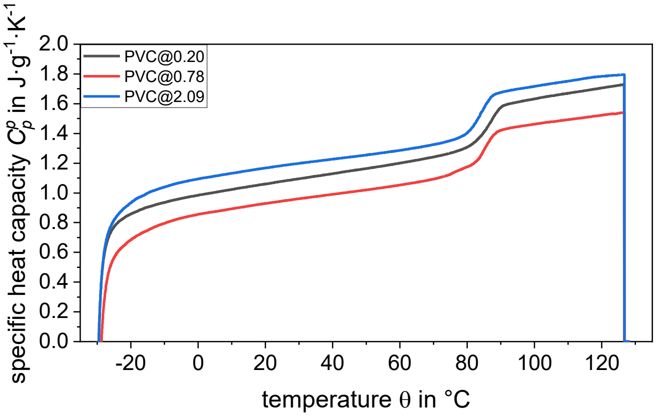

Fig. 6.16: Measured heat capacity between -30 °C and 130 °C for different sized PVC latices (PVC@0.20, PVC@0.78, PVC@2.09) determined with DSC.

6.6.3 Particle Sound Velocity

The sound velocity of the polymer particles was estimated through regression analysis of the measured sound velocities of the suspensions at various particle volume fractions. The Wood equation was used to interpret these measurements, taking into account the sound velocity of water as the dispersion medium.

Tab. 6.9: critical volume fraction φ_{cr}

sample	φ_{cr}[vol%]
PBAMM@0.10	33.83
PU@0.07	20.35
SBR@0.23	34.81
PVC@0.20	35.55
PVC@0.78	48.84
PVC@2.09	49.15
PTFE@0.08	41.04
PTFE@0.21	35.55

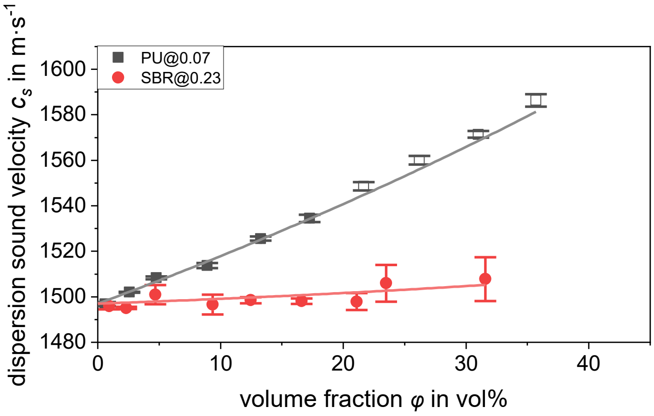

Fig. 6.17: Sound velocities of PU@0.07 and SBR@0.23 dispersions shown as functions of particle volume fraction. The data points represent experimentally measured values, while the solid lines correspond to fits using the Wood equation (Eq. 6.13). Unfilled data points were excluded from the fit calculations.

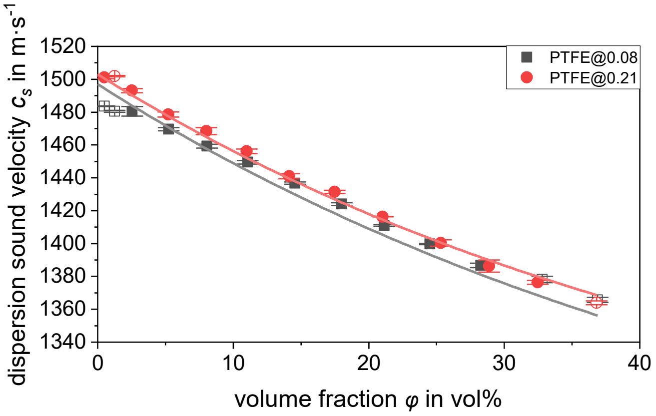

Fig. 6.18: Sound velocities of PTFE dispersions (PTFE@0.08, PTFE@0.21) shown as functions of particle volume fraction. The data points represent experimentally measured values, while the solid lines correspond to fits using the Wood equation (Eq. 6.13). Unfilled data points were excluded from the fit calculations.

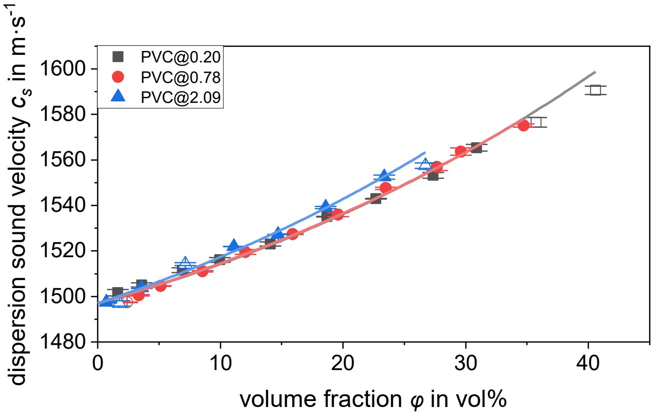

Fig. 6.19: Sound velocities of PVC dispersions (PVC@0.20, PVC@0.78, PVC@2.09) shown as functions of particle volume fraction. The data points represent experimentally measured values, while the solid lines correspond to fits using the Wood equation (Eq. 6.13). Unfilled data points were excluded from the fit calculations.

6.6.4 Thermophysical Parameters

This section presents the literature values of the thermophysical parameters for the polymer particles analysed in this study. The parameters include density ρ_p, specific heat capacity c_p^p, thermal expansion coefficient β_p, and sound velocity c_p .

Tab. 6.10: Literature values for thermophysical parameters: density ρ_p, specific heat capacity C_p^p, thermal expansion coefficient β_p and sound velocity c_p for various particles.

sample	ρ_p [g·cm^{-3}]	C_p^p [J·g^{-1}·K^{-1}]	β_p [·10^{-4}·K^{-1}]	c_p [m·s^{-1}]
PU	1.21 [40]	1.76 [57]	3-4.5 [58]	1815 [40]
SBR	0.94 [40]	1.874 [27]	6.1 [59]	1552 [31]
PTFE	2.13-2.23 [57]	1.0 [57]	3.3-5.4 [57]	1350 [40]
PVC	1.38-1.40 [57]	0.85-0.9 [57]	1.8 [60]	2180-2260 [40]

6.6.5 Various Loss Mechanisms

This section presents the various loss mechanisms observed in the attenuation spectrum, including intrinsic absorption, viscoinertial, thermal, and scattering losses for all samples that were not shown in the main paper. The samples included here are SBR@0.23, PTFE@0.08, PTFE@0.21, and PVC@0.78.

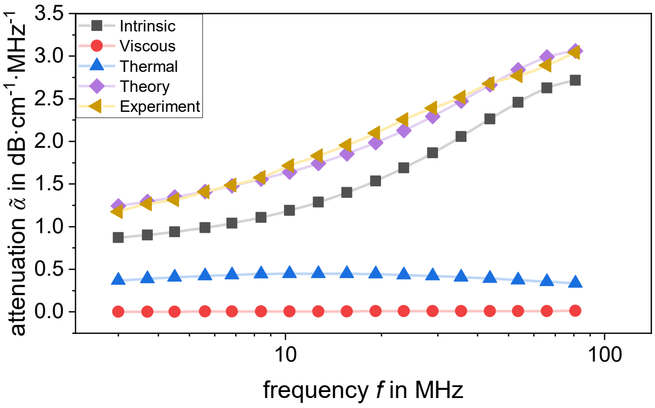

Fig. 6.20: Presentation of the attenuation spectrum of the SBR@0.23 sample with a particle volume fraction of 19.8 vol%. Plot includes the contributions from different attenuation mechanisms: intrinsic absorption α_{int} (Intrinsic), viscoinertial α_{vis} (Viscous) and thermal α_{th} (Thermal) losses. The sum of these mechanisms is labeled as Theory and the experimentally measured spectrum is labeled as Experiment.

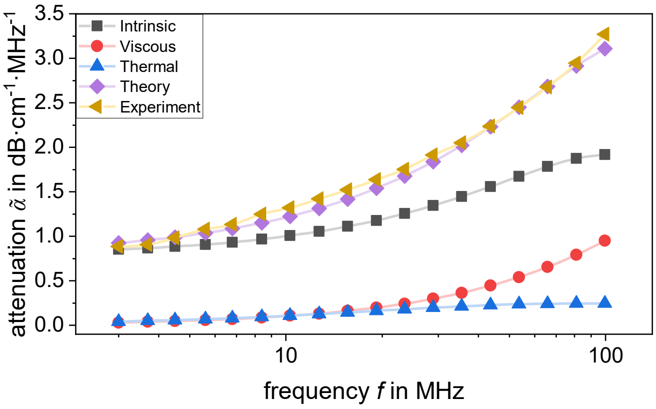

Fig. 6.21: Presentation of the attenuation spectrum of the PTFE@0.08 sample with a particle volume fraction of 21.1 vol%. Plot includes the contributions from different attenuation mechanisms: intrinsic absorption α_{int} (Intrinsic), viscoinertial α_{vis} (Viscous) and thermal α_{th} (Thermal) losses. The sum of these mechanisms is labeled as Theory and the experimentally measured spectrum is labeled as Experiment.

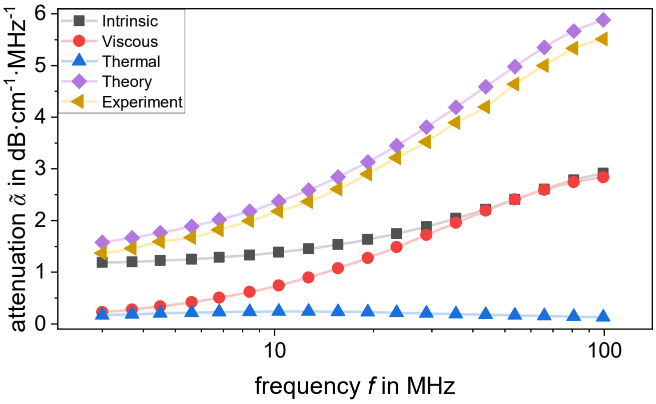

Fig. 6.22: Presentation of the attenuation spectrum of the PTFE@0.21 sample with a particle volume fraction of 20.9 vol%. Plot includes the contributions from different attenuation mechanisms: intrinsic absorption α_{int} (Intrinsic), viscoinertial α_{vis} (Viscous) and thermal α_{th} (Thermal) losses. The sum of these mechanisms is labeled as Theory and the experimentally measured spectrum is labeled as Experiment.

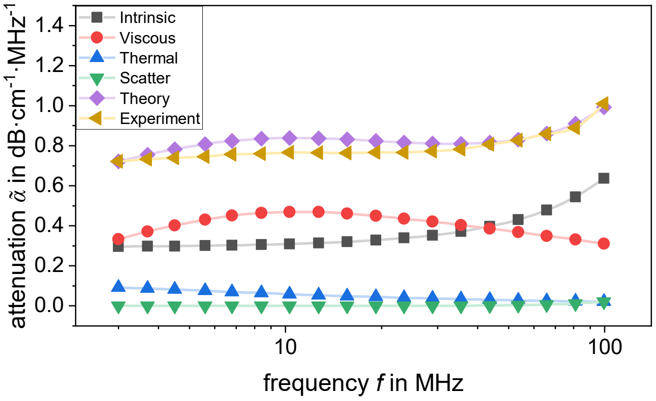

Fig. 6.23: Presentation of the attenuation spectrum of the PVC@0.78 sample with a particle volume fraction of 19.9 vol%. Plot includes the contributions from different attenuation mechanisms: intrinsic absorption α_{int} (Intrinsic), viscoinertial α_{vis} (Viscous) thermal α_{th} (Thermal) and scattering α_{sc} (Scatter) losses. The sum of these mechanisms is labelled as Theory and the experimentally measured spectrum is labelled as Experiment.

6.6.6 Averaged Intrinsic Absorption of PVC

This section provides a presentation of the single measuring points which were used to fit the averaged intrinsic absorption parameters for polyvinyl chloride (PVC) sample with a second-order polynomial function. More details about the fitted parameters can be found in Tab. 6.4 in the main article.

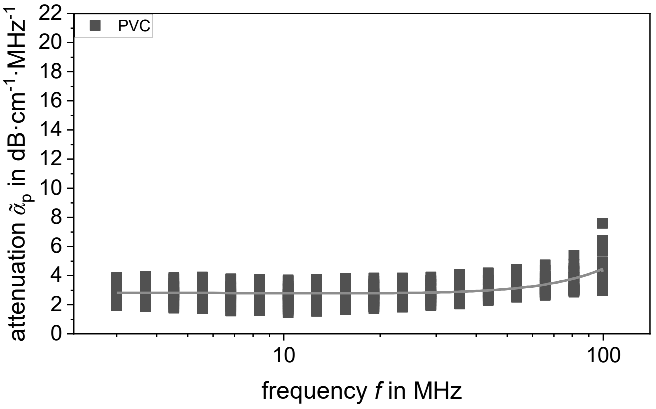

Fig. 6.24: Averaged intrinsic particle absorption for different sized PVC latices (PVC@0.20, PVC@0.78, PVC@2.09). The lines correspond to a second order polynomial fit. More details about the fitted parameters can be found in Tab. 6.4 in the main article.

Acknowledgments

This project has received fundings by the German Ministry of Education and Research (BMBF) as part of the funding program “Forschung an Fachhochschulen” under contract number13FH142PX6. We are also very grateful for valuable discussions and financial and material support provided by Westlake Vinnolit GmbH &Co. KG. Furthermore, we would like to thank A. S. Dukhin of Dispersion Technology Inc., Bedford Hills, NY, USA for fruitful discussions.

6.7 References

[1] Dukhin, A. S.; Goetz, P. J. *Characterization of Liquids, Dispersions, Emulsions, and Porous Materials Using Ultrasound*, Third edition; Elsevier: Amsterdam, Oxford, Cambridge, MA, 2017.

[2] McClements, D. J. Ultrasonic Measurements in Particle Size Analysis. In *Encyclopedia of analytical chemistry: Applications, theory and instrumentation*; Meyers, R. A., Ed.; Wiley: New York, 2000.

[3] Silva, C. A.; Saraiva, S. V.; Bonetti, D.; Higuti, R. T.; Cunha, R. L.; Pereira, L. O.; Silva, F. V.; Fileti, A. M. Application of acoustic models for polydisperse emulsion characterization using ultrasonic spectroscopy in the long wavelength regime. *Colloids Surf., A* **2020**, *602*, 125062. DOI: 10.1016/j.colsurfa.2020.125062.

[4] Dukhin, A. S.; Goetz, P. J. Acoustic Spectroscopy for Concentrated Polydisperse Colloids with High Density Contrast. *Langmuir* **1996**, *12*, 4987–4997. DOI: 10.1021/la951085y.

[5] Dukhin, A. S.; Goetz, P. J.; Hamlet, C. W. Acoustic Spectroscopy for Concentrated Polydisperse Colloids with Low Density Contrast. *Langmuir* **1996**, *12*, 4998–5003. DOI: 10.1021/la951572d.

[6] Babick, F.; Hinze, F.; Stintz, M.; Ripperger, S. Ultrasonic Spectrometry for Particle Size Analysis in Dense Submicron Suspensions. *Part. Part. Syst. Charact.* **1998**, *15*, 230–236. DOI: 10.1002/(SICI)1521-4117(199810)15:5<230:AID-PPSC230>3.0.CO;2-D.

[7] Hayashi, T.; Ohya, H.; Suzuki, S.; Endoh, S. Errors in Size Distribution Measurement of Concentrated Alumina Slurry by Ultrasonic Attenuation Spectroscopy. *J. Soc. Powder Technolo, Japan* **2000**, *37*, 498–504. DOI: 10.4164/sptj.37.498.

[8] Dukhin, A. S.; Goetz, P. J.; Travers, B. Use of ultrasound for characterizing dairy products. *Journal of dairy science* **2005**, *88*, 1320–1334. DOI: 10.3168/jds.S0022-0302(05)72798-3.

[9] Allegra, J. R.; Hawley, S. A. Attenuation of Sound in Suspensions and Emulsions: Theory and Experiments. *The Journal of the Acoustical Society of America* **1972**, *51*, 1545–1564. DOI: 10.1121/1.1912999.

[10] McClements, D. J. Ultrasonic determination of depletion flocculation in oil-in-water emulsions containing a non-ionic surfactant. *A collection of invited papers by Japanese researchers* **1994**, *90*, 25–35. DOI: 10.1016/0927-7757(94)02881-8.

[11] International Organization for Standardization. *Measurement and characterization of particles by acoustic methods - Part 2: Guidelines for linear theory*, 2022, *19.120* (ISO 20998-2:2022-08).

[12] Ono, K. A Comprehensive Report on Ultrasonic Attenuation of Engineering Materials, Including Metals, Ceramics, Polymers, Fiber-Reinforced Composites, Wood, and Rocks. *Applied Sciences* **2020**, *10*, 2230. DOI: 10.3390/app10072230.

[13] Jarzynski, J.; Balizer, E.; Fedderly, J. J.; Lee, G. Acoustic Properties. In *Encyclopedia of polymer science and technology,* 4th edition; Mark, H. F., Ed.; Wiley-Blackwell: Chichester, 2014.

[14] Sinha, M.; Buckley, D. J. Acoustic Properties of Polymers. In *Physical Properties of Polymers Handbook*; Mark, J. E., Ed.; Springer New York: New York, NY, 2007; pp 1021–1031.

[15] Biwa, S. Independent scattering and wave attenuation in viscoelastic composites. *Mechanics of Materials* **2001**, *33*, 635–647. DOI: 10.1016/S0167-6636(01)00080-1.

[16] Kinra, V. K.; Petraitis, M. S.; Datta, S. K. Ultrasonic wave propagation in a random particulate composite. *International Journal of Solids and Structures* **1980**, *16*, 301–312. DOI: 10.1016/0020-7683(80)90083-9.

[17] Adjadj, L. P.; Storti, G.; Morbidelli, M. Ultrasound Attenuation in Polystyrene Latexes. *Langmuir* **2003**, *19*, 3953–3957. DOI: 10.1021/la026893l.

[18] Bloomfield, P. E.; Lo, W. J.; Lewin, P. A. Experimental study of the acoustical properties of polymers utilized to construct PVDF ultrasonic transducers and the acousto-electric properties of PVDF and P(VDF/TrFE) films. *IEEE transactions on ultrasonics, ferroelectrics, and frequency control* **2000**, *47*, 1397–1405. DOI: 10.1109/58.883528.

[19] Zellouf, D.; Jayet, Y.; Saint-Pierre, N.; Tatibouët, J.; Baboux, J. C. Ultrasonic spectroscopy in polymeric materials. Application of the Kramers–Kronig relations. *Journal of Applied Physics* **1996**, *80*, 2728–2732. DOI: 10.1063/1.363190.

[20] Dukhin, A. S.; Goetz, P. J. Characterization of Concentrated Dispersions with Several Dispersed Phases by Means of Acoustic Spectroscopy. *Langmuir* **2000**, *16*, 7597–7604. DOI: 10.1021/la991600i.

[21] Wood, A. B. *A Textbook of Sound: Being an account of the Physics of Vibrations with special reference to recent theoretical and technical developments*; Bell and Sons: London, 1941.

[22] Bauer, J.; Gutke, M.; Heinrich, F.; Edling, M.; Stoycheva, V.; Kaltenbach, A.; Burkhardt, M.; Gruenefeld, M.; Gamp, M.; Gerhard, C.*; et al.* Novel UV-transparent 2-component polyurethane resin for chip-on-board LED micro lenses. *Opt. Mater. Express* **2020**, *10*, 2085. DOI: 10.1364/OME.393844.

[23] Khan, H. U.; Gupta, V. K.; Yamin, M. Specific Refractive Index Increments of Polybutadiene, Styrene-Butadiene Rubber, Crepe Rubber, Polystyrene, Polymethyl Methacrylate, and Styrene-Methyl Methacrylate in Various Solvents and Variation of Refractive Index Increment with Molecular Weight. *Journal of Macromolecular Science: Part A - Chemistry* **1983**, *20*, 503–513. DOI: 10.1080/00222338308060797.

[24] French, R. H.; Rodriguez-Parada, J. M.; Yang, M. K.; Derryberry, R. A.; Lemon, M. F.; Brown, M. J.; Haeger, C. R.; Samuels, S. L.; Romano, E. C.; Richardson, R. E. Optical properties of materials for concentrator photovoltaic systems. In *2009 34th IEEE Photovoltaic Specialists Conference (PVSC)*; IEEE, 2009; pp 394–399.

[25] Zhang, X.; Qiu, J.; Li, X.; Zhao, J.; Liu, L. Complex refractive indices measurements of polymers in visible and near-infrared bands. *Applied optics* **2020**, *59*, 2337–2344. DOI: 10.1364/AO.383831.

[26] Nielsen, L.; Ebert, H.-P.; Hemberger, F.; Fricke, J.; Biedermann, A.; Reichelt, M.; Rotermund, U. Thermal conductivity of nonporous polyurethane. *High Temp.-High Press.* **2000**, *32*, 701–707. DOI: 10.1068/htwu69.

[27] Bhowmick, T.; Pattanayak, S. Thermal conductivity, heat capacity and diffusivity of rubbers from 60 to 300 K. *Cryogenics* **1990**, *30*, 116–121. DOI: 10.1016/0011-2275(90)90256-C.

[28] Boudenne, A.; Ibos, L.; Gehin, E.; Candau, Y. A simultaneous characterization of thermal conductivity and diffusivity of polymer materials by a periodic method. *J. Phys. D: Appl. Phys.* **2004**, *37*, 132–139. DOI: 10.1088/0022-3727/37/1/022.

[29] Sheldon, R. P.; Lane, S. K. Thermal conductivities of polymers I—Polyvinyl chloride. *Polymer* **1965**, *6*, 77–83. DOI: 10.1016/0032-3861(65)90009-1.

[30] Babick, F.; Hinze, F.; Ripperger, S. Dependence of ultrasonic attenuation on the material properties. *Colloids Surf., A* **2000**, *172*, 33–46. DOI: 10.1016/S0927-7757(00)00571-9.

[31] Cao, R.; Deng, L.; Feng, Z.; Zhao, X.; Li, X.; Zhang, L. Preparation of natural bio-based Eucommia ulmoides gum/styrene-butadiene rubber composites and the evaluation of their damping and sound absorption properties. *Collected papers from PDM 2004. Polymers in Dispersed Media - Colloids: from Preparation to Application* **2021**, *213*, 123292. DOI: 10.1016/j.polymer.2020.123292.

[32] Sarkar, M. de; De, P. P.; Bhowmick, A. K. New polymeric blends from hydrogenated styrene–butadiene rubber and polyethylene. *Collected papers from PDM 2004. Polymers in Dispersed Media - Colloids: from Preparation to Application* **1998**, *39*, 6789–6800. DOI: 10.1016/S0032-3861(98)00171-2.

[33] Ngai, K. L.; Plazek, D. J. The Viscoelastic Behavior of Rubber. *Science and technology of rubber,* 3rd ed.; Elsevier Academic Press: Amsterdam, Boston, 2005; pp 183–236.

[34] Wada, Y.; Ito, R.; Ochiai, H. Comparison Between Mechanical Relaxations Associated with Volume and shear Deformations in Styrene-Butadiene Rubber. *J. Phys. Soc. Jpn.* **1962**, *17*, 213–218. DOI: 10.1143/jpsj.17.213.

[35] Faghihi, F.; Mohammadi, N.; Haghgoo, M. The effects of rigid polystyrene particles on the glass transition characteristics and mechanical wave attenuation of styrene-butadiene rubber: Particle size and acoustic mismatch. *J. Polym. Sci. B Polym. Phys.* **2010**, *48*, 82–88. DOI: 10.1002/polb.21846.

[36] Ebnesajjad, S. *Fluoroplastics, Volume 1, Non-melt processible fluoropolymers*, 2nd edition (Online-ausg.); William Andrew: Waltham, MA, 2015.

[37] Hung, B. N.; Goldstein, A. Acoustic Parameters of Commercial Plastics. *IEEE Trans. Son. Ultrason.* **1983**, *30*, 249–254. DOI: 10.1109/T-SU.1983.31415.

[38] Pouet, B. F.; Rasolofosaon, N. J. P. Measurement of broadband intrinsic ultrasonic attenuation and dispersion in solids with laser techniques. *J. Acoust. Soc. Am.* **1993**, *93*, 1286–1292. DOI: 10.1121/1.405413.

[39] Wypych, G. *Handbook of polymers*; ChemTec Publ: Toronto, 2012.

[40] Deutsch, V.; Platte, M.; Vogt, M. *Ultraschallprüfung: Grundlagen und industrielle Anwendungen*; Springer: Berlin, Heidelberg, 1997.

[41] Holmes, A. K.; Challis, R. E.; Wedlock, D. J. A Wide Bandwidth Study of Ultrasound Velocity and Attenuation in Suspensions: Comparison of Theory with Experimental Measurements. *J. Colloid Interface Sci.* **1993**, *156*, 261–268. DOI: 10.1006/jcis.1993.1109.

[42] Hipp, A. K.; Storti, G.; Morbidelli, M. Particle Sizing in Colloidal Dispersions by Ultrasound. Model Calibration and Sensitivity Analysis. *Langmuir* **1999**, *15*, 2338–2345. DOI: 10.1021/la981046x.

[43] Storti, G.; Hipp, A. K.; Morbidelli, M. Monitoring Latex Reactors by Ultrasonics. *Polym React Eng* **2000**, *8*, 77–94. DOI: 10.1080/10543414.2000.10744539.

[44] Holmes, A. K.; Challis, R. E.; Wedlock, D. J. A Wide Bandwidth Study of Ultrasound Velocity and Attenuation in Suspensions: Comparison of Theory with Experimental Measurements. *J. Colloid Interface Sci.* **1993**, *156*, 261–268. DOI: 10.1006/jcis.1993.1109.

[45] Kaatze, U.; Trachimow, C.; Pottel, R.; Brai, M. Broadband study of the scattering of ultrasound by polystyrene-latex-in-water suspensions. *Annalen der Physik* **1996**, *508*, 13–33. DOI: 10.1002/andp.2065080104.

[46] Dukhin, A. S.; Goetz, P. J. Acoustic and electroacoustic spectroscopy for characterizing concentrated dispersions and emulsions. *Adv. Colloid Interface Sci.* **2001**, *92*, 73–132. DOI: 10.1016/S0001-8686(00)00035-X.

[47] Dukhin, A. S. Acoustic spectroscopy for particle size measurement of concentrated nanodispersions. *Characterization of Nanoparticles*; Elsevier, 2020; pp 197–211.

[48] Ocepek, M.; Soucek, M. D.; Berce, P.; Meng, L. Comparison of Particle Size Techniques to Investigate Secondary Nucleation in HEMA-Rich Latexes. *Macromol. Chem. Phys.* **2015**, *216*, 400–416. DOI: 10.1002/macp.201400476.

[49] Aichele, C. P.; Venkataramani, D.; Smay, J. E.; McCann, M. H.; Richter, S.; Khanzadeh-Moradllo, M.; Aboustait, M.; Ley, M. T. A comparison of automated scanning electron microscopy (ASEM) and acoustic attenuation spectroscopy (AAS) instruments for particle sizing. *Colloids Surf., A* **2015**, *479*, 46–51. DOI: 10.1016/j.colsurfa.2015.03.052.

[50] Mende, S.; Stenger, F.; Peukert, W.; Schwedes, J. Mechanical production and stabilization of submicron particles in stirred media mills. *Powder Technology* **2003**, *132*, 64–73. DOI: 10.1016/S0032-5910(03)00042-1.

[51] Babick, F.; Richter, A. Sound attenuation by small spheroidal particles due to visco-inertial coupling. *The Journal of the Acoustical Society of America* **2006**, *119*, 1441–1448. DOI: 10.1121/1.2168427.

[52] Hipp, A. K.; Storti, G.; Morbidelli, M. Acoustic Characterization of Concentrated Suspensions and Emulsions. 2. Experimental Validation. *Langmuir* **2002**, *18*, 405–412. DOI: 10.1021/la015541w.

[53] Epstein, P. S.; Carhart, R. R. The Absorption of Sound in Suspensions and Emulsions. I. Water Fog in Air. *The Journal of the Acoustical Society of America* **1953**, *25*, 553–565. DOI: 10.1121/1.1907107.

[54] Boscher, V.; Helleboid, R.; Lasuye, T.; Stasik, B.; Riess, G. On-line acoustic attenuation spectroscopy of emulsions stabilized by vinyl alcohol–vinyl acetate copolymers: a model system for the suspension polymerization of vinyl chloride. *Polymer International* **2009**, *58*, 1209–1216. DOI: 10.1002/pi.2656.

[55] Stenger, F.; Mende, S.; Schwedes, J.; Peukert, W. Nanomilling in stirred media mills. *Chemical Engineering Science* **2005**, *60*, 4557–4565. DOI: 10.1016/j.ces.2005.02.057.

[56] Dukhin, A. S.; Goetz, P. J. Characterization of aggregation phenomena by means of acoustic and electroacoustic spectroscopy. *Colloids Surf., A* **1998**, *144*, 49–58. DOI: 10.1016/S0927-7757(98)00565-2.

[57] Lechner, M. D. Polymers. In *Springer Handbook of Materials Data*; Warlimont, Ed.; Springer: [Place of publication not identified], 2018; pp 489–540.

[58] Kia, H. G. Thermal expansion of polyurethane reinforced with continuous glass fibers. *Polymer Composites* **1988**, *9*, 237–241. DOI: 10.1002/pc.750090311.

[59] Salgueiro, W.; Somoza, A.; Silva, L.; Consolati, G.; Quasso, F.; Mansilla, M. A.; Marzocca, A. J. Temperature dependence on free volume in cured natural rubber and styrene-butadiene rubber blends. *Physical review. E, Statistical, nonlinear, and soft matter physics* **2011**, *83*, 51805. DOI: 10.1103/PhysRevE.83.051805.

[60] Haynes, W. M., Ed. *CRC handbook of chemistry and physics: A ready-reference book of chemical and physical data*, 97th edition; CRC Press: Boca Raton, London, New York, 2017.

7 Novel Approach for the Determination of the Critical Coagulation Concentration in Concentrated Dispersions

Matthias Frangenberg[a,b], Annette M. Schmidt[b], Jan Wilkens[a,*]

[a] Faculty of Applied Natural Sciences, TH Köln – University of Applied Sciences, Cologne, Germany

[b] Department of Chemistry, Institute of Physical Chemistry, University of Cologne, Cologne, Germany

* E-Mail: jan.wilkens@th-koeln.de; Phone: +49 214-32831-4614; Address: Campusplatz 1, 51379 Leverkusen, Germany

Abstract

This study examines colloidal stability of polyvinyl chloride (PVC) dispersions using acoustic attenuation, a sensitive, non-optical technique ideal for analysing concentrated dispersions. We investigated how surfactant type and coverage affect the critical coagulation concentration (CCC) of two PVC dispersions, differing in particle size and polymerization method. The smaller-particle dispersion, produced via emulsion polymerization, was stabilized with sodium dodecyl sulphate (SDS), while the larger-particle dispersion, synthesized through microsuspension polymerization, used a combination of SDS and linear alkylbenzene sulfonate (LAS). Results demonstrate that increased surfactant coverage elevates CCC, attributed to enhanced electrostatic repulsion between particles. Moreover, it was found that LAS-SDS mixture offers greater stability than SDS alone. These insights highlight acoustic attenuation's effectiveness for assessing stability in opaque, concentrated dispersions and offer guidance for optimizing colloidal formulations across various applications.

7.1 Introduction

The stability of colloidal systems is a cornerstone of numerous applications across a broad spectrum of industries, including pharmaceuticals [1], environmental technologies [2], food production [3,4], and materials science [5]. Colloids, by their nature, present a complex interplay of forces that govern their stability and behaviour in suspension. Understanding and controlling these forces is critical, particularly in processes involving the formulation and stabilization of emulsions, suspensions, and foams. A very useful parameter in assessing colloidal stability is the critical coagulation concentration (CCC), which defines the threshold concentration of electrolytes needed to induce rapid coagulation or flocculation by overcoming the electrostatic repulsion between particles.

Traditionally, the CCC is studied using a variety of optical methods such as dynamic light scattering [6], different ways of photometric monitoring [7–11], ultramicroscopy [12] or direct observation by a test-tube test (also called Jar Test) [13]. These methods involve measuring the intensity of light scattered or absorbed by particles in the dispersion to monitor aggregation and stability. Ultramicroscopy, in particular, allows for the direct observation of particle motion and aggregation, providing visual evidence of coagulation. However, these methods are limited by their sensitivity in opaque or highly concentrated systems, where light cannot penetrate effectively. Additionally, photometric monitoring techniques can be constrained by particle size; for instance, determining the CCC through turbidity measurements is effective only when particle sizes are smaller than the wavelength of light used in the analysis [14].

To overcome these limitations, non-optical methods have also been employed to determine the CCC. Direct force measurements using techniques like atomic force microscopy (AFM) provide quantitative data on the interactions between particles [15]. By measuring the forces between macroscopic surfaces or individual particles, researchers can infer the conditions that lead to coagulation [16]. However, AFM has several limitations, including sensitivity to environmental conditions, potential artifacts from tip-sample interactions, challenges in achieving reproducibility due to variations in sample preparation and calibration and the limitation that it typically analyses only monolayers or very thin films, which may not represent bulk properties. The capillary suction time (CST) is a technique that measures the migration speed of a dispersion medium in filter paper capillaries to identify the CCC [9,17]. This method provides a quantitative assessment by tracking how coagulation dynamics influence physical properties such as viscosity, hydrostatic pressure and capillary pressure. However, CST can be influenced by the heterogeneity of the dispersion medium and the properties of the filter paper, which may lead to varying results. An excellent overview of methods for analysing aggregation phenomena is provided in [14].

Acoustic attenuation measurement has proven to be an effective non-optical technique for probing dispersions non-invasively and deriving detailed insights into particle interactions [18]. This method quantifies the decrease in amplitude of ultrasonic acoustic waves as they pass through a medium. Changes in the concentration, size, and density of the particles, as well as their interaction energies, significantly affect the measured attenuation of a dispersion. As particles coagulate, the increased size and changed structural configuration of the aggregates alter the acoustic properties of the dispersion, as reflected in the attenuation data. Acoustic attenuation has been successfully utilized to assess particle size distribution [19–22] and stability characteristics [23–26] in concentrated dispersions. The determination of particle size distribution (PSD) using acoustic attenuation requires extensive thermophysical inputs and multi-frequency measurements. In contrast a quantitative consideration of the measured acoustic attenuation at a single frequency is often sufficient for the investigation of aggregation phenomena [27–29]. Despite its proven utility for observing aggregation phenomena, acoustic attenuation has not yet been employed to determine the CCC, representing an area for new application.

This study investigates the application of acoustic attenuation to determine the critical coagulation concentration (CCC) in concentrated polyvinyl chloride (PVC) dispersions. The approach is specifically designed for systems with high solid content, where conventional techniques are limited. To evaluate the plausibility of the method, dispersions with different particle sizes and surfactant coverage are examined, using either sodium dodecyl sulphate (SDS) alone or in combination with linear alkylbenzene sulfonate (LAS). Variation in surfactant adsorption thus serves to test the sensitivity of the method. In addition, a polyvinyl chloride dispersion with relatively large particle size was included to demonstrate that CCC determination by acoustic attenuation remains reliable in regimes where turbidity-based methods fail.

7.2 Theory

7.2.1 Critical Coagulation Concentration

The Critical Coagulation Concentration (CCC) is based on the balance between repulsive and attractive forces that govern the interactions among colloidal particles. Commonly, this balance is expressed as the total interaction energy V_T, which is quantitatively described by the Derjaguin-Landau-Verwey-Overbeek (DLVO) theory [30,31], which combines electrostatic and van der Waals interactions to predict the energy barrier that prevents particle coagulation. Electrostatic repulsion, arising from electrical double layer V_{EDL}, contributes to stabilize the dispersion by hindering particle aggregation. Conversely, van der Waals forces V_{vdW} tend to draw particles closer, promoting coagulation.

$$V_{\mathrm{T}} = V_{\mathrm{EDL}} - V_{\mathrm{vdW}} \tag{7.1}$$

At the CCC, the electrolyte concentration in the dispersion medium is sufficient to screen the electrostatic repulsions between particles V_{EDL}, thereby vanishing the energy barrier ($V_{\mathrm{T}} = 0$). Beyond this concentration, the attractive van der Waals forces predominate, leading to rapid particle aggregation.

The CCC can be quantitatively related to the surface potential ψ_0 and the Hamaker constant A. Within the framework of DLVO theory, Verwey and Overbeek derived an approximation for spherical particles using the Gouy–Chapman model [32,33] for the diffuse-layer potential. The relationship is given by:

$$\mathrm{CCC} = \frac{49.63(4\pi\varepsilon_{\mathrm{m}}\varepsilon_0)^3(k_{\mathrm{B}}T)^5}{e^6}\frac{\tanh^4\left(\frac{\overline{\psi_0}}{4}\right)}{A^2 z^6} \tag{7.2}$$

where $\overline{\psi_0}$ is the dimensionless surface potential:

$$\overline{\psi_0} = \frac{\mathrm{z e \psi_0}}{\mathrm{k_B T}} \tag{7.3}$$

here CCC is the critical coagulation concentration, ε_0 is the vacuum permittivity, ε_{m} is the relative permittivity of the dispersion medium, k_{B} is the Boltzmann constant, T is the thermodynamic temperature, e the elementary charge, A is the Hamaker constant, z is the valency of the counterions and ψ_0 the particle surface potential. This equation emphasizes the critical influence of counterion valency on the CCC, revealing an inverse sixth-power dependence of CCC on valency. Trivalent ions, such as Al^{3+}, are particularly effective at reducing CCC compared to monovalent ions like Na^+. This aligns with the well-known Schultze–Hardy rule [34,35], which also describes how ions of higher valency dramatically enhance coagulation by reducing the electrostatic repulsion between particles.

Additionally, the pH value of the dispersion medium plays a crucial role in colloidal stability. Changes in pH can alter the ionization state of the particles, thus affecting their surface charge and consequently the surface potential ψ_0 [36]. The surface potential is therefore a key factor in influencing the magnitude of the electrostatic repulsion V_{EDL}. While the zeta potential ζ is closely related to the surface potential and can be ease measured experimentally, it is often used instead as a practical alternative. Therefore, a high zeta potential correlates with a strong repulsive force, creating a higher barrier that prevents coagulation. On the other hand, reductions in zeta potential reduce the energy barrier, leading to significant aggregation as the repulsive forces are insufficient to counteract the attractive van der Waals forces.

The addition of ionic surfactants can significantly modify the surface potential/zeta potential and thus the CCC. Depending on their charge and hydrophobicity, ionic surfactants may adsorb onto the surfaces of colloidal particles, altering the surface charge density [37,38]. For example, anionic surfactants adsorbing on negatively charged particles can increase the absolute value of the surface or zeta potential, thereby strengthen electrostatic repulsion and shift the CCC to higher electrolyte concentrations. Conversely, a reduction in the absolute surface or zeta potential lowers the energy barrier and decreases the CCC, thus promoting coagulation, as occurs, for instance, when cationic surfactants are added to negatively charged particles.

The impact of particle size on CCC is also notable. Both attractive and repulsive interactions are dependent on particle size, where larger particles often experience dominance in attraction at longer ranges, leading to secondary minimum formations that facilitate reversible aggregation known as flocculation.[39,40]

7.2.2 Adsorption of Surfactant

The adsorption isotherm equation developed by Zhu and Gu provides an appropriate framework for the study of surfactant adsorption at solid-liquid interfaces [41–43]. This model can be expressed as:

$$\Gamma = \frac{\Gamma_\infty k_1 c_\mathrm{m}\left(\frac{1}{n}+k_2 c_\mathrm{m}^{\mathrm{n}-1}\right)}{1+k_1 c_\mathrm{m}\left(1+k_2 c_\mathrm{m}^{\mathrm{n}-1}\right)} \tag{7.4}$$

In this equation, Γ represents the amount of surfactant adsorbed per unit area, Γ_∞ is the maximum adsorption and k_1 is the equilibrium constant for the first adsorption step of surface-active species onto a solid surface, indicating the affinity of the surfactant for the surface. The constant k_2 represents the equilibrium constant for subsequent adsorption steps, governing the behaviour of additional surfactant layering or aggregation once the initial layer has been formed. c_m is the surfactant concentration in the medium, and n is known as the surface aggregation number, which quantifies the degree to which surfactant molecules interact with each other, but is in fact an adjustable parameter.

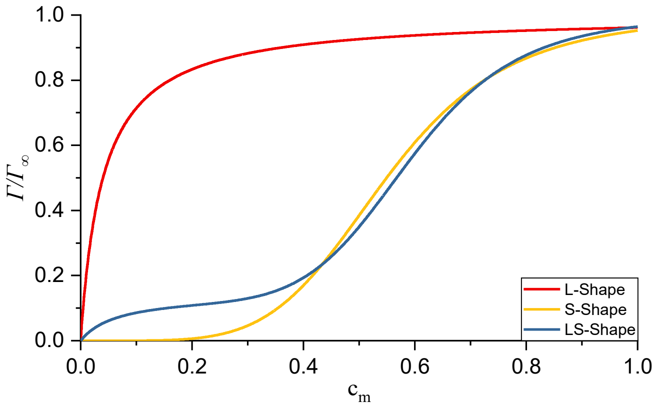

Fig. 7.1: Representation of the L-, S-, and LS-shape adsorption isotherms. Γ denotes the adsorption, while Γ_∞ is the maximum adsorption and c_m is the surfactant concentration in the surrounding medium. Reprint of [43]

This model can be used to describe adsorption isotherms with an L-shape (Langmuir), S-shape (sigmoidal type), and LS-shape (double plateau), as illustrated in Fig. 7.1. The L-shape curve, commonly observed in dilute solutions at a solid/liquid interface, is characterized by monomolecular adsorption, which can be described using Langmuir's adsorption isotherm [44]. The S-shape curve initially exhibits a gradual slope, followed by a sharp increase. In contrast, the LS-shape curve features two distinct plateaus.

In the limiting case, when $k_2 n - 1 \gg 1$ or $k_1 c_\mathrm{m} \ll 1$ and $k_1 c_\mathrm{m} \ll c_\mathrm{m}^\mathrm{n}$, the original Zhu and Gu equation reduces to:

$$\Gamma = \frac{\Gamma_\infty K c_\mathrm{m}^\mathrm{n}}{1 + K c_\mathrm{m}^\mathrm{n}} \tag{7.5}$$

where $K = k_1 k_2$. This simplified equation was originally developed to describe the adsorption of non-ionic surfactants on polar silica particles using a mass action law [45]. It is sufficient to describe L-shape and S-shape adsorption behaviour. When n is equal to 1 in Eq. 7.5, the equation simplifies further to the classical Langmuir isotherm model. In the study of Vale and Mc Kenna [46],this model was successfully used to describe the adsorption isotherms to a similar PVC system as studied in this paper.

The surface charge density σ_0^tit is directly related to the amount of surfactant adsorbed per unit area Γ, by the following equation:

$$\sigma_0^\mathrm{tit} = ze\Gamma N_\mathrm{A} \tag{7.6}$$

here z is the valency of the surfactant and N_A the Avogadro constant.

Alternatively, the surface charge density σ_0^ek can also be estimated from the surface potential ψ_0 or the zeta potential ζ which was determined by an electrokinetic experiment. For spherical particles in a symmetrical 1:1 electrolyte, Ohshima et al. [47] derived an expression that relates σ_0^ek to ψ_0:

$$\sigma_0^\mathrm{ek} = \frac{2\varepsilon_0 \varepsilon_\mathrm{m} \kappa k_\mathrm{B} T}{e} \sinh\left(\frac{\psi_0}{2}\right) \sqrt{1 + \frac{1}{\kappa a} \frac{2}{\cosh^2\left(\frac{\psi_0}{4}\right)} + \frac{1}{(\kappa a)^2} \frac{8 \ln\left(\cosh\left(\frac{\psi_0}{4}\right)\right)}{\sinh^2\left(\frac{\psi_0}{2}\right)}} \tag{7.7}$$

Where, $\varkappa$ is the Debye-Hückel parameter:

$$\varkappa = \sqrt{\frac{N_\mathrm{A}e^2}{\varepsilon_0\varepsilon_\mathrm{m}k_\mathrm{B}T}\sum_{i=1}^{N} z_i^2 c_i} \tag{7.8}$$

The relative error of Eq 7.7 is below 1 % for $\varkappa a \geq 0.5$. This expression enables comparison of surface charge densities derived from titration methods.

7.3 Experimental

The following section provides detailed descriptions of the methods used to measure surfactant adsorption and critical coagulation concentration. Information on additional measurements, such as particle size determination using dynamic light scattering (DLS) for the PVC@0.20 sample, laser diffraction spectroscopy (LDS) for the PVC@0.78 sample and the measurement of electrophoretic mobility using electrophoretic light scattering (ELS), can be found in a previously published work [48]. The zeta potential was calculated from the measured electrophoretic mobility using an approximation proposed by Ohshima et al. [49] (see also previous publication [50]).

7.3.1 Measurement of Surfactant Adsorption

In this study, two polyvinyl chloride (PVC) dispersions from Westlake Vinnolit GmbH & Co. KG were examined: PVC@0.20, produced by emulsion polymerization and PVC@0.78, produced by microsuspension polymerization. The PVC@0.20 dispersion was obtained as a stock dispersion stabilized with sodium dodecyl sulfate (SDS). For the adsorption studies, the SDS concentration was systematically increased by adding further amounts of SDS (Disponil® SDS 15 from BASF SE). The PVC@0.78 dispersion was obtained as a stock dispersion stabilized with linear alkylbenzene sulfonate (LAS, Disponil® LDBS 55 from BASF SE). In this system, the adsorption isotherm was investigated by incremental addition of SDS (Disponil® SDS 15, BASF SE) to the LAS-stabilized dispersion in order to study the effect of mixed anionic surfactants. To measure the surfactant adsorption per unit area (Γ), PVC stock dispersions with an initial particle concentration of approximately 50 wt.% were diluted with ultrapure water and a surfactant solution. The final particle concentration was adjusted to 10 wt.% in a total volume of 200 mL. These samples were stirred for 24 hours to ensure equilibrium adsorption.

After the stirring period, 40 mL of each sample was centrifuged in an Sorvall RC 5B Plus centrifuge with an SLA-3000 rotor at 10,000 rpm (≈17,500 RCF) for 2-4 hours to separate the solid particles from the liquid phase. The supernatant obtained from centrifugation was then filtered through a 0.2 µm syringe filter to obtain a clear solution of 2-5 mL for analysis. Both the filtered supernatant and the original 10 wt.% samples were subjected to titration to determine the surfactant concentration. Before every titration, the particle mass fraction was determined by drying a dispersion sample at 80 °C to constant weight, presuming the residue to be composed of pure PVC particles. The titration was performed using a 4 $\mathrm{mmol{\cdot}L^{-1}}$ solution of benzethonium chloride. A Ti-Touch 916 titrator equipped with a surfactant-sensitive electrode and a silver-silver chloride reference electrode from Metrohm was used for this purpose.

For the titration, the sample volume was first adjusted to 50 mL with ultrapure water. Next, 5 mL of methanol was added to enhance the solubility of the surfactants. The volume was then increased to 75 mL with additional ultrapure water. Subsequently, 10 mL of a borate buffer (pH 10, NIST standard buffer) was added to maintain a consistent pH throughout the titration process. Finally, the volume was topped up to 100 mL with ultrapure water. The titrator automatically adjusted the titrant addition rate based on changes in electrode potential and identified the equivalence point at the maximum slope of the voltage-titrant volume curve. The titration reaction involves the interaction between the surfactant in the sample ($R-SO_3^-$, which could be SDS or LAS) and the cationic surfactant benzethonium chloride ($C_{27}H_{42}NO_2^+$):

$$R-SO_3^- + C_{27}H_{42}NO_2^+ \xrightarrow{aq} R-SO_3^- \bullet C_{27}H_{42}NO_2^+ \tag{7.9}$$

At the equivalence point, the amount of anionic surfactant is stoichiometrically equivalent to the amount of benzethonium chloride added. Therefore, the concentration of the surfactant measured in the suspension C or suspension media C_m (in mmol·kg^{-1}) can be calculated by the following equations:

$$C = \frac{V_\mathrm{eq} c_\mathrm{titrant}}{m_\mathrm{sample}} \quad \text{or} \quad C_\mathrm{m} = \frac{V_\mathrm{eq} c_\mathrm{titrant}}{m_\mathrm{sample}} \tag{7.10}$$

where V_eq is the volume of benzethonium chloride titrant at equivalence point, c_titrant is the concentration of the benzethonium chloride solution and m_sample is the mass of the sample.

For the calculation of surfactant adsorption per unit area Γ, the following equations were used:

$$\Gamma = [C - C_\mathrm{m}(1-w)]\rho_s \frac{d_\mathrm{mean}}{6\varphi} \tag{7.11}$$

$$\rho_s = \varphi\rho_\mathrm{p} + (1-\varphi)\rho_\mathrm{m} \tag{7.12}$$

$$\varphi = \frac{\frac{w}{\rho_\mathrm{p}}}{\frac{w}{\rho_\mathrm{p}} + \frac{(1-w)}{\rho_\mathrm{m}}} \tag{7.13}$$

where w is the particle mass fraction, φ is the particle volume fraction, d_mean is the mean particle diameter, ρ_s is the density of the suspension, ρ_p is the particle density and ρ_m is the suspension media density. In addition to the surfactant adsorption per unit area, the concentration of surfactant in the suspension medium c_m (in mmol·L^{-1}), is required to analyse the adsorption isotherm. This concentration was determined using:

$$c_\mathrm{m} = C_\mathrm{m}\rho_\mathrm{m} \tag{7.14}$$

7.3.2 Measurement of the Critical Coagulation Concentration

To measure the CCC at different surfactant coverage rates, we studied the PVC@0.20 sample at surface coverage rates of 27 %, 53 %, and 94 % at a particle concentration of 15 wt%, as well as the PVC@0.78 sample at surface coverage rates of 62 % and 94 % at a particle concentration of 10 wt%. Additionally, the CCC of the PVC@0.78 sample was determined to extend the analysis to a large-particle system.

To determine the CCC, acoustic attenuation was measured at 99.5 MHz and varying potassium nitrate concentrations. For each measurement, a 200 mL solution was prepared in a 250 mL glass bottle. Ultrapure water was first mixed with the stock dispersion, followed by the addition of the appropriate amount of surfactant. The samples were gently stirred using a magnetic stirrer for 24 hours to ensure equilibrium. On the following day, the electrolyte solution was added, and each sample was gently stirred again using a magnetic stirrer for 30 minutes before measuring acoustic attenuation. When analysing the CCC in highly concentrated dispersions, it is essential to refer the electrolyte concentration to the volume of the dispersion medium and not to the volume of the dispersion. Acoustic attenuation measurements were conducted using a DT-1202 instrument from Dispersion Technology Inc. To maintain homogeneity and prevent particle settling during the measurement process, the samples were continuously circulated at low speed using a peristaltic pump. Both magnetic stirring and low-speed peristaltic pumping are considered low-shear methods. Consequently, we assume that the agitation and analysis of the samples occurred under conditions approximating perikinetic aggregation.

For the final determination of the CCC, the attenuation at 99.5 MHz was plotted against the potassium nitrate concentration and the data were fitted using the following logistic function:

$$\alpha_{99.5} = \alpha_{\mathrm{stb}} + \frac{\alpha_{\mathrm{inc}}}{(1+s\cdot\exp[-\delta(c_{\mathrm{m}}-c_{\mathrm{i}})])^{\frac{1}{s}}} \tag{7.15}$$

where $\alpha_{99.5}$ is the measured attenuation at 99.5 MHz, α_{stb} describes the acoustic attenuation of a stable dispersion, α_{inc} describes the maximum increase of the attenuation caused by coagulation, τ is a symmetry parameter which should be ≥ 0.02, δ represents the steepness parameter, c_{m} describes the electrolyte concentration in the dispersion media and c_{i} is the electrolyte concentration at the inflection point.

The onset concentration of coagulation c_{onset} is defined as the intersection of the attenuation of a stable dispersion with the tangent at the inflection point. It can be calculated by:

$$c_{\mathrm{onset}} = c_{\mathrm{i}} - \frac{1+s}{\delta} \tag{7.16}$$

The critical coagulation concentration CCC is defined as the intersection of the tangent at the inflection point with $\alpha_{\mathrm{stb}} + \alpha_{\mathrm{inc}}$, therefore it can be calculated using the following equation:

$$\mathrm{CCC} = c_{\mathrm{i}} + \frac{(1+s)^{\frac{1}{s}}-1}{\delta}(1+s) \tag{7.17}$$

7.4 Results and Discussion

This section examines the adsorption behaviour of surfactants on polyvinyl chloride (PVC) particles and the critical coagulation concentration (CCC) of PVC dispersions at various conditions.

We begin by presenting the adsorption isotherms of sodium dodecyl sulphate (SDS) and a mixture of linear alkylbenzene sulfonates (LAS) and SDS on PVC particles with distinct particle sizes. These isotherms are analysed to derive adsorption parameters, such as maximum adsorption capacity Γ_∞, equilibrium constants K and aggregation numbers n, which provide insight into the cooperative interactions between surfactant molecules. The results and discussion are shown in Chapter 7.4.1.

Next, we focus on the CCC of the dispersions, determined using acoustic attenuation measurements. By examining the influence of surfactant coverage, we identify distinct coagulation regimes and discuss how adsorption of surfactants impacts electrostatic stabilization. The zeta potential ζ and surface charge densities σ_0 are evaluated as they are a measure for the electrostatic interaction. Additionally, we determine the apparent Hamaker constant A and compare them with literature values. These findings are presented in Chapter 7.4.2.

7.4.1 Adsorption of Surfactant

To understand the adsorption behaviour of surfactants on polyvinyl chloride (PVC) particles, we investigated the adsorption isotherms of sodium dodecyl sulphate (SDS) on PVC@0.20 and a mixture of linear alkylbenzene sulfonates (LAS) and SDS on PVC@0.78. The aim was to determine the adsorption parameters, which will help us to analyse how surfactant adsorption influences the stability of the PVC dispersions.

The adsorption isotherms were obtained by measuring the amount of surfactant adsorbed per unit area Γ as a function of the surfactant concentration in the medium c_m. The experimental data were fitted using the simplified Zhu and Gu adsorption isotherm (Eq. 7.4), suitable for L- and S-shaped isotherms.

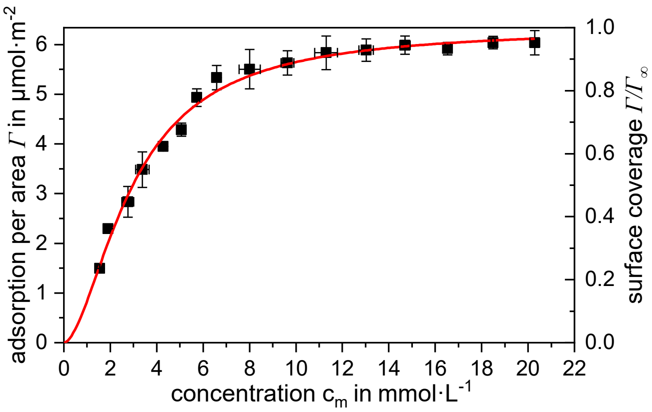

Fig. 7.2: Adsorption isotherm of SDS on PVC@0.20 particles at room temperature and 15 wt%. The fitted line (Eq. 7.4) represents data aligned with an S-shaped isotherm, reflecting cooperative adsorption behavior due to interactions between surfactant molecules on the particle surface.

Fig. 7.2 shows the adsorption isotherm for SDS on PVC@0.20 particles. While the Langmuir equation might seem applicable at first glance, a detailed analysis reveals a slight S-shape. This characteristic shape, common for ionic surfactants adsorbing onto a hydrophobic surface [46,51–53], indicates a gradual adsorption increase at low concentrations followed by a steep rise beyond a critical concentration.

The S-shape is directly linked to the fitted value of the aggregation number n=1.73, which is greater than 1, indicating deviations from the Langmuir model. This deviation reflects cooperative interactions between surfactant molecules on the surface. In the Langmuir isotherm, it is assumed that surfactant molecules adsorb independently, without significantly influencing one another. However, when n>1, the adsorption is no longer independent. Instead, when a surfactant molecule adsorbs to the surface, it facilitates the adsorption of additional molecules. This cooperative behaviour causes the isotherm to exhibit a slight curvature, leading to the S-shape. [54]

The adsorption equilibrium constant K provides insight into the surface affinity of the surfactant. For PVC@0.20, a K value of $1.5{\cdot}10^{2}$ $(\mathrm{mol\ L^{-1}})^{-1.73}$ was obtained. A higher K value generally corresponds to a stronger affinity between the surfactant and the surface, as it reflects the balance between adsorption and desorption [55]. However, many literature values are derived from classical Langmuir fits (n=1), while in the Zhu–Gu model n is typically different from 1. For this reason, direct comparison with published Langmuir constants is not meaningful and even within the Zhu–Gu framework comparisons are only meaningful for identical n, which is seldom met in practice.

As summarized in Tab. 7.1, the maximum adsorption Γ_∞ was determined to be 6.3 μmol·m^{-2} and the surface area per surfactant molecule $a_s = (\Gamma_\infty N_\mathrm{A})^{-1}$ was found to be 26 Å^{2}. The close agreement of those values with those reported by Vale and Mc Kenna [46] and Meconi et al. [51] underlines the reliability of the method and results.

Tab. 7.1: Key adsorption parameters, including maximum adsorption capacity Γ_∞, equilibrium adsorption constant K, aggregation number n and surface area per surfactant molecule a_s for PVC@0.20 and PVC@0.78 dispersions stabilized by SDS and LAS+SDS, respectively. The parameters reflect differences in adsorption behaviour and cooperative interactions between surfactant molecules on different PVC surfaces.

sample	surfactant	Γ_∞ [μmol·m^{-2}]	K [(mol L^{-1})$^{-n}$]	n [-]	a_s [Å^{2}]
PVC@0.20	SDS	6.3	$1.5{\cdot}10^{2}$	1.73	26
PVC@0.78	LAS+SDS	3.6	$8.6{\cdot}10^{2}$	2.69	46

For the PVC@0.78 dispersion, the adsorption isotherm presented in Fig. 7.3 shows a more pronounced S-shape, linked to a higher aggregation number n of 2.69, reflecting stronger cooperative interactions between the surfactants. The mixture of SDS and LAS surfactants in this system further influences the isotherm shape, as the presumably bulkier LAS molecules occupy more surface area, resulting in a lower overall maximum adsorption Γ_∞ with 3.6 μmol·m^{-2} and higher surface area per surfactant molecule a_s of 46 Å^{2}. The equilibrium constant, K of $8.6{\cdot}10^{2}$ $(\mathrm{mol\ L^{-1}})^{-2.69}$ was obtained. While a higher K within the same model and at fixed n indicates stronger surface affinity, but since n=2.69 here differs from the PVC@0.20 system, a direct comparison is not meaningful.

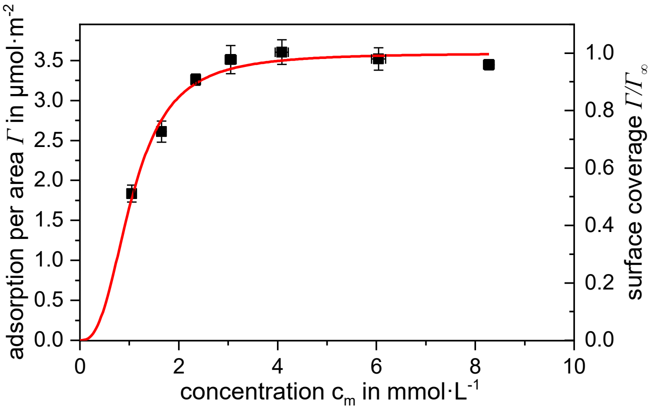

Fig. 7.3: Adsorption isotherm of a LAS+SDS mixture on PVC@0.78 particles at room temperature and 10 wt%. The fitted line (Eq. 7.4) displays a more pronounced S-shape, indicating stronger cooperative interactions between the surfactants.

When comparing both isotherms, a decisive difference lies in the initial surfactant coverage. For PVC@0.20, produced by emulsion polymerization, the surface was covered by roughly 24 %, whereas PVC@0.78, was produced by microsuspension polymerization, already exhibited a coverage of about 51 %. This difference can be attributed to the distinct nucleation mechanisms and the amount of surfactant required to achieve stable droplet or particle formation in each polymerization process. In microsuspension polymerization, relatively small monomer droplets must be sufficiently stabilized already at the start of the process to prevent droplet coalescence. As a result, a considerable portion of the surfactant is adsorbed at the droplet interfaces from the beginning, with the droplet size remaining largely constant during polymerization and therefore essentially corresponding to the final particle size. In contrast, during emulsion polymerization, only a limited amount of surfactant is needed initially to stabilize the larger monomer droplets and to form a small number of micelles. Particle nuclei then form in these micelles and grow during polymerization, progressively consuming available surfactant molecules. Consequently, a lower initial surface coverage of the particles is observed for the dispersion produced by emulsion polymerization compared to that obtained by microsuspension polymerization.[56]

In summary, the analysis of adsorption isotherms for PVC@0.20 and PVC@0.78 highlights notable differences in adsorption parameters (Tab. 7.1). While the dispersions were produced by different polymerization methods, this mainly affects the particle size and the initial surfactant coverage rather than the adsorption process itself. Therefore, the observed differences are most likely related to the distinct surfactant systems, although this assumption is based on a limited dataset.

7.4.2 Critical Coagulation Concentration

The critical coagulation concentration (CCC) marks the point at which sufficient addition of electrolytes causes the electrostatic repulsion between particles to be overcome by attractive forces, leading to rapid aggregation. In our study, this was observed through the significant increase in acoustic attenuation, as shown in Fig. 7.4. This increase correlates with particle aggregation, which is associated with the increase in particle size due to coagulation.

Fig. 7.4 serves as an exemplary representation of the influence of potassium nitrate on the PVC@0.78 sample with 54 % surface coverage, measured at 99.5 MHz. The figure demonstrates three distinct regions in the aggregation process. At low electrolyte concentrations, up to around 150 mmol·L^{-1}, the attenuation remains nearly constant, indicating a stable dispersion (green line). In this range, the electrostatic repulsion between particles, caused by the presence of ionic surfactant, prevents any significant aggregation.

As the electrolyte concentration increases beyond the onset concentration of 180 mmol·L^{-1}, marked by the intersection of the yellow line with the green line (stable regime), the system transitions into the slow coagulation regime. A gradual increase in attenuation is observed between approximately 200 mmol·L^{-1} and 400 mmol·L^{-1}, marking the intermediate stage where particle collisions lead to slow but measurable aggregation. During this phase, potassium ions partly screen the electrostatic repulsion between the negatively charged particles, reducing the energy barrier for aggregation.

At concentrations exceeding the CCC of 290 mmol·L^{-1}, indicated by the intersection of the yellow line (slow coagulation regime) with the red line, the system fully transitions into the fast coagulation regime. This intersection marks the point where the attenuation reaches a plateau, showing that the system is fully coagulated and further increase in electrolyte concentration no longer affects the particle size or structure. In this regime, the electrostatic repulsion is entirely compensated, allowing van der Waals forces to dominate and leading to rapid particle aggregation.

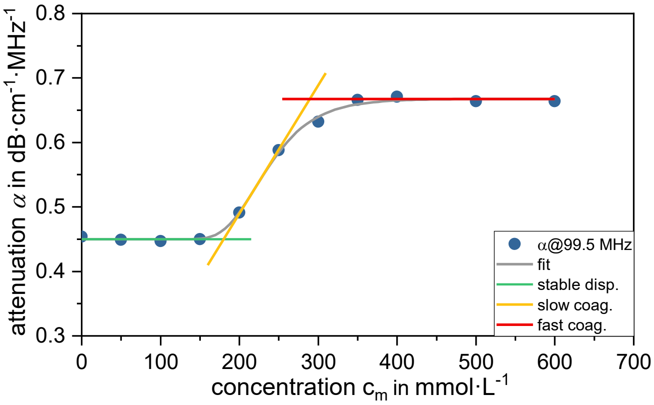

Fig. 7.4: Acoustic attenuation at 99.5 MHz and 10 wt% for PVC@0.78 with 54 % surface coverage, showing the influence of potassium nitrate concentration on dispersion stability. The plot illustrates distinct regions corresponding to stable, slow coagulation, and fast coagulation regimes as electrolyte concentration increases.

In preliminary investigations (see Fig. 7.7 in the Supporting Information), the measurements at 99.5 MHz proved most suitable for detecting the CCC for the tested samples, providing the largest change in attenuation values. Therefore, this frequency provided the best differentiation between stable and aggregated states. However, it is important to note that minima and maxima may also be present in the attenuation spectra [21] depending on the material under investigation, which is why other frequencies might be more suitable for other materials.

To validate our new approach for determining CCCs, we have included a comparison with established methods in the supporting information (see Tab. 7.5). This was carried out only for the

PVC@0.20 sample, as optical methods used in the comparison could not determine a CCC for larger particles, such as those in the PVC@0.78 sample. It was found that methods relying on low particle volume fractions and rapid measurement techniques tend to yield higher measured CCCs. Conversely, slower methods and those conducted at higher particle volume fractions typically result in lower CCCs. Our new method aligns with this general trend, and its behaviour can be plausibly explained by considering the kinetics of particle collisions within colloidal systems.

The rate of particle collisions and thus the rate of coagulation is directly proportional to the particle concentration [57]. Higher particle concentrations increase the frequency of collisions, leading to a higher probability of coagulation when the CCC is present. Moreover, the measurement duration plays a crucial role. Slower measurement methods provide lower temporal resolution when distinguishing between stable dispersion, slow coagulation and fast coagulation regimes. Extended measurement times allow more collisions to occur, potentially leading to fully coagulated dispersions even at electrolyte concentrations slightly below the true CCC. This results in a measured CCC that is lower than the actual value. Therefore, both increased particle concentration and prolonged measurement times can lower the observed CCC.

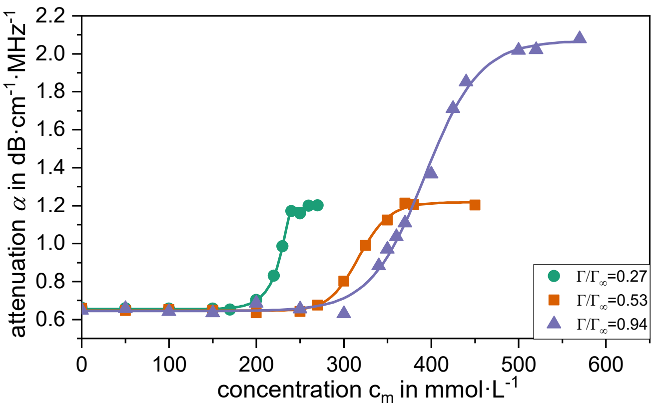

Fig. 7.5: Acoustic attenuation measurements at 99.5 MHz and 10 wt% for PVC@0.20 dispersion at varying potassium nitrate concentrations and surfactant coverage levels. Higher surfactant coverage shifts CCC to higher electrolyte concentrations, indicating enhanced electrostatic stabilization with increased surfactant adsorption. The lines represent the fits using Eq. 7.15.

For PVC@0.20, the CCC was measured at different surfactant coverage levels using acoustic attenuation measurements. As shown in Fig. 7.5 and Tab. 7.3, increasing the surface coverage of SDS from 27 % to 94 % shifts the CCC to higher electrolyte concentrations. The onset concentration also increases with coverage, starting at 220 mmol·L^{-1}for 27 % coverage and rising to 330 mmol·L^{-1} at 94 % coverage. The CCC similarly increases, from 240 mmol·L^{-1} at 27 % coverage to 460 mmol·L^{-1} at 94 % coverage. This indicates enhanced electrostatic stabilization of the dispersion as more surfactant molecules adsorb onto the particle surface, thereby increasing the repulsive forces between particles.

Tab. 7.2 summarizes the fitted coefficients of the fit with Eq. 7.15. It is noticeable that the fast coagulation regime is present with similar attenuation ($\alpha_{\text{stb}} + \alpha_{\text{inc}}$ ≈1.2 dB cm^{-1} MHz^{-1}) at a surface coverage rate of 27 % and 53 %. At a surface coverage rate of 94 %, however, the attenuation in the fast coagulation regime is significantly higher with approx. 2 dB cm^{-1} MHz^{-1}.

Tab. 7.2: Fitted parameters (Eq. 7.15) obtained from acoustic attenuation measurements at different KNO_3 concentration for different surfactant coverage rates on PVC@0.20 and PVC@0.78 dispersions. Parameters include initial attenuation in stable dispersions α_{stb}, maximum attenuation increase α_{inc}, the symmetry parameter s, the steepness parameter δ and electrolyte concentration at the inflection point c_{i}.

sample	surfactant	Γ/Γ_∞ [-]	α_{stb} [dB cm^{-1} MHz^{-1}]	α_{inc} [dB cm^{-1} MHz^{-1}]	s [-]	δ [L mmol^{-1}]	c_{i} [mmol·L^{-1}]
PVC@0.20	SDS	0.27	0.654	0.532	7.21	$4.70\cdot10^{-1}$	230
PVC@0.20	SDS	0.53	0.646	0.572	0.793	$5.40\cdot10^{-2}$	320
PVC@0.20	SDS	0.94	0.645	1.425	0.979	$3.18\cdot10^{-2}$	390
PVC@0.78	LAS+SDS	0.62	0.450	0.218	$2.00\cdot10^{-2}$	$2.51\cdot10^{-2}$	220
PVC@0.78	LAS+SDS	0.94	0.418	0.409	5.07	$3.01\cdot10^{-2}$	510

Given the constant particle concentration across all dispersions, this rise in attenuation at higher surfactant coverage suggests that increased surfactant concentration promotes the formation of larger or structurally distinct aggregates with higher acoustic attenuation. Consequently, while higher surfactant coverage raises colloidal stability by increasing the CCC, it may also affect aggregate morphology. Similar phenomena have been reported for other dispersions, e.g. in [58,59].

Tab. 7.3: Onset c_{onset} (Eq 7.16) and critical coagulation concentration CCC (Eq. 7.17) values for PVC@0.20 and PVC@0.78 dispersions at different surface coverage rates.

sample	surfactant	Γ/Γ_∞ [-]	c_{onset} [mmol·L^{-1}]	CCC [mmol·L^{-1}]
PVC@0.20	SDS	0.27	220	240
PVC@0.20	SDS	0.53	280	350
PVC@0.20	SDS	0.94	330	460
PVC@0.78	LAS+SDS	0.62	180	290
PVC@0.78	LAS+SDS	0.94	310	600

Fig. 7.6 shows the acoustic attenuation measurements for PVC@0.78. Similar to PVC@0.20, the CCC increases with greater surfactant coverage. The onset concentration rises from 180 mmol·L^{-1} at 62 % coverage to 310 mmol·L^{-1}at 94 % coverage, while the CCC progresses from 290 mmol·L^{-1} at 62 % coverage to 600 mmol·L^{-1} at 94 % coverage. The generally higher CCC values compared to PVC@0.20 at similar surface coverage suggest that the LAS–SDS combination may provide stronger electrostatic stabilization than SDS alone. However, this interpretation must be made with caution, as the difference in particle size between the two dispersions also contributes to the observed behaviour. A more reliable comparison would require additional experiments with PVC@0.20 at increased surfactant coverage using the LAS–SDS mixture.

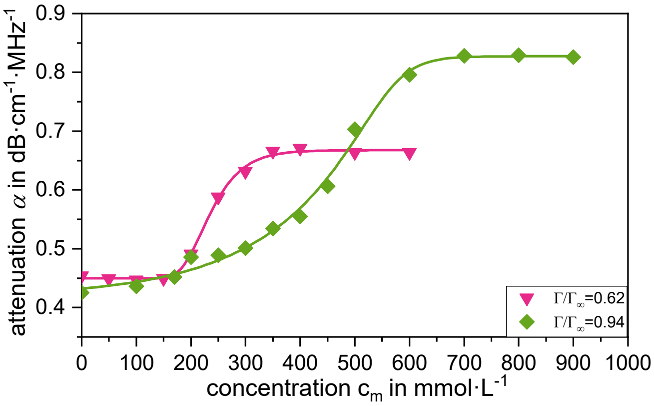

Fig. 7.6: Acoustic attenuation measurements at 99.5 MHz for PVC@0.78 dispersion at varying potassium nitrate concentrations and surfactant coverage levels. Higher surfactant coverage shifts CCC to higher electrolyte concentrations, indicating enhanced electrostatic stabilization with increased surfactant adsorption. The lines represent the fits using Eq. 7.15.

Tab. 7.4 presents key parameters, including titration-derived surface charge densities σ_0^{tit}, electrokinetic surface charge densities σ_0^{ek} electrophoretic mobilities μ, electrolyte concentrations c, zeta potentials ζ and apparent Hamaker constants A. These values reveal insights into how surfactant adsorption influences electrostatic properties and colloidal stability, as discussed below.

Tab. 7.4: Comparison of titration σ_0^{tit} and electrokinetic σ_0^{ek} derived surface charge densities for PVC@0.20 and PVC@0.78 at various surfactant coverages. Additional parameters such as electrophoretic mobility μ, zeta potential ζ and Hamaker constant A provide insights into how different surfactant systems influence electrostatic stabilization.

sample	surfactant	Γ/Γ_∞ [-]	σ_0^{tit} [mC·m^{-2}]	σ_0^{ek} [mC·m^{-2}]	μ [·10^{-8}m^2·s^{-1}·V^{-1}]	c [mmol·L^{-1}]	ζ [mV]	A [·10^{-20} J]
PVC@0.20	SDS	0.27	164	18	-4.80	11.6	-73.5	4.82
PVC@0.20	SDS	0.53	322	23	-5.26	13.4	-82.4	4.68
PVC@0.20	SDS	0.94	571	34	-5.71	25.0	-87.0	4.39
PVC@0.78	LAS+SDS	0.62	377	21	-6.05	10.9	-83.1	5.20
PVC@0.78	LAS+SDS	0.94	571	37	-7.28	15.2	-102.1	4.66

A notable observation from Tab. 7.4 is the significant discrepancy between $\sigma_0^{\mathrm{tit}}$and σ_0^{ek}. The titration-derived surface charge densities are approximately an order of magnitude higher than the electrokinetic surface charge densities obtained from electrophoretic mobility measurements. For example, in the PVC@0.20 sample with 27 % SDS coverage, σ_0^{tit} is 164 mC·m^{-2}, whereas σ_0^{ek} is only 18 mC·m^{-2}. Several factors may contribute to this discrepancy. One possible explanation is the effect of surface conductivity within the stagnant layer of the electrical double layer, which is often neglected in electrophoretic mobility measurements. Neglecting this factor can lead to an underestimation of the surface charge density in the calculations of σ_0^{ek}. Another consideration is that the charges may not be located exclusively on the particle surface but could also extend into an ion-permeable layer around the particles [60].

The electrophoretic mobility μ becomes increasingly negative with higher surfactant coverage, indicating enhanced electrostatic repulsion due to greater surface charge. Correspondingly, the zeta potential ζ also becomes more negative, changing from -73.5 mV at 27 % coverage to -87.0 mV at

94 % coverage for PVC@0.20 with SDS. These trends confirm that increased surfactant adsorption enhances the electrostatic stabilization of the particles, contributing to greater colloidal stability. Comparing PVC@0.20 stabilized with SDS to PVC@0.78 stabilized with a mixture of LAS and SDS, it is observed that the latter shows more negative zeta potentials and higher σ_0^{ek} values. For instance, at 94 % coverage, PVC@0.78 has a ζ potential of -102.1 mV compared to -87.0 mV for PVC@0.20. This suggests that the combination of LAS and SDS provides stronger electrostatic stabilization than SDS alone.

The apparent Hamaker constants A calculated from the CCC data are significantly higher than the typical literature values for aqueous latex dispersions, which are around $3\text{-}14 \cdot 10^{-21}$ J [61–63]. Our estimated values range from 4.39 to $5.20 \cdot 10^{-20}$ J. While experimental conditions, such as the use of high particle volume fractions and extended measurement times, may contribute to systematically lower CCC values and thereby to an overestimation of A, this effect alone cannot account for the discrepancy of nearly one order of magnitude. A more plausible explanation lies in the theoretical limitations of the DLVO approach itself. The calculation of the Hamaker constant neglects additional interactions such as hydrophobic forces, which are likely to be relevant for PVC particles stabilized by surfactants, as well as specific ion effects and surface roughness. Such factors can significantly alter the balance of interparticle interactions, leading to an overestimation of the Hamaker constant when interpreted solely within the DLVO framework. Consequently, the absolute values derived here should be treated with caution.

Nevertheless, despite the limitations in determining exact interaction parameters, the method proves to be highly effective for comparative analysis within the same system. The measurements performed in this study, which include different surfactant coverage levels and different PVC dispersions, serve as an internal plausibility and reliability check. The fact that the individual Hamaker constants remain consistent for all PVC dispersions examined suggests that the method captures reproducible trends. It provides confidence in the approach and demonstrates its robustness. Most importantly, the acoustic attenuation technique reliably detects changes in colloidal stability even at high particle concentrations and larger particle sizes. This makes it a valuable tool for practical applications, like the optimisation of dispersion stability.

7.5 Conclusion

We investigated two polyvinyl chloride (PVC) dispersions, PVC@0.20 and PVC@0.78, to examine how factors like particle size, and surfactant selection affect electrostatic stabilization. PVC@0.20, with a mean particle size of 0.202 μm was produced via emulsion polymerization and stabilized solely with sodium dodecyl sulphate (SDS). Conversely, PVC@0.78, synthesized through microsuspension polymerization and characterized by a larger mean particle size of 0.783 μm, was stabilized with a combination of SDS and linear alkylbenzene sulfonate (LAS).

Our results demonstrate that increasing surfactant coverage significantly raises the CCC, primarily due to enhanced electrostatic repulsion between particles. This increased stability arises from surfactants' capability to alter surface charge density, thereby necessitating higher electrolyte concentrations to overcome repulsive forces and induce coagulation. Notably, the surfactant combination of LAS and SDS in the PVC@0.78 dispersion, achieved higher CCC values than SDS alone, especially at high surface coverages. These results suggest that combining surfactants with different properties may provide an effective strategy for optimizing stability in complex dispersion systems.

Discrepancies were observed between surface charge densities derived from titration (σ_0^{tit}) and those obtained from electrophoretic (σ_0^{ek}) measurements, with titration values being higher. These differences may stem from factors such as surface conductivity within the stagnant layer of the electric double layer or the presence of ion-penetrable layers around the particles. This observation underscores the importance of employing multiple measurement techniques to gain a more comprehensive understanding of surface charge behaviour and colloidal stability in dispersions.

Our study establishes acoustic attenuation as a reliable method for characterising colloidal stability, particularly in cases where optical methods are insufficient. Furthermore, the method presented in this paper demonstrates the advantage of applicability to systems with large particle sizes, where commonly used techniques, such as turbidity measurements, often fail. The calculated Hamaker constants are higher than typical literature values. While experimental factors such as high particle volume fractions and extended measurement times may contribute to this trend, they cannot fully account for the discrepancy. More importantly, theoretical limitations of the DLVO approach, particularly the neglect of additional non-DLVO interactions, provide a more plausible explanation for the observed overestimation. Nonetheless, acoustic attenuation remains a valuable tool for researchers and industrial practitioners seeking to optimise dispersion formulations under diverse conditions.

Future research could extend this methodology to explore different surfactant and particle combinations and to assess the effects of environmental variables, such as pH, temperature or shear stress, on colloidal stability. These insights would deepen our understanding of stability mechanisms in colloidal systems and offer practical guidance for optimizing dispersion formulations across diverse industries.

7.6 Supporting Information

7.6.1 Frequency Selection

To develop an acoustic method for determining the CCC, attenuation was initially measured at various frequencies and $CaCl_2$ concentrations (see Fig. 7.7) for the PVC@0.20. The frequency of 99.5 MHz was selected for the final method, as it showed the largest absolute increase in attenuation between a stable and a coagulated dispersion (characterized by the sharp increase in attenuation between 4 and 6 mmol·L^{-1} $CaCl_2$).

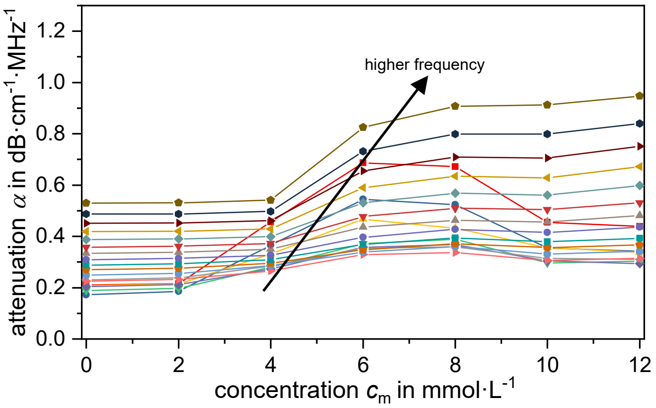

Fig. 7.7: Change in acoustic attenuation of PVC@0.20 at10 wt% due to the addition of $CaCl_2$ at different frequencies.

7.6.2 Comparison of Different CCC Measurement Methods

Several well-established turbidity methods exist for determining the CCC. They require significant dilution of the dispersion, introducing potential dilution artifacts that can affect the results. A further limitation of these methods is that they are effective only for particles smaller than the wavelength of visible light used in the analysis. To contextualize the results obtained using the newly developed Acoustic Attenuation method, CCC values were determined using multiple extinction methods for the PVC@0.20 dispersion.

7.6.2.1 Jar Test

A jar test involves preparing multiple jars, each containing the same colloidal suspension treated with different concentrations of an electrolyte or other additives. After controlled mixing, the results are evaluated to determine the concentration at which coagulation occurs. This evaluation can be enhanced with extinction or turbidity measurements, which provide quantitative insights into particle aggregation. [13,14]

Fig. 7.8 shows the measured extinction at 633 nm of the PVC@0.20 dispersion at a particle weight fraction of 0.1 wt%, recorded ten minutes after mixing with varying concentrations of $CaCl_2$ using a UV/Vis spectrophotometer (Thermo Scientific – Evolution 220). As coagulation progresses, the extinction increases caused by particle aggregation. Consistent with trends observed in acoustic attenuation, the extinction data reveal a clear transition from stable dispersion to slow coagulation and, eventually, to rapid coagulation. To analyse these transitions quantitatively, the data were also fitted to Eq. 7.15, and the Onset (Eq. 7.16) and CCC (Eq. 7.17) were determined. The results are summarized in Tab. 7.5.

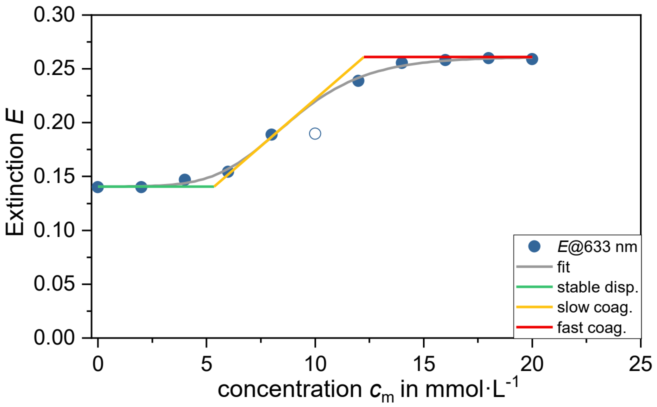

Fig. 7.8: Determination of the CCC for PVC@0.20 at 0.1 wt% by adding $CaCl_2$ and measuring the extinction using a UV/Vis spectrometer at 633 nm. The CCC is determined to be 12.3 mmol·L^{-1} $CaCl_2$. The onset of coagulation (intersection of the green and yellow lines) and the CCC (intersection of the yellow and red lines) were identified using a step function. Unfilled data points were not used in the fitting procedure.

7.6.2.2 Aggregation Rate

The aggregation rate method involves monitoring the time-dependent increase in extinction or particle size at varying electrolyte concentrations, using techniques such as UV/Vis spectroscopy [8] or dynamic light scattering (DLS) [6]. The analysis focuses on the initial slope of the extinction or particle size increase shortly after mixing the suspension with the electrolyte. In UV/Vis extinction measurements, this time window typically covers only the first few seconds. During this period, the aggregation process is dominated by the formation of doublets. Whereas in DLS measurements the accessible time scale is naturally longer due to the measurement principle.

Fig. 7.9 presents the time-dependent extinction measurements for the PVC@0.20 dispersion at a particle weight fraction of 0.1 wt% across varying electrolyte concentrations. The data collection began approx. 1 second after mixing, with measurements taken at intervals of 0.1 second over a 30 second period using a UV/Vis spectrophotometer (Thermo Scientific – Evolution 220) at a fixed wavelength of 633 nm. As shown in Fig. 7.9, the extinction curves exhibit an initial linear increase ($\mathrm{d}E/\mathrm{d}t$), corresponding to the rate of particle aggregation. In the stable dispersion regime, no aggregation occurs, and thus $\mathrm{d}E/\mathrm{d}t$ remains zero. However, as the electrolyte concentration increases, the initial slope ($\mathrm{d}E/\mathrm{d}t$) of the extinction curves transitions from zero and increases with further electrolyte concentration. Beyond the CCC, all slopes converge, indicating that the aggregation process has reached its maximum rate.

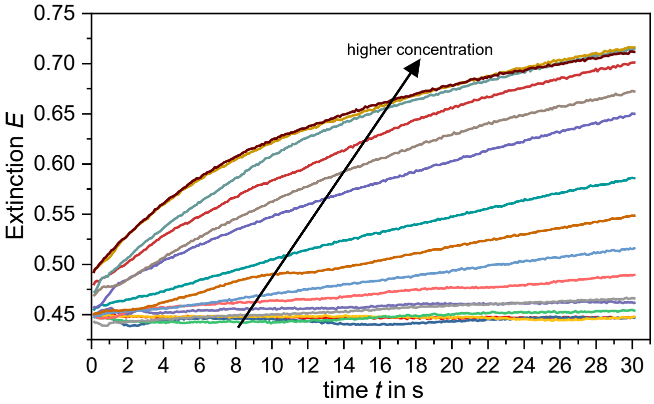

Fig. 7.9: Time-dependent extinction measurements for PVC@0.20 at 0.1 wt% and varying $CaCl_2$ concentrations, collected over 30 s at 633 nm. Initial slopes dE/dt indicate aggregation rates, converging beyond the CCC.

To determine the CCC quantitatively, the logarithm of the inverse initial slope log(dt/dE) were plotted against log(c_m), as shown in Fig. 7.10. This plot produces a straight line that bends to become parallel to the concentration axis at a specific electrolyte concentration. The intersection of these two segments provides the CCC value. The results obtained from this method are also summarized in Tab. 7.5.

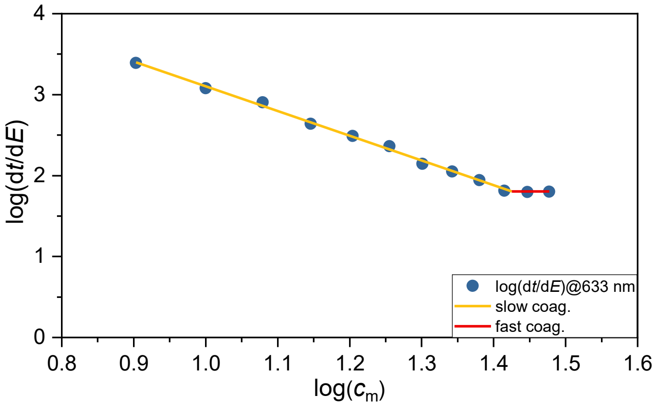

Fig. 7.10: Determination of the CCC for PVC@0.20 at 0.1 wt% by adding $CaCl_2$ and measuring the time-dependent extinction increase using a UV/Vis spectrometer at 633 nm. The CCC is determined to be 27 mmol·L^{-1} $CaCl_2$.

7.6.2.3 Wavelength Scan

The wavelength scan method is a spectroscopic technique used to determine the CCC by analysing changes in extinction across a range of wavelengths during particle aggregation [11,64]. Fig. 7.11 shows extinction measurements for PVC@0.20 dispersions at a particle weight fraction of 0.1 wt% under varying concentrations of $CaCl_2$ recorded ten minutes after mixing. The data, collected using a UV/Vis spectrophotometer (Thermo Scientific – Evolution 220) over a wavelength range of 400–633 nm in 5 nm steps, exhibit a linear relationship when log(E) is plotted against log(λ). With increasing electrolyte concentration, subtle decrease in the slope dlog(E)/dlog(λ) indicates the onset of aggregation. At high electrolyte concentrations, corresponding to rapid coagulation, the slope approaches a constant lower value, reflecting the presence of larger aggregates.

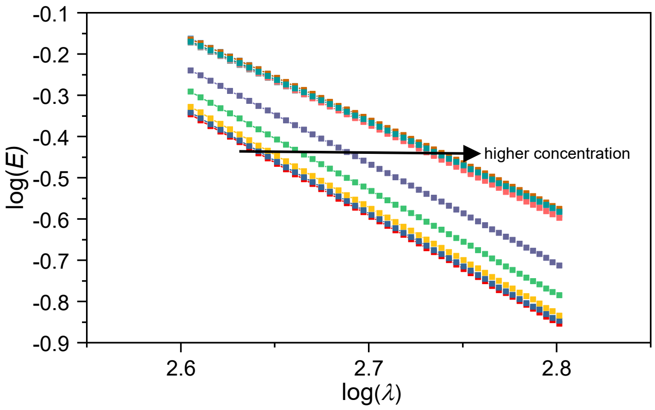

Fig. 7.11: Extinction measurements for PVC@0.20 at 0.1 wt% and varying $CaCl_2$ concentrations, recorded 10 min after mixing. log(*E*) vs. log(*λ*) plots show slope changes indicating aggregation onset and stabilization in the rapid coagulation regime.

To quantitatively determine the CCC, the slope $m = \mathrm{dlog}(E)/\mathrm{dlog}(\lambda)$ was calculated for each electrolyte concentration c_m. Fig. 7.12 presents the plot of m as a function of c_m. At low electrolyte concentrations, m remains constant, indicating a stable dispersion. As c_m increases, m decreases, marking the onset of aggregation, and approaches again a constant value at higher concentrations, consistent with a fully destabilized system. The stable, slow and fast coagulation regimes were further classified by fitting the data in Fig. 7.12 to Eq. 7.15, with the Onset and CCC values determined using Eqs. 7.16 and 7.17, respectively. The results are summarized in Tab. 7.5, providing a comprehensive comparison of the different CCC determination methods.

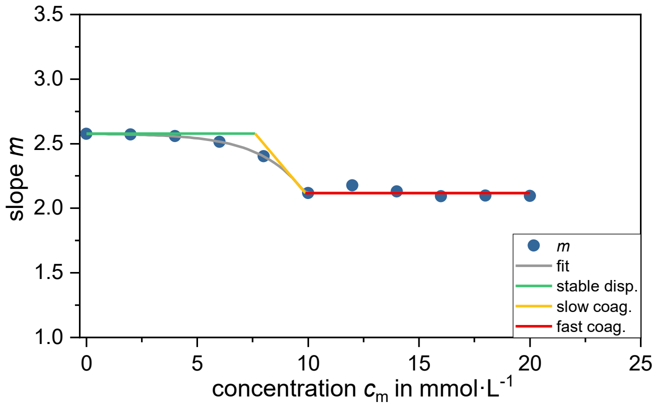

Fig. 7.12: Determination of the CCC for PVC@0.20 at 0.1 wt% by adding $CaCl_2$ and measuring the extinction at various wavelengths using a UV/Vis spectrometer. The CCC is determined to be 9.9 mmol·L^{-1} $CaCl_2$.The onset of coagulation (intersection of the green and yellow lines) and the CCC (intersection of the yellow and red lines) were identified using a step function.

7.6.2.4 Acoustic Attenuation

Fig. 7.13 illustrates the determination of the CCC using the acoustic attenuation method described in the main article. To compare with the reference methods detailed in the Supporting Information, the CCC of PVC@0.20 was evaluated as a function of $CaCl_2$ concentration at 10 wt%, with measurements performed at a frequency of 99.5 MHz, 30 minutes after mixing. Consistent with the procedure outlined in the main article, the evaluation involved fitting the measured attenuation at various electrolyte concentrations to Eq. 7.15, followed by the calculation of the Onset concentration and CCC using Eqs. 7.16 and 7.17. The results are likewise summarized in Tab. 7.5, providing a direct comparison across the different CCC determination methods.

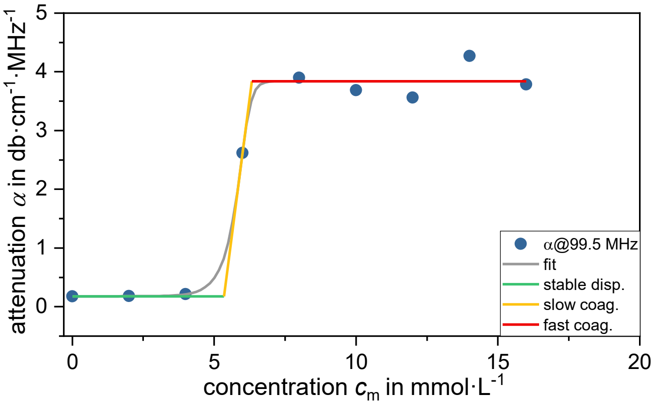

Fig. 7.13: Change in acoustic attenuation of PVC@0.20 at 10 wt% upon the addition of $CaCl_2$ at 99.5 MHz. The onset of coagulation (intersection of the green and yellow lines) and the CCC (intersection of the yellow and red lines) were determined using a sigmoidal function.

7.6.2.5 Comparison

The CCC and onset concentrations c_{onset} of PVC@0.20 were determined using aggregation rate, jar test, wavelength scan, and acoustic attenuation methods, with the results summarized in Tab. 7.5. The values indicate clear dependencies on the method, particle mass fraction w, and time elapsed between mixing and measurement t, reflecting the differing sensitivities of each technique to particle interactions and aggregation dynamics.

The c_{cr} values differ significantly between methods. The aggregation rate method, performed at 0.1 wt% with t of 1 s, yielded the highest c_{cr} of 27 mmol L^{-1}. The jar test and wavelength scan, both conducted at 0.1 wt% with t of 10 min, resulted in lower c_{cr} values of 12.3 and 9.9 mmol L^{-1}, respectively. The acoustic attenuation method, performed at 10 wt% and t of 30 min, yielded the lowest c_{cr} of 6.9 mmol L^{-1}. Despite these pronounced differences in c_{cr}, the c_{onset} values are relatively consistent across methods. This trend is attributed to the continuous progression of aggregation, even in the slow coagulation regime. Consequently, the lowest CCC observed with the acoustic attenuation method is a result of the longer observation time and higher particle concentration, which reflect higher progression of aggregation.

Tab. 7.5: Comparison of onset and CCC concentrations measured using different methods for PVC@0.20. The mass fraction and measurement duration significantly influence the determined CCC values.

method	c_{onset} [mmol·L^{-1}]	CCC[mmol·L^{-1}]	w [wt%]	t
Aggregation Rate	~4	27	0.1	1 s
Jar Test	5.4	12.3	0.1	10 min
Wavelength Scan	7.6	9.9	0.1	10 min
Acoustic Attenuation	4.0	6.9	10	30 min

Acknowledgments

This project has received fundings by the German Ministry of Education and Research (BMBF) as part of the funding program “Forschung an Fachhochschulen” under contract number13FH142PX6. We are also very grateful for valuable discussions and financial and material support provided by Westlake Vinnolit GmbH &Co. KG.

7.7 References

[1] Sokolova, V.; Epple, M. Inorganic nanoparticles as carriers of nucleic acids into cells. *Angewandte Chemie International Edition* **2008**, *47*, 1382–1395. DOI: 10.1002/anie.200703039.

[2] Tiwari, J. N.; Tiwari, R. N.; Kim, K. S. Zero-dimensional, one-dimensional, two-dimensional and three-dimensional nanostructured materials for advanced electrochemical energy devices. *Progress in Materials Science* **2012**, *57*, 724–803. DOI: 10.1016/j.pmatsci.2011.08.003.

[3] Dickinson, E. Food emulsions and foams: Stabilization by particles. *Current Opinion in Colloid & Interface Science* **2010**, *15*, 40–49. DOI: 10.1016/j.cocis.2009.11.001.

[4] Francis, M. J.; Glover, Z. J.; Yu, Q.; Povey, M. J.; Holmes, M. J. Acoustic characterisation of pH dependant reversible micellar casein aggregation. *Colloids Surf., A* **2019**, *568*, 259–265. DOI: 10.1016/j.colsurfa.2019.02.026.

[5] Kolman, K.; Nechyporchuk, O.; Persson, M.; Holmberg, K.; Bordes, R. Preparation of silica/polyelectrolyte complexes for textile strengthening applied to painting canvas restoration. *Colloids Surf., A* **2017**, *532*, 420–427. DOI: 10.1016/j.colsurfa.2017.04.051.

[6] Virden, J. W.; Berg, J. C. The use of photon correlation spectroscopy for estimating the rate constant for doublet formation in an aggregating colloidal dispersion. *J. Colloid Interface Sci.* **1992**, *149*, 528–535. DOI: 10.1016/0021-9797(92)90439-S.

[7] Bibeau, A.; Matijevic, E. Stability of polyvinyl chloride latex. *J. Colloid Interface Sci.* **1973**, *43*, 330–338. DOI: 10.1016/0021-9797(73)90380-9.

[8] Ottewill, R. H.; Watanabe, A. Studies on the mechanism of coagulation. *Kolloid-Zeitschrift* **1960**, *170*, 38–48. DOI: 10.1007/BF01520071.

[9] Bensley, C. N.; Hunter, R. J. The effect of particle volume fraction on the critical coagulation concentration. *J. Colloid Interface Sci.* **1982**, *88*, 546–561. DOI: 10.1016/0021-9797(82)90283-1.

[10] Cowell, C.; Vincent, B. Flocculation kinetics and equilibria in sterically stabilized dispersions. *J. Colloid Interface Sci.* **1983**, *95*, 573–582. DOI: 10.1016/0021-9797(83)90216-3.

[11] Long, J.; Osmond, D.; Vincent, B. The equilibrium aspects of weak flocculation. *J. Colloid Interface Sci.* **1973**, *42*, 545–553. DOI: 10.1016/0021-9797(73)90040-4.

[12] Ehringhaus, A. Objektive Demonstrationen mit Rutilsuspension. *Naturwissenschaften* **1934**, *22*, 149–150. DOI: 10.1007/BF01494784.

[13] Lagaly, G.; Schulz, O.; Zimehl, R. *Dispersionen und Emulsionen: Eine Einführung in die Kolloidik feinverteilter Stoffe einschließlich der Tonminerale*; Steinkopff: Heidelberg, 1997.

[14] Gregory, J. Monitoring particle aggregation processes. *Adv. Colloid Interface Sci.* **2009**, *147–148*, 109–123. DOI: 10.1016/j.cis.2008.09.003.

[15] Israelachvili, J. N. *Intermolecular and Surface Forces*; Academic Press, 2011.

[16] Sano, M.; Kamino, A.; Shinkai, S. Critical Coagulation of Langmuir Monolayers: 2D Schulze−Hardy Rule. *J. Phys. Chem. B* **2000**, *104*, 10339–10347. DOI: 10.1021/jp002387y.

[17] Perkins, R.; Brace, R.; Matijević, E. Colloid and surface properties of clay suspensions. I. Laponite CP. *J. Colloid Interface Sci.* **1974**, *48*, 417–426. DOI: 10.1016/0021-9797(74)90185-4.

[18] Dukhin, A. S.; Goetz, P. J. *Characterization of Liquids, Dispersions, Emulsions, and Porous Materials Using Ultrasound*, Third edition; Elsevier: Amsterdam, Oxford, Cambridge, MA, 2017.

[19] Epstein, P. S.; Carhart, R. R. The Absorption of Sound in Suspensions and Emulsions. I. Water Fog in Air. *The Journal of the Acoustical Society of America* **1953**, *25*, 553–565. DOI: 10.1121/1.1907107.

[20] Allegra, J. R.; Hawley, S. A. Attenuation of Sound in Suspensions and Emulsions: Theory and Experiments. *The Journal of the Acoustical Society of America* **1972**, *51*, 1545–1564. DOI: 10.1121/1.1912999.

[21] Dukhin, A. S.; Goetz, P. J. Acoustic Spectroscopy for Concentrated Polydisperse Colloids with High Density Contrast. *Langmuir* **1996**, *12*, 4987–4997. DOI: 10.1021/la951085y.

[22] Dukhin, A. S.; Goetz, P. J.; Hamlet, C. W. Acoustic Spectroscopy for Concentrated Polydisperse Colloids with Low Density Contrast. *Langmuir* **1996**, *12*, 4998–5003. DOI: 10.1021/la951572d.

[23] Dukhin, A. S.; Goetz, P. J. Characterization of aggregation phenomena by means of acoustic and electroacoustic spectroscopy. *Colloids Surf., A* **1998**, *144*, 49–58. DOI: 10.1016/S0927-7757(98)00565-2.

[24] Ali, S.; Bandyopadhyay, R. Aggregation and stability of anisotropic charged clay colloids in aqueous medium in the presence of salt. *Faraday Disc.* **2016**, *186*, 455–471. DOI: 10.1039/C5FD00124B.

[25] Tourbin, M.; Frances, C. Monitoring of the aggregation process of dense colloidal silica suspensions in a stirred tank by acoustic spectroscopy. *Powder Technology* **2009**, *190*, 25–30. DOI: 10.1016/j.powtec.2008.04.067.

[26] Hibberd, D.; Holmes, A.; Garrood, M.; Fillery-Travis, A.; Robins, M.; Challis, R. Ultrasonic Monitoring of Oil-in-Water Emulsions Undergoing Depletion Flocculation. *J. Colloid Interface Sci.* **1997**, *193*, 77–87. DOI: 10.1006/jcis.1997.5057.

[27] Chanamai, R.; Herrmann, N.; McClements, D. J. Probing Floc Structure by Ultrasonic Spectroscopy, Viscometry, and Creaming Measurements. *Langmuir* **2000**, *16*, 5884–5891. DOI: 10.1021/la991615g.

[28] Kippax, P.; Sherwood, J. D.; McClements, D. J. Ultrasonic Spectroscopy Study of Globule Aggregation in Parenteral Fat Emulsions Containing Calcium Chloride. *Langmuir* **1999**, *15*, 1673–1678. DOI: 10.1021/la981351i.

[29] Dukhin, A. S.; Goetz, P. J. Chapter 8 - Applications for Dispersions. In *Characterization of Liquids, Dispersions, Emulsions, and Porous Materials Using Ultrasound,* Third edition; Dukhin, A. S., Goetz, P. J., Eds.; Elsevier: Amsterdam, Oxford, Cambridge, MA, 2017; pp 307–355.

[30] Derjaguin, B.; Landau, L. Theory of the stability of strongly charged lyophobic sols and of the adhesion of strongly charged particles in solutions of electrolytes. *Progress in Surface Science* **1993**, *43*, 30–59. DOI: 10.1016/0079-6816(93)90013-L.

[31] Verwey, E. J. W.; Overbeek, J. T. G. *Theory of the Stability of Lyophobic Colloids*; Elsevier: New York, 1948.

[32] Gouy, M. Sur la constitution de la charge électrique à la surface d'un électrolyte. *J. Phys. Theor. Appl.* **1910**, *9*, 457–468. DOI: 10.1051/jphystap:019100090045700.

[33] Chapman, D. L. LI. A contribution to the theory of electrocapillarity. *The London, Edinburgh, and Dublin Philosophical Magazine and Journal of Science* **1913**, *25*, 475–481. DOI: 10.1080/14786440408634187.

[34] Schulze, H. Schwefelarsen in wässriger Lösung. *J. Prakt. Chem.* **1882**, *25*, 431–452. DOI: 10.1002/prac.18820250142.

[35] Hardy, W. B. A preliminary investigation of the conditions which determine the stability of irreversible hydrosols. *Proc. R. Soc. London* **1900**, *66*, 110–125. DOI: 10.1098/rspl.1899.0081.

[36] Kosmulski, M. The pH dependent surface charging and points of zero charge. X. Update. *Adv. Colloid Interface Sci.* **2023**, *319*, 102973. DOI: 10.1016/j.cis.2023.102973.

[37] Khademi, M.; Wang, W.; Reitinger, W.; Barz, D. P. J. Zeta Potential of Poly(methyl methacrylate) (PMMA) in Contact with Aqueous Electrolyte-Surfactant Solutions. *Langmuir* **2017.** DOI: 10.1021/acs.langmuir.7b02487.

[38] Kosmulski, M.; Kalbarczyk, M. Zeta Potential of Nanosilica in 50% Aqueous Ethylene Glycol and in 50% Aqueous Propylene Glycol. *Molecules (Basel, Switzerland)* **2023**, *28.* DOI: 10.3390/molecules28031335.

[39] Cosgrove, T., Ed. *Colloid science: Principles, methods and applications*, 2nd ed.; Wiley: Chichester, West Sussex, 2010.

[40] Agmo Hernández, V. An overview of surface forces and the DLVO theory. *ChemTexts* **2023**, *9.* DOI: 10.1007/s40828-023-00182-9.

[41] Zhu, B.-Y.; Gu, T. General isotherm equation for adsorption of surfactants at solid/liquid interfaces. Part 1. Theoretical. *J. Chem. Soc., Faraday Trans. 1* **1989**, *85*, 3813. DOI: 10.1039/f19898503813.

[42] Zhu, B.-Y.; Gu, T.; Zhao, X. General isotherm equation for adsorption of surfactants at solid/liquid interfaces. Part 2. Applications. *J. Chem. Soc., Faraday Trans. 1* **1989**, *85*, 3819. DOI: 10.1039/f19898503819.

[43] Zhu, B.-Y.; Gu, T. Surfactant adsorption at solid-liquid interfaces. *Adv. Colloid Interface Sci.* **1991**, *37*, 1–32. DOI: 10.1016/0001-8686(91)80037-K.

[44] Langmuir, I. The Adsorption of Gases on Plane Surfaces of Glass, Mica and Platinum. *J. Am. Chem. Soc.* **1918**, *40*, 1361–1403. DOI: 10.1021/ja02242a004.

[45] Gu, T.; Zhu, B.-Y. The S-type isotherm equation for adsorption of nonionic surfactants at the silica gel—water interface. *Colloids Surf.* **1990**, *44*, 81–87. DOI: 10.1016/0166-6622(90)80189-B.

[46] Vale, H. M.; McKenna, T. F. Adsorption of sodium dodecyl sulfate and sodium dodecyl benzenesulfonate on poly(vinyl chloride) latexes. *Colloids Surf., A* **2005**, *268*, 68–72. DOI: 10.1016/j.colsurfa.2005.05.061.

[47] Ohshima, H.; Healy, T. W.; White, L. R. Accurate analytic expressions for the surface charge density/surface potential relationship and double-layer potential distribution for a spherical colloidal particle. *J. Colloid Interface Sci.* **1982**, *90*, 17–26. DOI: 10.1016/0021-9797(82)90393-9.

[48] Frangenberg, M.; Schmidt, A. M.; Wilkens, J. Impact of surface conductivity on the zeta potential determination of concentrated aqueous polymer dispersions using electroacoustics and electrokinetic standard models. *Colloid Polym. Sci.* **2024**, *302*, 1801–1813. DOI: 10.1007/s00396-024-05301-7.

[49] Ohshima, H.; Healy, T. W.; White, L. R. Approximate analytic expressions for the electrophoretic mobility of spherical colloidal particles and the conductivity of their dilute suspensions. *J. Chem. Soc., Faraday Trans. 2* **1983**, *79*, 1613. DOI: 10.1039/f29837901613.

[50] Frangenberg, M.; Schmidt, A. M.; Wilkens, J. New Experimental Approach for the Proper Consideration of Stagnant and Diffuse Layer Conductivity in the Zeta Potential Determination. *Langmuir* **2025**, *41*, 5188–5201. DOI: 10.1021/acs.langmuir.4c04456.

[51] Meconi, G. M.; Ballard, N.; Asua, J. M.; Zangi, R. Adsorption and desorption behavior of ionic and nonionic surfactants on polymer surfaces. *Soft Matter* **2016**, *12*, 9692–9704. DOI: 10.1039/c6sm01878e.

[52] Hecht, L. L.; Schoth, A.; Muñoz-Espí, R.; Javadi, A.; Köhler, K.; Miller, R.; Landfester, K.; Schuchmann, H. P. Determination of the Ideal Surfactant Concentration in Miniemulsion Polymerization. *Macromolecular Chemistry and Physics* **2013**, *214*, 812–823. DOI: 10.1002/macp.201200583.

[53] Brown, W.; Zhao, J. Adsorption of sodium dodecyl sulfate on polystyrene latex particles using dynamic light scattering and zeta potential measurements. *Macromolecules* **1993**, *26*, 2711–2715. DOI: 10.1021/ma00063a012.

[54] Liu, S. Cooperative adsorption on solid surfaces. *J. Colloid Interface Sci.* **2015**, *450*, 224–238. DOI: 10.1016/j.jcis.2015.03.013.

[55] Israelachvili, J. N. *Intermolecular and surface forces*, 3rd ed.; Academic Press: Burlington, MA, 2011.

[56] Odian, G. G. *Principles of polymerization*, Fourth edition; Wiley: Hoboken, N.J, 2004.

[57] Smoluchowski, M. v. Versuch einer mathematischen Theorie der Koagulationskinetik kolloider Lösungen. *Zeitschrift für Physikalische Chemie* **1918**, *92U*, 129–168. DOI: 10.1515/zpch-1918-9209.

[58] Duangthanu, M.; Pattanaporkratana, A. Effect of surfactant concentration to aggregations of nanogold particles. *J. Phys.: Conf. Ser.* **2017**, *901*, 12098. DOI: 10.1088/1742-6596/901/1/012098.

[59] Helgason, T.; Awad, T. S.; Kristbergsson, K.; McClements, D. J.; Weiss, J. Effect of surfactant surface coverage on formation of solid lipid nanoparticles (SLN). *J. Colloid Interface Sci.* **2009**, *334*, 75–81. DOI: 10.1016/j.jcis.2009.03.012.

[60] Grau, C.; Schmidt, A. M.; Wilkens, J. Water-Based Polyurethane Dispersions: A Detailed Analysis of the Particle Charge Using Soft and Hard Particle Model. *Langmuir* **2024**, *40*, 22123–22135. DOI: 10.1021/acs.langmuir.4c02498.

[61] Israelachvili, J. N. Electrostatic Forces between Surfaces in Liquids. *Intermolecular and Surface Forces*; Elsevier, 2011; pp 291–340.

[62] Prieve, D. C.; Russel, W. B. Simplified predictions of Hamaker constants from Lifshitz theory. *J. Colloid Interface Sci.* **1988**, *125*, 1–13. DOI: 10.1016/0021-9797(88)90048-3.

[63] Hough, D. B.; White, L. R. The calculation of hamaker constants from liftshitz theory with applications to wetting phenomena. *Adv. Colloid Interface Sci.* **1980**, *14*, 3–41. DOI: 10.1016/0001-8686(80)80006-6.

[64] Cowell, C.; Li-In-On, R.; Vincent, B. Reversible flocculation of sterically-stabilised dispersions. *J. Chem. Soc., Faraday Trans. 1* **1978**, *74*, 337. DOI: 10.1039/f19787400337.

8 Comprehensive Discussion

The central aim of this dissertation is to improve the investigation of stability in concentrated polymer dispersions, where conventional characterisation techniques often fail due to optical opacity and the increasing complexity of interparticle interactions. Unlike dilute systems, where particle properties can often be treated in isolation, the behaviour of concentrated dispersions is governed by coupled effects which evolve nonlinearly with particle volume fraction. To address these challenges, this work employs two complementary acoustic techniques: electroacoustics (EA), based on colloidal vibration current (CVI) measurements and acoustic attenuation spectroscopy (AAS), also referred to as ultrasonic attenuation spectroscopy (UAS). These methods are selected for their ability to probe dispersions in their native, undiluted state and in optically opaque systems, overcoming major limitations of light-based techniques such as dynamic light scattering (DLS), laser diffraction spectroscopy (LDS) or electrophoretic light scattering (ELS). The experimental investigation focuses on a selection of polymer latices including PVC, PU, SBR, PTFE and PBAMM, which vary in particle size, material properties and surface chemistry.

The first part of the thesis focuses on the electrokinetic characterisation using CVI and ELS to determine the zeta potential in concentrated dispersions. In an initial study (Chapter 4), standard models such as the Helmholtz-Smoluchowski and Henry theories are used to evaluate the zeta potential. Surface conductivity is quantified via the Dukhin number. It is demonstrated that neglecting surface conductivity can cause substantial errors in zeta potential values, particularly in systems with high Dukhin numbers and at hight particle concentrations. In a second study (Chapter 5), advanced electrokinetic models are applied to incorporate polarization effects and explicitly resolve surface conductivity into stagnant and diffuse layer contributions. The combination of modified Ohshima-Healy-White and Dukhin-Semenikhin theories (for ELS), together with an advanced CVI theory, provides high zeta potential consistency between these methods, even at high volume fractions.

The second part of the thesis addresses the challenge of PSD determination in concentrated polymer dispersions using AAS (Chapter 6). Here, intrinsic particle absorption, which can be neglected for rigid inorganic dispersions, is modelled as an explicit contribution to the attenuation spectrum, alongside thermal and viscoinertial losses, using the coupled-phase model of Dukhin and Goetz. This extension allows for more accurate determination of median particle sizes, though uncertainties remain regarding the span and shape of the distribution.

The last part of the thesis turns to colloidal stability, quantified via the critical coagulation concentration (CCC) and explores how surfactant coverage, in type and amount, shifts the stability threshold (Chapter 7). Acoustic attenuation is shown to be a robust, non-optical method for determining CCC even in opaque or highly concentrated systems, offering practical advantages over turbidity-based methods.

This chapter now highlights the scientific contributions of the dissertation and illustrates them through selected experimental examples. The aim is to clarify the added value of the work as a whole, critically assess key limitations, and outline perspectives for future developments.

8.1 Electrokinetic Characterization

8.1.1 Standard Models

8.1.1.1 Scientific Contributions and Experimental Foundations

To assess the validity of conventional electrokinetic models in concentrated polymer dispersions, the sample PVC@0.20 is presented as an illustrative example. This polyvinyl chloride dispersion, with a median particle diameter of 0.20 µm, is produced via emulsion polymerisation by Westlake Vinnolit GmbH & Co. KG. The PVC@0.20 sample is used here and in subsequent sections for the comprehensive discussion because it is investigated in every part of the thesis. Its consistent inclusion allows for a coherent illustration of key findings and a direct comparison of results obtained in the different studies.

A key contribution of this study (Chapter 4) lies in the correct consideration of the effective internal electric field (E_{int}) by incorporating conductivity measurements of both the dispersion (K_{s}) and the dispersion medium (K_{m}). This correction is crucial in polymer dispersions, where surface conductivity can have a substantial impact on zeta potential determination, especially at high particle volume fractions. As shown in Fig. 4.1 the measured conductivity relative conductivities $K_{\mathrm{s}}K_{\mathrm{m}}^{-1}$ for PVC@0.20 deviate markedly from the behaviour expected for systems without surface conductivity ($Du = 0$). Evaluation based on Maxwell–Wagner–O'Konski (MWO) theory [146–148], yields a significant Dukhin number ($Du = 0.41$), confirming the strong influence of surface conductivity (refer to Chapter 4.4.1.1). Neglecting this effect leads to pronounced errors up to 100 % in the calculated zeta potential, especially at higher particle, as demonstrated in Fig. 4.4, which compares three approaches to zeta potential evaluation based on the Helmholtz-Smoluchowski model. The first approach, which is the default in commercial CVI evaluation routines, neglects surface conductivity and systematically overestimates the zeta potential with increasing φ. In contrast, the second approach applies a direct consideration of the measured conductivity ratio $K_{\mathrm{s}}K_{\mathrm{m}}^{-1}$, while the third approach relies on the Dukhin number derived from the MWO fit. Both corrected approaches yield nearly constant zeta potentials over the entire concentration range. For PVC@0.20, the zeta potentials obtained from CVI and ELS are in excellent agreement across all applied models, confirming the reliability of both methods and the validity of the conductivity-based corrections (Chapter 4.4.2.1). This consistency demonstrates that conventional electrokinetic models remain applicable to concentrated dispersions when surface conductivity is properly accounted for.

This study thus provides an important methodological improvement: standard electrokinetic models such as the Helmholtz-Smoluchowski and Henry equations in principle remain applicable, but require explicit correction for surface conductivity to yield reliable results in concentrated dispersions. This requirement is particularly critical for polymer latexes, which often exhibit pronounced surface conductivity at low ionic strengths. The difficulties introduced by such effects may, in part, explain why polymer dispersions have historically been underrepresented in electroacoustic research.

8.1.1.2 Limitations and Outlook

In contrast to PVC@0.20, which demonstrates how conductivity-based corrections can extend the applicability of standard models, the sample PTFE@0.21 reveals clear limitations. This polytetrafluoroethylene dispersion, with a median particle diameter of 0.21 μm, corresponds to the commercial product PFA 6900 GZ and is supplied by 3M Dyneon GmbH. The measured relative conductivities ($K_s K_m^{-1}$) of this system show no consistent trend with particle concentration and deviate markedly from the behaviour predicted by Maxwell–Wagner–O'Konski theory. As a result, the Dukhin number cannot be reliably estimated, which in turn precludes application of the third, model-based correction approach (see Fig. 4.2 and Chapter 4.4.1.1).

The zeta potential is therefore evaluated using only the first and second approaches, as presented in Fig. 8.1. The first approach, which neglects surface conductivity, leads to a slight but systematic increase in zeta potential with rising particle concentration. In contrast, the second approach, based on direct incorporation of the measured conductivity ratio $K_s K_m^{-1}$, yields nearly constant zeta potential values over the full volume fraction range. This outcome again confirms the empirical robustness of conductivity-based correction, even where MWO theory is not applicable.

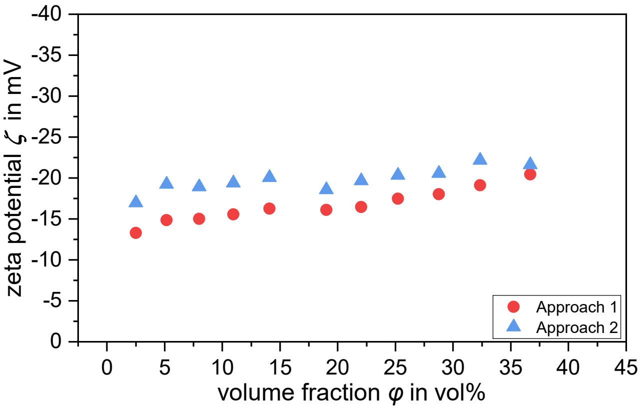

Fig. 8.1: Electrokinetic characterisation of PTFE@0.21. Measurements were performed at pH 9.3 using equilibrium dilution with the supernatant; the exact electrolyte concentration is unknown. Zeta potentials were calculated using the first and second Helmholtz–Smoluchowski approaches (Chapter 4.2): approach 1 (red circles) and approach 2 (blue triangles). The third approach was not applicable due to inconsistencies in the conductivity behaviour.

Independent measurement using ELS further supports these findings. The zeta potentials obtained from CVI and ELS show close agreement for PTFE@0.21, confirming the reliability of the CVI results even in the absence of a validated surface conductivity model. The consistency across these methods underscores the reliability of the CVI results, even in the absence of a validated model for surface conductivity (Chapter 4.4.2.1).

The unusual conductivity behaviour observed may be attributed to the surface chemistry of the particles. Both studied PTFE samples (PTFE@0.21 and PTFE@0.08) are stabilised using non-ionic surfactants and exhibit comparable deviations from theoretical predictions. Similar deviations are reported for systems containing non-ionic polymers [136]. In this light, PTFE@0.21 is regarded as a limiting case that marks the boundary of model applicability. Although empirical correction still yields consistent zeta potential values, the inability to apply MWO theory reveals a conceptual gap.

While standard electrokinetic models remain valuable due to their simplicity and widespread use, their applicability to concentrated systems is inherently limited without accounting for surface conductivity. This study demonstrates that conductivity-based corrections are essential for reliable zeta potential determination when surface conductivity is non-negligible (say $Du > 0.1$), particularly at high particle volume fractions.

A practical challenge associated with such measurements lies in the preparation of equilibrium dilutions. Artefacts caused by an uncontrolled variation of the electrolyte concentration during dilution can affect the reliability of both conductivity and zeta potential data. Further refinement and simplification of the sample preparation protocol would therefore be highly beneficial. One yet untested but potentially effective approach involves isolating small volumes of the dispersion medium from the undiluted dispersion, for example by centrifugation, followed by measurement of its conductivity and pH value. A simulated dispersion medium matching these parameters can then be prepared and used to dilute the concentrated dispersion, enabling almost equilibrium dilution with significantly reduced experimental effort.

Even with reliable sample preparation, full conductivity characterisation across a wide concentration range remains time-consuming. One practical option, for example, is to reduce the number of measurements across the entire concentration range. For instance, the example below demonstrates that Dukhin numbers can be determined with sufficient accuracy using only three representative volume fractions (see Tab. 8.1). Specifically, values of $K_\mathrm{s}K_\mathrm{m}^{-1}$ measured at approximately 10, 20 and 30 vol% are sufficient to capture the overall trend (see column $Du_{10,20,30}$), yielding results that are in most cases, comparable to those obtained from full-range fitting (see column Du). This strategy substantially reduces the experimental effort.

Tab. 8.1: Comparison of Dukhin numbers calculated using different methods: full conductivity fit Du, reduced dataset at 10, 20, 30 vol% $Du_{10,20,30}$ and approach 3 based on zeta potential consistency Du_CVI

sample	Du	$Du_{10,20,30}$	Du_CVI
PVC@0.20	0.410	0.443	0.553
PVC@0.78	0.254	0.229	0.582
PVC@2.09	0.283	0.273	0.256
SBR@0.23	0.256	0.370	0.279
PU@0.07	0.348	0.324	0.106
PBAMM@0.10	0.114	0.126	0.050

An increase in the absolute value of the zeta potential observed with the first evaluation approach (as illustrated in Fig. 4.4, for example) may indicate the presence of surface conductivity. This characteristic behaviour can be exploited as a complementary strategy for estimating the Dukhin number based on the electrokinetic consistency principle. According to this principle, the zeta potential of a dispersion should remain constant with increasing particle volume fraction, provided that surface conductivity is correctly accounted for. In this approach, the Dukhin number in Eq. 4.20 is adjusted with a least-square fit until the calculated zeta potentials are as uniform as possible across the entire concentration range (refer to Chapter 4.2 and Chapter 4.6.1). In this way, the Dukhin number cab be determined even in the absence of direct conductivity measurements. However, the results in Tab. 8.1 (see column Du_{CVI}) show that this approach leads to significant deviations in most samples when compared to the values obtained from conductivity-based determination. Only in a few cases, such as PVC@2.09 or SBR@0.23, the results are in good agreement.

8.1.2 Advanced Models

8.1.2.1 Scientific Contributions and Experimental Foundations

A central achievement of this work lies in the comprehensive electrokinetic characterisation of concentrated polymer dispersions using advanced theoretical models that account for surface conductivity contributions from the diffuse layer conductivity (DLC) and the stagnant layer conductivity (SLC), as detailed in Chapter 5. As a representative example, the PVC@0.20 sample is employed again in this section due to its well-defined equilibrium dilution and the availability of ELS and CVI data across a wide concentration range.

Accurate determination of the zeta potential in both concentrated and dilute systems requires proper consideration of the relaxation effect, which becomes important in case of high potentials. It arises from the polarization of the electrical double layer and manifests as surface conductivity. In contrast to the classical approximation of Bikerman, which considers only the DLC, the present study applies the Maxwell–Wagner–O'Konski (MWO) theory in combination with experimental conductivity data to evaluate the Dukhin number, $Du^{\mathrm{d+s}}$. This parameter captures the combined contributions from both SLC and DLC.

As shown in Fig. 5.2, the application of the advanced CVI theory by Dukhin et al. (Eqs. 5.12 and 5.13) to the PVC@0.20 dispersion clearly demonstrates the impact of including full surface conductivity in the evaluation. When both the dispersion (K_{s}) and the dispersion medium (K_{m}) conductivities are experimentally measured and combined through the Maxwell–Wagner–O'Konski (MWO) framework, the resulting zeta potential ($\zeta^{\mathrm{d+s}}_{\mathrm{CVI}}$) remains nearly constant over the examined concentration range. This concentration independence confirms that the relaxation effect is correctly accounted for in the analysis. In contrast, evaluations that rely on the Dukhin number estimated internally by the CVI instrument ($Du^{\mathrm{d}}_{\mathrm{DT}}$), following Bikerman approximation, neglect the stagnant layer contribution and depend solely on the measured dispersion conductivity (K_{s}). Although this simplified procedure yields zeta potentials ($\zeta^{\mathrm{d}}_{\mathrm{CVI}}$) of similar magnitude, these values exhibit a clear dependence on concentration and therefore do not meet fundamental requirements (Chapter 5.4.2.1).

Complementary support is provided by independent ELS measurements conducted in highly diluted samples. Three distinct electrokinetic models were applied to evaluate the ELS data: the modified Ohshima-Healy-White (OHW) theory (Eq.°5.14 under consideration of Eq. 5.21), the full Dukhin–Semenikhin (DS) theory (Eqs. 5.22-5.28) and the classical OHW model (Eq.°5.14 under consideration of Eq. 5.16). Both the modified OHW and DS approaches yield nearly identical zeta potentials, whereas the classical OHW model predicts noticeably smaller absolute zeta potentials because it neglects stagnant layer conductivity (SLC). The close agreement between the advanced ELS models and the CVI results further supports the consistency of the electrokinetic parameters derived in this study (see Tab. 5.3).

Thus, the PVC@0.20 sample exemplifies the methodological innovation and scientific contribution of this study. By evaluation of the experimentally measured conductivity of the dispersion K_s and of the dispersion medium K_m with the MWO theory, the Dukhin number $Du^{\mathrm{d+s}}$ can be determined. This parameter provides the basis for an accurate and consistent evaluation of the zeta potential across a wide range of particle concentrations. This proves particularly essential in systems with significant SLC contributions, such as the PVC@0.20 dispersion. This approach substantially improves the accurate determination of the zeta potential, both in concentrated systems via CVI and in dilute conditions via ELS measurements.

The study further demonstrates that once $Du^{\mathrm{d+s}}$ is known, the parameter p introduced in the full Dukhin–Semenikhin theory to account for diffusional asymmetries in the stagnant layer becomes unnecessary for accurate zeta potential determination (see Chapter 5.6.3). Additionally, the classical Ohshima-Healy-White (OHW) theory is modified by incorporating the Dukhin number to account for the surface conductivity, enabling its application to systems with significant SLC. This modified OHW theory (see Chapter 5.2.5.1), represents another key contribution of this work. Altogether, these advances establish a generalised and experimentally validated framework for electrokinetic characterisation in colloidal systems, enhancing the accuracy and interpretability of both CVI and ELS measurements.

8.1.2.2 Limitations and Outlook

The advanced CVI theory presented in this work enables a consistent determination of the zeta potential across a broad range of particle volume fractions. However, its practical applicability is limited by the considerable experimental effort required. A reliable evaluation of the zeta potential demands, experimental determination of the Dukhin number $Du^{\mathrm{d+s}}$, which involves conductivity measurements of the dispersion (K_s) and dispersion medium (K_m). This effort can only be reduced if the SLC is negligible compared to the DLC, a condition that itself must be verified experimentally, for instance by CVI measurements at several particle volume fractions. In systems such as SBR@0.23, this prerequisite is fulfilled, and simplified evaluations provide comparable results (see Fig. 5.5 C and Chapter 5.4.2.4). A more fundamental limitation of the presented method arises in systems where the Dukhin number cannot be determined at all. This occurs, for example, with the PTFE samples discussed earlier. If the relative conductivity data are too noisy, inconsistent, or do not exhibit a plausible trend with particle volume fraction, the MWO theory fails. As a result, no

Dukhin number and therefore no reliable zeta potential can be extracted using the advanced models. This scenario defines the practical limit of applicability for the new experimental approach introduced in this work.

To further develop the methodological framework established in this study, future investigations should extend the analysis to a wider selection of colloidal systems with systematically varied physicochemical properties. These include differences in chemical composition and type of electrostatic or steric stabilisation. Beyond refining the applicability of advanced electrokinetic models, such studies could address an open question: why do certain systems exhibit surface conductivity and under which conditions do either diffuse layer conductivity (DLC) or stagnant layer conductivity (SLC) dominate its contribution?

To provide an initial perspective on this aspect, additional experimental results on several inorganic dispersions are presented in the Appendix (see Chapter 12.1). These supplementary measurements offer first qualitative insights into the occurrence and magnitude of surface conductivity in oxide-based systems and emphasize the need for further systematic investigations.

8.2 Particle Size Determination

8.2.1 Scientific Contributions and Experimental Foundations

To evaluate the applicability of advanced acoustic models for determining particle size distributions (PSD) in concentrated polymer dispersions, the polyurethane dispersion PU@0.07 is presented as an exemplary case. This latex, with a d_{50} of 0.069 µm, is synthesized in the laboratory using a polyester-based prepolymer. PU@0.07 is chosen for this section due to its consistent PSD results across various volume fractions and its good agreement with reference measurements, providing a robust basis for illustrating the methodical advances introduced in this study.

A central contribution of this work lies in the incorporation of intrinsic particle absorption into the PSD determination using acoustic attenuation spectroscopy (AAS). In practical applications of AAS, intrinsic absorption is often neglected. This omission may be acceptable for rigid or inorganic particles but introduces significant error when applied to soft polymer dispersions. However, as shown in Chapter 6, the intrinsic absorption of polymer particles contributes substantially to the total attenuation spectrum. The intrinsic absorption is estimated for all polymer dispersions studied by subtracting modelled attenuation from experimentally measured attenuation spectra. The simulated attenuation is calculated using the Dukhin-Goetz coupled-phase model, [12,97,101] with input from measured thermophysical parameters and reference particle size distributions. For the PU@0.07 dispersion, the experimentally determined intrinsic particle attenuation at various particle volume fractions is shown in Fig. 6.1 and is well described by a second-order polynomial fit (Eq. 6.10). In most literature, the intrinsic particle attenuation of polymers is described by a single longitudinal attenuation constant (Eq. 6.9). The data for PU@0.07 are consistent with this description up to approximately 70 MHz; at higher frequencies, a systematic deviation from this model becomes evident. However, the existing literature on polymer dispersions is generally restricted to single-frequency measurements or to frequency ranges well below 10 MHz, in contrast to the broader range investigated in the present study (3-100 MHz; refer to Chapter 6.4.2).

Importantly, the particle size distributions (PSDs) determined by AAS, using the intrinsic absorption described by the second-order polynomial fit, show excellent agreement with those obtained from dynamic light scattering (DLS) across all investigated particle volume fractions (see Fig. 6.7). Both methods yield consistent median particle sizes and comparable span values, confirming that incorporation of the experimentally determined intrinsic particle attenuation enables accurate PSD determination by AAS. This holds, even for soft colloidal systems at high particle concentrations (up to 42 vol%), where optical methods such as DLS become unreliable (Chapter 6.4.4).

The excellent agreement between modelled and experimental attenuation spectra for PU@0.07 supports the validity of the derived intrinsic attenuation function. Intrinsic particle absorption is identified as the dominant dissipative mechanism across the entire frequency range (refer to Fig. 6.4). In contrast, viscoinertial contributions are minor and scattering losses are neglected due to the small particle size (see Chapter 6.4.3). Overall, the PU@0.07 sample provides a convincing proof of concept for the proposed AAS-based PSD determination methodology.

8.2.2 Limitations and Outlook

While the polyurethane sample PU@0.07 illustrates the potential of acoustic attenuation spectroscopy (AAS) for reliable PSD determination in concentrated polymer dispersions, the PVC@0.20 sample is selected as a representative example that reveals important limitations of the approach. In principle, most of these limitations apply to all investigated dispersions except for the PU@0.07 sample.

For the PVC@0.20 dispersion, the determined intrinsic particle attenuation spectrum, shown in Fig. 6.3, is also well described by a second-order polynomial function. However, the intrinsic particle attenuation values exhibit greater variation across the different examined particle volume fractions. As with the PU@0.07 sample, the intrinsic particle attenuation follows a single longitudinal attenuation constant up to about 30 MHz, but systematic deviations from this simplified model become evident at higher frequencies (Chapter 6.4.2).

As shown in Fig. 6.9, the median particle sizes determined by AAS remain consistent across all concentrations and are in good agreement with the DLS reference. However, the span values exhibit a systematic and physically implausible decrease with increasing particle concentration. This trend raises critical concerns about the robustness of the PSD fitting, particularly regarding the accurate determination of distribution width (refer to Chapter 6.4.4).

As detailed in Fig. 6.5, the attenuation spectra can be reproduced with acceptable accuracy using the Dukhin-Goetz model and the fitted intrinsic absorption function. However, the progressive decrease of the span values with increasing φ suggests that the algorithm's sensitivity to minor deviations in the measured attenuation, may introduce significant artefacts in the distribution width. Discrepancies, particularly in the low-frequency range (3 and 12.7 MHz), suggest that the current model does not fully capture all dissipative mechanisms (Chapter 6.4.3), a similar discrepancy has also been reported in earlier studies on PVC dispersions.[245]

In summary, PVC@0.20 serves as a representative example of the current methodical boundaries. Although the modelled d_{50} values are consistent with reference methods, the implausible variation in span values and the unexplained excess attenuation at low frequencies highlight unresolved theoretical and experimental challenges.

The preceding text highlight both the strengths and limitations of using acoustic attenuation spectroscopy (AAS) to determine particle size distributions (PSDs) in concentrated polymer dispersions. The findings underscore the feasibility of this method for extracting consistent median particle diameters (d_{50}) across a wide range of materials and volume fractions, provided that intrinsic particle absorption is explicitly accounted for. However, the results also expose persistent limitations in accurately resolving the PSD width.

From a methodological perspective, one key insight of this study is that the median particle diameter can be reliably determined even when simplified or averaged input parameters are used, as demonstrated for the PVC samples (see Chapter 6.4.5). This opens up practical opportunities for PSD analysis in routine settings where access to detailed thermophysical characterisation is limited. In such cases, the use of literature-based or sample-averaged parameter sets may provide sufficient accuracy for process control, batch comparison, or quality assurance applications, especially in industrial contexts such as emulsion polymerisation or wet milling, where relative changes in PSD are often more relevant than absolute values.

Another way to improve the accuracy of the results presented in this study is to apply alternative theoretical models that may be able to describe the underlying attenuation mechanisms more comprehensively. For example, the so-called universal coupled-phase model proposed by Babick [77], which is originally developed for emulsions, or modern theories of multiple scattering [312,313] could provide more accurate results, especially for systems with higher concentrations or complex interactions.

Overall, AAS provides a promising method for the determination of median particle diameters in systems inaccessible to optical techniques, even when using averaged input parameters. While it does not yet resolve full PSDs, particularly in terms of width, the results highlight its practical value for routine analysis. With continued model development and validation, AAS shows strong potential for in situ characterisation in both scientific and industrial contexts.

8.3 Colloidal Stability

8.3.1 Scientific Contributions and Experimental Foundations

A key objective of this work is to establish acoustic attenuation as a robust method for a quantitative determination of the critical coagulation concentration (CCC) in concentrated colloidal dispersions (for more details refer to Chapter 7). To illustrate this, the PVC@0.20 sample is again used as a representative example. In this section, it serves to exemplify the role of surface coverage in modulating the CCC. These findings show how changes in surface chemistry can significantly shift the onset of electrolyte-induced aggregation.

Fig 7.2 shows the adsorption isotherm of SDS on the PVC@0.20 particles at a particle concentration of 15 wt%. For each data point, the dispersion was equilibrated with a defined amount of SDS, then centrifuged and filtered to separate the supernatant. The residual surfactant concentration is quantified by ionic surfactant titration, and the adsorbed amount per unit surface area is calculated from the difference between added and free surfactant. The fitted curve follows an S-type isotherm, and the analysis indicates cooperative adsorption behaviour (Chapter 7.4.1). The obtained parameters are consistent with literature data for comparable PVC systems.[296,299]

As described Chapter 7.4.2 and shown in Fig. 7.5, the influence of surfactant coverage on colloidal stability is investigated by measuring acoustic attenuation as a function of electrolyte concentration. Dispersions with different degrees of surfactant coverage are examined to assess the influence of surface chemistry on colloidal stability. At all surface coverage levels, the attenuation initially remains constant with increasing electrolyte concentration, indicating a stable dispersion. Beyond a certain concentration, a pronounced rise in attenuation signals the onset of particle aggregation caused by electrostatic destabilisation. The data are fitted with a logistic function (Eq. 7.15) to determine the onset of coagulation (Eq. 7.16) and the corresponding CCC (Eq. 7.17).

The results reveal a clear stabilising effect of increasing surfactant coverage. With higher surface coverage, the critical coagulation concentration (CCC) shifts to higher electrolyte levels, reflecting stronger electrostatic repulsion between the particles. This trend is consistent with the measured zeta potentials, which become more negative as the amount of adsorbed surfactant increases. Together, these observations confirm that enhanced surface charge density leads to a higher energy barrier against coagulation.

As mentioned before, in contrast to conventional techniques, the acoustic method remains applicable in dispersions with high optical density, elevated particle volume fractions, or larger particle sizes, where optical approaches often fail. The PVC@0.20 example demonstrates its capability to resolve stability shifts induced by surface-active additives.

8.3.2 Limitations and Outlook

While the critical coagulation concentrations determined for PVC@0.20 demonstrate the suitability of acoustic attenuation as a stability probe in concentrated dispersions, some methodical limitations must be considered. These are best illustrated through a comparison of different CCC determination techniques, as summarised in Tab. 7.5. Despite being conducted on the same dispersion system, the methods yield substantially different results, revealing the strong influence of particle concentration and measurement duration on the determined CCC values (refer to Chapter 7.6.2).

The comparison reveals a systematic dependence of the measured CCC on both the particle mass fraction and the time interval between electrolyte addition and data acquisition. Fast methods at low particle concentrations, such as the aggregation rate approach, tend to yield higher CCC values, while slower methods at higher concentrations, such as acoustic attenuation result in lower CCC values. This trend is comprehensible as it reflects the underlying aggregation kinetics: higher particle concentrations increase collision frequencies and longer measurement times allow more aggregation to occur before detection. Consequently, the measured CCC appears at lower electrolyte concentrations.

In principle, measurement techniques with fast data acquisition and low particle volume fractions, like the aggregation rate method, are the most accurate in capturing a reliable kinetic threshold, at which the energy barrier to aggregation vanishes. This threshold, defined as the CCC, is fundamentally governed by interparticle forces, but its experimentally determined value also depends on parameters of the measurement protocol, including particle concentration and time resolution. However, as already noted, such rapid methods are typically constrained to dilute systems and are less suitable for larger particles. In this context, acoustic attenuation remains practical and robust, even if the CCC values are slightly underestimated. Its ability to operate under realistic, industrially relevant conditions underscores its value for monitoring stability trends rather than extracting precise interaction parameters.

The application of acoustic attenuation measurement to determine the critical coagulation concentration in concentrated dispersions opens promising perspectives for future studies on colloidal stability. The method proves particularly valuable when undiluted and optically opaque systems are investigated, where conventional optical techniques are no longer applicable. Further research may focus on highly concentrated dispersions, in which double-layer overlap becomes significant. At elevated volume fractions, the local ionic environment can be strongly influenced by neighbouring particles. Dilution disrupts this arrangement, so stability behaviour observed at low concentrations may not represent the original system. By enabling direct measurements, acoustic attenuation measurement offers a unique advantage for obtaining stability information under these conditions.

Another important aspect concerns the influence of process-related stresses. In practical applications, dispersions are often exposed to mixing, pumping, stirring or heating at high solids concentrations. Both shear and temperature changes can significantly affect aggregation processes and these effects cannot be captured adequately in diluted systems. Time-resolved acoustic measurements therefore offer a powerful tool of analysing stability under realistic processing environments. Strongly light-absorbing dispersions containing pigments such as carbon black represent material where conventional optical methods fail. In these cases, acoustic attenuation measurement remains applicable and allows the determination of CCC under realistic formulation conditions. Overall, these findings suggest that acoustic attenuation measurements can provide valuable insights into dispersion stability under realistic and industrially relevant conditions.

In summary, this comprehensive discussion demonstrates that acoustic and electroacoustic methods together provide a coherent framework for characterising concentrated polymer dispersions under conditions inaccessible to optical techniques. By explicitly accounting for surface conductivity in electrokinetic analysis and intrinsic particle absorption in acoustic attenuation spectroscopy, reliable zeta potentials and median particle sizes can be obtained even at high solids contents. Although challenges remain in accurately describing the particle size distribution width and in determining the fundamentally correct critical coagulation concentration (CCC), the results clearly establish the potential of acoustic techniques as practical tools for assessing dispersion stability under formulation conditions relevant to industrial applications.

9 Summary

This dissertation presents a detailed investigation of the stability of concentrated polymer dispersions, focusing on zeta potential determination, particle size distribution (PSD) analysis and colloidal stability evaluation. By utilizing advanced acoustic techniques, such as colloidal vibration potential (CVI) and acoustic attenuation spectroscopy (AAS), this work addresses key challenges in colloid science, offering novel methodologies and theoretical frameworks that enhance the accuracy and applicability of these techniques. The experimental material concept is based on a diverse set of aqueous polymer dispersions differing in chemical composition, particle size, and interfacial properties, including poly vinyl chloride (PVC), styrene-butadiene rubber (SBR), polytetrafluoroethylene (PTFE), polyurethane (PU) and polymethyl methacrylate-*co*-butyl acrylate (PBAMM). These systems are selected to represent a broad range of mechanical stiffness, polarity, and density contrasts relevant to acoustic and electrokinetic behaviour. PVC serves as the primary reference material throughout this work because of its intermediate mechanical and interfacial properties, enabling systematic comparison across all measurement techniques. Furthermore, this work explores an underrepresented area in the scientific literature, as electroacoustic methods and AAS have predominantly been applied to inorganic materials. The findings thus contribute to a deeper understanding of the underlying mechanisms while offering improvements in the methods used for analysing and formulating dispersions.

Chapter 4 investigates the zeta potential of aqueous polymer dispersions using colloidal vibration current (CVI) measurements at high particle concentrations and electrokinetic light scattering (ELS) in the dilute state as reference. Data from both methods are interpreted using the Helmholtz-Smoluchowski (HS) and Henry equations, which in principal disregard surface conductivity effects. Nevertheless, this work shows that this parameter can have a significant influence on the results. To quantify the influence of surface conductivity, the dimensionless Dukhin number is estimated based on Maxwell-Wagner-O'Konski theory, utilizing the ratio of the dispersion's conductivity (K_s) to that of the medium (K_m). In suspensions with high particle volume fraction, nonconductive particles (dielectrics) lower the effective internal electric field, while surface conductivity counteracts this reduction by enabling charge transport along particle surfaces. The ratio $K_\mathrm{s}K_\mathrm{m}^{-1}$ effectively captures both effects on the zeta potential determination within the HS and Henry model. All investigated dispersions exhibit notable surface conductivity, which significantly influences zeta potential measurements in electroacoustic experiments. Neglecting the surface conductivity can result in significant measurement errors up to 100 %, particularly when particle volume fractions or Dukhin numbers are large. Equilibrium dilution represents the most reliable approach for preparing samples to achieve accurate zeta potential measurements. However, even when equilibrium dilution conditions are not fulfilled (i.e. when dilution alters the ionic composition of the dispersion medium), zeta potential values derived from CVI measurements remain highly consistent with those obtained via the ELS method.

Chapter 5 extends the theoretical foundation established in Chapter 4 by applying advanced models that incorporate polarization effects to improve the accuracy of zeta potential measurements. An electrokinetic consistency test is performed to evaluate the agreement between the CVI and ELS measurement results. The ELS data are analysed using the full and simplified Dukhin-Semenikhin (DS) theory, as well as the original Ohshima-Healy-White (OHW) theory. We also modify the OHW theory to account for surface conductivity via the Dukhin number. The advanced CVI theory, is applied to incorporate the Dukhin number for a more precise evaluation. The study underscores the importance of considering for surface conductivity effects in CVI measurements and introduces a combined approach that again utilizes conductivity data from both the dispersion and the dispersion medium to refine zeta potential analysis. Detailed insights are provided into stagnant layer conductivity (SLC) and diffuse layer conductivity (DLC). The Dukhin number is identified as a crucial parameter for quantifying the contributions of SLC and DLC, determined experimentally via Maxwell-Wagner-O'Konski theory, as shown in Chapter 4. The results confirm the significant role of surface conductivity in all investigated polymer dispersions, with both SLC and DLC contributing notably. Neglecting SLC leads to underestimations of zeta potential. It is shown for the full DS theory that the parameter p, which accounts for ion diffusion differences in the stagnant layer, is unnecessary for zeta potential determination if the Dukhin number is known. The advanced CVI theory is validated for high-volume fractions and provided excellent zeta potential consistency with ELS results. Shortcomings of the original OHW theory for samples with high SLC conductivity become evident when comparing with the DS theory or modified OHW theory.

The determination of particle size distribution (PSD) in concentrated polymer latices, a long-standing challenge in colloid science, is systematically examined in Chapter 6. This section especially examines how intrinsic particle absorption impacts PSD analysis using acoustic attenuation spectroscopy (AAS). A new approach based on the coupled phase model developed by Dukhin and Goetz is developed to account for the viscoinertial, thermal and scattering losses, with intrinsic particle absorption explicitly included as an essential component of the attenuation spectrum. Intrinsic absorption is determined by isolating its contribution to the total attenuation spectrum through comparison of the experimental data with theoretical predictions for viscoinertial and thermal losses. The findings demonstrate that by incorporation of the intrinsic absorption into the AAS model, the accuracy of PSD determination is significantly enhanced. As shown by good agreement between AAS and DLS particle size distribution results. However, discrepancies observed for some samples indicate the presence of additional attenuation mechanisms, necessitating further refinement of the model. While AAS proves effective for approximating mean particle size (d_{50}) in concentrated dispersions, challenges remain in accurately capturing the PSD span. The study also highlights material-dependent attenuation behavior, with intrinsic absorption potentially affected by properties such as crystallinity and elasticity. The methodology offers a robust framework for addressing the complexity of PSD determination in concentrated polymer dispersions, contributing to a deeper understanding of their colloidal properties and broadening the applicability of acoustic techniques in colloid science.

Chapter 7 examines the colloidal stability of two concentrated PVC dispersions differing in particle size and surfactant composition, with the objective of establishing acoustic attenuation as a method for the determination of the critical coagulation concentration (CCC). The results demonstrate that AAS can reliably capture stability behaviour even at high solids contents, where optical methods cannot be used. Increasing amounts of adsorbed surfactant shift the CCC toward higher electrolyte concentrations, reproducing established stabilization trends and validating the method especially for high solids content. At the same time, deviations from dilute-sample measurements reveal how particle concentration and measurement duration influence the experimentally determined CCC. Under non-dilute conditions or during prolonged measurements, aggregation may proceed faster than it can be accurately resolved, causing the experimentally observed CCC to appear lower than its true value and making its reliable determination more challenging. The internal consistency for both PVC dispersions and different surfactant coverages underscores the robustness of acoustic attenuation for comparative stability analysis. The principal contribution of this study is methodological, demonstrating that acoustic attenuation enables CCC determination in concentrated, industrially relevant dispersions where conventional methods are often limited.

Dispersion stability provides the unifying theme of this dissertation, which addresses key challenges in the characterization of concentrated polymer dispersions. It introduces refined models and novel approaches for electroacoustics and acoustic attenuation spectroscopy, enabling improved determination of zeta potential, particle size distribution and colloidal stability in concentrated systems, where conventional techniques often fail. Altogether, the presented methodologies offer practical tools for the improvement of dispersion characterization and stabilization, while opening new perspectives in colloidal science.

10 Experimental Section

10.1 Experimental Methods

10.1.1 Zeta Potential Determination

10.1.1.1 Colloidal Vibration Current

The zeta potential was measured using the DT-1202 device (Dispersion Technology) at room temperature. The instrument operates at frequency of 3 MHz, and the "more precise" mode was selected to improve the signal-to-noise ratio. Samples were continuously circulated using a peristaltic pump during measurement to prevent settling and maintain homogeneity. Each measurement was conducted in triplicate and averaged. Measurement of Ion vibration current (IVI) was neglected due to the high particle volume fractions (>2.5 vol%).

10.1.1.2 Electrophoretic Light Scattering

Zeta potentials were determined with a ZetaSizer Nano ZS (Malvern Panalytical) employing folded capillary cells (DTS 1070). Measurements utilized a 633 nm wavelength laser at 25 °C, with an equilibration time of 180 s and 50 runs per measurement. Attenuation, measurement position and voltage were automatically set by the device software. Samples were diluted across five particle volume fractions (approximately 0.1 to 0.001 vol%) to minimize multiple scattering effects, and only consistent results were averaged.

10.1.2 Conductivity Measurements

Conductivity measurements were performed at room temperature using the DT-1202 device from Dispersion Technology. Both the conductivity of the dispersion K_s and that of the dispersion medium K_m, were recorded. For determining K_m, particles were removed via centrifugation using an Optima XPN-90 ultracentrifuge (Beckman Coulter; 25,000 rpm, 4 °C, 2–8 h). All measurements were repeated three times and averaged

10.1.3 pH Measurement

A Horiba 9615S-10D glass electrode, calibrated at room temperature using standard buffers (pH 4.01, 7.00 and 9.21; Mettler Toledo), was used. The electrode was integrated into the DT-1202 measuring system for simultaneous measurements.

10.1.4 Particle Size Determination

10.1.4.1 Acoustic Attenuation Spectroscopy

A DT-1202 instrument (Dispersion Technology) was employed, measuring attenuation over a frequency range from 3 to 99.5 MHz at room temperature. Samples were circulated with a peristaltic pump. The particle size distribution was determined by fitting attenuation spectra to a monomodal lognormal distribution model.

10.1.4.2 Dynamic Light Scattering

Particle size was measured with a ZetaSizer Nano ZS (Malvern Panalytical) at 25 °C using a 633 nm laser in backscatter mode (173° angle). Polymethylmethacrylate macro cuvettes were used and measurements were performed across five dilution levels to mitigate multiple scattering effects, averaging only consistent results.

10.1.4.3 Laser Diffraction Spectroscopy

A MasterSizer 2000 with Hydro 2000MU (Malvern Panalytical) measured particle size distributions at room temperature, using wavelengths of 633 nm and 433 nm. Sample addition was adjusted to achieve laser obscuration of 10–20 %. Triplicate measurements were averaged by the instrument's software.

10.1.5 Density Determination

Particle densities were measured using a calibrated 50 mL glass pycnometer at 25 °C. The particle mass fraction was determined by drying samples at 80 °C to constant weight, allowing calculation of particle density from dispersion density measurements.

10.1.6 Thermal Expansion Coefficient

To determine the thermal expansion coefficient of the particle material, particle densities were measured at three temperatures: 20 °C, 25 °C and 30 °C. Each measurement was repeated three times to ensure reproducibility. The thermal expansion coefficient was derived from the slope of the particle density as a function of temperature.

10.1.7 Heat Capacity

Heat capacities were measured using a Q2000 DSC (TA Instruments). Samples were dried and analyzed through two heating/cooling cycles from -30 to 130 °C at 10 K/min, with heat capacities reported at 25 °C from the second heating cycle.

10.1.8 Sound Velocity Determination

Sound velocity measurements were carried out using the DT-1202 device (Dispersion Technology) at 10 MHz frequency, parallel to acoustic attenuation measurements. The sound velocity of the dispersed material was calculated from these data using the Wood equation.

10.1.9 Surfactant Adsorption Measurement

Surfactant adsorption was quantified using titration with benzethonium chloride (4 $\mathrm{mmol\cdot L^{-1}}$) employing a Ti-Touch 916 titrator (Metrohm). Samples were centrifuged, filtered and diluted appropriately. Adsorption per unit area and concentration in the dispersion medium were calculated from titration data.

10.2 Chemicals

A complete overview of all solvents and reagents utilized in this work is provided in Tab. 10.1.

Tab. 10.1: List of chemicals.

chemical	company	purity
1,4-butanediol	Merck	≥99.0 %
acetone	various	≥99.8 %
aluminaoxid (activated)	Acros Organics	99 %
benzethonium chloride solution	VWR Chemicals	4 mmol·L^{-1}
Desmophen® 90B	Covestro	≈1000 g/mol
dibutylamine	Merck	≥99.0 %
dibutyltin dilaurate	Merck	≥99.1 %
Disponil® LDBS 55	BASF SE	≈55 wt%
Disponil® SDS 15	BASF SE	≈15 wt%
ethanol	various	99.8 %
hydrochloric acid (conc.)	Fisher Scientific	37 %
hydrochloric acid solution	Fisher Scientific	10 mmol·L^{-1}
hydroquinone	Sigma Aldrich	≥99.0 %
isophorone diisocyanate	Merck	≥99.0 %
isophoronediamine	Sigma Aldrich	≥98.0 %
methanol	Fisher Scientific	≥99.9 %
methyl methacrylate	VWR Chemicals	≥99 % (15 ppm MEHQ)
n-butyl acrylate	Alfa Aesar	≥98% (50 ppm MEHQ)
octadecyl acrylate	TCI Chemicals	≥99% (MEHQ stabilized)
2-[(2-aminoethyl)amino]acetic acid solution (PUD salt)	Covestro	41.68 wt%
potassium nitrate	VWR Chemicals	≥97 %
potassium persulfate	Carl Roth	≥99.0 %
sodium bicarbonate	VWR Chemicals	99 %
sodium chloride	Merck	≥99.8 %
sodium dodecyl sulfate	Merck	85 %
sodium hydroxide pellets	Carl Roth	≥98 %
sodium hydroxide solution	Fisher Scientific	10 mmol·L^{-1}
standard pH buffer solutions	Mettler Toledo	pH 4.01, 7.00, 9.21
water	-	deionized

10.3 Preparation of Samples and Dispersions

10.3.1 General Sample Handling Procedures (CVI and AAS)

Typically, a dispersion of 150 mL at the required particle volume fraction was prepared by diluting a highly concentrated stock dispersion. When adjustments to the original pH were necessary, minor quantities of 0.1 mol·L^{-1} HCl or NaOH were added using an Eppendorf Research plus G single-channel pipette with volume ranges of 10–100 µL or 20–200 µL. Typically, adjustments were performed up to three times, with larger volumes required at lower particle concentrations. Since the added volumes of acid and base were negligible, their exact amounts were not recorded.

10.3.2 Equilibrium Dilution (CVI and AAS)

For the PVC samples (PVC@0.20, PVC@0.78, PVC@2.09) and PTFE samples (PTFE@0.08, PTFE@0.21), equilibrium dilution was performed by first separating particles using centrifugation (Sorvall RC 5B Plus centrifuge, SLA-3000 rotor, 10,000 rpm, ≈17,500 RCF, 2–6 h at 4 °C). The supernatant served as the diluent, thus preserving chemical equilibrium between particle surfaces and the medium, avoiding the need for pH adjustments.

10.3.3 Non-Equilibrium Dilution (CVI and AAS)

For the SBR sample (SBR@0.23), a non-equilibrium dilution procedure was followed involving dialysis against deionized water for 10 days using a 200,000 MWCO membrane, changing water twice daily. After dialysis, dilution with 2 mol·L^{-1} KCl and deionized water achieved an electrolyte concentration of 10 mmol·L^{-1} KCl. Due to limited sample quantities, PU@0.07 and PBAMM@0.10 samples were diluted directly with deionized water and a 2 mol·L^{-1} KCl solution to achieve the same nominal electrolyte concentration. Slight electrolyte concentration variations during dilution were possible, since the electrolyte background of the original stock dispersion was neglected.

10.3.4 Preparation of Surfactant-Modified Dispersions

Surfactant adsorption studies employed PVC dispersions stabilized with surfactants. PVC@0.20, initially stabilized with SDS, underwent further surfactant addition (Disponil® SDS 15 from BASF SE). PVC@0.78 was initially stabilized with LAS (Disponil® LDBS 55 from BASF SE), with further SDS additions for isotherm determination. Final dispersions, with a particle concentration of 10 wt.% in a total volume of 200 mL, were stirred for 24 hours to achieve adsorption equilibrium. Centrifugation (Sorvall RC 5B Plus, SLA-3000 rotor, 10,000 rpm, ≈17,500 RCF, 2–4 h) separated the solid phase for surfactant analysis via titration using benzethonium chloride.

10.3.5 Sample Preparation for CCC Determination

Samples for critical coagulation concentration (CCC) determination were prepared with varying surfactant coverage rates (PVC@0.20: 27 %, 53 %, 94 % with a solids content of 15 wt.%; PVC@0.78: 62 %, 94 % with a solids content of 10 wt.%). Following gentle stirring for 24 hours, potassium nitrate solution was added and stirred for an additional 30 minutes before measuring the acoustic attenuation at 99.5 MHz. Electrolyte concentration was always referenced to the volume of the dispersion medium, not to that of the dispersion.

10.4 Synthesis of Polymer Dispersions

10.4.1 Synthesis of Polyurethane Dispersion

The polyurethane dispersion investigated in this work was synthesized via the acetone process. All reactions were carried out in a 500 mL four-necked round-bottom flask equipped with a mechanical overhead stirrer (IKA Eurostar ST-P-DV), a PT-100 temperature sensor, a reflux condenser and a nitrogen inlet. As the polymer backbone, 24.2 g of the polyester polyol Desmophen® 90B was weighed in, melted at 100 °C and then stirred at 150 rpm for one hour under house vacuum at approximately 200 mbar to ensure dehydration.

In a next step, 1.9 g of 1,4-butanediol was added as a low molar mass chain extender that contributes to the linear structure of the prepolymer and influences the final flexibility of the polyurethane. The mixture was homogenized and heated to 75°C before adding the catalyst. To catalyze the reaction between hydroxyl and isocyanate groups, 250 µL of a 0.5 wt% solution of dibutyltin dilaurate (DBTL) in acetone was added. Subsequently, 17 g of isophorone diisocyanate (IPDI) was added dropwise over 10 to 15 minutes using a dropping funnel to initiate urethane formation. As viscosity increased during prepolymer formation, the stirring speed was gradually increased to 180 rpm. The temperature was raised to 100 °C and the reaction progress was monitored by determining the NCO content via dibutylamine back-titration using a TitroLine® 7800 titrator (Si Analytics), according to ISO 14896 [314]. Once the theoretical NCO content of 6.14 % was nearly reached, the reaction was interrupted by cooling to 80 °C and adding 76.63 g of acetone dropwise using a dropping funnel with approximately 2 mL min^{-1}. After complete addition, the prepolymer solution was cooled to 40 °C in preparation for the chain extension.

For the chain extension, 5 g of 2-[(2-aminoethyl)amino]acetic acid (PUD salt) was dissolved together with 2.47 g of isophoronediamine (IPDA) in 6.33 g of deionized water. The PUD salt acts as an intrinsic stabilizer, while IPDA serves as a difunctional chain extender for the NCO-terminated prepolymer. This aqueous solution was added dropwise over approximately 10 minutes to the prepolymer solution while stirring at 150 to 180 rpm and maintaining the temperature at 40 °C. The mixture was stirred for at least 30 minutes to complete the chain extension reaction.

The resulting polyurethane was dispersed by adding 99.2 mL of deionized water at a constant rate of 2.3 mL min^{-1} using two syringe pumps (KDS Legato 100 Series, KD Scientific Inc.) while maintaining a temperature of 40 °C and a stirring speed of 360 rpm. The amount of water and chain extenders was adjusted based on the prepolymer mass removed during NCO determination to ensure stoichiometric balance. After dispersion, the acetone was removed under reduced pressure at 40 °C and approximately 200 mbar using house vacuum.

The synthesis was repeated six times under identical conditions. The resulting dispersions were combined and stirred gently to ensure homogeneity. To obtain the particle volume fraction required for further experiments, the final dispersion was concentrated by partial removal of water using a rotary evaporator (IKA RV 10).

10.4.2 Synthesis of Polymethyl methacrylate-*co*-butyl acrylate Dispersion

The synthesis of the polymethyl methacrylate-co-butyl acrylate dispersion was carried out by miniemulsion polymerization under nitrogen atmosphere at 70 °C using methyl methacrylate (MMA) and n-butyl acrylate (n-BU) as monomers. Octadecyl acrylate (ODA) was added as a hydrophobe to suppress Ostwald ripening, sodium dodecyl sulfate (SDS) served as the surfactant, and potassium persulfate (KPS) was used as a water-soluble initiator.

Before use, both MMA and n-BU were purified to remove polymerization inhibitors. Each monomer was passed through a column of basic activated alumina to eliminate stabilizers. The purified monomers were immediately stored in sealed amber glass bottles at 4 °C in a refrigerator and used within 24 hours.

The organic phase was prepared by dissolving 3 g of ODA in a mixture of 36 g of MMA and 53 g of n-BU with gentle stirring until a clear solution was obtained. In parallel, the aqueous phase was prepared by dissolving 3 g of SDS and 1 g of sodium bicarbonate in 106 g of deionized water. Sodium bicarbonate was added as a buffer to stabilize the pH during polymerization.

Once both phases were prepared, the organic phase was added slowly to the aqueous phase under magnetic stirring (500 rpm) to form a crude emulsion. This mixture was then homogenized by ultrasonication using a SONOPLUS HD 2200 ultrasonic processor (Bandelin) with a KE76 sonotrode. The dispersion was sonicated for 7 minutes at 72 % amplitude in pulse mode while being cooled in an ice bath to prevent premature polymerization.

The resulting miniemulsion was transferred to a 500 mL four-necked round-bottom flask equipped with a mechanical stirrer, PT100 temperature probe, reflux condenser and nitrogen inlet. The system was purged with nitrogen for approximately 20 minutes while stirring at 150 rpm and gradually heated to 70 °C using a Heat-On block on a MR Hei-Tec magnetic stirrer (Heidolph). Once the target temperature was reached, the polymerization was initiated by adding 0.7 g of KPS dissolved in approximately 2 mL of deionized water.

Polymerization proceeded for two hours under constant temperature and stirring until full conversion was achieved. After cooling to room temperature, the resulting dispersion was stored at 4 °C in a refrigerator. To ensure sufficient material for subsequent characterization and application, this synthesis was repeated six times under identical conditions. The resulting dispersions were combined and stirred to ensure homogeneity.

10.5 Data Processing and Software

Data analysis and processing were primarily performed using device-specific software and Microsoft Excel. The evaluation of colloidal vibration current (CVI), acoustic attenuation spectroscopy (AAS) and electrophoretic light scattering (ELS) data was carried out using the respective manufacturer software: DT-1202 software (versions 12 m56030 and 12 m56060) from Dispersion Technology Inc. and Zetasizer/Mastersizer software (version 7.13) from Malvern

Panalytical. Measurements were typically repeated three times and averaged values were used for further analysis as described in the corresponding sections.

Advanced theoretical evaluations of the ELS data, including calculations based on the original and modified Ohshima-Healy-White theory and the Dukhin-Semenikhin theory, were performed using Maple 2023 (Waterloo Maple Inc.).

Graphical representations of experimental results were generated using OriginPro (OriginLab), allowing for high-quality scientific visualization and consistent formatting. Schematic illustrations and graphical abstracts were created using Adobe Illustrator 2022.

11 Bibliography

[1] Wang, Y.; Zheng, Y.; Zhang, L.; Wang, Q.; Zhang, D. Stability of nanosuspensions in drug delivery. *Journal of controlled release : official journal of the Controlled Release Society* **2013**, *172*, 1126–1141. DOI: 10.1016/j.jconrel.2013.08.006.

[2] Müller, B.; Poth, U. *Coatings Formulation*; Vincentz Network, 2019.

[3] Dickinson, E. Colloids in food: ingredients, structure, and stability. *Annual review of food science and technology* **2015**, *6*, 211–233. DOI: 10.1146/annurev-food-022814-015651.

[4] Pyun, J. Nanocomposite Materials from Functional Polymers and Magnetic Colloids. *Polymer Reviews* **2007**, *47*, 231–263. DOI: 10.1080/15583720701271294.

[5] Russel, W. B. Review of the Role of Colloidal Forces in the Rheology of Suspensions. *J. Rheol.* **1980**, *24*, 287–317. DOI: 10.1122/1.549564.

[6] Heurtault, B.; Saulnier, P.; Pech, B.; Proust, J.-E.; Benoit, J.-P. Physico-chemical stability of colloidal lipid particles. *Biomaterials* **2003**, *24*, 4283–4300. DOI: 10.1016/S0142-9612(03)00331-4.

[7] Flory, F. Optical properties of nanostructured materials: a review. *J. Nanophoton* **2011**, *5*, 52502. DOI: 10.1117/1.3609266.

[8] Tjong, S. C. Structural and mechanical properties of polymer nanocomposites. *Materials Science and Engineering: R: Reports* **2006**, *53*, 73–197. DOI: 10.1016/j.mser.2006.06.001.

[9] Studart, A. R.; Amstad, E.; Gauckler, L. J. Colloidal stabilization of nanoparticles in concentrated suspensions. *Langmuir* **2007**, *23*, 1081–1090. DOI: 10.1021/la062042s.

[10] Babick, F. *Suspensions of Colloidal Particles and Aggregates*; Springer International Publishing: Cham, 2016.

[11] Xu, R.; Scarlett, B. *Particle Characterization: Light Scattering Methods*, 1st ed. 2002; Springer Netherlands: Dordrecht, 2002.

[12] Dukhin, A. S.; Goetz, P. J., Eds. *Characterization of Liquids, Dispersions, Emulsions, and Porous Materials Using Ultrasound*, Third edition; Elsevier: Amsterdam, Oxford, Cambridge, MA, 2017.

[13] Mohammadi-Jam, S.; Waters, K. E.; Greenwood, R. W. A review of zeta potential measurements using electroacoustics. *Adv. Colloid Interface Sci.* **2022**, *309*, 102778. DOI: 10.1016/j.cis.2022.102778.

[14] Derjaguin, B.; Landau, L. Theory of the stability of strongly charged lyophobic sols and of the adhesion of strongly charged particles in solutions of electrolytes. *Progress in Surface Science* **1993**, *43*, 30–59. DOI: 10.1016/0079-6816(93)90013-L.

[15] Verwey, E. J. W.; Overbeek, J. T. G. *Theory of the Stability of Lyophobic Colloids*; Elsevier: New York, 1948.

[16] Verwey, E. J. W.; Overbeek, J. T. G. Theorie der Stabilität lyophober Kolloide. *Kolloid-Zeitschrift* **1955**, *141*, 44–45. DOI: 10.1007/BF01511752.

[17] Lyklema, J. *Fundamentals of interface and colloid science: Vol. 1: Fundamentals*; Academic Press: London, 1991.

[18] Hamaker, H. C. The London—van der Waals attraction between spherical particles. *Physica* **1937**, *4*, 1058–1072. DOI: 10.1016/S0031-8914(37)80203-7.

[19] Lifshitz, E. M.; Hamermesh, M. The theory of molecular attractive forces between solids. *Perspectives in Theoretical Physics*; Elsevier, 1992; pp 329–349.

[20] Bowen, W.; Jenner, F. The calculation of dispersion forces for engineering applications. *Adv. Colloid Interface Sci.* **1995**, *56*, 201–243. DOI: 10.1016/0001-8686(94)00233-3.

[21] Viravathana, P.; Marr, D. W. Optical Trapping of Titania/Silica Core-Shell Colloidal Particles. *J. Colloid Interface Sci.* **2000**, *221*, 301–307. DOI: 10.1006/jcis.1999.6603.

[22] Tadros, T. F. *Colloid Stability*; Wiley-VCH Verlag GmbH & Co. KGaA: Weinheim, Germany, 2010.

[23] Hunter, R. J. *Foundations of Colloid Science*, 2. ed., reprinted.; Oxford Univ. Press: Oxford, 2009.

[24] Bell, G. M.; Levine, S.; McCartney, L. N. Approximate methods of determining the double-layer free energy of interaction between two charged colloidal spheres. *J. Colloid Interface Sci.* **1970**, *33*, 335–359. DOI: 10.1016/0021-9797(70)90228-6.

[25] Hsu, J.-P., Ed. *Interfacial forces and fields: Theory and applications*; Dekker: New York, NY, 1999.

[26] Chan, D. Y.; Mitchell, D. The free energy of an electrical double layer. *J. Colloid Interface Sci.* **1983**, *95*, 193–197. DOI: 10.1016/0021-9797(83)90087-5.

[27] Carnie, S. L.; Chan, D. Y. Interaction Free Energy between Plates with Charge Regulation: A Linearized Model. *J. Colloid Interface Sci.* **1993**, *161*, 260–264. DOI: 10.1006/jcis.1993.1464.

[28] Carnie, S. L.; Chan, D. Y. C.; Gunning, J. S. Electrical Double Layer Interaction between Dissimilar Spherical Colloidal Particles and between a Sphere and a Plate: The Linearized Poisson-Boltzmann Theory. *Langmuir* **1994**, *10*, 2993–3009. DOI: 10.1021/la00021a024.

[29] Napper, D. Steric stabilization. *J. Colloid Interface Sci.* **1977**, *58*, 390–407. DOI: 10.1016/0021-9797(77)90150-3.

[30] Israelachvili, J. N. *Intermolecular and surface forces*, 3rd ed.; Academic Press: Burlington, MA, 2011.

[31] Napper, D. H. *Polymeric stabilization of colloidal dispersions*; Academic Pr: London, 1983.

[32] Feigin, R. I.; Napper, D. H. Depletion stabilization and depletion flocculation. *J. Colloid Interface Sci.* **1980**, *75*, 525–541. DOI: 10.1016/0021-9797(80)90475-0.

[33] Leikin, S.; Parsegian, V. A.; Rau, D. C.; Rand, R. P. Hydration forces. *Annual review of physical chemistry* **1993**, *44*, 369–395. DOI: 10.1146/annurev.pc.44.100193.002101.

[34] Israelachvili, J.; Wennerström, H. Role of hydration and water structure in biological and colloidal interactions. *Nature* **1996**, *379*, 219–225. DOI: 10.1038/379219a0.

[35] Paunov, V. N.; Dimova, R. I.; Kralchevsky, P. A.; Broze, G.; Mehreteab, A. The Hydration Repulsion between Charged Surfaces as an Interplay of Volume Exclusion and Dielectric Saturation Effects. *J. Colloid Interface Sci.* **1996**, *182*, 239–248. DOI: 10.1006/jcis.1996.0456.

[36] Vigil, G.; Xu, Z.; Steinberg, S.; Israelachvili, J. Interactions of Silica Surfaces. *J. Colloid Interface Sci.* **1994**, *165*, 367–385. DOI: 10.1006/jcis.1994.1242.

[37] Pashley, R. M. Hydration forces between mica surfaces in electrolyte solutions. *Adv. Colloid Interface Sci.* **1982**, *16*, 57–62. DOI: 10.1016/0001-8686(82)85006-9.

[38] Rand, R. P.; Parsegian, V. A. Hydration forces between phospholipid bilayers. *Biochimica et Biophysica Acta (BBA) - Reviews on Biomembranes* **1989**, *988*, 351–376. DOI: 10.1016/0304-4157(89)90010-5.

[39] Meyer, E. E.; Rosenberg, K. J.; Israelachvili, J. Recent progress in understanding hydrophobic interactions. *Proceedings of the National Academy of Sciences of the United States of America* **2006**, *103*, 15739–15746. DOI: 10.1073/pnas.0606422103.

[40] Gouy, M. Sur la constitution de la charge électrique à la surface d'un électrolyte. *J. Phys. Theor. Appl.* **1910**, *9*, 457–468. DOI: 10.1051/jphystap:019100090045700.

[41] Chapman, D. L. LI. A contribution to the theory of electrocapillarity. *The London, Edinburgh, and Dublin Philosophical Magazine and Journal of Science* **1913**, *25*, 475–481. DOI: 10.1080/14786440408634187.

[42] Stern, O. Zur Theorie der elektrolytischen Doppelschicht. *Zeitschrift für Elektrochemie und angewandte physikalische Chemie* **1924**, *30*, 508–516. DOI: 10.1002/bbpc.192400182.

[43] Grahame, D. C. The Electrical Double Layer and the Theory of Electrocapillarity. *Chem. Rev.* **1947**, *41*, 441–501. DOI: 10.1021/cr60130a002.

[44] Bockris, J. O.; Devanathan, M. A. V.; Müller, K. On the structure of charged interfaces. *Proc. R. Soc. London, Ser. A* **1963**, *274*, 55–79. DOI: 10.1098/rspa.1963.0114.

[45] Trasatti, S.; Buzzanca, G. Ruthenium dioxide: A new interesting electrode material. Solid state structure and electrochemical behaviour. *Journal of Electroanalytical Chemistry and Interfacial Electrochemistry* **1971**, *29*, A1-A5. DOI: 10.1016/S0022-0728(71)80111-0.

[46] Marcus, R. A. On the Theory of Oxidation-Reduction Reactions Involving Electron Transfer. I. *J Chem Phys* **1956**, *24*, 966–978. DOI: 10.1063/1.1742723.

[47] Hunter, R. J. *Zeta potential in colloid science: Principles and applications*, New paperback edition; Academic Press: London, San Diego, 1988.

[48] Overbeek, J. Th. G. Theorie der Elektrophorese: Der Relaxationseffekt. *Kolloid-Beihefte* **1943**, *54*, 287–364. DOI: 10.1007/BF02556774.

[49] Delgado, A. V.; González-Caballero, F.; Hunter, R. J.; Koopal, L. K.; Lyklema, J. Measurement and interpretation of electrokinetic phenomena. *J. Colloid Interface Sci.* **2007**, *309*, 194–224. DOI: 10.1016/j.jcis.2006.12.075.

[50] Lyklema, J.; Minor, M. On surface conduction and its role in electrokinetics. *Colloids Surf., A* **1998**, *140*, 33–41. DOI: 10.1016/S0927-7757(97)00266-5.

[51] Mangelsdorf, C. S.; White, L. R. Effects of stern-layer conductance on electrokinetic transport properties of colloidal particles. *J. Chem. Soc., Faraday Trans.* **1990**, *86*, 2859. DOI: 10.1039/ft9908602859.

[52] Dukhin, S. S.; Derjaguin, B. V. *Surface and Colloid Science*; J. Wiley & Sons: New York, 1974.

[53] Ware, B. R. Electrophoretic light scattering. *Adv. Colloid Interface Sci.* **1974**, *4*, 1–44. DOI: 10.1016/0001-8686(74)80001-1.

[54] Uzgiris, E. E. Laser doppler spectroscopy: Applications to cell and particle electrophoresis. *Adv. Colloid Interface Sci.* **1981**, *14*, 75–171. DOI: 10.1016/0001-8686(81)85015-4.

[55] Lagaly, G.; Schulz, O.; Zimehl, R. *Dispersionen und Emulsionen: Eine Einführung in die Kolloidik feinverteilter Stoffe einschließlich der Tonminerale*; Steinkopff: Heidelberg, 1997.

[56] Corbett, J. C. W.; McNeil-Watson, F. Electrophoretic Light Scattering. In *Encyclopedia of Biophysics*; Roberts, G., Watts, A., Eds.; Springer Berlin Heidelberg: Berlin, Heidelberg, 2018; pp 1–10.

[57] Enderby, J. A. On electrical effects due to sound waves in colloidal suspensions. *Proc. R. Soc. London, Ser. A* **1951**, *207*, 329–342. DOI: 10.1098/rspa.1951.0121.

[58] Booth, F.; Enderby, J. A. On Electrical Effects due to Sound Waves in Colloidal Suspensions. *Proc. Phys. Soc. A* **1952**, *65*, 321–324. DOI: 10.1088/0370-1298/65/5/303.

[59] Marlow, B. J.; Fairhurst, D.; Pendse, H. P. Colloid vibration potential and the electrokinetic characterization of concentrated colloids. *Langmuir* **1988**, *4*, 611–626. DOI: 10.1021/la00081a021.

[60] Levine, S.; Neale, G.; Epstein, N. The prediction of electrokinetic phenomena within multiparticle systems. *J. Colloid Interface Sci.* **1976**, *57*, 424–437. DOI: 10.1016/0021-9797(76)90221-6.

[61] O'Brien, R. W. Electro-acoustic effects in a dilute suspension of spherical particles. *J. Fluid Mech.* **1988**, *190*, 71. DOI: 10.1017/S0022112088001211.

[62] Rider, P. F.; O'Brien, R. W. The dynamic mobility of particles in a non-dilute suspension. *J. Fluid Mech.* **1993**, *257*, 607. DOI: 10.1017/S0022112093003234.

[63] Ohshima, H. Dynamic Electrophoretic Mobility of Spherical Colloidal Particles in Concentrated Suspensions. *J. Colloid Interface Sci.* **1997**, *195*, 137–148. DOI: 10.1006/jcis.1997.5146.

[64] Ennis; Shugai; Carnie. Dynamic Mobility of Two Spherical Particles with Thick Double Layers. *J. Colloid Interface Sci.* **2000**, *223*, 21–36. DOI: 10.1006/jcis.1999.6587.

[65] Dukhin, A. S.; Shilov, V. N.; Ohshima, H.; Goetz, P. J. Electroacoustic Phenomena in Concentrated Dispersions: New Theory and CVI Experiment. *Langmuir* **1999**, *15*, 6692–6706. DOI: 10.1021/la990317g.

[66] Dukhin, A. S.; Shilov, V. N.; Ohshima, H.; Goetz, P. J. Electroacoustic Phenomena in Concentrated Dispersions: Effect of the Surface Conductivity. *Langmuir* **2000**, *16*, 2615–2620. DOI: 10.1021/la991305y.

[67] Dukhin, A. S.; Goetz, P. J. Acoustic and electroacoustic spectroscopy for characterizing concentrated dispersions and emulsions. *Adv. Colloid Interface Sci.* **2001**, *92*, 73–132. DOI: 10.1016/S0001-8686(00)00035-X.

[68] Leschonski, K. Representation and Evaluation of Particle Size Analysis Data. *Particle & Particle Systems Characterization* **1984**, *1*, 89–95. DOI: 10.1002/ppsc.19840010115.

[69] International Organization for Standardization. *Representation of results of particle size analysis - Part 1: Graphical representation*, 2004, *19.120* (ISO 9276-1:2004-09).

[70] Bellantone, M.; Scarlett, B.; Merkus, H. G., Eds. *Particle size measurements: Fundamentals, practice, quality*; Springer Netherlands: Dordrecht, 2009.

[71] McClements, D. J. Ultrasonic determination of depletion flocculation in oil-in-water emulsions containing a non-ionic surfactant. *A collection of invited papers by Japanese researchers* **1994**, *90*, 25–35. DOI: 10.1016/0927-7757(94)02881-8.

[72] Babick, F.; Hinze, F.; Stintz, M.; Ripperger, S. Ultrasonic Spectrometry for Particle Size Analysis in Dense Submicron Suspensions. *Part. Part. Syst. Charact.* **1998**, *15*, 230–236. DOI: 10.1002/(SICI)1521-4117(199810)15:5<230:AID-PPSC230>3.0.CO;2-D.

[73] Pellam, J. R.; Galt, J. K. Ultrasonic Propagation in Liquids: I. Application of Pulse Technique to Velocity and Absorption Measurements at 15 Megacycles. *J Chem Phys* **1946**, *14*, 608–614. DOI: 10.1063/1.1724072.

[74] Pinkerton, J. M. M. A pulse method for the measurement of ultrasonic absorption in liquids; results for water. *Nature* **1947**, *159*, 128. DOI: 10.1038/160128b0.

[75] Andreae, J. H.; Joyce, P. L. 30 to 230 megacycle pulse technique for ultrasonic absorption measurements in liquids. *Br. J. Appl. Phys.* **1962**, *13*, 462–467. DOI: 10.1088/0508-3443/13/9/307.

[76] Edmonds, P. D.; Pearce, V. F.; Andreae, J. H. 1.5 to 28.5 Mc/s pulse apparatus for automatic measurement of sound absorption in liquids and some results for aqueous and other solutions. *Br. J. Appl. Phys.* **1962**, *13*, 551–560. DOI: 10.1088/0508-3443/13/11/310.

[77] Babick, F. Schallspektroskopische Charakterisierung von submikronen Emulsionen. PhD thesis, Technische Universität Dresden, 2005.

[78] Epstein, P. S.; Carhart, R. R. The Absorption of Sound in Suspensions and Emulsions. I. Water Fog in Air. *The Journal of the Acoustical Society of America* **1953**, *25*, 553–565. DOI: 10.1121/1.1907107.

[79] Allegra, J. R.; Hawley, S. A. Attenuation of Sound in Suspensions and Emulsions: Theory and Experiments. *The Journal of the Acoustical Society of America* **1972**, *51*, 1545–1564. DOI: 10.1121/1.1912999.

[80] Babick, F.; Hinze, F.; Ripperger, S. Dependence of ultrasonic attenuation on the material properties. *Colloids Surf., A* **2000**, *172*, 33–46. DOI: 10.1016/S0927-7757(00)00571-9.

[81] International Organization for Standardization. *Measurement and characterization of particles by acoustic methods - Part 2: Guidelines for linear theory*, 2022, *19.120* (ISO 20998-2:2022-08).

[82] McClements, D. J.; Coupland, J. N. Theory of droplet size distribution measurements in emulsions using ultrasonic spectroscopy. *Colloids Surf., A* **1996**, *117*, 161–170. DOI: 10.1016/0927-7757(96)03673-4.

[83] International Organization for Standardization. *Measurement and characterization of particles by acoustic methods - Part 3:Guidelines for non-linear theory*, 2017, *19.120* (ISO 20998-3:2017-04).

[84] Lloyd, P.; Berry, M. V. Wave propagation through an assembly of spheres: IV. Relations between different multiple scattering theories. *Proc. Phys. Soc.* **1967**, *91*, 678–688. DOI: 10.1088/0370-1328/91/3/321.

[85] Waterman, P. C.; Truell, R. Multiple Scattering of Waves. *Journal of Mathematical Physics* **1961**, *2*, 512–537. DOI: 10.1063/1.1703737.

[86] Fikioris, J. G.; Waterman, P. C. Multiple Scattering of Waves. II. “Hole Corrections” in the Scalar Case. *Journal of Mathematical Physics* **1964**, *5*, 1413–1420. DOI: 10.1063/1.1704077.

[87] Povey, M. J. *Ultrasonic techniques for fluids characterization*; Academic Press: San Diego, 1997.

[88] Challis, R. E.; Povey, M. J. W.; Mather, M. L.; Holmes, A. K. Ultrasound techniques for characterizing colloidal dispersions. *Rep. Prog. Phys.* **2005**, *68*, 1541–1637. DOI: 10.1088/0034-4885/68/7/r01.

[89] Hemar, Y.; Herrmann, N.; Lemaréchal, P.; Hocquart, R.; Lequeux, F. Effective Medium Model for Ultrasonic Attenuation Due to the Thermo-Elastic Effect in Concentrated Emulsions. *J. Phys. II France* **1997**, *7*, 637–647. DOI: 10.1051/jp2:1997148.

[90] McClements, D. J.; Hemar, Y.; Herrmann, N. Incorporation of thermal overlap effects into multiple scattering theory. *The Journal of the Acoustical Society of America* **1999**, *105*, 915–918. DOI: 10.1121/1.426949.

[91] Chanamai, R.; Herrmann, N.; McClements, D. J. Influence of Thermal Overlap Effects on the Ultrasonic Attenuation Spectra of Polydisperse Oil-in-Water Emulsions. *Langmuir* **1999**, *15*, 3418–3423. DOI: 10.1021/la981195f.

[92] Hipp, A. K.; Storti, G.; Morbidelli, M. Acoustic Characterization of Concentrated Suspensions and Emulsions. 1. Model Analysis. *Langmuir* **2002**, *18*, 391–404. DOI: 10.1021/la015538c.

[93] Harker, A. H.; Temple, J. A. G. Velocity and attenuation of ultrasound in suspensions of particles in fluids. *J. Phys. D: Appl. Phys.* **1988**, *21*, 1576–1588. DOI: 10.1088/0022-3727/21/11/006.

[94] Evans, J. M.; Attenborough, K. Sound propagation in concentrated emulsions: comparison of coupled phase model and core-shell model. *J. Acoust. Soc. Am.* **2002**, *112*, 1911–1917. DOI: 10.1121/1.1510142.

[95] Vand, V. Viscosity of solutions and suspensions; theory. *J. Phys. Chem.* **1948**, *52*, 277–299. DOI: 10.1021/j150458a001.

[96] Happel, J. Viscosity of Suspensions of Uniform Spheres. *Journal of Applied Physics* **1957**, *28*, 1288–1292. DOI: 10.1063/1.1722635.

[97] Dukhin, A. S.; Goetz, P. J. Acoustic Spectroscopy for Concentrated Polydisperse Colloids with High Density Contrast. *Langmuir* **1996**, *12*, 4987–4997. DOI: 10.1021/la951085y.

[98] Baudoin, M.; Thomas, J.-L.; Coulouvrat, F.; Lhuillier, D. An extended coupled phase theory for the sound propagation in polydisperse concentrated suspensions of rigid particles. *J. Acoust. Soc. Am.* **2007**, *121*, 3386–3397. DOI: 10.1121/1.2723648.

[99] Baudoin, M.; Thomas, J.-L.; Coulouvrat, F. On the influence of spatial correlations on sound propagation in concentrated solutions of rigid particles. *J. Acoust. Soc. Am.* **2008**, *123*, 4127–4139. DOI: 10.1121/1.2912445.

[100] Happel, J. Viscous flow in multiparticle systems: Slow motion of fluids relative to beds of spherical particles. *AIChE J.* **1958**, *4*, 197–201. DOI: 10.1002/aic.690040214.

[101] Dukhin, A. S.; Goetz, P. J.; Hamlet, C. W. Acoustic Spectroscopy for Concentrated Polydisperse Colloids with Low Density Contrast. *Langmuir* **1996**, *12*, 4998–5003. DOI: 10.1021/la951572d.

[102] Cummins, H. Z.; Knable, N.; Yeh, Y. Observation of Diffusion Broadening of Rayleigh Scattered Light. *Phys. Rev. Lett.* **1964**, *12*, 150–153. DOI: 10.1103/PhysRevLett.12.150.

[103] International Organization for Standardization. *Particle size analysis - Dynamic light scattering (DLS), 19.120* (ISO 22412:2017).

[104] Jena, S. S.; Bohidar, H. B. Determination of absolute polydispersity and molecular weight distribution of high molecular weight polymers from dynamic light scattering. *J Chem Phys* **1993**, *99*, 673–681. DOI: 10.1063/1.465739.

[105] Bolle, G.; Cametti, C.; Codastefano, P.; Tartaglia, P. Kinetics of salt-induced aggregation in polystyrene lattices studied by quasielastic light scattering. *Physical review. A, General physics* **1987**, *35*, 837–841. DOI: 10.1103/PhysRevA.35.837.

[106] Kroon, M.; Wegdam, G. H.; Sprik, R. Dynamic light scattering studies on the sol-gel transition of a suspension of anisotropic colloidal particles. *Physical review. E, Statistical physics, plasmas, fluids, and related interdisciplinary topics* **1996**, *54*, 6541–6550. DOI: 10.1103/PhysRevE.54.6541.

[107] Manley, S.; Davidovitch, B.; Davies, N. R.; Cipelletti, L.; Bailey, A. E.; Christianson, R. J.; Gasser, U.; Prasad, V.; Segre, P. N.; Doherty, M. P.*; et al.* Time-dependent strength of colloidal gels. *Phys. Rev. Lett.* **2005**, *95*, 48302. DOI: 10.1103/PhysRevLett.95.048302.

[108] Stetefeld, J.; McKenna, S. A.; Patel, T. R. Dynamic light scattering: a practical guide and applications in biomedical sciences. *Biophysical reviews* **2016**, *8*, 409–427. DOI: 10.1007/s12551-016-0218-6.

[109] Einstein, A. *Investigations on the Theory of the Brownian Movement*; Courier Corporation, 1956.

[110] Siegert, A. J. *On the fluctuations in signals returned by many independently moving scatterers*; Radiation Laboratory, Massachusetts Institute of Technology, 1943.

[111] Wiese, H.; Horn, D. Single-mode fibers in fiber-optic quasielastic light scattering: A study of the dynamics of concentrated latex dispersions. *J Chem Phys* **1991**, *94*, 6429–6443. DOI: 10.1063/1.460272.

[112] Peters, R.; Georgalis, Y.; Saenger, W. Accessing lysozyme nucleation with a novel dynamic light scattering detector. *Acta crystallographica. Section D, Biological crystallography* **1998**, *54*, 873–877. DOI: 10.1107/S0907444998002455.

[113] Dhont, J. K. G.; Kruif, C. G. de. Scattered light intensity cross correlation. I. Theory. *J Chem Phys* **1983**, *79*, 1658–1663. DOI: 10.1063/1.446009.

[114] Phillies, G. D. J. Suppression of multiple scattering effects in quasielastic light scattering by homodyne cross-correlation techniques. *J Chem Phys* **1981**, *74*, 260–262. DOI: 10.1063/1.440884.

[115] Schätzel, K. Suppression of Multiple Scattering by Photon Cross-correlation Techniques. *Journal of Modern Optics* **1991**, *38*, 1849–1865. DOI: 10.1080/09500349114551951.

[116] Dukhin, A. S.; Dukhin, S. S.; Goetz, P. J. Gravity as a factor of aggregative stability and coagulation. *Adv. Colloid Interface Sci.* **2007**, *134-135*, 35–71. DOI: 10.1016/j.cis.2007.04.006.

[117] Batchelor, G. K. Sedimentation in a dilute polydisperse system of interacting spheres. Part 1. General theory. *J. Fluid Mech.* **1982**, *119*, 379–408. DOI: 10.1017/S0022112082001402.

[118] International Organization for Standardization. *Particle size analysis — Laser diffraction methods*, 2020, *19.120* (ISO13320:2020-01).

[119] Xu, R. Light scattering: A review of particle characterization applications. *Particuology* **2015**, *18*, 11–21. DOI: 10.1016/j.partic.2014.05.002.

[120] Fraunhofer, J. von. *Neue Modifikation des Lichtes durch gegenseitige Einwirkung und Beugung der Strahlen, und Gesetze derselben*; Lentner, 1820.

[121] Boer, G. B. J. de; Weerd, C. de; Thoenes, D.; Goossens, H. W. J. Laser Diffraction Spectrometry: Fraunhofer Diffraction Versus Mie Scattering. *Particle & Particle Systems Characterization* **1987**, *4*, 14–19. DOI: 10.1002/ppsc.19870040104.

[122] Mie, G. Beiträge zur Optik trüber Medien, speziell kolloidaler Metallösungen. *Ann. Phys.* **1908**, *330*, 377–445. DOI: 10.1002/andp.19083300302.

[123] Xu, R. *Particle characterization: Light scattering methods*; Kluwer: Dordrecht, 2000.

[124] Rawal, S. U.; Patel, M. M. Lipid nanoparticulate systems. *Lipid Nanocarriers for Drug Targeting*; Elsevier, 2018; pp 49–138.

[125] Pei, Y.; Hinchliffe, B. A.; Minelli, C. Measurement of the Size Distribution of Multimodal Colloidal Systems by Laser Diffraction. *ACS omega* **2021**, *6*, 14049–14058. DOI: 10.1021/acsomega.1c00411.

[126] Jores, K.; Mehnert, W.; Drechsler, M.; Bunjes, H.; Johann, C.; Mäder, K. Investigations on the structure of solid lipid nanoparticles (SLN) and oil-loaded solid lipid nanoparticles by photon correlation spectroscopy, field-flow fractionation and transmission electron microscopy. *Drug Delivery Research in North America – Part I* **2004**, *95*, 217–227. DOI: 10.1016/j.jconrel.2003.11.012.

[127] Frangenberg, M.; Schmidt, A. M.; Wilkens, J. Impact of surface conductivity on the zeta potential determination of concentrated aqueous polymer dispersions using electroacoustics and electrokinetic standard models. *Colloid Polym. Sci.* **2024**, *302*, 1801–1813. DOI: 10.1007/s00396-024-05301-7.

[128] International Organization for Standardization. *Colloidal systems - Methods for zeta-potential determination - Part 1: Electroacoustic and electrokinetic phenomena*, 2012, *19.120* (ISO 13099-1:2012-06).

[129] International Organization for Standardization. *Colloidal systems - Methods for zeta-potential determination - Part 2: Optical methods*, 2012, *19.120* (ISO 13099-2:2012-06).

[130] International Organization for Standardization. *Colloidal systems - Methods for zeta potential determination - Part 3: Acoustic methods*, 2014, *19.120* (13099-3:2014-07).

[131] Hunter, R. J. Recent developments in the electroacoustic characterisation of colloidal suspensions and emulsions. *Colloids Surf., A* **1998**, *141*, 37–66. DOI: 10.1016/S0927-7757(98)00202-7.

[132] Smoluchowski, M. v. Elektrische Endosmose und Strömungsströme. In *Handbuch der Elektrizität und des Magnetismus*; Graetz, L., Ed.; Johann Ambrosius: Barth, Leipzig, 1921; pp 366–428.

[133] Henry, D. C. The Cataphoresis of Suspended Particles. Part I. The Equation of Cataphoresis. *Proc. R. Soc. London, Ser. A* **1931**, *133*, 106–129. DOI: 10.1098/rspa.1931.0133.

[134] Midmore, B.; O'Brien, R. The conductivity of concentrated suspensions at low frequencies. *J. Colloid Interface Sci.* **1988**, *123*, 486–493. DOI: 10.1016/0021-9797(88)90270-6.

[135] Van Der Put, A.G; Bijsterbosch, B. Electrical conductivity of dilute and concentrated aqueous dispersions of monodisperse polystyrene particles. Influence of surface conductance and double-layer polarization. *J. Colloid Interface Sci.* **1980**, *75*, 512–524. DOI: 10.1016/0021-9797(80)90474-9.

[136] Bárány, S.; Dukhin, S. Effect of adsorbed polymers on the surface conductivity of dispersed particles. *Colloids Surf., A* **2001**, *192*, 307–316. DOI: 10.1016/S0927-7757(01)00731-2.

[137] O'Brien, R.; Perrins, W. The electrical conductivity of a porous plug. *J. Colloid Interface Sci.* **1984**, *99*, 20–31. DOI: 10.1016/0021-9797(84)90081-X.

[138] Minor, M.; van der Linde, A. J.; van Leeuwen, H. P.; Lyklema, J. Streaming potentials and conductivities of porous silica plugs. *Colloids Surf., A* **1998**, *142*, 165–173. DOI: 10.1016/S0927-7757(98)00365-3.

[139] Löbbus, M.; van Leeuwen, H. P.; Lyklema, J. Streaming potentials and conductivities of latex plugs. Influence of the valency of the counterion. *Colloids Surf., A* **2000**, *161*, 103–113. DOI: 10.1016/S0927-7757(99)00329-5.

[140] Hughes, M. P.; Morgan, H.; Flynn, M. F. The Dielectrophoretic Behavior of Submicron Latex Spheres: Influence of Surface Conductance. *J. Colloid Interface Sci.* **1999**, *220*, 454–457. DOI: 10.1006/jcis.1999.6542.

[141] Midmore, B.; Hunter, R.; O'Brien, R. The dielectric response of concentrated latices. *J. Colloid Interface Sci.* **1987**, *120*, 210–217. DOI: 10.1016/0021-9797(87)90342-0.

[142] Jiménez, M. L.; Arroyo, F. J.; Carrique, F.; Delgado, A. V. Surface conductivity of colloidal particles: experimental assessment of its contributions. *J. Colloid Interface Sci.* **2007**, *316*, 836–843. DOI: 10.1016/j.jcis.2007.07.016.

[143] Kijlstra, J.; van Leeuwen, H. P.; Lyklema, J. Low-frequency dielectric relaxation of hematite and silica sols. *Langmuir* **1993**, *9*, 1625–1633. DOI: 10.1021/la00031a005.

[144] Minor, M.; van Leeuwen, H. P.; Lyklema, J. Low-Frequency Dielectric Response of Polystyrene Latex Dispersions. *J. Colloid Interface Sci.* **1998**, *206*, 397–406. DOI: 10.1006/jcis.1998.5619.

[145] Roldán-Toro, R.; Solier, J. D. Wide-frequency-range dielectric response of polystyrene latex dispersions. *J. Colloid Interface Sci.* **2004**, *274*, 76–88. DOI: 10.1016/j.jcis.2004.02.068.

[146] Maxwell, J. C. *A treatise on electricity and magnetism vol.1*; Oxford University Press: Oxford, 1873.

[147] Wagner, K. W. Erklärung der dielektrischen Nachwirkungsvorgänge auf Grund Maxwellscher Vorstellungen. *Archiv f. Elektrotechnik* **1914**, *2*, 371–387. DOI: 10.1007/bf01657322.

[148] O'Konski, C. T. Electric Properties of Macromolecules. V. Theory of Ionic Polarization in Polyelectrolytes. *J. Phys. Chem.* **1960**, *64*, 605–619. DOI: 10.1021/j100834a023.

[149] James, R. O.; Texter, J.; Scales, P. J. Frequency dependence of electroacoustic (electrophoretic) mobilities. *Langmuir* **1991**, *7*, 1993–1997. DOI: 10.1021/la00058a002.

[150] Klingbiel, R. T.; Coll, H.; James, R. O.; Texter, J. Electrokinetic sonic amplitude of colloidal poly(methyl methacrylate) and Ludox®-TM. *Colloids Surf.* **1992**, *68*, 103–109. DOI: 10.1016/0166-6622(92)80151-Q.

[151] Gibb; Hunter. Dynamic Mobility of Colloidal Particles with Thick Double Layers. *J. Colloid Interface Sci.* **2000**, *224*, 99–111. DOI: 10.1006/jcis.1999.6676.

[152] Goetz, R. J.; El-Aasser, M. S. Effects of dispersion concentration on the electroacoustic potentials of o/w miniemulsions. *J. Colloid Interface Sci.* **1992**, *150*, 436–452. DOI: 10.1016/0021-9797(92)90213-6.

[153] Hunter, R. J.; Midmore, B. R.; Zhang, H. Zeta Potential of Highly Charged Thin Double-Layer Systems. *J. Colloid Interface Sci.* **2001**, *237*, 147–149. DOI: 10.1006/jcis.2001.7423.

[154] Shubin, V. E.; Hunter, R. J.; O'Brien, R. W. Electroacoustic and Dielectric Study of Surface Conduction. *J. Colloid Interface Sci.* **1993**, *159*, 174–183. DOI: 10.1006/jcis.1993.1309.

[155] Dahlsten, P.; Próchniak, P.; Kosmulski, M.; Rosenholm, J. B. Electrokinetic behavior of melamine–formaldehyde latex particles at moderate electrolyte concentration. *J. Colloid Interface Sci.* **2009**, *339*, 409–415. DOI: 10.1016/j.jcis.2009.07.029.

[156] Kosmulski, M.; Dahlsten, P.; Próchniak, P.; Rosenholm, J. B. High ionic strength electrokinetics of melamine–formaldehyde latex. *J. Colloid Interface Sci.* **2006**, *301*, 538–541. DOI: 10.1016/j.jcis.2006.05.052.

[157] Ishikawa, Y.; Aoki, N.; Ohshima, H. Characterization of latex particles for aqueous polymeric coating by electroacoustic method. *Colloids Surf., B* **2005**, *46*, 147–151. DOI: 10.1016/j.colsurfb.2005.10.005.

[158] Hozumi, Y.; Furusawa, K. Electrokinetic study on concentrated suspensions using colloid vibration potential measurements. *Colloid Polym. Sci.* **1990**, *268*, 469–475. DOI: 10.1007/bf01411006.

[159] Rasmusson, M. Volume Fraction Effects in Electroacoustic Measurements. *J. Colloid Interface Sci.* **2001**, *240*, 432–447. DOI: 10.1006/jcis.2001.7559.

[160] Ohshima, H. A Simple Expression for Henry's Function for the Retardation Effect in Electrophoresis of Spherical Colloidal Particles. *J. Colloid Interface Sci.* **1994**, *168*, 269–271. DOI: 10.1006/jcis.1994.1419.

[161] Dukhin, S. S. Non-equilibrium electric surface phenomena. *Adv. Colloid Interface Sci.* **1993**, *44*, 1–134. DOI: 10.1016/0001-8686(93)80021-3.

[162] Dukhin, A. S.; Goetz, P. J. *Characterization of Liquids, Dispersions, Emulsions, and Porous Materials Using Ultrasound*, Third edition; Elsevier: Amsterdam, Oxford, Cambridge, MA, 2017.

[163] Kruyt, H. R., Ed. *Colloid science: Volume 1: Irreversible systems*; Elsevier: New York [etc.], 1952.

[164] Dukhin, A. S.; Shilov, V.; Borkovskaya, Y. Dynamic Electrophoretic Mobility in Concentrated Dispersed Systems. Cell Model. *Langmuir* **1999**, *15*, 3452–3457. DOI: 10.1021/la981382d.

[165] Ohshima, H.; Dukhin, A. S. Colloid Vibration Potential in a Concentrated Suspension of Spherical Colloidal Particles. *J. Colloid Interface Sci.* **1999**, *212*, 449–452. DOI: 10.1006/jcis.1998.6059.

[166] Zhang, X.; Qiu, J.; Li, X.; Zhao, J.; Liu, L. Complex refractive indices measurements of polymers in visible and near-infrared bands. *Applied optics* **2020**, *59*, 2337–2344. DOI: 10.1364/AO.383831.

[167] Khan, H. U.; Gupta, V. K.; Yamin, M. Specific Refractive Index Increments of Polybutadiene, Styrene-Butadiene Rubber, Crepe Rubber, Polystyrene, Polymethyl Methacrylate, and Styrene-Methyl Methacrylate in Various Solvents and Variation of Refractive Index Increment with Molecular Weight. *Journal of Macromolecular Science: Part A - Chemistry* **1983**, *20*, 503–513. DOI: 10.1080/00222338308060797.

[168] Sultanova, N. G.; Kasarova, S. N.; Nikolov, I. D. Characterization of optical properties of optical polymers. *Opt Quant Electron* **2013**, *45*, 221–232. DOI: 10.1007/s11082-012-9616-6.

[169] Bauer, J.; Gutke, M.; Heinrich, F.; Edling, M.; Stoycheva, V.; Kaltenbach, A.; Burkhardt, M.; Gruenefeld, M.; Gamp, M.; Gerhard, C.; *et al.* Novel UV-transparent 2-component polyurethane resin for chip-on-board LED micro lenses. *Opt. Mater. Express* **2020**, *10*, 2085. DOI: 10.1364/OME.393844.

[170] French, R. H.; Rodriguez-Parada, J. M.; Yang, M. K.; Derryberry, R. A.; Lemon, M. F.; Brown, M. J.; Haeger, C. R.; Samuels, S. L.; Romano, E. C.; Richardson, R. E. Optical properties of materials for concentrator photovoltaic systems. In *2009 34th IEEE Photovoltaic Specialists Conference (PVSC)*; IEEE, 2009; pp 394–399.

[171] Dukhin, A. S.; Reisel, A. Overlapping double layers in electrokinetics of concentrated dispersions. *J. Colloid Interface Sci.* **2022**, *609*, 764–774. DOI: 10.1016/j.jcis.2021.11.092.

[172] Lyklema, J. *Fundamentals of Interface and Colloid Science: Solid-Liquid Interfaces*; Academic Press: Burlington, 1995.

[173] Lowry, G. V.; Hill, R. J.; Harper, S.; Rawle, A. F.; Hendren, C. O.; Klaessig, F.; Nobbmann, U.; Sayre, P.; Rumble, J. Guidance to improve the scientific value of zeta-potential measurements in nanoEHS. *Environ. Sci.: Nano* **2016**, *3*, 953–965. DOI: 10.1039/C6EN00136J.

[174] Kuwabara, S. The Forces experienced by Randomly Distributed Parallel Circular Cylinders or Spheres in a Viscous Flow at Small Reynolds Numbers. *J. Phys. Soc. Jpn.* **1959**, *14*, 527–532. DOI: 10.1143/JPSJ.14.527.

[175] Shilov, V. N.; Zharkikh, N. I.; Borkovskaya, Y. B. Theory of non-equilibrium electrical surface phenomena in concentrated disperse systems. 1: Application of the method of thermodynamics of irreversble processes to the cellular model of a concentrated dispersion. *Colloid J.* **1981**, *43*, 434–438.

[176] Hückel, E. Die Kataphorese der Kugel. *Phys. Z.* **1924**, *25*, 204–210.

[177] Hidalgo-Álvarez, R.; Martín, A.; Fernández, A.; Bastos, D.; Martínez, F.; las Nieves, F. de. Electrokinetic properties, colloidal stability and aggregation kinetics of polymer colloids. *Adv. Colloid Interface Sci.* **1996**, *67*, 1–118. DOI: 10.1016/0001-8686(96)00297-7.

[178] Hunter, R. J. The significance of stagnant layer conduction in electrokinetics. *Adv. Colloid Interface Sci.* **2003**, *100-102*, 153–167. DOI: 10.1016/S0001-8686(02)00060-X.

[179] Bouhaik, I. S.; Leroy, P.; Ollivier, P.; Azaroual, M.; Mercury, L. Influence of surface conductivity on the apparent zeta potential of TiO2 nanoparticles: application to the modeling of their aggregation kinetics. *J. Colloid Interface Sci.* **2013**, *406*, 75–85. DOI: 10.1016/j.jcis.2013.05.034.

[180] Djerdjev, A. M.; Beattie, J. K.; Hunter, R. J. Stagnant Layer Conduction in Surfactant-Stabilized Hexadecane Emulsion Systems Measured by Electroacoustics. *Aust. J. Chem.* **2003**, *56*, 1081. DOI: 10.1071/CH03013.

[181] Gómez-Merino, A. I.; Rubio-Hernández, F. J.; Velázquez-Navarro, J. F.; Aguiar, J. Estimation of Ion Diffusion Coefficients at the Stagnant Layer Using TiO 2 Aqueous Suspension Zeta Potential Data. *Soft Mater.* **2015**, *13*, 127–137. DOI: 10.1080/1539445X.2015.1017769.

[182] Jiménez, M. L.; Arroyo, F. J.; Carrique, F.; Kaatze, U.; Delgado, A. V. Determination of stagnant layer conductivity in polystyrene suspensions: temperature effects. *J. Colloid Interface Sci.* **2005**, *281*, 503–509. DOI: 10.1016/j.jcis.2004.08.093.

[183] Leroy, P.; Devau, N.; Revil, A.; Bizi, M. Influence of surface conductivity on the apparent zeta potential of amorphous silica nanoparticles. *J. Colloid Interface Sci.* **2013**, *410*, 81–93. DOI: 10.1016/j.jcis.2013.08.012.

[184] Leroy, P.; Tournassat, C.; Bizi, M. Influence of surface conductivity on the apparent zeta potential of TiO2 nanoparticles. *J. Colloid Interface Sci.* **2011**, *356*, 442–453. DOI: 10.1016/j.jcis.2011.01.016.

[185] Li, S.; Leroy, P.; Heberling, F.; Devau, N.; Jougnot, D.; Chiaberge, C. Influence of surface conductivity on the apparent zeta potential of calcite. *J. Colloid Interface Sci.* **2016**, *468*, 262–275. DOI: 10.1016/j.jcis.2016.01.075.

[186] Löbbus, M.; Sonnfeld, J.; van Leeuwen, H. P.; Vogelsberger, W.; Lyklema, J. An Improved Method for Calculating Zeta-Potentials from Measurements of the Electrokinetic Sonic Amplitude. *J. Colloid Interface Sci.* **2000**, *229*, 174–183. DOI: 10.1006/jcis.2000.6980.

[187] Minor, M.; Wal, A.; Lyklema, J. Dielectric Spectroscopy of Model Colloids, and the Role of Conduction Behind the Plane of Shear. *Pelizzetti, E. (eds) Fine Particles Science and Technology. NATO ASI Series, vol 12*; Springer: Dordrecht, 1996; pp 225–238.

[188] O'Brien, R. W.; Rowlands, W. N. Measuring the Surface Conductance of Kaolinite Particles. *J. Colloid Interface Sci.* **1993**, *159*, 471–476. DOI: 10.1006/jcis.1993.1348.

[189] O'Brien, R. W.; Wade, T. A.; Carasso, M. L.; Hunter, R. J.; Rowlands, W. N.; Beattie, J. K. Electroacoustic Determination of Droplet Size and Zeta Potential in Concentrated Emulsions. In *Particle size distribution III: Assessment and characterization*; Provder, T., Ed.; American Chemical Society: Washington, DC, 1998; pp 311–319.

[190] Pochapski, D. J.; Carvalho Dos Santos, C.; Leite, G. W.; Pulcinelli, S. H.; Santilli, C. V. Zeta Potential and Colloidal Stability Predictions for Inorganic Nanoparticle Dispersions: Effects of Experimental Conditions and Electrokinetic Models on the Interpretation of Results. *Langmuir* **2021**, *37*, 13379–13389. DOI: 10.1021/acs.langmuir.1c02056.

[191] Rasmusson, M.; Rowlands, W.; O'Brien, R. W.; Hunter, R. J. The Dynamic Mobility and Dielectric Response of Sodium Bentonite. *J. Colloid Interface Sci.* **1997**, *189*, 92–100. DOI: 10.1006/jcis.1997.4793.

[192] Rowlands, W. N.; O'Brien, R. W. The Dynamic Mobility and Dielectric Response of Kaolinite Particles. *J. Colloid Interface Sci.* **1995**, *175*, 190–200. DOI: 10.1006/jcis.1995.1445.

[193] Sonnefeld, J.; Löbbus, M.; Vogelsberger, W. Determination of electric double layer parameters for spherical silica particles under application of the triple layer model using surface charge density data and results of electrokinetic sonic amplitude measurements. *J. Colloid Interface Sci.* **2001**, *195*, 215–225. DOI: 10.1016/S0927-7757(01)00845-7.

[194] Spanos, N.; Tsevis, A.; Koutsoukos, P. G.; Minor, M.; van der Linde, A. J.; Lyklema, J. Electro-kinetic measurements on plugs of doped titania. *Colloids Surf., A* **1998**, *141*, 101–109. DOI: 10.1016/S0927-7757(98)00206-4.

[195] Ohshima, H. Electrical Conductivity of a Concentrated Suspension of Spherical Colloidal Particles. *J. Colloid Interface Sci.* **1999**, *212*, 443–448. DOI: 10.1006/jcis.1998.6048.

[196] Carrique, F.; Arroyo, F. J.; Delgado, A. V. Electrokinetics of Concentrated Suspensions of Spherical Colloidal Particles: Effect of a Dynamic Stern Layer on Electrophoresis and DC Conductivity. *J. Colloid Interface Sci.* **2001**, *243*, 351–361. DOI: 10.1006/jcis.2001.7903.

[197] Carrique, F.; Cuquejo, J.; Arroyo, F. J.; Jiménez, M. L.; Delgado, A. V. Influence of cell-model boundary conditions on the conductivity and electrophoretic mobility of concentrated suspensions. *Adv. Colloid Interface Sci.* **2005**, *118*, 43–50. DOI: 10.1016/j.cis.2005.04.001.

[198] Dukhin, S. S. Electrochemical characterization of the surface of a small particle and nonequilibrium electric surface phenomena. *Adv. Colloid Interface Sci.* **1995**, *61*, 17–49. DOI: 10.1016/0001-8686(95)00258-R.

[199] Ohshima, H.; Healy, T. W.; White, L. R. Approximate analytic expressions for the electrophoretic mobility of spherical colloidal particles and the conductivity of their dilute suspensions. *J. Chem. Soc., Faraday Trans. 2* **1983**, *79*, 1613. DOI: 10.1039/f29837901613.

[200] Dukhin, S. S.; Derjaguin, B. V. *Electrophoresis (on russian)*; Nauka: Moskva, 1976.

[201] Moncho, A.; Martínez-López, F.; Hidalgo-Álvarez, R. Comparative study of theories of conversion of electrophoretic mobility into ζ-potential. *Colloids Surf., A* **2001**, *192*, 215–226. DOI: 10.1016/S0927-7757(01)00726-9.

[202] Chabalgoity-Rodríguez, A.; Martín-Rodríguez, A.; Galisteo-González, F.; Hidalgo-Alvarez, R. Electrophoretic mobility, primary electroviscous effect and colloid stability of highly charged polystyrene latexes. *Progr. Colloid Polym. Sci.* **1991**, *84*, 416–424. DOI: 10.1007/BFb0116015.

[203] Hidalgo-Alvarez, R.; Moleon, J. A.; De Las Nieves, F. J; Bijsterbosch, B. H. Effect of anomalous surface conductance on ζ-potential determination of positively charged polystyrene microspheres. *J. Colloid Interface Sci.* **1992**, *149*, 23–26. DOI: 10.1016/0021-9797(92)90386-Z.

[204] Galisteo-González, F.; Moleón-Baca, J. A.; Hidalgo-Alvarez, R. On the structure of electrical double layer of IgG immobilized on polystyrene microspheres. *J. Biomater. Sci., Polym. Ed.* **1993**, *4*, 631–641. DOI: 10.1163/156856293X00267.

[205] Fernández-Barbero, A.; Martín-Rodríguez, A.; Callejas-Fernández, J.; Hidalgo-Alvarez, R. On the Calculation of Electrokinetic Potential and Hamaker Constant of Model Colloids. *J. Colloid Interface Sci.* **1994**, *162*, 257–260. DOI: 10.1006/jcis.1994.1035.

[206] Rubio-Hernández, F. J. Effect of Liquid Composition on the Double Layer of Polystyrene Model Colloids. *J. Non-Equilib. Thermodyn.* **1996**, *21*, 30–40. DOI: 10.1515/jnet.1996.21.1.30.

[207] Unzueta, E.; Forcada, J.; Hidalgo-Alvarez, R. Colloidal and electrokinetic behaviour of poly(methyl methacrylate-co-butyl acrylate) latex particles. *Polymer* **1997**, *38*, 6097–6102. DOI: 10.1016/S0032-3861(97)00185-7.

[208] Peula-García, J. M.; Hidalgo-Alvarez, R.; las Nieves, F. J. de. Colloid stability and electrokinetic characterization of polymer colloids prepared by different methods. *Colloids Surf., A* **1997**, *127*, 19–24. DOI: 10.1016/S0927-7757(96)03890-3.

[209] Bárány, S. Complex electrosurface investigations of dispersed microphases. *Adv. Colloid Interface Sci.* **1998**, *75*, 45–78. DOI: 10.1016/S0001-8686(97)00043-2.

[210] Bárány, S. On the use of the Smoluchowski equation in the calculation of the electrokinetic potential. *Magyar Kemiai Folyoirat, Kemiai Kozlemenyek* **2005**, *111*, 105–109.

[211] Dukhin, A. S.; Ohshima, H.; Shilov, V. N.; Goetz, P. J. Electroacoustics for Concentrated Dispersions. *Langmuir* **1999**, *15*, 3445–3451. DOI: 10.1021/la9813836.

[212] O'Brien, R. W.; White, L. R. Electrophoretic mobility of a spherical colloidal particle. *J. Chem. Soc., Faraday Trans. 2* **1978**, *74*, 1607. DOI: 10.1039/f29787401607.

[213] Kobayashi, M. Electrophoretic mobility of latex spheres in the presence of divalent ions: experiments and modeling. *Colloid Polym. Sci.* **2008**, *286*, 935–940. DOI: 10.1007/s00396-008-1851-9.

[214] Chassagne, C.; Ibanez, M. Electrophoretic mobility of latex nanospheres in electrolytes: Experimental challenges. *Pure Appl. Chem.* **2012**, *85*, 41–51. DOI: 10.1351/PAC-CON-12-02-12.

[215] McClements, D. J. Ultrasonic Measurements in Particle Size Analysis. In *Encyclopedia of analytical chemistry: Applications, theory and instrumentation*; Meyers, R. A., Ed.; Wiley: New York, 2000.

[216] Silva, C. A.; Saraiva, S. V.; Bonetti, D.; Higuti, R. T.; Cunha, R. L.; Pereira, L. O.; Silva, F. V.; Fileti, A. M. Application of acoustic models for polydisperse emulsion characterization using ultrasonic spectroscopy in the long wavelength regime. *Colloids Surf., A* **2020**, *602*, 125062. DOI: 10.1016/j.colsurfa.2020.125062.

[217] Hayashi, T.; Ohya, H.; Suzuki, S.; Endoh, S. Errors in Size Distribution Measurement of Concentrated Alumina Slurry by Ultrasonic Attenuation Spectroscopy. *J. Soc. Powder Technolo, Japan* **2000**, *37*, 498–504. DOI: 10.4164/sptj.37.498.

[218] Dukhin, A. S.; Goetz, P. J.; Travers, B. Use of ultrasound for characterizing dairy products. *Journal of dairy science* **2005**, *88*, 1320–1334. DOI: 10.3168/jds.S0022-0302(05)72798-3.

[219] Ono, K. A Comprehensive Report on Ultrasonic Attenuation of Engineering Materials, Including Metals, Ceramics, Polymers, Fiber-Reinforced Composites, Wood, and Rocks. *Applied Sciences* **2020**, *10*, 2230. DOI: 10.3390/app10072230.

[220] Jarzynski, J.; Balizer, E.; Fedderly, J. J.; Lee, G. Acoustic Properties. In *Encyclopedia of polymer science and technology,* 4th edition; Mark, H. F., Ed.; Wiley-Blackwell: Chichester, 2014.

[221] Sinha, M.; Buckley, D. J. Acoustic Properties of Polymers. In *Physical Properties of Polymers Handbook*; Mark, J. E., Ed.; Springer New York: New York, NY, 2007; pp 1021–1031.

[222] Biwa, S. Independent scattering and wave attenuation in viscoelastic composites. *Mechanics of Materials* **2001**, *33*, 635–647. DOI: 10.1016/S0167-6636(01)00080-1.

[223] Kinra, V. K.; Petraitis, M. S.; Datta, S. K. Ultrasonic wave propagation in a random particulate composite. *International Journal of Solids and Structures* **1980**, *16*, 301–312. DOI: 10.1016/0020-7683(80)90083-9.

[224] Adjadj, L. P.; Storti, G.; Morbidelli, M. Ultrasound Attenuation in Polystyrene Latexes. *Langmuir* **2003**, *19*, 3953–3957. DOI: 10.1021/la026893l.

[225] Bloomfield, P. E.; Lo, W. J.; Lewin, P. A. Experimental study of the acoustical properties of polymers utilized to construct PVDF ultrasonic transducers and the acousto-electric properties of PVDF and

P(VDF/TrFE) films. *IEEE transactions on ultrasonics, ferroelectrics, and frequency control* **2000**, *47*, 1397–1405. DOI: 10.1109/58.883528.

[226] Zellouf, D.; Jayet, Y.; Saint-Pierre, N.; Tatibouët, J.; Baboux, J. C. Ultrasonic spectroscopy in polymeric materials. Application of the Kramers–Kronig relations. *Journal of Applied Physics* **1996**, *80*, 2728–2732. DOI: 10.1063/1.363190.

[227] Dukhin, A. S.; Goetz, P. J. Characterization of Concentrated Dispersions with Several Dispersed Phases by Means of Acoustic Spectroscopy. *Langmuir* **2000**, *16*, 7597–7604. DOI: 10.1021/la991600i.

[228] Wood, A. B. *A Textbook of Sound: Being an account of the Physics of Vibrations with special reference to recent theoretical and technical developments*; Bell and Sons: London, 1941.

[229] Nielsen, L.; Ebert, H.-P.; Hemberger, F.; Fricke, J.; Biedermann, A.; Reichelt, M.; Rotermund, U. Thermal conductivity of nonporous polyurethane. *High Temp.-High Press.* **2000**, *32*, 701–707. DOI: 10.1068/htwu69.

[230] Bhowmick, T.; Pattanayak, S. Thermal conductivity, heat capacity and diffusivity of rubbers from 60 to 300 K. *Cryogenics* **1990**, *30*, 116–121. DOI: 10.1016/0011-2275(90)90256-C.

[231] Boudenne, A.; Ibos, L.; Gehin, E.; Candau, Y. A simultaneous characterization of thermal conductivity and diffusivity of polymer materials by a periodic method. *J. Phys. D: Appl. Phys.* **2004**, *37*, 132–139. DOI: 10.1088/0022-3727/37/1/022.

[232] Sheldon, R. P.; Lane, S. K. Thermal conductivities of polymers I—Polyvinyl chloride. *Polymer* **1965**, *6*, 77–83. DOI: 10.1016/0032-3861(65)90009-1.

[233] Cao, R.; Deng, L.; Feng, Z.; Zhao, X.; Li, X.; Zhang, L. Preparation of natural bio-based Eucommia ulmoides gum/styrene-butadiene rubber composites and the evaluation of their damping and sound absorption properties. *Collected papers from PDM 2004. Polymers in Dispersed Media - Colloids: from Preparation to Application* **2021**, *213*, 123292. DOI: 10.1016/j.polymer.2020.123292.

[234] Sarkar, M. de; De, P. P.; Bhowmick, A. K. New polymeric blends from hydrogenated styrene–butadiene rubber and polyethylene. *Collected papers from PDM 2004. Polymers in Dispersed Media - Colloids: from Preparation to Application* **1998**, *39*, 6789–6800. DOI: 10.1016/S0032-3861(98)00171-2.

[235] Ngai, K. L.; Plazek, D. J. The Viscoelastic Behavior of Rubber. *Science and technology of rubber,* 3rd ed.; Elsevier Academic Press: Amsterdam, Boston, 2005; pp 183–236.

[236] Wada, Y.; Ito, R.; Ochiai, H. Comparison Between Mechanical Relaxations Associated with Volume and shear Deformations in Styrene-Butadiene Rubber. *J. Phys. Soc. Jpn.* **1962**, *17*, 213–218. DOI: 10.1143/jpsj.17.213.

[237] Faghihi, F.; Mohammadi, N.; Haghgoo, M. The effects of rigid polystyrene particles on the glass transition characteristics and mechanical wave attenuation of styrene-butadiene rubber: Particle size and acoustic mismatch. *J. Polym. Sci. B Polym. Phys.* **2010**, *48*, 82–88. DOI: 10.1002/polb.21846.

[238] Ebnesajjad, S. *Fluoroplastics, Volume 1, Non-melt processible fluoropolymers*, 2nd edition (Online-ausg.); William Andrew: Waltham, MA, 2015.

[239] Hung, B. N.; Goldstein, A. Acoustic Parameters of Commercial Plastics. *IEEE Trans. Son. Ultrason.* **1983**, *30*, 249–254. DOI: 10.1109/T-SU.1983.31415.

[240] Pouet, B. F.; Rasolofosaon, N. J. P. Measurement of broadband intrinsic ultrasonic attenuation and dispersion in solids with laser techniques. *J. Acoust. Soc. Am.* **1993**, *93*, 1286–1292. DOI: 10.1121/1.405413.

[241] Wypych, G. *Handbook of polymers*; ChemTec Publ: Toronto, 2012.

[242] Deutsch, V.; Platte, M.; Vogt, M. *Ultraschallprüfung: Grundlagen und industrielle Anwendungen*; Springer: Berlin, Heidelberg, 1997.

[243] Holmes, A. K.; Challis, R. E.; Wedlock, D. J. A Wide Bandwidth Study of Ultrasound Velocity and Attenuation in Suspensions: Comparison of Theory with Experimental Measurements. *J. Colloid Interface Sci.* **1993**, *156*, 261–268. DOI: 10.1006/jcis.1993.1109.

[244] Hipp, A. K.; Storti, G.; Morbidelli, M. Particle Sizing in Colloidal Dispersions by Ultrasound. Model Calibration and Sensitivity Analysis. *Langmuir* **1999**, *15*, 2338–2345. DOI: 10.1021/la981046x.

[245] Storti, G.; Hipp, A. K.; Morbidelli, M. Monitoring Latex Reactors by Ultrasonics. *Polym React Eng* **2000**, *8*, 77–94. DOI: 10.1080/10543414.2000.10744539.

[246] Holmes, A. K.; Challis, R. E.; Wedlock, D. J. A Wide Bandwidth Study of Ultrasound Velocity and Attenuation in Suspensions: Comparison of Theory with Experimental Measurements. *J. Colloid Interface Sci.* **1993**, *156*, 261–268. DOI: 10.1006/jcis.1993.1109.

[247] Kaatze, U.; Trachimow, C.; Pottel, R.; Brai, M. Broadband study of the scattering of ultrasound by polystyrene-latex-in-water suspensions. *Annalen der Physik* **1996**, *508*, 13–33. DOI: 10.1002/andp.2065080104.

[248] Dukhin, A. S. Acoustic spectroscopy for particle size measurement of concentrated nanodispersions. *Characterization of Nanoparticles*; Elsevier, 2020; pp 197–211.

[249] Ocepek, M.; Soucek, M. D.; Berce, P.; Meng, L. Comparison of Particle Size Techniques to Investigate Secondary Nucleation in HEMA-Rich Latexes. *Macromol. Chem. Phys.* **2015**, *216*, 400–416. DOI: 10.1002/macp.201400476.

[250] Aichele, C. P.; Venkataramani, D.; Smay, J. E.; McCann, M. H.; Richter, S.; Khanzadeh-Moradllo, M.; Aboustait, M.; Ley, M. T. A comparison of automated scanning electron microscopy (ASEM) and acoustic attenuation spectroscopy (AAS) instruments for particle sizing. *Colloids Surf., A* **2015**, *479*, 46–51. DOI: 10.1016/j.colsurfa.2015.03.052.

[251] Mende, S.; Stenger, F.; Peukert, W.; Schwedes, J. Mechanical production and stabilization of submicron particles in stirred media mills. *Powder Technology* **2003**, *132*, 64–73. DOI: 10.1016/S0032-5910(03)00042-1.

[252] Babick, F.; Richter, A. Sound attenuation by small spheroidal particles due to visco-inertial coupling. *The Journal of the Acoustical Society of America* **2006**, *119*, 1441–1448. DOI: 10.1121/1.2168427.

[253] Hipp, A. K.; Storti, G.; Morbidelli, M. Acoustic Characterization of Concentrated Suspensions and Emulsions. 2. Experimental Validation. *Langmuir* **2002**, *18*, 405–412. DOI: 10.1021/la015541w.

[254] Epstein, P. S.; Carhart, R. R. The Absorption of Sound in Suspensions and Emulsions. I. Water Fog in Air. *The Journal of the Acoustical Society of America* **1953**, *25*, 553–565. DOI: 10.1121/1.1907107.

[255] Boscher, V.; Helleboid, R.; Lasuye, T.; Stasik, B.; Riess, G. On-line acoustic attenuation spectroscopy of emulsions stabilized by vinyl alcohol–vinyl acetate copolymers: a model system for the suspension polymerization of vinyl chloride. *Polymer International* **2009**, *58*, 1209–1216. DOI: 10.1002/pi.2656.

[256] Stenger, F.; Mende, S.; Schwedes, J.; Peukert, W. Nanomilling in stirred media mills. *Chemical Engineering Science* **2005**, *60*, 4557–4565. DOI: 10.1016/j.ces.2005.02.057.

[257] Dukhin, A. S.; Goetz, P. J. Characterization of aggregation phenomena by means of acoustic and electroacoustic spectroscopy. *Colloids Surf., A* **1998**, *144*, 49–58. DOI: 10.1016/S0927-7757(98)00565-2.

[258] Lechner, M. D. Polymers. In *Springer Handbook of Materials Data*; Warlimont, Ed.; Springer: [Place of publication not identified], 2018; pp 489–540.

[259] Kia, H. G. Thermal expansion of polyurethane reinforced with continuous glass fibers. *Polymer Composites* **1988**, *9*, 237–241. DOI: 10.1002/pc.750090311.

[260] Salgueiro, W.; Somoza, A.; Silva, L.; Consolati, G.; Quasso, F.; Mansilla, M. A.; Marzocca, A. J. Temperature dependence on free volume in cured natural rubber and styrene-butadiene rubber blends. *Physical review. E, Statistical, nonlinear, and soft matter physics* **2011**, *83*, 51805. DOI: 10.1103/PhysRevE.83.051805.

[261] Haynes, W. M., Ed. *CRC handbook of chemistry and physics: A ready-reference book of chemical and physical data*, 97th edition; CRC Press: Boca Raton, London, New York, 2017.

[262] Sokolova, V.; Epple, M. Inorganic nanoparticles as carriers of nucleic acids into cells. *Angewandte Chemie International Edition* **2008**, *47*, 1382–1395. DOI: 10.1002/anie.200703039.

[263] Tiwari, J. N.; Tiwari, R. N.; Kim, K. S. Zero-dimensional, one-dimensional, two-dimensional and three-dimensional nanostructured materials for advanced electrochemical energy devices. *Progress in Materials Science* **2012**, *57*, 724–803. DOI: 10.1016/j.pmatsci.2011.08.003.

[264] Dickinson, E. Food emulsions and foams: Stabilization by particles. *Current Opinion in Colloid & Interface Science* **2010**, *15*, 40–49. DOI: 10.1016/j.cocis.2009.11.001.

[265] Francis, M. J.; Glover, Z. J.; Yu, Q.; Povey, M. J.; Holmes, M. J. Acoustic characterisation of pH dependant reversible micellar casein aggregation. *Colloids Surf., A* **2019**, *568*, 259–265. DOI: 10.1016/j.colsurfa.2019.02.026.

[266] Kolman, K.; Nechyporchuk, O.; Persson, M.; Holmberg, K.; Bordes, R. Preparation of silica/polyelectrolyte complexes for textile strengthening applied to painting canvas restoration. *Colloids Surf., A* **2017**, *532*, 420–427. DOI: 10.1016/j.colsurfa.2017.04.051.

[267] Virden, J. W.; Berg, J. C. The use of photon correlation spectroscopy for estimating the rate constant for doublet formation in an aggregating colloidal dispersion. *J. Colloid Interface Sci.* **1992**, *149*, 528–535. DOI: 10.1016/0021-9797(92)90439-S.

[268] Bibeau, A.; Matijevic, E. Stability of polyvinyl chloride latex. *J. Colloid Interface Sci.* **1973**, *43*, 330–338. DOI: 10.1016/0021-9797(73)90380-9.

[269] Ottewill, R. H.; Watanabe, A. Studies on the mechanism of coagulation. *Kolloid-Zeitschrift* **1960**, *170*, 38–48. DOI: 10.1007/BF01520071.

[270] Bensley, C. N.; Hunter, R. J. The effect of particle volume fraction on the critical coagulation concentration. *J. Colloid Interface Sci.* **1982**, *88*, 546–561. DOI: 10.1016/0021-9797(82)90283-1.

[271] Cowell, C.; Vincent, B. Flocculation kinetics and equilibria in sterically stabilized dispersions. *J. Colloid Interface Sci.* **1983**, *95*, 573–582. DOI: 10.1016/0021-9797(83)90216-3.

[272] Long, J.; Osmond, D.; Vincent, B. The equilibrium aspects of weak flocculation. *J. Colloid Interface Sci.* **1973**, *42*, 545–553. DOI: 10.1016/0021-9797(73)90040-4.

[273] Ehringhaus, A. Objektive Demonstrationen mit Rutilsuspension. *Naturwissenschaften* **1934**, *22*, 149–150. DOI: 10.1007/BF01494784.

[274] Gregory, J. Monitoring particle aggregation processes. *Adv. Colloid Interface Sci.* **2009**, *147–148*, 109–123. DOI: 10.1016/j.cis.2008.09.003.

[275] Israelachvili, J. N. *Intermolecular and Surface Forces*; Academic Press, 2011.

[276] Sano, M.; Kamino, A.; Shinkai, S. Critical Coagulation of Langmuir Monolayers: 2D Schulze−Hardy Rule. *J. Phys. Chem. B* **2000**, *104*, 10339–10347. DOI: 10.1021/jp002387y.

[277] Perkins, R.; Brace, R.; Matijević, E. Colloid and surface properties of clay suspensions. I. Laponite CP. *J. Colloid Interface Sci.* **1974**, *48*, 417–426. DOI: 10.1016/0021-9797(74)90185-4.

[278] Ali, S.; Bandyopadhyay, R. Aggregation and stability of anisotropic charged clay colloids in aqueous medium in the presence of salt. *Faraday Disc.* **2016**, *186*, 455–471. DOI: 10.1039/C5FD00124B.

[279] Tourbin, M.; Frances, C. Monitoring of the aggregation process of dense colloidal silica suspensions in a stirred tank by acoustic spectroscopy. *Powder Technology* **2009**, *190*, 25–30. DOI: 10.1016/j.powtec.2008.04.067.

[280] Hibberd, D.; Holmes, A.; Garrood, M.; Fillery-Travis, A.; Robins, M.; Challis, R. Ultrasonic Monitoring of Oil-in-Water Emulsions Undergoing Depletion Flocculation. *J. Colloid Interface Sci.* **1997**, *193*, 77–87. DOI: 10.1006/jcis.1997.5057.

[281] Chanamai, R.; Herrmann, N.; McClements, D. J. Probing Floc Structure by Ultrasonic Spectroscopy, Viscometry, and Creaming Measurements. *Langmuir* **2000**, *16*, 5884–5891. DOI: 10.1021/la991615g.

[282] Kippax, P.; Sherwood, J. D.; McClements, D. J. Ultrasonic Spectroscopy Study of Globule Aggregation in Parenteral Fat Emulsions Containing Calcium Chloride. *Langmuir* **1999**, *15*, 1673–1678. DOI: 10.1021/la981351i.

[283] Dukhin, A. S.; Goetz, P. J. Chapter 8 - Applications for Dispersions. In *Characterization of Liquids, Dispersions, Emulsions, and Porous Materials Using Ultrasound,* Third edition; Dukhin, A. S., Goetz, P. J., Eds.; Elsevier: Amsterdam, Oxford, Cambridge, MA, 2017; pp 307–355.

[284] Schulze, H. Schwefelarsen in wässriger Lösung. *J. Prakt. Chem.* **1882**, *25*, 431–452. DOI: 10.1002/prac.18820250142.

[285] Hardy, W. B. A preliminary investigation of the conditions which determine the stability of irreversible hydrosols. *Proc. R. Soc. London* **1900**, *66*, 110–125. DOI: 10.1098/rspl.1899.0081.

[286] Kosmulski, M. The pH dependent surface charging and points of zero charge. X. Update. *Adv. Colloid Interface Sci.* **2023**, *319*, 102973. DOI: 10.1016/j.cis.2023.102973.

[287] Khademi, M.; Wang, W.; Reitinger, W.; Barz, D. P. J. Zeta Potential of Poly(methyl methacrylate) (PMMA) in Contact with Aqueous Electrolyte-Surfactant Solutions. *Langmuir* **2017.** DOI: 10.1021/acs.langmuir.7b02487.

[288] Kosmulski, M.; Kalbarczyk, M. Zeta Potential of Nanosilica in 50% Aqueous Ethylene Glycol and in 50% Aqueous Propylene Glycol. *Molecules (Basel, Switzerland)* **2023**, *28.* DOI: 10.3390/molecules28031335.

[289] Cosgrove, T., Ed. *Colloid science: Principles, methods and applications*, 2nd ed.; Wiley: Chichester, West Sussex, 2010.

[290] Agmo Hernández, V. An overview of surface forces and the DLVO theory. *ChemTexts* **2023**, *9.* DOI: 10.1007/s40828-023-00182-9.

[291] Zhu, B.-Y.; Gu, T. General isotherm equation for adsorption of surfactants at solid/liquid interfaces. Part 1. Theoretical. *J. Chem. Soc., Faraday Trans. 1* **1989**, *85*, 3813. DOI: 10.1039/f19898503813.

[292] Zhu, B.-Y.; Gu, T.; Zhao, X. General isotherm equation for adsorption of surfactants at solid/liquid interfaces. Part 2. Applications. *J. Chem. Soc., Faraday Trans. 1* **1989**, *85*, 3819. DOI: 10.1039/f19898503819.

[293] Zhu, B.-Y.; Gu, T. Surfactant adsorption at solid-liquid interfaces. *Adv. Colloid Interface Sci.* **1991**, *37*, 1–32. DOI: 10.1016/0001-8686(91)80037-K.

[294] Langmuir, I. The Adsorption of Gases on Plane Surfaces of Glass, Mica and Platinum. *J. Am. Chem. Soc.* **1918**, *40*, 1361–1403. DOI: 10.1021/ja02242a004.

[295] Gu, T.; Zhu, B.-Y. The S-type isotherm equation for adsorption of nonionic surfactants at the silica gel—water interface. *Colloids Surf.* **1990**, *44*, 81–87. DOI: 10.1016/0166-6622(90)80189-B.

[296] Vale, H. M.; McKenna, T. F. Adsorption of sodium dodecyl sulfate and sodium dodecyl benzenesulfonate on poly(vinyl chloride) latexes. *Colloids Surf., A* **2005**, *268*, 68–72. DOI: 10.1016/j.colsurfa.2005.05.061.

[297] Ohshima, H.; Healy, T. W.; White, L. R. Accurate analytic expressions for the surface charge density/surface potential relationship and double-layer potential distribution for a spherical colloidal particle. *J. Colloid Interface Sci.* **1982**, *90*, 17–26. DOI: 10.1016/0021-9797(82)90393-9.

[298] Frangenberg, M.; Schmidt, A. M.; Wilkens, J. New Experimental Approach for the Proper Consideration of Stagnant and Diffuse Layer Conductivity in the Zeta Potential Determination. *Langmuir* **2025**, *41*, 5188–5201. DOI: 10.1021/acs.langmuir.4c04456.

[299] Meconi, G. M.; Ballard, N.; Asua, J. M.; Zangi, R. Adsorption and desorption behavior of ionic and nonionic surfactants on polymer surfaces. *Soft Matter* **2016**, *12*, 9692–9704. DOI: 10.1039/c6sm01878e.

[300] Hecht, L. L.; Schoth, A.; Muñoz-Espí, R.; Javadi, A.; Köhler, K.; Miller, R.; Landfester, K.; Schuchmann, H. P. Determination of the Ideal Surfactant Concentration in Miniemulsion Polymerization. *Macromolecular Chemistry and Physics* **2013**, *214*, 812–823. DOI: 10.1002/macp.201200583.

[301] Brown, W.; Zhao, J. Adsorption of sodium dodecyl sulfate on polystyrene latex particles using dynamic light scattering and zeta potential measurements. *Macromolecules* **1993**, *26*, 2711–2715. DOI: 10.1021/ma00063a012.

[302] Liu, S. Cooperative adsorption on solid surfaces. *J. Colloid Interface Sci.* **2015**, *450*, 224–238. DOI: 10.1016/j.jcis.2015.03.013.

[303] Odian, G. G. *Principles of polymerization*, Fourth edition; Wiley: Hoboken, N.J, 2004.

[304] Smoluchowski, M. v. Versuch einer mathematischen Theorie der Koagulationskinetik kolloider Lösungen. *Zeitschrift für Physikalische Chemie* **1918**, *92U*, 129–168. DOI: 10.1515/zpch-1918-9209.

[305] Duangthanu, M.; Pattanaporkratana, A. Effect of surfactant concentration to aggregations of nanogold particles. *J. Phys.: Conf. Ser.* **2017**, *901*, 12098. DOI: 10.1088/1742-6596/901/1/012098.

[306] Helgason, T.; Awad, T. S.; Kristbergsson, K.; McClements, D. J.; Weiss, J. Effect of surfactant surface coverage on formation of solid lipid nanoparticles (SLN). *J. Colloid Interface Sci.* **2009**, *334*, 75–81. DOI: 10.1016/j.jcis.2009.03.012.

[307] Grau, C.; Schmidt, A. M.; Wilkens, J. Water-Based Polyurethane Dispersions: A Detailed Analysis of the Particle Charge Using Soft and Hard Particle Model. *Langmuir* **2024**, *40*, 22123–22135. DOI: 10.1021/acs.langmuir.4c02498.

[308] Israelachvili, J. N. Electrostatic Forces between Surfaces in Liquids. *Intermolecular and Surface Forces*; Elsevier, 2011; pp 291–340.

[309] Prieve, D. C.; Russel, W. B. Simplified predictions of Hamaker constants from Lifshitz theory. *J. Colloid Interface Sci.* **1988**, *125*, 1–13. DOI: 10.1016/0021-9797(88)90048-3.

[310] Hough, D. B.; White, L. R. The calculation of hamaker constants from liftshitz theory with applications to wetting phenomena. *Adv. Colloid Interface Sci.* **1980**, *14*, 3–41. DOI: 10.1016/0001-8686(80)80006-6.

[311] Cowell, C.; Li-In-On, R.; Vincent, B. Reversible flocculation of sterically-stabilised dispersions. *J. Chem. Soc., Faraday Trans. 1* **1978**, *74*, 337. DOI: 10.1039/f19787400337.

[312] Luppé, F.; Conoir, J.-M.; Norris, A. N. Effective wave numbers for thermo-viscoelastic media containing random configurations of spherical scatterers. *J. Acoust. Soc. Am.* **2012**, *131*, 1113–1120. DOI: 10.1121/1.3672690.

[313] Luppé, F.; Conoir, J.-M.; Valier-Brasier, T. Longitudinal and transverse coherent waves in media containing randomly distributed spheres. *Wave Motion* **2022**, *115*, 103082. DOI: 10.1016/j.wavemoti.2022.103082.

[314] International Organization for Standardization. *Plastics — Polyurethane raw materials — Determination of isocyanate content*, 2009, *83.080.10* (ISO 14896:2009).

[315] Leroy, P.; Tournassat, C.; Bernard, O.; Devau, N.; Azaroual, M. The electrophoretic mobility of montmorillonite. Zeta potential and surface conductivity effects. *J. Colloid Interface Sci.* **2015**, *451*, 21–39. DOI: 10.1016/j.jcis.2015.03.047.

[316] Crespy, A.; Bolève, A.; Revil, A. Influence of the Dukhin and Reynolds numbers on the apparent zeta potential of granular porous media. *J. Colloid Interface Sci.* **2007**, *305*, 188–194. DOI: 10.1016/j.jcis.2006.09.038.

12 Appendix

12.1 Additional Experimental Data

This section contains supplementary electrokinetic measurements of three inorganic dispersions are presented here. This study includes two silica dispersions, silica@0.03 and silica@0.16 and one rutile dispersion, rutile@0.38, selected to represent typical metal oxide systems. The dispersions of silica@0.16 and rutile@0.38 were diluted to an intended ionic strength of 10 mmol·L^{-1}, while silica@0.03, which also serves as a calibration standard for CVI measurements with the DT 1202 device, was diluted to 8.8 mmol·L^{-1} in accordance with the calibration protocol. In all cases, KCl solutions were used for dilution. Due to limited sample availability, no pre-treatment such as dialysis could be performed. Consequently, slight deviations in electrolyte concentration between samples could not be excluded.

Fig. 12.1 summarises the corresponding electrokinetic characterisation, presented analogously to the diagrams before. Diagrams A–C show the measured relative conductivities $K_\mathrm{s}K_\mathrm{m}^{-1}$ as black squares for each system, along with the conductivity of the medium K_m as blue circles (secondary axis). The red dashed line shows the expected course for $Du = 0$ and the solid black line represents the MWO-based fit. For the silica@0.03 and rutile@0.38 samples, a clear trend in K_m for different volume fraction φ reveals distinct non-equilibrium dilution, which complicates interpretation of the data. Nevertheless, both systems exhibit only minor deviations from the $Du = 0$ case, suggesting negligible surface conductivity under the experimental conditions. In contrast, silica@0.16 shows a moderate deviation from this case, yielding an estimated Dukhin number $Du^{\mathrm{d+s}} = 0.084$, indicative of a modest surface conductivity contribution. Despite the limitations imposed by non-equilibrium dilution, the overall results suggest that surface conductivity remains low in the investigated inorganic dispersions. Whether this observation reflects a general trend that inorganic systems exhibit lower surface conductivity than polymer dispersions under similar ionic strength conditions cannot yet be confirmed, given the small sample set and the absence of rigorous equilibrium dilution. Moreover, previous studies have reported significant surface conductivity for inorganic systems [183,184,193,315,316].

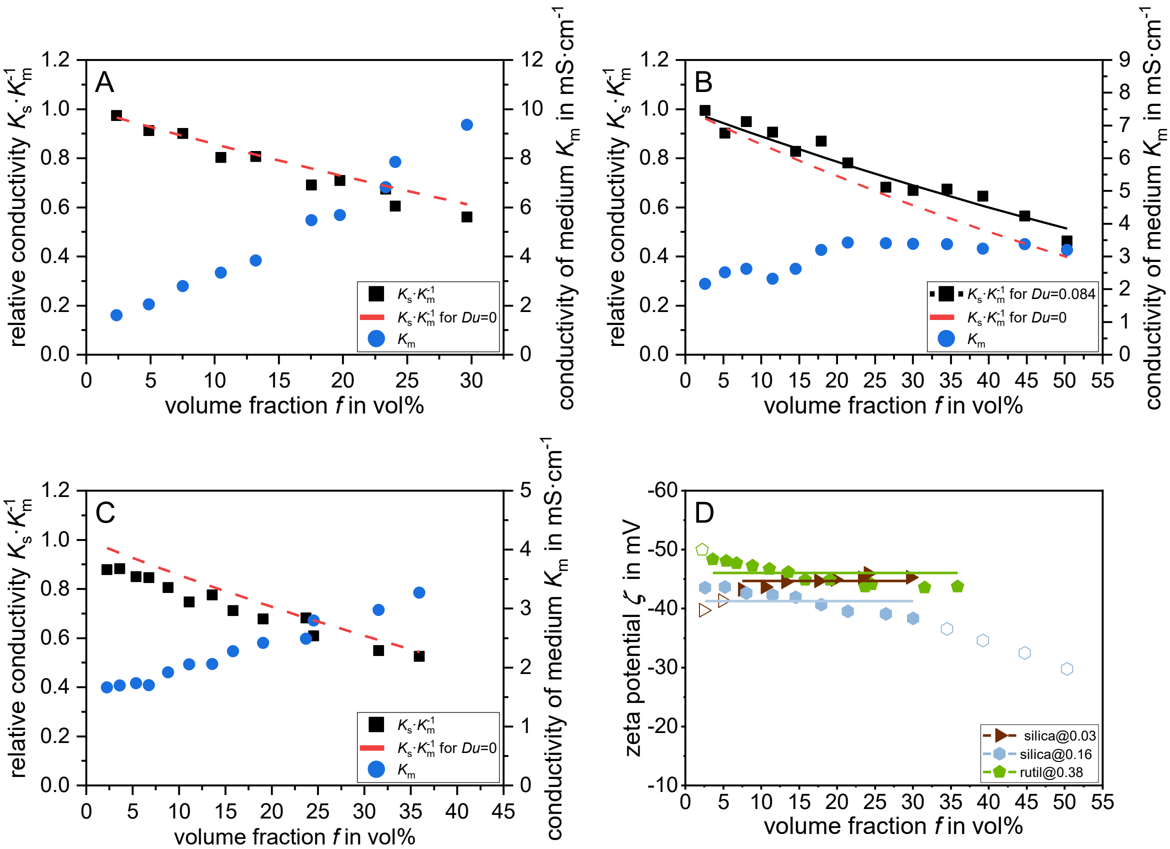

Fig. 12.1: Conductivity of media and relative conductivity of samples, which were not presented in the main article. Where **A** is silica@0.03 (pH value of 9.5), **B** is silica@0.16 (pH value of 10.5), **C** is rutile@0.38 (pH value of 8.4). Measured relative conductivities $K_s \cdot K_m^{-1}$ are plotted as black squares. The black solid line refers to the fit of $K_s \cdot K_m^{-1}$ according to MWO theory. For comparison, the course of $K_s \cdot K_m^{-1}$ for $Du = 0$ has been plotted as a red dashed line. Conductivities of the medium K_m are shown as blue dots on the secondary y axis. **D** is showing Zeta potential ζ measured by the CVI method as a function of particle volume fraction φ for samples silica@0.03, silica@0.16 and rutile@0.38. Filled data points were considered for the calculation of the average zeta potential value $\zeta_{\mathrm{CVI}}^{\mathrm{d+s}}$ (shown as solid line), whereas unfilled data points were neglected.

The corresponding zeta potentials determined via the CVI method are shown in Fig. 12.1 D. Filled symbols represent data points included in the calculation of the average $\zeta_{\mathrm{CVI}}^{\mathrm{d+s}}$ value (solid line), while unfilled symbols were excluded due to inconsistencies or suspected measurement artefacts. The samples silica@0.03 and rutile@0.38 exhibit nearly constant zeta potentials with an average value of -44.7 mV and –45.7 mV, respectively. The zeta potential of silica@0.16 has slight variation across the concentration range and an average zeta potential of –41.3 mV. These relatively low values are consistent with the low surface conductivity observed in these systems. For silica@0.16, the $\zeta_{\mathrm{CVI}}^{\mathrm{d+s}}$ and $Du^{\mathrm{d+s}}$ yield a diffuse layer contribution of $Du^{\mathrm{d}} = 0.029$, implying a ratio $Du^{\mathrm{s}}/Du^{\mathrm{d}} = 1.90$. This finding suggests that stagnant layer conductivity can play a substantial role even in dispersions with moderate zeta potential.

12.2 List of Symbols

Γ_∞	maximum adsorption
Λ^0	limiting molar conductivity at infinite dilution
C_p	specific heat capacity
N_A	Avogadro constant
R^2	coefficient of determination
g_1	field correlation function
g_2	autocorrelation function
k^{-1}	Debye length
k_B	Boltzmann constant
α	absolute attenuation
ε_0	vacuum permittivity
σ_0	surface charge density
ψ_0	surface potential
ψ_d	Stern potential
ΔP	pressure difference
h	separation distance
Γ	surfactant adsorbed per unit area or decay rate
Ω	drag coefficient
A	instrument constant or Hamaker constant
C	coefficient
D	diffusion coefficient
Du	Dukhin number
E	electric field strength or extinction
F	function/factor
G	function/factor
H	function/factor or heat transfer coefficient
I	intensity
K	conductivity or function/factor
T	thermodynamic temperature
V	volume or interaction energy
Z	acoustic impendence
Z	function/factor
a	particle radius
c	concentration or sound velocity
d	particle diameter
e	elementary charge
f	frequency of ultrasound or function
g	function or factor
i	imaginary number

k	complex wave number or equilibrium constant
m	dimensionless ion mobility or slope of $\mathrm{dlog}(E)/\mathrm{dlog}(\lambda)$
n	surface aggregation number or refractive index
p	ion diffusion ratio parameter
q	scattering vector
s	symmetry parameter
t	time or function/factor
v	velocity
w	weight fraction
z	charge number/valency
α	attenuation coefficient
β	volumetric thermal expansion
δ	steepness parameter
ε	relative permittivity
ζ	zeta potential
η	dynamic viscosity
θ	scattering angle
κ	Debye-Hückel parameter
λ	wave length
μ	electrophoretic mobility
ρ	density
τ	thermal conductivity or delay time
φ	volume fraction
ω	angular frequency of ultrasonic wave

12.2.1 List of Subscripts

$-$	anions
$+$	cations
0	initial
10	10th percentile
50	median
90	90th percentile
99.5	measured at 99.5 MHz
A1	first approach
A2	second approach
A3	third approach
B	Born
c	counterion
co	co-ion
cr	critical or characteristic
CVI	colloid vibration current

d	dynamic or dissipative
EDL	electrical double layer
eff	effective
ELS	electrophoretic light scattering
ext	external
H	Henry
h	hydrodynamic
hd	hydrodynamic relaxation
i	inflection point or inertial
inc	maximum increase
int	internal or intrinsic absorption
m	medium
M	molecular
max	maximum
meas	measured
min	minimum
mod	modelle
MW	Maxwell-Wagner
p	particle
res	residual
s	dispersion or static
sc	scattering
st	structural
stb	stable dispersion
T	total or transducer
th	thermal
vdW	van der Waals
vis	viscoinertial
i	ionic species
x	distance
η	viscous
ω	angular frequency of ultrasonic wave

12.2.2 List of Superscripts

$-$	dimensionless
AAS	acoustic attenuation spectroscopy
d	diffuse layer
ek	electrokinetic
H	Henry
HS	Helmholtz-Smoluchowski
m	medium

p	particle
REF	reference
s	stagnant layer
tit	titration
σ	surface

12.3 List of Abbreviations

AAS	acoustic attenuation spectroscopy
AFM	atomic force microscopy
$CaCl_2$	calcium chloride
CCC	critical coagulation concentration
CDF	cumulative distribution function
CST	capillary suction time
CVI	colloid vibration current
CVP	colloid vibration potential
DBTL	dibutyltin dilaurate
DLC	diffuse layer conductivity
DLS	dynamic light scattering
DLVO	Derjaguin-Landau-Verwey-Overbeek
DS	Dukhin-Semenikhin
EA	electroacoustics
ECAH	Epstein-Carhart-Allegra-Hawley
EDL	electrical double layer
ELS	electrophoretic light scattering
ESA	electrokinetic sonic amplitude
HB-B	Henry-Booth or Bruggeman
HCl	hydrochloric acid
HS	Helmholtz-Smoluchowski
IHP	inner Helmholtz plane
IPDA	isophoronediamine
IPDI	isophorone diisocyanate
IVI	ion vibration current
KCl	potassium chloride
KPS	potassium persulfate
LAS	linear alkylbenzene sulfonate
LDS	laser diffraction spectroscopy
LED	light-emitting diode
LWR	long wave regime
MWO	Maxwell-Wagner-O'Konski
NaOH	sodium hydroxide
n-BU	n-butyl acrylate
NCO	isocyanate functional group
ODA	octadecyl acrylate
OHP	outer Helmholtz plane
OHW	Ohshima-Healy-White
PBAMM	polymethyl methacrylate-*co*-butyl acrylate

PCS	photon correlation spectroscopy
PDF	probability density function
PIDS	polarization intensity differential scattering
PPVE	perfluoro(propyl vinyl ether)
PSD	particle size distribution
PTFE	polytetrafluoroethylene
PU	polyurethane
PUD	polyurethane dispersion
PVC	polyvinyl chloride
QELS	quasi-elastic light scattering
SBR	styrene-butadiene rubber
SDS	sodium dodecyl sulphate
SEM	scanning electron microscopy
SLC	stagnant layer conductivity
SP	slip or shear plane
TEM	transmission electron microscopy
TVI	total vibration current
UAS	ultrasonic attenuation spectroscopy
UV	ultraviolet
Vis	visible

12.4 List of Figures

12.5 List of Tables

12.6 Declaration of Individual Contributions

Chapter 4: The experimental work, conceptualization, methodology, data evaluation, and visualization were performed by Matthias Frangenberg. Prof. Dr. Annette M. Schmidt supervised the work, contributed to discussions and reviewed and edited the manuscript. Prof. Dr. Jan Wilkens supervised the work, provided conceptual and methodological guidance, contributed to discussions and was responsible for project administration, resources, funding acquisition and the review and editing of the manuscript. Discussions with Dr. Andrei S. Dukhin of Dispersion Technology Inc., Bedford Hills, NY, USA, contributed to the development of the experimental and analytical approaches used in this study. The polymer latices examined in this study were provided by Westlake Vinnolit GmbH & Co. KG (PVC), Arlanxeo Switzerland S.A. (SBR), 3M Dyneon GmbH (PTFE) and synthesized as part of master's theses by Christina Gassner (PU; supervised by Christoph Grau) at Heinrich Heine University Düsseldorf in 2021 and Sven Kroß (PBAMM; supervised by Matthias Frangenberg) at TH Köln in 2021.

Chapter 5: The experimental work, conceptualization, methodology, data evaluation, and visualization were performed by Matthias Frangenberg. Prof. Dr. Annette M. Schmidt supervised the work, contributed to discussions and reviewed and edited the manuscript. Prof. Dr. Jan Wilkens supervised the work, provided conceptual and methodological guidance, contributed to discussions and was responsible for data evaluation, project administration, resources, funding acquisition and the review and editing of the manuscript. Sarah Voigt measured the zeta potentials as a function of electrolyte concentration, as part of her bachelor's theses at TH Köln in 2022 (supervised by Matthias Frangenberg) Discussions with Dr. Andrei S. Dukhin of Dispersion Technology Inc., Bedford Hills, NY, USA, contributed to the development of the experimental and analytical approaches used in this study. He also provided software support for the DT-1202 measuring device, which was utilized in the analysis. The polymer latices examined in this study were provided by Westlake Vinnolit GmbH & Co. KG (PVC), Arlanxeo Switzerland S.A. (SBR) and synthesized as part of master's theses by Christina Gassner (PU; supervised by Christoph Grau) at Heinrich Heine University Düsseldorf in 2021 and Sven Kroß (PBAMM; supervised by Matthias Frangenberg) at TH Köln in 2021.

Chapter 6: The experimental work, conceptualization, methodology, data evaluation, and visualization were performed by Matthias Frangenberg. Prof. Dr. Annette M. Schmidt supervised the work and contributed to discussions. Prof. Dr. Jan Wilkens supervised the work, contributed to discussions and was responsible for project administration, resources and funding acquisition. Discussions with Andrei S. Dukhin of Dispersion Technology Inc., Bedford Hills, NY, USA, contributed to the development of the experimental and analytical approaches used in this study. The polymer latices examined in this study were provided by Westlake Vinnolit GmbH & Co. KG (PVC), Arlanxeo Switzerland S.A. (SBR), 3M Dyneon GmbH (PTFE) and synthesized as part of master's theses by Christina Gassner (PU; supervised by Christoph Grau) at Heinrich Heine University Düsseldorf in 2021 and Sven Kroß (PBAMM; supervised by Matthias Frangenberg) at TH Köln in 2021.

Chapter 7: The conceptualization, methodology, data evaluation, and visualization were performed by Matthias Frangenberg. Prof. Dr. Annette M. Schmidt supervised the work. Prof. Dr. Jan Wilkens supervised the work, contributed to discussions and was responsible for project administration, resources and funding acquisition. The development of the measurement protocol for determining the surfactant adsorption isotherm was proposed by Matthias Frangenberg and validated by Enrico Pauly during a practical project at TH Köln in 2020 (supervised by Matthias Frangenberg). The investigation of the adsorption isotherm for the SDS surfactant on the PVC@0.20 sample was conducted as part of Enrico Pauly's bachelor thesis in 2021 at TH Köln (supervised by Matthias Frangenberg). The investigation of the adsorption isotherm for the SDS surfactant on the PVC@0.78 sample, which was stabilized with LAS surfactant, was performed as part of Adinda Abdu's bachelor thesis in 2021 at TH Köln (supervised by Matthias Frangenberg). The development of the measurement protocol for determining the critical coagulation concentration (CCC) via acoustic attenuation was proposed by Matthias Frangenberg and validated by Sarah Voigt during a practical project at TH Köln in 2022 (supervised by Matthias Frangenberg). The determination of CCCs using acoustic attenuation was carried out by Sarah Voigt as part of her bachelor thesis in 2022 at TH Köln (supervised by Matthias Frangenberg). All other measurements presented in the supporting information were performed by Matthias Frangenberg. The PVC latices used in this study were provided by Westlake Vinnolit GmbH & Co. KG.

General: Financial and material support, as well as valuable discussions, were provided by Westlake Vinnolit GmbH & Co. KG, enhancing the scope and quality of the work. This project received funding from the German Ministry of Education and Research (BMBF) as part of the funding program "Forschung an Fachhochschulen" under contract number 13FH142PX6.

12.7 Danksagung

An dieser Stelle möchte ich mich bei den Menschen bedanken, die mich während meiner Dissertation und meiner wissenschaftlichen Laufbahn unterstützt, begleitet und inspiriert haben.

Mein besonderer Dank gilt meiner Familie, insbesondere meinen Eltern, die mir stets Rückhalt und Unterstützung gegeben haben, und meiner Schwester, die immer für mich da war.

Ein ganz besonderer und herzlicher Dank geht an meine Freundin Anna-Lena. Deine Liebe, Geduld und unerschütterliche Unterstützung haben mich durch alle Höhen und Tiefen dieser Zeit getragen. Du warst nicht nur meine größte Motivation, sondern auch mein Anker, wenn die Herausforderungen übermächtig schienen. Deine Stärke und dein Glaube an mich haben diese Arbeit möglich gemacht, und dafür bin ich dir unendlich dankbar.

Ich möchte auch meinen Kolleg:innen danken, die mich auf meinem wissenschaftlichen Weg begleitet haben: Suzi, Thomas und insbesondere Tobias und Christopher, mit denen ich während des Studiums und der Promotion viele prägende Momente teilen durfte.

Mein Dank gilt ebenfalls meinen Freund:innen aus dem Studium, insbesondere Stefan, der mich während des Studiums und der Promotion begleitet hat, sowie Vanessa, Jil und allen weiteren, die diese Zeit unvergesslich gemacht haben, darunter Simon, Tim, Jan, Mario, Viktor, Marvin, Alexander, Pascal und Annicke.

In der Promotionszeit war ich ebenso von wunderbaren Menschen umgeben, die diese Phase bereichert haben: Flore, Kevin, Leonard, Niels, Hendrik und Janine. Danke für eure Unterstützung und die gemeinsamen Erlebnisse.

Ein großer Dank gilt auch den Studierenden Daniel, Billy, Sarah, Sven, Christina, Enrico, Emre, Stalyo, Benedikt und Adinda, die durch ihre Abschlussarbeiten und ihre Unterstützung einen wertvollen Beitrag zu meiner Forschung geleistet haben.

Mein tief empfundener Dank gilt meinem Betreuer, Herrn Prof. Dr. Jan Wilkens, der mir nicht nur ein spannendes und inspirierendes Thema ermöglicht hat, sondern mir auch stets Vertrauen entgegengebracht, fachliche Unterstützung geleistet und die nötigen Ressourcen bereitgestellt hat. Deine Leidenschaft für die Wissenschaft und dein Engagement für meine Arbeit haben mich nachhaltig geprägt und motiviert. Dafür möchte ich dir von Herzen danken.

Ein ebenso großer Dank geht an Frau Prof. Dr. Annette Schmidt. Deine Förderung, dein fachlicher Rat und deine Bereitschaft, mich auf diesem Weg zu begleiten, waren von unschätzbarem Wert.

Diese Dissertation wäre ohne die Unterstützung, den Glauben und die Hilfe all dieser Menschen nicht möglich gewesen. Ich danke euch allen von Herzen!